Detection of stratigraphic heterogeneities at sub-seismic scale
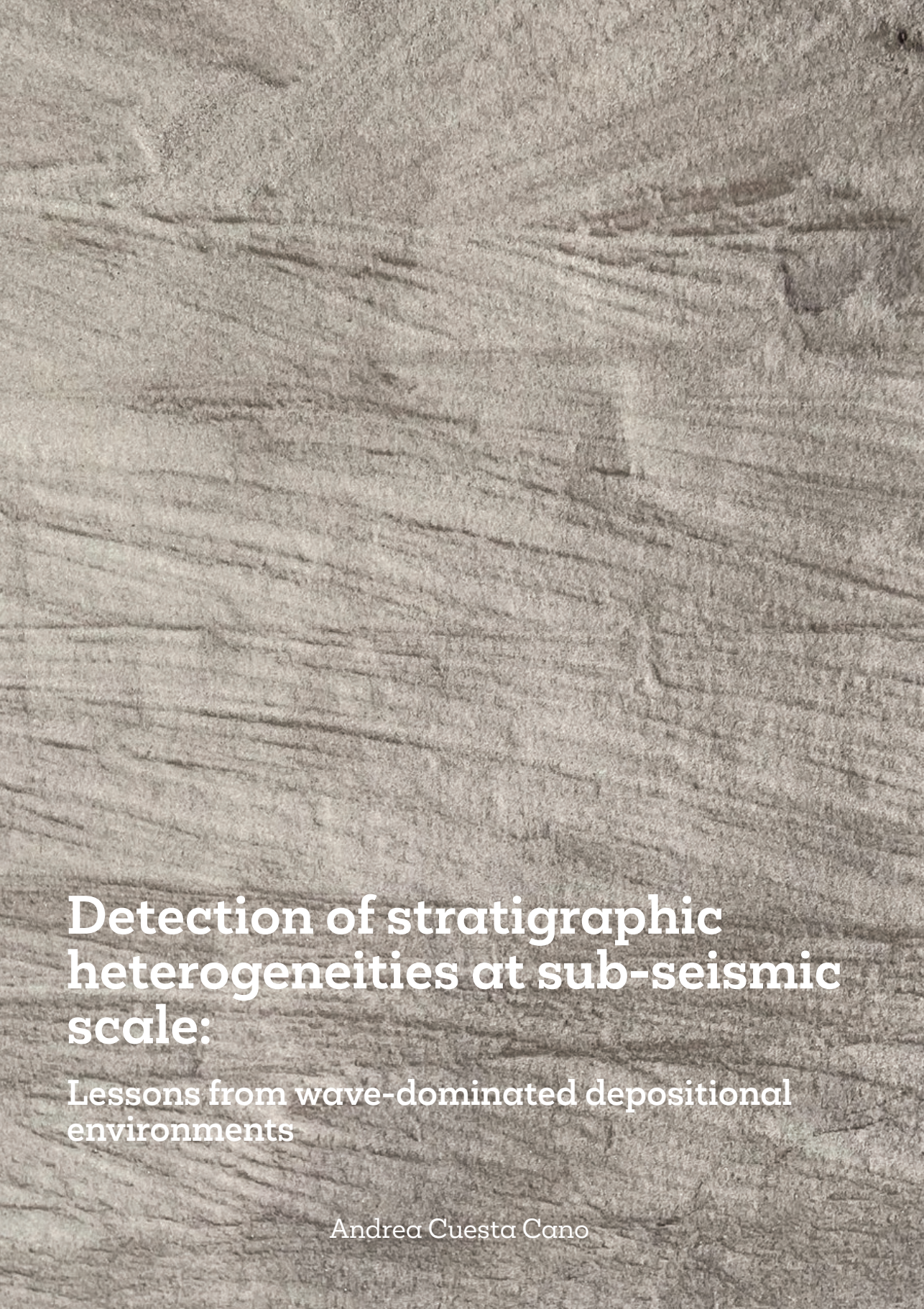Lessons from wave-dominated depositional environments

Cuesta Cano, A.

Important note
To cite this publication, please use the final published version (if applicable).
Please check the document version above.

Detection of stratigraphic heterogeneities at sub-seismic scale:

Lessons from wave-dominated depositional environments

Andrea Cuesta Cano

Propositions

accompanying the dissertation

Detection of stratigraphic heterogeneities at sub-seismic scale:
Lessons from wave-dominated depositional environments

by

Andrea CUESTA CANO

1. From outcrop analysis we know that sedimentological properties—such as grain size, sorting, and organic matter content —in shallow marine clastic environments vary both vertically and laterally below seismic resolution. Petrophysical properties within the rock samples that formed in similar depositional conditions can vary by more than 30%, resulting in overlapping average values across facies. (Chapter 2)

2. Distributing petrophysical and acoustic properties based on lithology is a good starting point for reservoir characterisation. However, accounting for finer-scale sedimentological variability enables a more accurate representation of reservoir architecture. (Chapter 4)

3. Asymmetry in angle-gather data statistically relates to P-wave velocity changes at meter scale within the reservoir. However, such data are also influenced by illumination artifacts and the inherent discretisation of the model grid. (Chapter 5)

4. Advancing scientific knowledge requires collaboration across disciplines. Future research must foster cross-departmental and interdisciplinary partnerships to push the boundaries of what we know. (This thesis)

5. Publishing failed methodologies and experimental designs can be as valuable—if not more so—than publishing only those that enabled the analysis of scientific hypotheses.

6. Despite our responsibility to society, scientists often overlook outreach and science communication. We must do more to share our research and its possible impact with the society.

7. The consequence of flex desk and clean desk policies is offices that lack the personal imprint of those who inhabit them.

8. Ensuring an adequate number of microwaves in the workplace, based on employee demand, is a simple step toward a more inclusive work environment.

9. One step forward for reaching true gender equality is equal, compulsory parental leave for both parents—same duration, same financial conditions—regardless of employment sector. Then starting a family would have the same impact on the career of both female and male professionals.

10. Governments must prioritize high-quality, free healthcare and education by combating fiscal evasion by the wealthy. These are people's rights, not privileges.

These propositions are regarded as opposable and defendable, and have been approved as such by the promotor Prof. dr. A.W. Martinius and promotor dr. J.E.A. Storms.

Detection of stratigraphic heterogeneities at sub-seismic scale:

Lessons from wave-dominated depositional environments

Detection of stratigraphic heterogeneities at sub-seismic scale:

Lessons from wave-dominated depositional environments

Dissertation

for the purpose of obtaining the degree of doctor

at Delft University of Technology

by the authority of the Rector Magnificus, prof. dr. ir. T.H.J.J. van der Hagen,

chair of the Board for Doctorates

to be defended publicly on

Thursday 11, December 2025 at 10:00 o'clock

by

Andrea CUESTA CANO

Master of Science in Earth Sciences, Utrecht University, The Netherlands

born in Valle de Trápaga / Trapagaran, Spain

This dissertation has been approved by the promotors.

Composition of the doctoral committee:

Rector Magnificus,	chairperson
Prof. dr. A.W. Martinius,	Delft University of Technology, *promotor*
Dr. J.E.A. Storms,	Delft University of Technology, *promotor*

Independent member:

Prof. dr. ir. E.C. Slob,	Delft University of Technology
Prof. dr. G.J. Hampson,	Imperial College London
Dr. M. Huuse,	The University of Manchester
Dr. H. van der Vegt,	Deltares
Prof. dr. H. Hajibeygi,	Delft University of Technology, reserve member

Other member:

Dr. G. Rongier,	Delft University of Technology

An electronic copy of this dissertation is available at
https://repository.tudelft.nl/.

Las cosas de palacio van despacio.

Traditional Spanish proverb

The mills of God grind slowly, but they grind exceeding small.

Proverb, attributed to Sextus Empiricus

Contents

Summary

As the world shifts away from fossil fuels, accurate subsurface characterization is becoming increasingly vital for projects like CO_2 sequestration, hydrogen storage, mining, and geothermal energy. These projects often operate within narrow economic margins, requiring predictions with minimal and quantifiable uncertainty to ensure safe and cost-effective decision-making. Characterizing the subsurface is a complex task due to its heterogeneous nature, composed of varying rock types, characterised by varying properties, and intricate geological structures at multiple scales. Since direct observations are limited, we primarily rely on indirect techniques — most notably seismic data — to image the subsurface. However, the resolution of seismic data is limited, often failing to capture small-scale, metre-level heterogeneities. Despite their size, these features can significantly affect fluid flow and reservoir behaviour, making their detection and characterization crucial. Therefore, advancing workflows that maximize the extraction of detailed information from indirect data is essential for developing precise geological models that support the efficient and safe exploitation of subsurface resources in the ongoing energy transition.

The goal of this thesis is to develop a workflow capable of improving the detection of sub-seismic scale stratigraphic heterogeneities in the reservoir. To achieve this, the research integrates stratigraphic forward modelling with seismic forward modelling and migration, a combination believed to enable the inclusion of multi-scale stratigraphic heterogeneities in geological models to better understand their seismic response. The underlying hypothesis is that such integration allows for the identification of heterogeneities that remain undetectable through conventional seismic analysis alone, by bridging geological, petrophysical, and geophysical data domains. To evaluate this hypothesis, the study focuses on heterogeneities developed in clastic, wave-dominated shoreface systems.

The study begins with a detailed characterization of a wave-dominated shoreface outcrop in Montana (Chapter 2). This initial study aims at understanding the distribution of stratigraphic heterogeneities at outcrop analogue level. The results highlight the complexity and variability of stratigraphic heterogeneities and their associated petrophysical and acoustic properties. The observed spatial variability and subtle transitions of the measured properties underscore the challenges in capturing these features using conventional, lithology-based, forward seismic methods.

Next, this thesis presents a novel workflow, developed to integrate stratigraphic forward modelling with forward seismic modelling (Chapter 4). By translating grain-

size distributions obtained from the stratigraphic simulations into acoustic properties, synthetic seismic data are generated. This approach provides a more nuanced representation of metre-scale heterogeneities than traditional lithology-based models and proves that a grain-size based acoustic property distribution results in better seismic representation of the stratigraphic structures of wave-dominated shoreface systems.

Thereafter, the potential of angle-dependent seismic data is assessed as a means to detect and characterise the heterogeneities of acoustic property distributions (Chapter 5). The observed moderate correlations between angle-gather asymmetry and acoustic property variations, especially P-wave velocity, demonstrate promise. However, the analysis also reveals limitations inherent in current forward-modelling techniques, emphasizing the need for further refinement of forward seismic methods to better capture the geological heterogeneities.

The approach of this thesis bridges geological, petrophysical, and seismic data, enabling a more nuanced understanding of subsurface complexity beyond traditional lithology-based methods. Results reveal significant variability in petrophysical properties within depositional environments, highlighting the limitations of conventional seismic inversion workflows. The investigation of angle-dependent seismic data demonstrates its potential for detecting subtle acoustic variations, though challenges remain in synthetic data accuracy.

Lastly, this research highlights that there is still significant room for further investigation. Opportunities lie in deepening our understanding of the links between sedimentological, petrophysical, and acoustic properties; in integrating more complex geological models that capture multiple depositional environments and complex stratigraphic patterns; and in incorporating subsurface data for more targeted studies. Additionally, the exploration of in-well seismic data acquisition techniques offers potential for constructing high-resolution, reservoir-scale models, for which the impact of the overburden would be restricted. The role of machine learning also emerges as a promising avenue, particularly in analysing lateral heterogeneities and their impact on the asymmetry of angle-gather data. What remains evident is that advancing this field will require close collaboration among experts in geology, petrophysics, and geophysics.

1

Introduction

1.1. Rationale

The subsurface is rich in resources that society has exploited for centuries and that have led to major technological and economic developments. Examples of these resources are minerals, water, hydrocarbons, and heat. If we look back in time, the first mining activities to exploit materials – such as flint, gold, or copper – from the shallow subsurface date back to prehistoric times [1–4]. Moreover, wells have been used to extract potable water from shallow aquifers since the Bronze Age [5]. For centuries, only the resources in the shallower tens of metres of the subsurface were exploited, so defining the deeper structures of the subsurface was unnecessary. However, in the second half of the 19th century, interest in the subsurface exponentially increased once the energy capacities of natural gas and oil were discovered, starting the 'Age of Oil' [6]. From then on, major investments were devoted to improving our capacity to decipher the structure of the subsurface.

Now, as we embark on an energy transition towards a world without dependency on fossil fuels, the subsurface has gained renewed interest. Subsurface characterisation is essential for the development of projects related to CO_2 sequestration, H_2 storage, mining, and geothermal production, projects where the economic benefit margin is restricted, and for which project managers and stakeholders need predictions with minimal, quantifiable uncertainty [7, 8]. Consequently, some research projects, like presented here, work on improving the workflows that we use to study the subsurface, to be able to extract as much information as possible from the data and elaborate complete and detailed models of the geological structures underneath our feet. These geological models will then help us answer questions related to, for example, the location of mining resources, the shape of traps for CO_2 sequestration or H_2 storage, or the path that fluids would follow in geothermal and groundwater studies.

The characterisation of the subsurface, i.e. deciphering its structure and property distribution, is a tricky assignment. The first reason is the presence of heterogeneities in the rocks. The subsurface is not a laterally homogeneous medium. Instead, it is a combination of different rock types, that experience changes in their properties at different spatial scales and that are arranged in different types of structures. As for the second reason, we mainly rely on indirect data to characterize these changes, and the amount of detail that we can extract from these data is limited. Extracting as much and as precise information as possible from indirect data has become one of the grand challenges of the energy transition, as accurate models are critical for the safe and efficient use and exploitation of the subsurface.

This research focuses on understanding the relation between small- to intermediate-scale, stratigraphic heterogeneities and a specific type of indirect data, seismic data. By stratigraphic heterogeneity we refer to spatial changes in the rock properties, such as grain size or porosity that can be abrupt or gradual in nature. Small- to intermediate-scale heterogeneities are those that develop at metre-scale. This type

of heterogeneities develops in all depositional environments, but here I focus on the heterogeneities developed in clastic, wave-dominated shoreface deposits. The main heterogeneities in wave-dominated shoreface systems develop perpendicular to the coastline, allowing a simplified two-dimensional approach, in contrast to other environments where heterogeneities are more complex and three-dimensional.

1.2. Seismic data for subsurface characterisation

The analysis of core data allows the collection of direct observations and measurements of the lithology and rock properties from the subsurface. These measurements, however, are limited to a very small volume of the reservoir and they provide little to no information on how structures extend in the lateral direction (Figure 1.1). To capture the three-dimensional nature of these structures, we rely on geophysical techniques, indirect measurements of the subsurface properties, such as the seismic data collected from the surface or well log data measured from boreholes. Seismic reflection is one of the main techniques employed for imaging the subsurface [9–12]. This method works similarly to the medical ultrasound analysis, by providing an image of the organization of the layers at depth, the same way an ultrasound gives us an image of the interior of our bodies. To do so, we record the way sound waves travel through the different materials that constitute the subsurface (Figure 1.2).
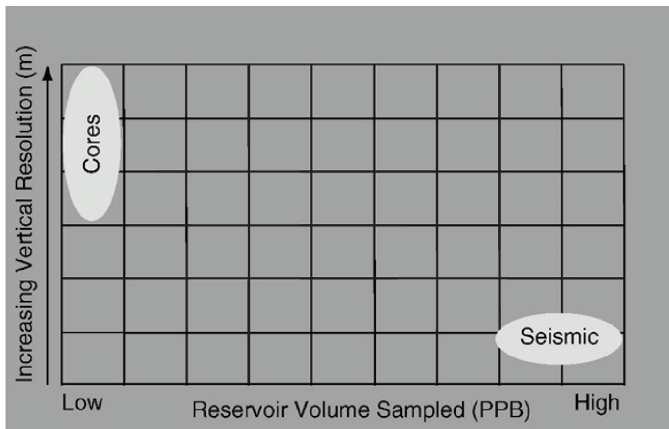
Figure 1.1: Graph showing the different subsurface data types that sample the reservoir volume plotted against the corresponding vertical resolution of each data type. Note that a large reservoir volume is not sampled and needs to be addressed using other measurement tools – or outcrops. Modified from Keogh, Martinius and Osland [13]

Even though the reservoir volume sampled with seismic data is large, the amount of detail that we can interpret from this type of data, namely the resolution, is limited
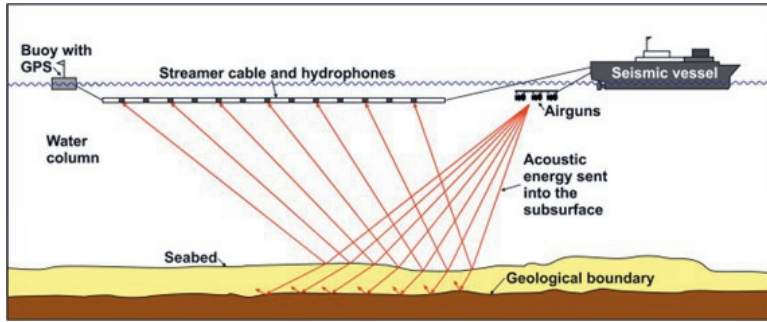
Figure 1.2: Schematic of the seismic data acquisition process. During acquisition, acoustic energy generated by airguns is sent into the subsurface and the energy that reflects back at geological boundaries in the subsurface is recorded by the hydrophones. From Cox, Newton and Huuse [12]

(Figure 1.1). Seismic resolution is the ability to differentiate two features, e.g. two layers with different properties, from one another [12]). The resolution depends on the depth of the reservoir, the velocity of seismic waves through the layers in the subsurface and the frequency used for the data acquisition. The seismic resolution is defined in both vertical and horizontal directions. The vertical resolution represents the ability to recognise changes in the medium in the vertical direction, the direction in which sedimentary layers accumulate over time. Under perfect conditions, the vertical resolution equals $\frac{1}{4}$ of the wavelength, and this distance is known as "tuning thickness" [9, 12]. The value of the wavelength depends on the frequency used for the acquisition of seismic data and the dominant wave velocity of the materials through which the sound wave travels [10, 14]. Because of attenuation processes, the loss of wave energy due to absorption and scattering as waves travel through the Earth [9], the wavelength increases with depth, which results in an increase of the tuning thickness and, thus, lower resolution. The horizontal resolution is the ability to recognise changes in the medium in the horizontal direction, capturing for example lateral changes in rock types and/or erosional features, and it is defined by the Fresnel zone [15]. The Fresnel zone is the area around a reflection point from which seismic energy constructively contributes to the recorded signal due to travel-time differences smaller than half a wavelength. The Fresnel zone also depends on the wavelength and depth of the target and its size increases with depth [9, 12].

After acquisition, seismic data require some heavy processing to get prepared for the visualisation and interpretation stage. The processing steps include a series of techniques, such as denoising or multiple removal [10–12, 16, 17]. These techniques are meant to improve the signal-to-noise ratio, but when applied, a part of the targeted signal is lost. Once the desired signal-to-noise ratio is achieved, the seismic data are inverted to generate structural images, the images that show the stratigraphy and structure of rocks in the subsurface. Each structural image is

paired with a velocity model, which describes the distribution of the seismic wave velocities in the subsurface. Inversion is an iterative process in which both the structural image and the velocity models are updated to reduce the residual between them. Inversion is a non-unique process, as multiple different velocity models can match the same seismic data [18]. For more information, a general summary on the different methods of data acquisition, processing steps, and interpretation techniques is given in Cox, Newton and Huuse [12] and references herein.

The combination of the acquisition parameters, applied processing techniques, and inversion workflows results in subsurface interpretations based on seismic data being inherently uncertain. But this is not a problem of seismic data alone. There are other indirect techniques used for the analysis of the subsurface that also rely heavily on data inversion. Such is the case of electromagnetic surveys, resistivity surveys or ground penetrating radar data when they record hyperbolic signals. Constraining the interpretation uncertainty thereby defining the changes of the properties in the subsurface as accurately as possible is essential for the development of projects where economic benefit margin is restricted, as it is the case in the energy transition.

1.3. Stratigraphic heterogeneities

To study the relationship between stratigraphic heterogeneities and seismic data, we first need to define what heterogeneities are and how they form. Heterogeneity is anything consisting of parts that are different from each other (Cambridge Dictionary). In geology, stratigraphic heterogeneities can be of two types: discrete or continuous. Examples of discrete heterogeneities include channel deposits encased in fine-grained deposits or the stacking of different depositional facies[1]. Examples of continuous heterogeneities, and the focus of this thesis, include gradual changes in grain size distribution that can result in gradual porosity changes. Stratigraphic heterogeneities also occur at different scales, including those below the seismic resolution [19–26]. When spatial dimensions of heterogeneities are smaller than the seismic resolution of a particular dataset, we refer to them as sub-seismic scale heterogeneities. However, under different conditions of depth, average velocities of the medium, and acquisition frequencies, the dimensions of what we consider sub-seismic will be different [10, 12, 14, 15].

Stratigraphic heterogeneities occur in all depositional environments due to spatially and temporally varying erosion and deposition processes. These heterogeneities may impact reservoir porosity and permeability distributions [24, 27–29]. Corbett and Jensen [30] tried to quantify the impact of heterogeneities in reservoir properties by calculating the coefficient of variation of permeability values. From this and other studies, it is known that certain depositional environments, such as fluvial and

---

[1]A lithofacies is a rock type deposited under particular environmental conditions and that, therefore, has similar lithological characteristics such as a gradational porosity change.

shallow marine settings, exhibit particularly high degrees of heterogeneity, making them especially problematic in reservoir characterization [22, 31–35] (Figure 1.3).
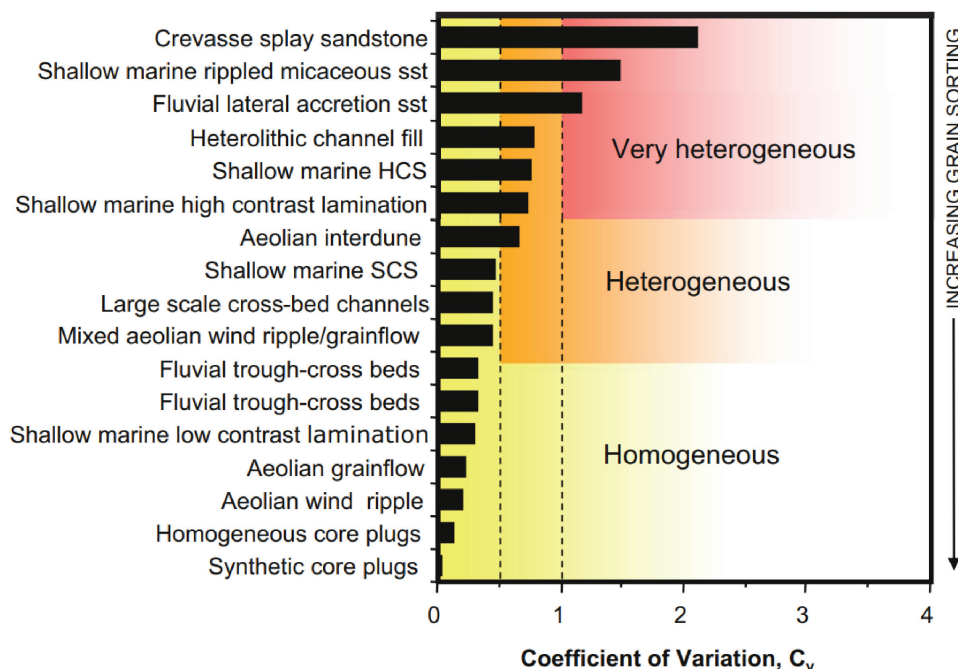
Figure 1.3: Reservoir heterogeneity data for a range of depositional environments, stratigraphic heterogeneities and sample types ranked based on the Coefficient of Variation, C_v. Based on data from Corbett and Jensen [30] and adapted from Ringrose and Bentley [24]

Fluvial systems display a wide range of sub-environments, where lithologically very different sediment bodies, which can also include high contrast in permeability, are interconnected [13, 36]. An example of this is the contrast that might happen between sandy channel deposits and clayey floodplain deposits, especially in braided fluvial deposits. This contrast occurs at different scales, from the depositional system to the lithofacies scale [26, 36, 37].

Similarly, in deposits of wave-dominated shallow marine systems, as result of the generation of erosional surfaces, stacking of lithofacies with contrasting values of porosity and permeability might occur [38–41]. Tide-dominated and river-dominated deltas also show a complex interplay between coarser channel deposits and finer plain deposits and clinoform development [24, 42].

To some extent, the reservoir quality of the sandstone bodies depends on the

depositional environment. For example, beach deposits tend to consist of sands free of significant amounts of silt, clay and organic matter, often well sorted, laterally continuous, and with promising reservoir potential [43, 44]. On the contrary, fluvial channel deposits can be mud- or sand-rich, be moderately to poorly sorted, be connected to other channel deposits or not. Identifying the depositional environment in which the sandstone bodies were formed can help predict the type of internal sedimentary structures or distribution of grains that are expected within the body [22, 36, 40, 45].

This thesis aims to study the seismic response of metre-scale stratigraphic heterogeneities. We expect that, even though these features are often smaller than the resolution of seismic data, they can still produce detectable signals if modelled correctly. To investigate this, we will develop a workflow that captures these heterogeneities and maintains them during the conversion to petrophysical and elasto-acoustic properties, using geological principles based on empirical data or field analogues. We also aim to explore how much information can be extracted from seismic data to help identify heterogeneities near the resolution limit. As a starting point, we will examine how these heterogeneities form, how well they can be resolved, and how previous studies have attempted to detect them using seismic methods.

1.3.1. Heterogeneities in clastic, wave-dominated system deposits

Wave-dominated shallow marine deposits are characterised by sand or gravel, free of significant amounts of silt, clay and organic matter, often quite well sorted and abraded [43]. These deposits have been targeted in the subsurface because of their reservoir potential [44, 46–48]. Deposits of clastic, wave-dominated systems also have metre-scale stratigraphic heterogeneities and the formation of the heterogeneities is associated with (1) erosional surfaces and abrupt or gradual transitions between diverse lithologies [38, 49, 50], and (2) gradual rock property changes, including porosity and permeability, within the same lithology [39–41, 51].

In outcrops, shoreface deposits, including those developed under wave-dominated conditions, are divided into a series of depositional sub-environments and associated facies [52–54]. These sub-environments are characterised by their relative location to the shoreline and their deposits include specific sedimentary structures, bioturbation and grain size distributions [55] and, consequently, specific distributions of petrophysical properties, such as porosity. From outcrop data, we know that traditional depositional sub-environment divisions fail at capturing the small-scale, stratigraphic heterogeneities of present wave-dominated systems [56, 57]. The presence of such stratigraphic structures results in lateral and vertical changes in grain size distributions. Outcrop observations also show that the vertical

juxtaposition of deposits from different sub-environments can happen at different scales, including layers a couple of metres thick [38, 50, 58].

The formation of stratigraphic heterogeneities in wave-dominated shoreface deposits is, to certain degree, predictable, as their development is controlled by sedimentological processes that are understood through conceptual models [57, 59–67]. The sedimentological processes acting within a depositional environment define erosion, transport, and deposition of sand grains, and are affected by processes, such as relative sea level variation, sediment input, wave height, and storm frequency, among others [43, 57, 59, 61, 62, 65, 66].

1.3.2. General analysis on the dimension of different sandstone deposit types

In this section I will evaluate if the dimensions of sandstone bodies can be used as proxy for the identification of the depositional environment and, therefore, predict the possible stratigraphic heterogeneities that might occur within and in between the sandstone bodies. I will base the analysis on measurements of thickness and horizontal width. Thickness and width of individual sandstone bodies can be measured directly from seismic data whenever the seismic resolution allows it. The analysis presented here is based on outcrop data extracted from the SafariDB (https://safaridb.com, last access: 1 August 2021). SafariDB is a research collaboration between Universities of Aberdeen (UK) and University of Bergen (Norway), currently supported by a consortium of 11 companies, with the aim, among others, of improving the links between the subsurface and outcrop analogues. The results from the analysis of the data from SafariDB are compared to previous studies on sandstone body dimensions to verify the outcomes [68, 69].

This analysis will assess:

- Whether individual sandstone deposits can be identified in seismic data.

- Whether specific sandstone types exhibit characteristic dimension ranges.

- If such dimension ranges exist, whether they overlap among different sandstone types or remain distinct for each type.

- Whether we can use dimension ranges to identify specific depositional environments.

If individual sandstone types are characterised by distinct dimension ranges, we could use the dimensions of the deposits to differentiate sandstone types and assign depositional environments. Knowing the depositional environment of a subsurface target solely based on seismic data would provide information on the

nature of stratigraphic heterogeneities that the target might contain, for instance abrupt changes in lithology, smooth changes in porosity, heterogeneous grain size distribution, etc. If individual sandstone deposits cannot be identified in seismic data, we need to rely on other methods to create geological scenarios where stratigraphic heterogeneities at different scales are captured.

Data compilation from SafariDB

To assess the range of expected heterogeneity scales, I selected published outcrop-based descriptions of fluvial and shallow-marine depositional environments from SafariDB. SafariDB compiles information from more than 600 outcrops from all around the world. At present, the database consists of mainly clastic sedimentology data. It contains quantitative data on the dimensions of sandstone bodies. From SafariDB, dimension data of sandstone deposits formed in fluvial and shallow marine environments were extracted. Table 1.1 displays a summary of sandstone deposit types, their depositional environment, the number of outcrops from which data points have been collected, and the number of data points that were downloaded. The SafariDB website includes a "Wiki" tab where the description, diagnostic features, reservoir characteristics and modelling strategies for each sandstone deposit type are defined. In total, this analysis includes 11 different sandstone deposit types, from both fluvial and shallow marine environments, including more than 4900 data points from over 50 outcrops (Table 1.1). The SafariDB is mainly focused on fluvial environments and the majority of data points are related to channel belt measurements. There are 1074 data points from other sandstone types.

From the database, I downloaded the thickness (in m) and horizontal width (in m) data. Each data point also includes a label for completeness (complete, incomplete, partial or unknown) and the type of measurement (absolute or average). The ratio between width and thickness is also calculated. This parameter has been added to assess whether it could help better visualise possible clusters of sandstone types.

Sandstone dimension data analysis

SafariDB data analysis

For each sandstone type, we observe that the data points group in clusters for both thickness versus horizontal width and width-to-thickness ratio versus horizontal width (Figure 1.4, more clearly in subfigures B and D). But these clusters overlap each other. This means that, even if specific sandstone types exhibit characteristic dimension ranges, we cannot recognise different sandstone body types only based

on their dimensions and, therefore, assign depositional environments. Consequently, from seismic data only we cannot know the heterogeneities that we might encounter.

Sandstone type	Depositional environment	Number outcrops	Total data point
Channel fill	Fluvial	3	51
Point bar	Fluvial	5	313
Crevasse splay sheet	Fluvial	5	272
Crevasse channel	Fluvial	2	15
Fluvial sheetflood	Fluvial	1	143
Mid-channel bar	Fluvial	2	54
Channel belt	Fluvial	31	3887
Upper delta (front) deposits	Shallow marine	1	167
Shoreface - foreshore	Shallow marine	3	46
Beach ridge	Shallow marine	3	8
Distributary channels	Shallow marine	2	31
TOTAL		58	4961

Table 1.1: Summary of the different sandstone types that were analysed, together with the depositional environment in which they develop, the number of outcrops where each sandstone type was measured, and the number of data points collected.

For around 83% of the data points, the thickness values are below $10m$ (Figures 1.4A and 1.4B). This value lies close to the tuning thickness of conventional seismic surveys. Hence, in the majority of individual sandstone bodies, key heterogeneity information lies in the sub-seismic range. This has an impact on the way we interpret seismic data. Those areas in seismic data that are interpreted as "sandstone" often do not correspond to individual bodies, but closely spaced individual bodies. This is a source of uncertainty for the characterisation of subsurface targets, because we are not able to adequately evaluate the connectivity between sandstone bodies nor observe the material that separates the individual bodies. Conceivably, the material deposited in between the sandstones can be a potential flow barrier, like thin shale or mudstone layers or carbonate-cemented intervals [22, 25, 70, 71].

For fluvial depositional environments, all data points from crevasse splay sheet, crevasse channel, fluvial sheetflood, channel fill and mid channel bars have thicknesses under the $10m$ (Figure 1.4B). Consequently, it is not possible to interpret individual sandstone bodies of any of these deposits. Point bars are the only sandstone bodies that form in fluvial environments that are sometimes preserved at thicknesses above the $10m$ mark (Figures 1.4A and 1.4B). Channel belt deposits can also be thicker than $10m$, however, they are not strictly individual sandstone bodies, but a combination of deposits associated to the area of the river channel [72]. For shallow marine environments, the preserved thickness of beach ridges, defined as the linear, shore-parallel deposits that form on top of the foreshore,
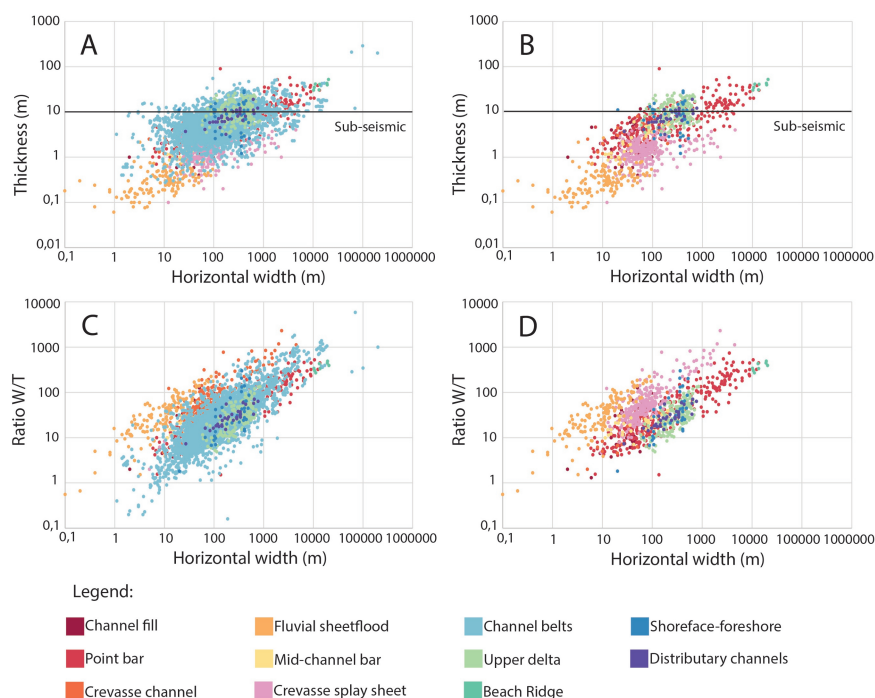
Figure 1.4: Relationship between horizontal width (m) and thickness (m) for eleven sandstone types, with all the data points obtained from SafariDB (A) and without the channel belt data (B). Relationship between horizontal width (m) and ratio width to thickness for eleven sandstone bodies, with all data points obtained from SafariDB (C) and without the channel belt data points (D). Subfigures B and D allow the recognition of different clusters for different sandstone types. Even if trends are observed within the clusters, the clusters overlap each other. Subfigures A and B include a $10m$-thickness line, to determine the approximate border between sub-seismic and seismic scale. The majority of the data points fall within the sub-seismic scale space.

always exceeds $10m$, which allows the interpretation of individual bodies (Figure 1.4B). For the remaining sandstone types – upper delta front, distributary channels and shoreface-foreshore systems –, thickness values above and below the $10m$ have been reported, indicating that the geometry of individual sandstone bodies can only be interpreted in some cases (Figure 1.4B).

Comparison between SafariDB-based sandstone dimension analysis results and previous research

In the literature, other dimension analysis of sandstone deposits, in terms of thickness and width, based on quantitative outcrop data are available [68, 69]. The

analysis from Gibling [68] recognised dimension regions for different sandstone deposits (Figure 1.5). Three of the deposit types analysed in SafariDB are also present in Gibling's study (2006): distributary channels, crevasse spay sheets, and crevasse channels. For fluvial sandstone deposits, both the SafariDB and Gibling datasets agree that the thickness of crevasse-related deposits is always below the 10-m mark (Figure 1.5). However, the dimension ranges defined by SafariDB and Gibling [68] for crevasse channel deposits do not match, with SafariDB defining a broader area than Gibling. Regarding the shallow marine sandstone deposits, the (delta) distributary channel data points from SafariDB match with the area defined by Gibling [68] (red dots in subfigure 1.5A) and both datasets agree that the thickness of distributary channels can be above and below the $10m$ mark. According to Gibling [68] data, distributary channels display a wide variation on thickness values, ranging from 1 to $40m$ and with an average value of $7,8m$, indicating a tendency towards sub-seismic scale thickness values.
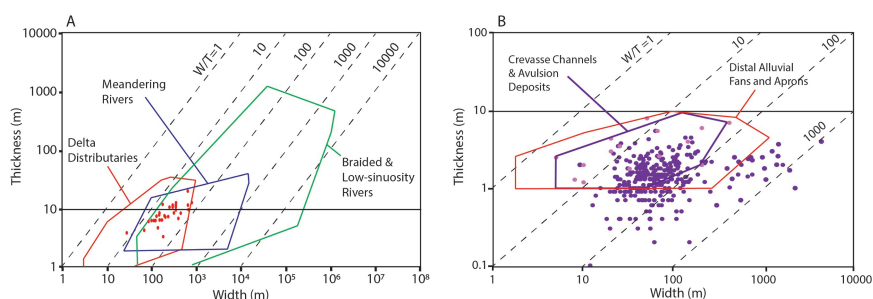
Figure 1.5: Modified from Gibling [68] showing the thickness (m) versus width (m) relationships for different sandstone bodies in fluvial environments. The data of distributary channels (in red), crevasse channels (in purple) and crevasse splay sheets (in pink) from SafariDB are superimposed. Distributary channels show a good match with the results from Gibling [68]. The crevasse channel data lie in and out of the region defined by Gibling [68]. The crevasse splay sheet data match with the avulsion deposit region. For both figures, the $10m$-thickness mark has been added (black line).

Reynolds' study (1999) analysed thickness and width relationships for distributary channels, beach ridge, shoreface – foreshore, crevasse channels, and crevasse splay sheets, among others, based on published outcrop data and studies commissioned by British Petroleum (BP) (Figure 1.6). For sandstones deposited in fluvial environments, Reynolds [69] supports the findings from SafariDB, showing that crevasse channel and splay sheets often display thickness values below $10m$ (Figures 1.6C and 1.6E). Reynolds (1999) also reported examples of thinner crevasse channel sandstones than SafariDB, and included data points of wider crevasse splay sheets than the ones from SafariDB. Regarding the shallow marine sandstone deposits, Reynolds (1999) shows that distributary channels and shoreface – foreshore systems also record thickness values below and above $10m$ (Figures 1.6A and 1.6D), in agreement with the observations from SafariDB. In

the case of beach ridge, however, Reynolds (1999) only reports data points with thickness values under $10m$ (Figure 1.6B), whilst all data points from SafariDB display values above $10m$, a difference of one order of magnitude. The datasets of deposits associated to beach ridges only overlap in their width.
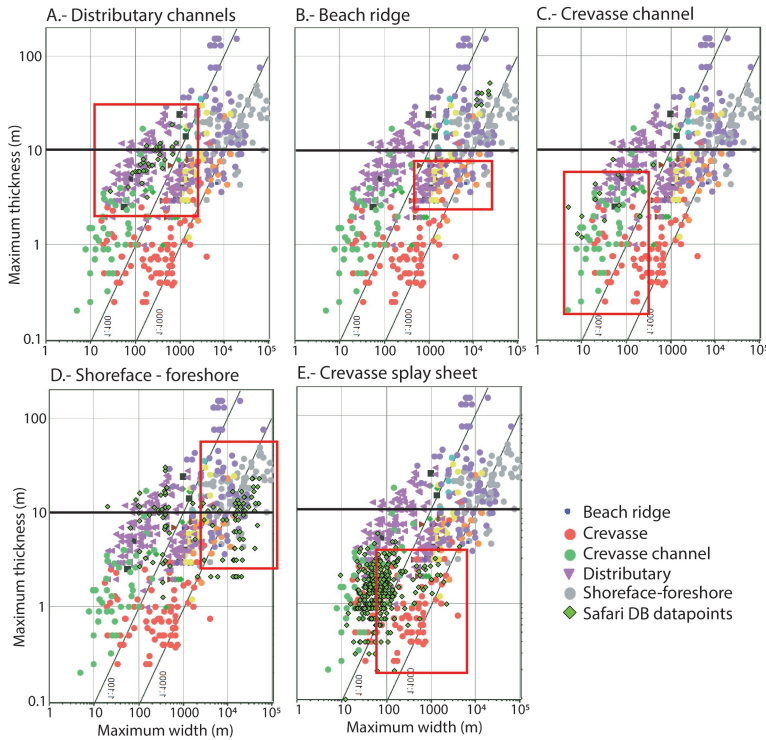
Figure 1.6: Overlapping of the data points from the SafariDB with the graphs generated by Reynolds [69]. For more clarity, the areas where the majority of the points for each sandstone type from Reynolds [69] are located have been highlighted in a red square. The legend only includes the sandstone body types here analysed. There is a good match between the results obtained by Reynolds [69] and the SafariDB data for distributary channels. There are mismatches between the clusters defined by Reynolds [69] and SafariDB for beach ridge, crevasse channel, shoreface-foreshore, and crevasse splay sheets. The 10 m-thickness mark has been added (black line). Majority of data points display thickness values below $10m$.

Conclusions and implications of the sandstone dimension analysis

The SafariDB dataset analysis shows that the thickness of most of the analysed data points, over 80%, is under the $10m$ mark. This thickness is close or below the

tuning thickness for conventional reflection seismic surveys that analysed targets from $1km$ to several kilometres deep, where the vertical resolution is around or lower than $10m$. This finding is supported by other datasets available in literature [68, 69]. Consequently, the majority of individual sandstone bodies formed in the selected depositional environments are sub-seismic scale heterogeneities.

Even if we were able to recognise the individual sandstone bodies, the dimensions of bodies from different depositional environments overlap with each other, in agreement with previous dimension analysis of sandstone deposit dimensions. This means that we cannot distinguish between sandstone deposits from different depositional environments based only on their thickness and width data. Fortunately, in subsurface seismic datasets, additional observations—such as stratigraphic context, seismic facies, and architectural elements—provide further lines of reasoning that help constrain the depositional environment.

If we cannot use the dimensions of the sandstones to distinguish between sandstone deposits and the depositional environment they were formed in, we need to rely on other methods to create geological scenarios where heterogeneities at different scales are captured. A possible path is creating simulations with stratigraphic modelling tools. We can, then, apply forward seismic modelling techniques to study the seismic response of the simulated stratigraphic heterogeneities.

1.4. Sub-seismic scale feature detection

1.4.1. Current state of research

Throughout the years, the resolution that seismic data techniques are able to provide has improved, by making use of more sophisticated acquisition devices and strategies, and by implementing improved mathematical and physics-based algorithms to process seismic data [12]. For instance, researchers have designed more efficient acquisition plans (e.g. [73]), improved the sensitivity of seismic data receivers (e.g. [74] and references therein), improved filters that allow de-noising the seismic data (e.g. [75]), developed algorithms that remove multiples from the data (e.g. [76]), or created optimized data inversion workflows [77]. But these efforts are still insufficient to resolve and interpret some of the heterogeneities that control fluid pathways through reservoirs [78]. For the study of the near-surface, the top couple hundred metres of the subsurface, we can apply new technologies that enable ultra-high- and ultra-ultra-high-resolution seismic surveys, allowing the characterisation of seismic velocities even at the centimetre-scale [79–81]. However, the extent to which surveys penetrate the subsurface is determined by the energy that the survey equipment outputs into the ground. High-resolution techniques rely on high frequencies, which inject little energy into the earth and, thus, are only suitable for near-surface settings [82]. High frequencies are not useful for targets

located deeper than a couple of hundreds of metres, because sound waves at those frequencies do not penetrate far enough into the subsurface [83].

We can also apply an inverse approach to quantify the uncertainty when interpreting seismic data. Instead of focusing on improving the imaging acquisition and the data processing, we can aim at better understanding the seismic response of heterogeneities. This approach consists of using geological data to create models of stratigraphic architecture that contain heterogeneities at a particular spatial scale and applying forward seismic modelling tools to produce synthetic seismograms of those heterogeneities. The geological data can be collected from subsurface analogues, outcrops, or it can be obtained from numerical stratigraphic models. Such approach has already been applied in a number of case studies and has led to improved interpretations of sub-seismic scale stratigraphic heterogeneities for those specific studies by constraining geometrical features in a variety of subsurface targets in deep-water and deltaic environments (e.g. [42, 84–86].

The workflow of many of the forward seismic modelling studies includes collecting outcrop data (architecture, lithology and/or facies) for the construction of static geological models and generating synthetic seismograms, often deploying different seismic frequencies [85–90]. The goal is to find common features between the synthetic data and real seismic data from subsurface targets.

An essential step in forward seismic modelling workflows is the population of the geological model with petrophysical and elasto-acoustic properties, such as mass-density, P-wave velocity, S-wave velocity, etc. Most often, subsurface data from cores and core plugs are used [87, 89, 91–94]. Then, the core data must be matched to the outcrop data, using lithology or facies. Different strategies are applied to correlate the outcrop data with subsurface properties. Some studies use the gamma-ray response of intervals in the subsurface to match the gamma-ray response on outcrop [89] or the net-to-gross relationship of different depositional facies [95]. Other studies use average values recorded in subsurface intervals of their reservoir targets [85, 87, 93, 94, 96]. Yet other studies obtain the data from literature without specifying what the value represents [92, 97]. There is another group of studies that apply empirical equations based on shale volume, porosity, density and/or clay content to obtain P-wave velocity [88, 90, 98]. The use of data that have been directly taken from outcrop is normally disregarded due to the imprint that basin-specific diagenesis due to burial and uplift, and weathering exert on the rock properties [94]. Weathering and exhumation processes are responsible for modifying the petrophysical and elastic properties by cement dissolution, chemical alteration of the grains, or fracturing. In case the seismic velocity and density values are obtained from core plug data or empirical equations, authors typically allocate only one value of the elasto-acoustic properties to all the cells of the geomodel with the same lithology or facies [85, 87, 89–91, 94, 96].

Once the elasto-acoustic properties are assigned to the geological model, seismic modelling methods are applied to artificially generate seismic data with the aim to

mimic real-world seismic signals. These synthetic data are created by simulating the way wavefields travel through the geological model and numerically solving wave equations that capture the interaction between waves and the medium. Synthetic seismic data are used to study the seismic response of geological structures at different scales, and to test new acquisition and processing methods.

Seismic forward modelling methods can be divided into two main types based on how they simulate the propagation of seismic waves through subsurface models: first, the methods that numerically solve the wave equation and, second, the asymptotic ray tracing methods [99]. When using ray tracing methods, the seismic wavefield is broken down into separate elementary waves that propagate along rays [100]. These rays follow paths of minimum travel time and can reflect or change velocity when they encounter geological boundaries or heterogeneities [101]. These changes can be calculated with the Zoeppritz equations for elastic materials, which can be found in standard geophysics textbooks (e.g. [9]). Researchers have extensively used ray tracing methods for the modelling of geological structures [85, 86, 88, 93, 97], because it simplifies calculations by treating each wave independently. While ray tracing provides accurate travel-times and amplitudes in simpler geological settings, it fails at correctly resolving these parameters for mildly to severely heterogeneous media [102, 103].

Wave equation methods, on the other hand, simulate wave propagation throughout the entire model, providing more accurate results in complex media, but at higher computational costs [103]. Among these methods, finite-difference modelling is particularly effective for capturing the seismic response in complex geological settings [99, 104]. The input data required for the application of finite difference forward modelling techniques is an impedance model based on velocity and density distributions [105].

Regarding the source signal used for the seismic forward modelling, the Ricker wavelet technique is the most common [85, 86, 88, 93, 94, 97]. A Ricker wavelet is a symmetrical, zero-phase waveform derived from the Stokes differential equation, which considers the effects of Newtonian viscosity [106–108]. The Ricker wavelet can be used to simulate seismic waves propagating through viscoelastic homogeneous materials. When applying the Ricker wavelet, the typical peak frequency range is from 15 to $120 Hz$.

1.4.2. Stratigraphic forward modelling: a tool for stratigraphic heterogeneity analysis

Another approach to understand the impact of seismic and sub-seismic stratigraphic heterogeneities on seismic data is creating geological simulations that include those heterogeneities and apply forward seismic modelling. As mentioned in section 4.1, the research on sub-seismic scale heterogeneities has relied on models

that are normally created from outcrop data. This limits the number of examples of heterogeneities to those that are properly represented in good quality and accessible outcrops.

The acquired knowledge about sedimentological and geological processes that control deposition of sediment in various depositional environments is the basis for Stratigraphic Forward Modelling (SFM) tools. Such tools represent sedimentological processes to generate synthetic stratigraphy. These tools are normally depositional-environment specific and some of them are specially designed for the simulation of processes in wave-dominated shoreface environments [109–114].

There are three characteristics of SFM from which we can benefit when analysing the formation of metre-scale heterogeneities and their seismic response without depending on outcrop data [115]. Firstly, SFM obey the basic rules of nature, which leads to geological simulations with deposition patterns that follow Walthers' law. Secondly, SFM deals with preservation potential, where erosion will remove part of the strata in a predictable manner as erosion is also a predictable response to processes that affect the depositional environments (e.g. sea level rise/fall). Thirdly, experiments can be repeated, and a large number of simulations will give insights in the key heterogeneities that may be expected (or are most relevant) for a specific depositional environment.

1.5. Ph.D. research

1.5.1. Hypothesis

The Applied Geophysics community has made great efforts to enhance seismic data resolution through advancements in acquisition and data processing techniques. Despite these improvements, there is a clear need to better understand, detect, and image the seismic response of metre-scale stratigraphic heterogeneities and architecture present (but most often hidden) in the seismic cube. Addressing this gap can significantly improve reservoir characterization.

Stratigraphic forward modelling has the potential to reduce the uncertainty in reservoir modelling by helping to reconstruct the internal geometry of reservoirs and to reduce structural uncertainty [116]. Applications of forward seismic modelling have shown its efficacy in increasing the resolution of stratigraphical features in subsurface targets [84–87, 89, 91, 95, 97].

The *main hypothesis* of this thesis is that stratigraphic forward modelling, when integrated with seismic forward modelling and migration, enables the detection and characterization of metre-scale stratigraphic heterogeneities — ranging from a few metres up to less than $10m$ — that are otherwise undetectable using conventional

seismic analysis methods.

To test this hypothesis, the research focuses on clastic, wave-dominated shoreface environments as a representative geological setting where metre-scale heterogeneities are present.

There have been previous efforts to develop workflows that combine forward stratigraphic modelling and seismic modelling [117], with the goal of differentiating the contribution of different processes on the construction of deep-water stratigraphy in subsurface reservoirs. Wan *et al.* [117] did not pay specific attention to the stratigraphic heterogeneities, and worked at the vertical resolutions of approximately $10m$. Here we aim at finer vertical resolutions, with grid cells of $2x2m$ and at depths of $1000m$.

To test the hypothesis, this research develops a workflow that integrates forward seismic modelling with: (1) the use of stratigraphic forward modelling tools to generate geological simulations including metre-scale heterogeneities; and (2) the assignation of petrophysical and acoustic properties based on a continuous property, namely grain size distribution. The effectiveness of this workflow will be evaluated by analysing the impact of the workflow on the detection and characterization of metre-scale heterogeneities, in comparison to conventional seismic analysis approaches.

1.5.2. Goal and research objectives

The goal of this thesis is to design and assess the effectiveness of a new workflow for the characterisation of metre-scale stratigraphic heterogeneities that (1) does not depend on outcrop data collection to create the geological models, but instead uses stratigraphic forward modelling to simulate plausible geological scenarios, (2) where the grid cell is smaller than the vertical resolution of seismic acquisition, and (3) that is integrated with forward seismic modelling, migration and inversion techniques. This workflow aims at enabling a smooth transition from geology-related input parameters to seismic data. In this thesis, I will focus on the stratigraphic heterogeneities developed in clastic, wave-dominated, shallow marine depositional environments.

The research objectives of this thesis are:

1. To assess metre-scale, stratigraphic heterogeneities and the distribution of petrophysical, elastic and acoustic properties in outcrop data, to describe potential trends on their distribution. (Chapter 2).

2. To develop a methodology that converts sedimentological data, specifically grain size distribution, into petrophysical and elasto-acoustic properties,

enabling a transition from geological models to seismic data analysis. (Chapter 2).

3. To evaluate the effectiveness of assigning petrophysical and acoustic properties based on grain-size distribution in comparison to conventional inversion techniques by analysing the resulting seismic response. (Chapter 4).

4. To investigate the potential of angle-dependent seismic data, a seismic data type that includes information about how the seismic response varies with the angle of incidence, for detecting and characterizing metre-scale heterogeneities by analysing statistical measures of asymmetry across various shallow marine depositional scenarios. (Chapter 5).

This Ph.D. project has been developed together with a parallel project. The general goal for the two projects is to explore alternative methods to characterise the seismic response of metre-scale, stratigraphic heterogeneities. While the project discussed here analyses the heterogeneity distribution, the bridge between geological – petrophysical – acoustic data and the possibility to use angle-dependent seismic data to characterise the heterogeneities, the parallel project develops optimised forward seismic modelling tools and machine learning algorithms for the interpretation of heterogeneities in the seismic data.

1.5.3. Thesis outline

The outline of this thesis is as follows:

Chapter 2

In Chapter 2, **"Reservoir heterogeneity characterisation of a wave-dominated system within the Western Interior Seaway (Judith River Formation, Late Cretaceous): sedimentological, stratigraphic and, petrophysical analysis of a field analogue"**, I analyse an outcrop analogue of clastic, wave-dominated, shoreface system to characterise the distribution of facies associations and distribution of petrophysical, acoustic and elastic properties and describe potential trends on their distribution. The outcrop is a continuous section of around $70m$ in the vertical direction and $4km$ in the lateral direction, of which $1,5km$ were studied, located in Bridger (Montana, USA). The collected data include stratigraphic logs, a photogrammetry survey, and rock samples. Field data show that most sandstone layers are less than $10m$ thick, which is close to the sub-seismic scale limit in reflection seismic data at reservoir depths deeper than $2km$. The measured petrophysical and elasto-acoustic properties are non-unique to facies associations, and the variation ranges per association overlap with each other. The property

values did not describe lateral nor vertical variation trends, but proved that allocating single values per facies association when constructing reservoir models might not capture the variability within the associations.

Chapter 3

In Chapter 3, **"Introduction to stratigraphic forward modelling"**, I review some of the basics of stratigraphic forward modelling tools and define the requirements that a modelling tool should meet to be incorporated into the workflow for the analysis of stratigraphic heterogeneities at a metre scale. This chapter includes a description of available modelling tools for shallow marine depositional environments and an assessment of their compatibility with the workflow. From this assessment, I conclude that BarSim is the stratigraphic forward modelling tool that best fits into the workflow.

Chapter 4

In Chapter 4, **"Discretization of small-scale, stratigraphic heterogeneities and its impact on the seismic response: lessons from the application of process-based modelling"**, I develop a methodology that converts sedimentological data into petrophysical and elasto-acoustic properties, and evaluate the impact that calculating petrophysical and acoustic properties at different discretisation levels has on the seismic response of heterogeneities formed in wave-dominated, shoreface depositional environments. The most detailed distribution of properties is based on the grain-size distribution. The detailed acoustic property distribution is achieved by following the workflow introduced in this thesis, which links the grain-size data simulated through stratigraphic forward modelling with porosity, mass-density and P-wave velocity. The coarsest acoustic property distribution is based on lithology, a common assumption in conventional inversion workflows. I also include a simulation where the properties are based on facies data. This chapter shows that the adequate characterisation of some metre-scale stratigraphic heterogeneities in the seismic data will only be possible when allocating petrophysical and acoustic properties based on grain-size data.

Chapter 5

In Chapter 5, **"Characterising subsurface acoustic heterogeneity through angle-gather asymmetry analysis"**, I investigate the potential of angle-dependent seismic data to detect and characterise metre-scale heterogeneities by analysing the correlation between the asymmetry of angle-dependent seismic data and

variations in acoustic properties. To do so, I apply the workflow developed in this thesis to generate angle-dependent seismic data from nine geological simulations from wave-dominated shoreface systems. For each horizontal location, I calculate and correlate, both visually and numerically, statistical parameters that capture the variations in mass-density, P-wave velocity, and asymmetry of angle-dependent seismic data. The results show that there are moderate complex, non-linear, and non-monotonic correlations between the statistical parameters of the different properties. Visually, I identify strong correlations between sharp lateral changes of P-wave velocity and high asymmetry, which stresses the limitations of synthetic modelling based on fixed grids and shows the potential of angle-gather data asymmetry to detect sharp changes of properties.

Chapter 6

In Chapter 6, **"Conclusions and Future research"**, I summarize the conclusions and implications of the thesis. I introduce a number of possible improvements that could be applied to the workflow developed in this thesis and I discuss some knowledge gaps and possible research topics that could be beneficial for future improvements on the characterisation of metre-scale, stratigraphic heterogeneities.

References

[1]   M. Russell. *Flint Mines in Neolithic Britain*. First edition. Tempus Publishing, 2000, pp. 1–160.

[2]   D. Klemm, R. Klemm and A. Murr. 'Gold of the Pharaohs – 6000 years of gold mining in Egypt and Nubia'. In: *Journal of African Earth Sciences* 33 (3-4 Jan. 2001), pp. 643–659. ISSN: 1464343X. DOI: 10.1016/S0899-5362(01)00094-X.

[3]   D. Klemm and R. Klemm. 'Mining in Ancient Egypt and Nubia'. In: *Encyclopaedia of the History of Science, Technology, and Medicine in Non-Western Cultures*. Springer Netherlands, 2008, pp. 1685–1698. DOI: 10.1007/978-1-4020-4425-0_9731.

[4]   P. Allard, F. Bostyn, F. Giligny and J. Lech. *Flint Mining in Prehistoric Europe: Interpreting the archaeological records*. Ed. by D. Bossut. Archaeopress, 2014, pp. 1–95.

[5]   A. N. Angelakis, K. S. Voudouris and I. Mariolakos. 'Groundwater utilization through the centuries focusing n the Hellenic civilizations'. In: *Hydrogeology Journal* 24 (5 Aug. 2016), pp. 1311–1324. ISSN: 1431-2174. DOI: 10.1007/s10040-016-1392-0.

[6]   C. Campbell. 'The Oil Age in Perspective'. In: *Energy Exploration & Exploitation* 31 (2 2013), pp. 149–165.

[7]   J. de Jager. *Handbook: Risk and Volume Assessment*. Tech. rep. De Jager Geological Consulting, 2021, pp. 1–124.

[8]   M. Simmons, A. Davies and L. Cowliff. 'Plausible Characterisation of Subsurface Geology is Essential for the Energy Transition'. In: *First Break* 41 (6 June 2023), pp. 69–74. ISSN: 0263-5046. DOI: 10.3997/1365-2397.fb2023045.

[9]   R. E. Sheriff and L. P. Geldart. *Exploration Seismology*. Cambridge University Press, Aug. 1995. ISBN: 978-0-521-46282-2. DOI: 10.1017/CBO9781139168359.

[10] Ö. Yilmaz. *Seismic Data Analysis*. Society of Exploration Geophysicists, 2001.

[11] W. Ashcroft. *A petroleum geologist's guide to seismic reflection*. Wiley-Blackwell, 2011, pp. 1–176.

[12] D. R. Cox, A. M. Newton and M. Huuse. 'An introduction to seismic reflection data: acquisition, processing and interpretation'. In: *Regional Geology and Tectonics: Principles of Geologic Analysis*. Elsevier, 2020, pp. 571–603. DOI: 10.1016/B978-0-444-64134-2.00020-1.

[13] K. Keogh, A. Martinius and R. Osland. 'The development of fluvial stochastic modelling in the Norwegian oil industry: A historical review, subsurface implementation and future directions'. In: *Sedimentary Geology* 202 (1-2 2007), pp. 249–268. DOI: 10.1016/j.sedgeo.2007.05.009.

[14] R. Kallweit and L. Wood. 'The limits of resolution of zero-phase wavelets'. In: *Geophysics* 47 (7 July 1982), pp. 1035–1046. DOI: 10.1190/1.1441367.

[15] S. Chopra, J. Castagna and O. Portniaguine. 'Seismic resolution and thin-bed reflectivity inversion'. In: *CSEG RECORDER* (Jan. 2006), pp. 19–25.

[16] D. Hale. 'Dip-moveout by Fourier transform'. In: *GEOPHYSICS* 49 (6 June 1984), pp. 741–757. ISSN: 0016-8033. DOI: 10.1190/1.1441702.

[17] I. Jones, R. Bloor, B. Biondi and J. Etgen. *Prestack Depth Migration and Velocity Model Building*. Society of Exploration Geophysicists, Jan. 2008. ISBN: 978-1-56080-147-4. DOI: 10.1190/1.9781560801917.

[18] K. Hayashi. 'Non-Uniqueness in Seismic Refraction Analysis'. In: *Symposium on the Application of Geophysics to Engineering and Environmental Problems 2011*. Environment and Engineering Geophysical Society, Jan. 2011, pp. 40–52. DOI: 10.4133/1.3614108.

[19] C. A. Hartkamp-Bakker and M. E. Donselaar. 'Permeability Patterns in Point Bar Deposits: Tertiary Loranca Basin, Central Spain'. In: *The Geological Modelling of Hydrocarbon Reservoirs and Outcrop Analogues*. Wiley, Nov. 1992, pp. 157–168. DOI: 10.1002/9781444303957.ch9.

[20] J. A. Howell, A. Skorstad, A. MacDonald, A. Fordham, S. Flint, B. Fjellvoll and T. Manzocchi. 'Sedimentological parameterization of shallow-marine reservoirs'. In: *Petroleum Geoscience* 14 (1 2008), pp. 17–34. DOI: 10.1144/1354-079307-787.

[21] A. Hurst. 'Sedimentary Flow Units in Hydrocarbon Reservoirs: Some Shortcomings and a Case for High-Resolution Permeability Data'. In: *The Geological Modelling of Hydrocarbon Reservoirs and Outcrop Analogues*. Wiley, Nov. 1992, pp. 189–204. DOI: 10.1002/9781444303957.ch12.

[22] M. Jackson, G. Hampson and R. Sech. 'Three-dimensional modeling of a shoreface-shelf parasequence reservoir analog: Part 2. geologic controls on fluid flow and hydrocarbon recovery'. In: *American Association of Petroleum Geologists Bulletin* 93 (9 2009), pp. 1183–1208. DOI: 10.1306/05110908145.

[23] C. D. Meirovitz, L. Stright, S. M. Hubbard and B. W. Romans. 'The influence of inter- and intra-channel architecture on deep-water turbidite reservoir performance'. In: *Petroleum Geoscience* 27 (2 May 2021). ISSN: 1354-0793. DOI: 10.1144/petgeo2020-005.

[24] P. Ringrose and M. Bentley. *Reservoir Model Design A Practitioner's Guide*. Springer, 2015.

[25] R. Sech, M. Jackson and G. Hampson. 'Three-dimensional modeling of a shoreface-shelf parasequence reservoir analog: Part 1. surface-based modeling to capture high-resolution fades architecture'. In: *American Association of Petroleum Geologists Bulletin* 93 (9 2009), pp. 1155–1181. DOI: 10.1306/05110908144.

[26] K. Weber. 'Influence of Common Sedimentary Structures on Fluid Flow in Reservoir Models'. In: *Journal of Petroleum Technology* 34 (03 Mar. 1982), pp. 665–672. ISSN: 0149-2136. DOI: 10.2118/9247-PA.

[27] G. Ciammetti, P. S. Ringrose, T. R. Good, J. M. L. Lewis and K. S. Sorbie. 'Waterflood Recovery and Fluid Flow Upscaling in a Shallow Marine and Fluvial Sandstone Sequence'. In: *All Days*. SPE, Oct. 1995. DOI: 10.2118/30783-MS.

[28] M. R. Gani and J. P. Bhattacharya. 'Basic Building Blocks and Process Variability of a Cretaceous Delta: Internal Facies Architecture Reveals a More Dynamic Interaction of River, Wave, and Tidal Processes Than Is Indicated by External Shape'. In: *Journal of Sedimentary Research* 77 (4 Apr. 2007), pp. 284–302. ISSN: 1527-1404. DOI: 10.2110/jsr.2007.023.

[29] M. J. Pranter, A. I. Ellison, R. D. Cole and P. E. Patterson. 'Analysis and modeling of intermediate-scale reservoir heterogeneity based on a fluvial point-bar outcrop analog, Williams Fork Formation, Piceance Basin, Colorado'. In: *AAPG Bulletin* 91 (7 July 2007), pp. 1025–1051. ISSN: 0149-1423. DOI: 10.1306/02010706102.

[30] P. Corbett and J. Jensen. 'Estimating the mean permeability: how many measurements do you need?' In: *First Break* 10 (1992), pp. 89–94.

[31] D. J. Goggin, M. A. Chandler, G. Kocurek and L. W. Lake. 'Patterns of Permeability in Eolian Deposits: Page Sandstone (Jurassic), Northeastern Arizona'. In: *SPE Formation Evaluation* 3 (02 June 1988), pp. 297–306. ISSN: 0885-923X. DOI: 10.2118/14893-PA.

[32] S. Hossain, G. J. Hampson, C. Jacquemyn, M. D. Jackson, D. Petrovskyy, S. Geiger, J. D. M. Silva, S. Judice, F. Rahman and M. C. Sousa. 'Effective permeability of fluvial lithofacies in the Bunter Sandstone Formation, UK'. In: *Advances in Water Resources* 199 (May 2025), p. 104936. ISSN: 03091708. DOI: 10.1016/j.advwatres.2025.104936.

[33] A. Hurst and K. J. Rosvoll. 'PERMEABILITY VARIATIONS IN SANDSTONES AND THEIR RELATIONSHIP TO SEDIMENTARY STRUCTURES'. In: *Reservoir Characterization II*. Elsevier, 1991, pp. 166–196. DOI: 10.1016/B978-0-12-434066-4.50011-4.

[34] M. Huysmans, L. Peeters, G. Moermans and A. Dassargues. 'Relating small-scale sedimentary structures and permeability in a cross-bedded aquifer'. In: *Journal of Hydrology* 361 (1-2 Oct. 2008), pp. 41–51. ISSN: 00221694. DOI: 10.1016/j.jhydrol.2008.07.047.

[35]   R. W. Ritzi, Z. Dai, D. F. Dominic and Y. N. Rubin. 'Spatial correlation of permeability in cross-stratified sediment with hierarchical architecture'. In: *Water Resources Research* 40 (3 Mar. 2004). ISSN: 0043-1397. DOI: 10.1029/2003WR002420.

[36]   K. Nordahl and P. Ringrose. 'Identifying the representative elementary volume for permeability in heterolithic deposits using numerical rock models'. In: *Mathematical Geosciences* 40 (7 2008), pp. 753–771. DOI: 10.1007/s11004-008-9182-4.

[37]   P. Ringrose, A. Martinius and J. Alvestad. *Multiscale geological reservoir modelling in practice*. Vol. 309. 2008, pp. 123–134. DOI: 10.1144/SP309.9.

[38]   K. Charvin, G. J. Hampson, K. L. Gallagher and R. Labourdette. 'Intra-parasequence architecture of an interpreted asymmetrical wave-dominated delta'. In: *Sedimentology* 57 (3 Apr. 2010), pp. 760–785. ISSN: 00370746. DOI: 10.1111/j.1365-3091.2009.01118.x.

[39]   J. M. Ketzer, S. Morad, R. Evans and I. S. Al-Aasm. 'Distribution of Diagenetic Alterations in Fluvial, Deltaic, and Shallow Marine Sandstones Within a Sequence Stratigraphic Framework: Evidence from the Mullaghmore Formation (Carboniferous), NW Ireland'. In: *Journal of Sedimentary Research* 72 (6 Nov. 2002), pp. 760–774. ISSN: 1527-1404. DOI: 10.1306/042202720760.

[40]   T. Sømme, J. Howell, G. Hampson and J. Storms. 'Genesis, Architecture, and Numerical Modeling of Intra-Parasequence Discontinuity Surfaces In Wave-Dominated Deltaic Deposits: Upper Cretaceous Sunnyside Member, Blackhawk Formation, Book Cliffs, Utah, U.S.A.' In: *Recent Advances in Models of Siliciclastic Shallow-Marine Stratigraphy* (2008), pp. 421–441. DOI: 10.2110/PEC.08.90.0421.

[41]   K. G. Taylor, R. L. Gawthorpe, C. D. Curtis, J. D. Marshall and D. N. Awwiller. 'Carbonate Cementation in a Sequence-Stratigraphic Framework: Upper Cretaceous Sandstones, Book Cliffs, Utah-Colorado'. In: *Journal of Sedimentary Research* 70 (2 Mar. 2000), pp. 360–372. ISSN: 1527-1404. DOI: 10.1306/2DC40916-0E47-11D7-8643000102C1865D.

[42]   N. Holgate, G. Hampson, C.-L. Jackson and S. Petersen. 'Constraining uncertainty in interpretation of seismically imaged clinoforms in deltaic reservoirs, Troll field, Norwegian North Sea: Insights from forward seismic models of outcrop analogs'. In: *AAPG Bulletin* 98 (12 2014), pp. 2629–2663. DOI: 10.1306/05281413152.

[43]   P. S. Roy, P. J. Cowell, M. A. Ferland, B. G. Thom and O. van de Plassche. 'Wave-dominated coasts'. In: *Coastal Evolution: Late Quaternary Shoreline Morphodynamics*. Cambridge University Press, 1995, pp. 121–186.

[44] N. Tyler and R. J. Finley. 'Architectural Controls on the Recovery of Hydrocarbons From Sandstone Reservoers'. In: *The Three-Dimensional Facies Architecture of Terrigenous Clastic Sediments and its Implications for Hydrocarbon Discovery and Recovery*. SEPM Society for Sedimentary Geology, 1991, pp. 1–5. DOI: 10.2110/csp.91.03.0001.

[45] Y. Wang, T. F. Baars, H. Sahoo, J. E. A. Storms, A. W. Martinius, P. Gingerich and H. A. Abels. 'Sandstone body character and river planform styles of the lower Eocene Willwood Formation, Bighorn Basin, Wyoming, USA'. In: *Sedimentology* 69 (7 Dec. 2022), pp. 2897–2924. ISSN: 0037-0746. DOI: 10.1111/sed.13027.

[46] J. Bhattacharya and R. G. Walker. 'River- and wave-dominated depositional systems of the Upper Cretaceous Dunvegan Formation, northwestern Alberta'. In: *Bulleting of Canadian Petroleum Geology* 39 (2 June 1991), pp. 165–191.

[47] P. Lis and A. Wysocka. 'Middle Miocene Deposits in Carpathian Foredeep: Facies Analysis and Implications for Hydrocarbon Reservoir Prospecting'. In: *Annales Societatis Geologorum Poloniae* 82 (2012), pp. 239–253.

[48] S. Tahir, B. Musta, J. Asis and F. Hanis. 'Wave and tide influence in Neogene paralic hydrocarbon potential reservoirs in Sabah'. In: *ASM Science Journal* 11 (2 2018), pp. 278–292.

[49] G. J. Hampson and J. E. A. Storms. 'Geomorphological and sequence stratigraphic variability in wave-dominated, shoreface-shelf parasequences'. In: *Sedimentology* 50 (4 Aug. 2003), pp. 667–701. ISSN: 0037-0746. DOI: 10.1046/j.1365-3091.2003.00570.x.

[50] M. F. Isla, E. Schwarz and G. D. Veiga. 'Bedset characterization within a wave-dominated shallow-marine succession: An evolutionary model related to sediment imbalances'. In: *Sedimentary Geology* 374 (Oct. 2018), pp. 36–52. ISSN: 00370738. DOI: 10.1016/j.sedgeo.2018.07.003.

[51] M. F. Isla, M. D. Coronel, E. Schwarz and G. D. Veiga. 'Depositional architecture of a wave-dominated clastic shoreline (Pilmatué Member, Argentina): Linking dynamics and stratigraphic record of bar-trough systems'. In: *Marine and Petroleum Geology* 118 (Aug. 2020), p. 104417. ISSN: 02648172. DOI: 10.1016/j.marpetgeo.2020.104417.

[52] R. Walker and A. Plint. 'Wave-and Storm-Dominated Shallow Marine Systems'. In: *Facies Models: Response to Sea Level Change*. Ed. by R. Walker and N. James. Geological Association of Canada, 1992, pp. 219–238.

[53] W. E. Galloway and D. K. Hobday. 'Terrigenous Clastic Depositional Systems'. In: *Terrigenous Clastic Depositional Systems* (1996). DOI: 10.1007/978-3-642-61018-9.

[54] H. Reading and J. Collinson. 'Clastic Coasts'. In: *Sedimentary environments : processes, facies, and stratigraphy*. Blackwells, 1996, pp. 154–231.

[55] S. G. Pemberton, J. A. MacEachern, S. E. Dashtgard, K. L. Bann, M. K. Gingras and J.-P. Zonneveld. 'Shorefaces'. In: 2012, pp. 563–603. DOI: 10.1016/B978-0-444-53813-0.00019-8.

[56] H. Clifton, R. Hunter and R. Phillips. 'Depositional structures and processes in the non-barred high-energy nearshore'. In: *Journal of Sedimentary Research* 41 (1971), pp. 651–670. DOI: 10.1306/74D7231A-2B21-11D7-8648000102C1865D.

[57] R. Davidson-Arnott. 'Wave-Dominated Coasts'. In: *Treatise on Estuarine and Coastal Science*. Elsevier, 2011, pp. 73–116. DOI: 10.1016/B978-0-12-374711-2.00305-3.

[58] M. F. Isla, M. S. Olivo, J. J. Zuazo, E. Schwarz and G. D. Veiga. 'Exceptional preservation of a barred shoreline under forced-regressive conditions (Lower Cretaceous, Neuquén Basin, Argentina)'. In: *Sedimentology* 69 (2 Feb. 2022), pp. 891–913. ISSN: 0037-0746. DOI: 10.1111/sed.12931.

[59] E. J. Anthony. 'Storms, shoreface morphodynamics, sand supply, and the accretion and erosion of coastal dune barriers in the southern North Sea'. In: *Geomorphology* 199 (Oct. 2013), pp. 8–21. ISSN: 0169-555X. DOI: 10.1016/J.GEOMORPH.2012.06.007.

[60] E. J. Anthony and T. Aagaard. 'The lower shoreface: Morphodynamics and sediment connectivity with the upper shoreface and beach'. In: *Earth-Science Reviews* 210 (Nov. 2020), p. 103334. ISSN: 0012-8252. DOI: 10.1016/J.EARSCIREV.2020.103334.

[61] J. Backstrom, D. Jackson, A. Cooper and C. Loureiro. 'Contrasting geomorphological storm response from two adjacent shorefaces'. In: *Earth Surface Processes and Landforms* 40 (15 Dec. 2015), pp. 2112–2120. ISSN: 1096-9837. DOI: 10.1002/ESP.3788.

[62] M. E. Field and P. S. Roy. 'Offshore transport and sand-body formation; evidence from a steep, high-energy shoreface, southeastern Australia'. In: *Journal of Sedimentary Research* 54 (4 Dec. 1984), pp. 1292–1302. ISSN: 1527-1404. DOI: 10.1306/212F85C1-2B24-11D7-8648000102C1865D.

[63] T. R. Keen, R. L. Slingerland, S. J. Bentley, Y. Furukawa, W. J. Teague and J. D. Dykes. 'Sediment Transport on Continental Shelves: Storm Bed Formation and Preservation in Heterogeneous Sediments'. In: *Sediments, Morphology and Sedimentary Processes on Continental Shelves* (Jan. 2012), pp. 295–310. DOI: 10.1002/9781118311172.CH14.

[64] N. Kumar and J. E. Sanders. 'Characteristics of shoreface storm deposits; modern and ancient examples'. In: *Journal of Sedimentary Research* 46 (1 Mar. 1976), pp. 145–162. ISSN: 1527-1404. DOI: 10.1306/212F6EDD-2B24-11D7-8648000102C1865D.

[65] O. Madsen. 'Mechanics of Cohesionless Sediment Transport in Coastal Waters'. In: *Proc. Coastal Sediments* ASCE (1991), pp. 15–27.

[66] N. C. Mitchell and Z. Zhao. 'Effects of currents and waves on the morphologies of coastal sandy clinoforms: sediment mobility calculations based on current meter and wave data from Southern California, U.S.A.' In: *Journal of Sedimentary Research* 93 (7 July 2023), pp. 488–501. ISSN: 1527-1404. DOI: 10.2110/JSR.2023.002.

[67] D. Swift, P. S. and J. Thorne. 'Sedimentation on continental margins, IV. Lithofacies and depositional systems.' In: *Shelf Sand and Sandstone Bodies*. Ed. by D. Swift, G. Oertel, R. Tillman and J. Thorne. Vol. 14. Int. Assoc. Sedimentol. Spec. Publ., 1991, pp. 89–152.

[68] M. R. Gibling. 'Width and Thickness of Fluvial Channel Bodies and Valley Fills in the Geological Record: A Literature Compilation and Classification'. In: *Journal of Sedimentary Research* 76 (5 May 2006), pp. 731–770. ISSN: 1527-1404. DOI: 10.2110/jsr.2006.060.

[69] A. Reynolds. 'Dimensions of Paralic Sandstone Bodies'. In: *AAPG Bulletin* 83 (2 Feb. 1999), pp. 211–229. ISSN: 0149-1423. DOI: 10.1306/00AA9A48-1730-11D7-8645000102C1865D.

[70] Q. Fisher, I. Kaminskaite and A. del Pino Sanchez. 'Shale barrier performance in petroleum systems: implications for CO_2 storage and nuclear waste disposal'. In: *Geoenergy* 1 (1 Dec. 2023). ISSN: 2755-1725. DOI: 10.1144/geoenergy2023-006.

[71] J. A. Howell, A. W. Martinius and T. R. Good. 'The application of outcrop analogues in geological modelling: a review, present status and future outlook'. In: *GSLSP* 387 (1 Jan. 2014), pp. 1–25. ISSN: 0305-8719. DOI: 10.1144/SP387.12.

[72] B. Nyberg, G. Henstra, R. L. Gawthorpe, R. Ravnås and J. Ahokas. 'Global scale analysis on the extent of river channel belts'. In: *Nature Communications* 14 (1 Apr. 2023), p. 2163. ISSN: 2041-1723. DOI: 10.1038/s41467-023-37852-8.

[73] B. Revelo-Obando and G. Blacquière. 'Target-oriented acquisition geometry design based on full-wavefield migration'. In: *GEOPHYSICS* 89 (3 May 2024), P21–P32. ISSN: 0016-8033. DOI: 10.1190/geo2023-0578.1.

[74] T. Dean and M. Grant. 'A beginner's guide to seismic sensors'. In: *Preview* 2024 (230 May 2024), pp. 38–44. ISSN: 1443-2471. DOI: 10.1080/14432471.2024.2395647.

[75] Y. Zhang, B. Gu, Z. Sun, X. Yan and S. Zhang. 'Seismic data denoising with two-step prediction strategy based on Neural Network'. In: *Computers & Geosciences* 187 (May 2024), p. 105595. ISSN: 00983004. DOI: 10.1016/j.cageo.2024.105595.

[76] P.-N. Bao, Y. Shi, W.-H. Wang, W. Zhang and Z.-J. Pan. 'An improved method for internal multiple elimination using the theory of virtual events'. In: *Petroleum Science* 19 (6 Dec. 2022), pp. 2663–2674. ISSN: 19958226. DOI: 10.1016/j.petsci.2022.05.021.

[77] P. Yang and D. Gajewski. 'An optimized workflow for source localization and joint velocity inversion using wavefront attributes'. In: *82nd EAGE Annual Conference & Exhibition*. European Association of Geoscientists & Engineers, 2021, pp. 1–5. DOI: 10.3997/2214-4609.202113228.

[78] D. Stojkovic, M. Shringarpure, Y. Kim, H. Alqassab, T. Rapstine, J. Fedele, S. Fullmer and R. Sain. 'Improving Reservoir Characterization and Prediction Via Machine Learning-Driven Integration of Subseismic Geologic Concepts, Geophysical Attributes, and Wells'. In: *SPE Journal* 29 (04 Apr. 2024), pp. 1967–1973. ISSN: 1086-055X. DOI: 10.2118/218420-PA.

[79] H. Duarte, N. Wardell and O. Monrigal. 'Advanced processing for UHR3D shallow marine seismic surveys'. In: *Near Surface Geophysics* 15 (4 Aug. 2017), pp. 347–358. ISSN: 1569-4445. DOI: 10.3997/1873-0604.2017022.

[80] M. J. Faggetter, M. E. Vardy, J. K. Dix, J. M. Bull and T. J. Henstock. 'Time-lapse imaging using 3D ultra-high-frequency marine seismic reflection data'. In: *GEOPHYSICS* 85 (2 Mar. 2020), P13–P25. ISSN: 0016-8033. DOI: 10.1190/geo2019-0258.1.

[81] L. MacGregor, L. Scott, R. Cooper and J. Nicholls. 'Ultra-High Resolution Seismic: Applications of P-Cable in the Energy Transition'. In: *First Break* 40 (11 Nov. 2022), pp. 67–70. ISSN: 0263-5046. DOI: 10.3997/1365-2397.fb2022096.

[82] L. P. Geldart and R. E. Sheriff. *Problems in Exploration Seismology and their Solutions*. Society of Exploration Geophysicists, Jan. 2004, pp. 221–252. ISBN: 978-1-56080-115-3. DOI: 10.1190/1.9781560801733.

[83] F. Richart, J. Hall and R. Woods. *Vibrations of soils and foundations.* Prentice-Hall, Inc., 1970, pp. 1–432.

[84] H. Zeng, X. Zhu and R. Zhu. 'New insights into seismic stratigraphy of shallow-water progradational sequences: Subseismic clinoforms'. In: *Interpretation* 1 (1 Aug. 2013). doi: 10.1190/INT-2013-0017.1, SA35–SA51. ISSN: 2324-8858. DOI: 10.1190/INT-2013-0017.1.

[85] E. Pemberton, L. Stright, S. Fletcher and S. Hubbard. 'The influence of stratigraphic architecture on seismic response: Reflectivity modeling of outcropping deepwater channel units'. In: *Interpretation* 6 (3 2018), T783–T808. DOI: 10.1190/INT-2017-0170.1.

[86] N. Grasseau, C. Grélaud, M. López-Blanco and P. Razin. 'Forward seismic modeling as a guide improving detailed seismic interpretation of deltaic systems: Example of the Eocene Sobrarbe delta outcrop (South-Pyrenean foreland basin, Spain), as a reference to the analogous subsurface Albian-Cenomanian Torok-Nanushuk Delta of the Colville Basin (NPRA, USA)'. In: *Marine and Petroleum Geology* 100 (Feb. 2019), pp. 225–245. ISSN: 02648172. DOI: 10.1016/J.MARPETGEO.2018.11.010.

[87] A. Schwab, B. Cronin and H. Ferreira. 'Seismic expression of channel
      outcrops: Offset stacked versus amalgamated channel systems'. In: *Marine
      and Petroleum Geology* 24 (6-9 June 2007), pp. 504–514. ISSN: 02648172.
      DOI: 10.1016/j.marpetgeo.2006.10.009.

[88] D. A. Armitage and L. Stright. 'Modeling and interpreting the seismic-
      reflection expression of sandstone in an ancient mass-transport deposit
      dominated deep-water slope environment'. In: *Marine and Petroleum
      Geology* 27 (1 Jan. 2010), pp. 1–12. ISSN: 0264-8172. DOI: 10.1016/J.
      MARPETGEO.2009.08.013.

[89] K. Bakke, I. Kane, O. Martinsen, S. Petersen, T. Johansen, S. Hustoft,
      F. Jacobsen and A. Groth. 'Seismic modeling in the analysis of deep-water
      sandstone termination styles'. In: *AAPG Bulletin* 97 (9 2013), pp. 1395–1419.
      DOI: 10.1306/03041312069.

[90] R. Feng, S. Luthi, D. Gisolf and S. Sharma. 'Obtaining a high-resolution
      geological and petrophysical model from the results of reservoir-orientated
      elastic wave-equation-based seismic inversion'. In: *Petroleum Geoscience*
      23 (3 2017), pp. 376–385. DOI: 10.1144/petgeo2015-076.

[91] D. Hodgetts and J. A. Howell. 'Synthetic seismic modelling of a
      large-scale geological cross-section from the Book Cliffs, Utah, USA'. In:
      Petroleum Geoscience 6 (3 2000), pp. 221–229. ISSN: 13540793. DOI:
      10.1144/PETGEO.6.3.221.

[92] O. Falivene, P. Arbués, J. Ledo, B. Benjumea, J. A. Muñoz, O. Fernández and
      S. Martínez. 'Synthetic seismic models from outcrop-derived reservoir-scale
      three-dimensional facies models: The Eocene Ainsa turbidite system
      (southern Pyrenees)'. In: *AAPG Bulletin* 94 (3 Mar. 2010), pp. 317–343. ISSN:
      0149-1423. DOI: 10.1306/08030908157.

[93] O. Rabbel, O. Galland, K. Mair, I. Lecomte, K. Senger, J. B. Spacapan
      and R. Manceda. 'From field analogues to realistic seismic modelling:
      A case study of an oil-producing andesitic sill complex in the Neuquén
      Basin, Argentina'. In: *Journal of the Geological Society* 175 (4 July 2018),
      pp. 580–593. ISSN: 00167649. DOI: 10.1144/JGS2017-116.

[94] A. Grippa, A. Hurst, G. Palladino, D. Iacopini, I. Lecomte and M. Huuse.
      'Seismic imaging of complex geometry: Forward modeling of sandstone
      intrusions'. In: *Earth and Planetary Science Letters* 513 (2019), pp. 51–63.
      DOI: 10.1016/j.epsl.2019.02.011.

[95] K. Bakke, J. Gjelberg and S. A. Petersen. 'Compound seismic
      modelling of the Ainsa II turbidite system, Spain: Application to deep-
      water channel systems offshore Angola'. In: *Marine and Petroleum
      Geology* 25 (10 Dec. 2008), pp. 1058–1073. ISSN: 02648172. DOI:
      10.1016/j.marpetgeo.2007.10.009.

[96] M. Tomasso, R. Bouroullec and D. Pyles. 'The use of spectral recomposition in tailored forward seismic modeling of outcrop analogs'. In: *American Association of Petroleum Geologists Bulletin* 94 (4 2010), pp. 457–474. DOI: 10.1306/08240909051.

[97] I. Anell, I. Lecomte, A. Braathen and S. J. Buckley. 'Synthetic seismic illumination of small-scale growth faults, paralic deposits and low-angle clinoforms: A case study of the Triassic successions on Edgeøya, NW Barents Shelf'. In: *Marine and Petroleum Geology* 77 (Nov. 2016), pp. 625–639. ISSN: 02648172. DOI: 10.1016/j.marpetgeo.2016.07.005.

[98] M. W. Shuster and T. Aigner. 'Two-Dimensional Synthetic Seismic and Log Cross Sections from Stratigraphic Forward Models'. In: *AAPG Bulletin* 78 (3 Mar. 1994), pp. 409–431. ISSN: 0149-1423. DOI: 10.1306/BDFF90C8-1718-11D7-8645000102C1865D.

[99] O. Holberg, J. Pajchel, P. Riste and H. B. Helle. 'Comparison of ray tracing and finite-difference modeling'. In: *SEG Technical Program Expanded Abstracts 1990*. Society of Exploration Geophysicists, Jan. 1990, pp. 1037–1041. DOI: 10.1190/1.1889901.

[100] V. Červený, L. Klimeš and I. Pšenčík. 'Seismic ray method: Recent developments'. In: *Advances in Wave Propagation in Heterogenous Earth*. Ed. by R.-S. Wu, V. Maupin and R. Dmowska. Vol. 48. Elsevier, 2007, pp. 1–126. DOI: 10.1016/S0065-2687(06)48001-8.

[101] S. W. Fagin. *Seismic Modeling of Geologic Structures : Applications to Exploration Problems*. Society of Exploration Geophysicists, Jan. 1991. ISBN: 978-1-56080-050-7. DOI: 10.1190/1.9781560802754.

[102] V. Červený. *Seismic Ray Theory*. Cambridge University Press, 2001.

[103] N. Rawlinson, J. Hauser and M. Sambridge. 'Seismic ray tracing and wavefront tracking in laterally heterogeneous media'. In: *Advances in Geophysics* 49 (Jan. 2008), pp. 203–273. ISSN: 0065-2687. DOI: 10.1016/S0065-2687(07)49003-3.

[104] J. Yang, J. Huang, H. Zhu, G. McMechan and Z. Li. 'Introduction to a Two-Way Beam Wave Method and Its Applications in Seismic Imaging'. In: *Journal of Geophysical Research: Solid Earth* 127 (6 June 2022). ISSN: 2169-9313. DOI: 10.1029/2021JB023357.

[105] D. M. Boore. 'Finite Difference Methods for Seismic Wave Propagation in Heterogeneous Materials'. In: 11 (Jan. 1972), pp. 1–37. ISSN: 0076-6860. DOI: 10.1016/B978-0-12-460811-5.50006-4.

[106] C. Clay. *Elementary exploration seismology*. Prentice Hall, 1990.

[107] N. Ricker. 'The form and laws of propagation of seismic waveletes'. In: *GEOPHYSICS* 18 (1 Jan. 1953), pp. 10–40. ISSN: 0016-8033. DOI: 10.1190/1.1437843.

[108] Y. Wang. 'Frequencies of the Ricker wavelet'. In: *GEOPHYSICS* 80 (2 Mar. 2015), A31–A37. ISSN: 0016-8033. DOI: 10.1190/geo2014-0441.1.

[109] L. Laigle, P. Joseph, G. D. Marsily and S. Violette. '3-D process modelling of ancient storm-dominated deposits by an event-based approach: Application to Pleistocene-to-modern Gulf of Lions deposits.' In: *Marine Geology* 335 (2012), pp. 177–199. DOI: 10.1016/j.margeo.2012.11.007.

[110] J. H. Nienhuis and J. Lorenzo-Trueba. 'Simulating barrier island response to sea level rise with the barrier island and inlet environment (BRIE) model v1.0'. In: *Geoscientific Model Development* 12 (9 Sept. 2019), pp. 4013–4030. ISSN: 1991-9603. DOI: 10.5194/gmd-12-4013-2019.

[111] A. Quiquerez, P. Allemand, G. Dromart and J.-P. Garcia. 'Impact of storms on mixed carbonate and siliciclastic shelves: insights from combined diffusive and fluid-flow transport stratigraphic forward model'. In: *Basin Research* 16 (4 2004), pp. 431–449. ISSN: 0950-091X. DOI: https://doi.org/10.1111/j.1365-2117.2004.00247.x.

[112] J. Storms. 'Event-based stratigraphic simulation of wave-dominated shallow-marine environments'. In: *Marine Geology* 199 (1-2 2003), pp. 83–100. DOI: 10.1016/S0025-3227(03)00144-0.

[113] J. Storms, G. Weltje, J. V. Duke, C. Geel and S. Kroonenberg. 'Process-response modeling of wave-dominated coastal systems: Simulating evolution and stratigraphy on geological timescales'. In: *Journal of Sedimentary Research* 72 (2 2002), pp. 226–239. DOI: 10.1306/052501720226.

[114] D. M. Tetzlaff. 'Modelling Coastal Sedimentation through Geologic Time'. In: *Journal of Coastal Research* 21 (3 (213) May 2005), pp. 610–617. ISSN: 0749-0208. DOI: 10.2112/04-704A.1.

[115] M. J. Pyrcz, R. P. Sech, J. A. Covault, B. J. Willis, Z. Sylvester and T. Sun. 'Stratigraphic rule-based reservoir modeling'. In: *Bulletin of Canadian Petroleum Geology* 63 (4 Dec. 2015), pp. 287–303. ISSN: 0007-4802. DOI: 10.2113/GSCPGBULL.63.4.287.

[116] Q. Sacchi, E. S. Borello, G. J. Weltje and R. Dalman. 'Increasing the predictive power of geostatistical reservoir models by integration of geological constraints from stratigraphic forward modeling'. In: *Marine and Petroleum Geology* 69 (Jan. 2016), pp. 112–126. ISSN: 02648172. DOI: 10.1016/j.marpetgeo.2015.10.018.

[117] L. Wan, S. Hurter, V. Bianchi, P. Li, J. Wang and T. Salles. 'The roles and seismic expressions of turbidites and mass transport deposits using stratigraphic forward modeling and seismic forward modeling'. In: *Journal of Asian Earth Sciences* 232 (July 2022), p. 105110. ISSN: 13679120. DOI: 10.1016/j.jseaes.2022.105110.

2

Characterising reservoir heterogeneity in a wave-dominated system: Sedimentological, stratigraphic, and petrophysical analysis of a field analogue (Judith River Formation, Late Cretaceous)

The outcrop of the Parkman Sandstone from the Judith River formation in Bridger, south Montana (USA), is an example of a clastic, wave-dominated shoreface system. In this location, the section forms a continuous outcrop of around 70 m in the vertical direction and more than $4km$ in the lateral direction. The outcrop includes a continuous depositional record from the offshore-shoreface transition to the backshore. We identified 7 different facies associations (FA) based on their petrographic and sedimentological properties, each of them linked to a different depositional subenvironment. All facies have in common a lack of clay/mud, scarce bioturbation, and a strongly weathered rock surface with weak cementation of the sediments. Rock samples from 5 FAs were collected and analysed in the lab to measure properties on grain density, bulk density, porosity, P-wave velocity, S-wave velocity, and Vp/Vs ratio. Field data show that the thickness of many of

the sandstone bed sets is less than $10m$, which is close to the sub-seismic scale limit in reflection seismic data at a typical reservoir depth ($> 2km$). The retrieved properties of the sandstone samples are non-unique to the FA, and the variation ranges per facies overlap with each other. With the available data, it was not possible to identify a correlation between properties per FA, or to characterise the lateral variations of the properties within the FA. However, the variation ranges show that allocating a single property value per facies association when constructing geo-models underestimate the variability the FAs.

2.1. Introduction

Outcrop analogues are important sources of information for subsurface reservoir characterisation, because they allow for direct observations of rock type distribution and stratigraphic architecture, including spatial relationships at different heterogeneity scales. Outcrops also allow for rock property analysis at a range of scales and at high densities. Observations of this type have been used as analogues to better understand the stratigraphic architecture of subsurface reservoirs (e.g. [1–4]). The spatial characteristics and rock property distributions of meter-scale horizontal and vertical heterogeneities can be used to better interpret similar features in reflection seismic data at typical reservoir depths ($> 2km$) (e.g. [5–7]). Often, attention is focused only on the architecture and facies distribution of the system, including recognition of erosional surfaces, lateral and vertical continuity and transitions of facies and facies associations, and lateral thickness changes. However, outcrops also make it possible to analyse the spatial variations of petrophysical properties [8].

Wave-dominated shoreface systems are targeted in the subsurface because of their promising reservoir potential [9–12]. They are typically formed by accumulations of sand and gravel, often well sorted and abraded, with relatively few heterogeneities but characteristic vertical grain size and bedding profile [13]. Shoreface systems can be easily overlooked in seismic data due to their subtle stratal relationships and their limited thickness, with some systems being as thin as $10m$ [1, 14–16]. Previous research has defined key diagnostic seismic criteria for the recognition of shorefaces in the subsurface [1], but little attention has been paid to the relationship between stratigraphic heterogeneities within wave-dominated shorefaces and the distribution of petrophysical properties. Stratigraphic heterogeneities in wave-dominated shoreface systems are associated with (1) erosional surfaces that result in vertical and lateral transitions between diverse lithologies [17], and (2) abrupt or gradual, vertical and lateral rock property changes, including porosity [18–20]. Understanding the impact of these heterogeneities on petrophysical properties and fluid flow behaviour can help build more robust energy transition workflows in reservoir modelling towards applications in subsurface storage (CO_2 or H_2) or geothermal heat production.

Petrophysical properties measured on outcrop samples cannot be directly correlated with subsurface measurements from core plugs due to the impact of weathering and diagenesis on the samples [21]. However, outcrops with extensive lateral and vertical continuity give the opportunity to sample rocks consistently, enabling the lateral and vertical analysis of petrophysical parameter variation and identify trends [22]. The shoreface outcrops of the Judith River Formation, whose basal section is referred to as the Parkman Sandstone, close to Bridger (Montana, USA) is an accessible outcrop with continuous exposure for several kilometres, and, therefore, a suitable analogue for subsurface wave-dominated shoreface systems.

This paper focuses on the sedimentological and petrophysical characterization of the parasequence at the base of the Judith River Formation. The first goal is to provide a field-based sedimentological and stratigraphic description of the outcrop, including information about the thickness and lateral continuity of the facies associations. The second goal is to analyse the distribution of petrophysical, acoustic, and elastic property values from outcrop samples, the distribution of these values at facies association level, and their spatial trends or correlations. To achieve our goals, first we will introduce the field location, the data collection, and the methodologies applied in this research. Subsequently, we will provide a description and interpretation of the facies associations, grain size analysis together with a correlation of the stratigraphic logs. Thereafter, the results and interpretation of the petrophysical measurements are presented, followed by a discussion focusing on the relation between the observed stratigraphic and petrophysical heterogeneities.

2.2. Geographical and Geological setting

The field analogue selected for this study is located next to the town of Bridger, in south-central Montana, $75km$ south from Billings (Carbon County, Montana, USA) (Figure 2.1). The study area is located west of the Pryor mountains and north of the Nye-Bowler Fault Zone, on the Eastern flank of the Reed Point syncline [23] (Figures 2.1B and 2.1C). The section is part of the Campanian Judith River Formation [24, 25]. The base of the Judith River formation includes a interval of sandstone, named Parkman Sandstone.

The Judith River formation, including the Parkman sandstone, was deposited in the Crazy Mountain Basin [23] close to the margin of the Bighorn Basin formed by the Nye-Bowler Fault Zone (Figure 2.1C). The Crazy Mountain basin is located in the western margin of the larger Western Interior Basin (WIB) [26]. The deposition of the Parkman Sandstone occurred in the Claggett T-R cycle, one of the five transgressive-regressive depositional cycles identified in the Upper Cretaceous of the WIB [26, 27]. The Claggett cycle was a period that lasted approximately $4m.y.$ during the Middle to Late Campanian, with relatively high and stable sea levels [28, 29]. The paleoclimate during the Upper Cretaceous was characterised by warmer mean annual temperatures than nowadays [30]. The research area was located in a temperature transition zone, with cold arctic waters to the North and warm tropical waters to the South [31].

The Parkman Sandstone is an important water and hydrocarbon reservoir in the area [23, 32, 33] and previous research worked on defining the age and depositional environment to better characterize the reservoir. In the Carbon County, where the analysed outcrop is located, the Parkman Sandstone is described as estuarine and brackish deposits [25]; other studies in the Bighorn basin area and surroundings, around $250km$ south of Bridger, describe the Parkman Sandstone as coastal plain [34], wave-dominated delta [32, 35], and river-dominated delta [36]. Previous

petrographic studies on the Judith River formation in Carbon County defined the formation as an alternation of grey and brown, andesitic sandstones, brown carbonaceous shale with coal streaks, and brown sandy shale [37]. Paleontological data and absolute dating of bentonite beds from the Parkman Sandstone in the Powder River Basin, northern Wyoming, constrained the deposition of the formation to Middle Campanian to a duration of $1.9 m.y.$ from 78.5 to $76.6 \pm 0.51 Ma$ [28, 38].
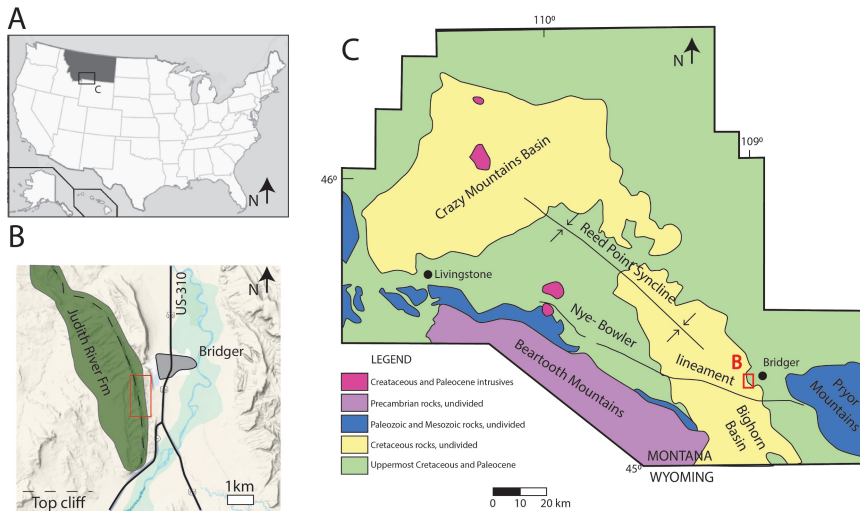
Figure 2.1: Geographical location and geological context of the study area. A - The study area is located in the southern border of Montana with Wyoming (USA). B - Judith River Formation outcrops in Bridger. In dashed lines the top of the continuous cliffs and in red the study area. Modified from Google Maps. C - Structural elements and distribution of the sediment age that outcrop around Bridger. The study area is located to the West of Bridger, highlighted in red. Modified from Johnson *et al.* [23].

The outcrop area is a NW-SE running cliff with over $7 km$ of lateral extent (Figure 2.1B). In the area, the thickness of the outcrops of the Judith River Formation varies between 75 and 100 meters [25]. In our study, we have included sections between 50 and $70 m$ thick, which, at their base, might include part of the top of the Claggett Shale formation, because the contact between the underlying Claggett Shale and the Judith River Formation is not well-defined in the outcrop. The paleo-shoreline in this area had a NW-SE direction [26]. The outcrop is composed by sandstone layers and minor silt layers, dipping $4°$ towards the SW ($224°$).

2.3. Methods and material

2.3.1. Field campaign: logging, paleocurrent data, sampling, and photogrammetry

Five sedimentary logs were recorded at a scale of $1:50$ and include data on colour, mineralogy, grain size, grain roundness and sorting, sedimentary structures, and paleocurrents. The logs cover 1500 meters along the outcrop, with spacings ranging from 200 to 500 meters. Based on the outcrop observations, different facies and facies associations (FA) were identified. The bounding surfaces between the FAs were defined based on changes in lithology, grain size, and sedimentary structures. Both the FAs and the bounding surfaces between them were convincingly correlated laterally due to excellent continuity and exceptional outcrop quality along the cliffs.

During the logging, different types of rock and coal samples were collected for petrographic analysis. A total of 44 plugs were drilled for petrophysical property analysis, with diameters values ranging from $2,74$ to $2,94cm$. They cover the different lithofacies observed on the outcrop. The plugs were collected parallel to the bedding using a Makita drill with diamond bites and using water to remove the while-drilling debris. For each sample, an extra rock sample from the same location was collected for other potential analysis. 30 samples were collected at the locations of the stratigraphic logs and 14 samples in between logs. 12 loose silt samples were collected and analysed for micropaleontology and palynology. Ten thin sections were prepared with blue taint, to highlight the sample porosity. The samples were selected to represent different FAs observed in the field. There were used for grain size analysis. In Appendix 2, a dataset with the sample information is provided.

Two 3D models of the study area were produced using UAV-based photogrammetry along the NW-SE running cliffs using an AUV (DJI Mavic 2 Pro). 532 photos were taken at three seconds intervals, ranging in file size from 8 to $12Mb$. The UAV was manually flown parallel to the outcrop surface. To geo-localize the 3-D photogrammetry panel, 13 ground control points (GCPs) were placed and surveyed using an Emlid Reach global navigation satellite system (GNSS) receiver. Raw GNSS measurements recorded by both the rover and base stations were processed using the open-source GNSS post-processing package RTKLIB, which allowed for the determination of the GCP positions with centimetre accuracy relative to the local base station.

The software Agisoft Metashape Pro (Version $1.8.4$, July 2022) was used to build the 3D photogrammetry models. To manage the large image set, the photogrammetric images were divided into 3 model sections for each model. For each section, the position of the corresponding GCPs were added. The complete 3D outcrop model was imported into VRGS (see [39]) for visualization and interpretation.

2.3.2. Grain-size analysis

We analysed the grain size distribution of the thin sections by applying an image-based, non-destructive workflow. The thin sections were photographed using a Axioscan from Zeiss microscope to obtain high quality images. The best grain-segmentation results were achieved with the open-source tool 'segmenteverygrain' ([40]; version summer 2023). 'segmenteverygrain' is a Python package that relies on the Segment Anything Model (SAM) to detect grains in images [41]. SAM is developed by Meta and enables high-quality grain border detection. To deal with some of the limitations that SAM poses, 'segmenteverygrain' includes a Unet-style, patch-based convolutional neural network which speeds up the process and limits the number of overlapping masks. 'segmenteverygrain' includes modules for the user to clean up the initial segmentation results by deleting, merging and adding new grains in the generated dataset [40]. The workflow for the calculation of the grain size distribution is depicted in Figure 2.2. 'segmenteverygrain' provides the area, major axis, minor axis, and perimeter measurements per grain. With the area information and under the assumption of circular grains, we calculated the diameter per grain and, from these results, we generated the grain size distribution curve. We also calculated sphericity and circularity based on the equations suggested by Li, Wilkinson and Patchigolla [42] and that depend on the diameter based on the perimeter of the grains.
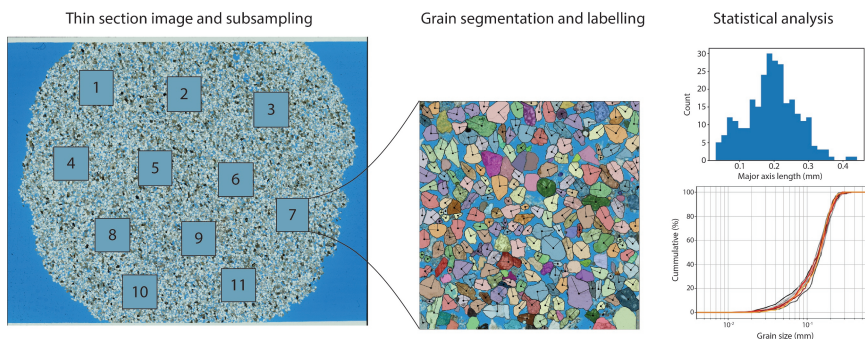
Figure 2.2: Workflow for the analysis of grain size distribution based on the application of the 'segmenteverygrain' machine-learning tool for grain segmentation on images. First, the high-resolution images of the thin sections are pre-processed to increase the contrast by 40% and enhance grain border detection. From the images, $10-12$ subsamples are selected (with a resolution of $300\,ppi$ and sizes ranging from 1900 to 2100 pixels per side), with a scale included. Sharpening techniques available in Photoshop were applied to subsamples located near the edges of the sample. We run the 'segmenteverygrain' tool, with processing times ranging from 15 to 60 minutes. From the resulting segmentation and labelling, different measurements from each grain are extracted and the statistical analysis applied.

2.3.3. Petrophysical analysis

The rock plugs were prepared for petrophysical analysis by cutting and smoothing of the edges for measurement. The length of some samples exceeds the recommended length for petrophysical and acoustic property measurement, so they were cut into smaller subsamples. This also allowed to measure the same properties several times.

The measured properties included grain density, P-wave velocity, and S-wave velocity. With the obtained measurements, bulk density, porosity and Vp/Vs ratio were calculated. Per facies association, a different number of measurements were performed depending on the number of samples available and the size of the samples. One grain density, porosity, and S-wave velocity measurement per sample was taken.

For the porosity and grain density, the Ultrapyc 5000 with medium and large cell sizes was used. Both cells have an accuracy of 0.02% and a repeatability of 0.01%. Previous research with the same device has shown good reliability with high percentage of data falling within 95% confidence interval [43]. With the porosity and grain density data, we calculated bulk density by assuming that the porosity is filled with air at room temperature.

P-wave and S-wave velocity measurements were obtained from the rock plugs with an active acoustic device. The measurements were taken applying a voltage of $40V$ and $66000khz$ waves, with an average arrival time between 20 and $50\mu s/dv$ and a resolution of 8 bits. To measure the P-wave velocity, we used electric transducers designed for concrete and rock samples. We used a Normal Incidence Shear Wave Transducer V1548 of 1 inch of diameter and with frequencies up to $0.1Mhz$ from Panametrics. With the Shear Wave Transducer, P-wave velocity is also calculated. The results were compared between both devices to check the reliability of the data. The S-wave velocity arrival time is observed as the first interference over the P-wave. This moment is not always clear in the readings, and therefore a minimum and maximum S-wave velocity has been calculated; the average value between those two measurements is used in our analysis. We spread coupling paste for shear waves (Echo Shear Wave Couplant from Echo Ultrasonics) in between the samples and the transducer and receiver to ensure that the transducer and receiver were properly attached to the sample.

2.4. Results and Interpretation

In this section, results and interpretations from the outcrop field data collection, sedimentological analysis, stratigraphic architecture, micropaleontology and palynology analysis, and the petrophysical and acoustic properties are presented.

2.4.1. Sedimentological analysis

The outcrop and samples are characterized by clastic rocks with grain sizes ranging from silt to coarse sand, with very little to no bioturbation. Seven facies associations (FA) were recognised in this study based on lithology, grain size, thickness, and sedimentary structures (Table 2.1), reflecting different depositional environments. The characteristics of the facies associations match those previously described for wave-dominated, shallow-marine environments, thus, we have followed the scheme used in previous analysis of these systems [17, 44, 45]. Facies associations FA1, FA2, FA3 and FA4 are characterized by a general upward increase in the sand proportion with very little variation in grain size. The coarser grained sandstone layers are found within the intercalation of sandstone-siltstone layers at the base of the section, in FA2 (Figure 2.3A), and in FA5 (Figure 2.4C). Some sandstone samples from FA2, and all samples from FA1, FA3, FA4, FA5, and FA6 show very poorly developed cement or no cement, as depicted by the thin section image in Figure 2.5.

Table 2.1: Summary of the facies associations studied and their characteristics. For each facies association, we include a nomenclature, texture, thickness, sedimentary structures, fossil content and bioturbation, and other remarkable features. When acquired, paleocurrent information is also available (graphs in Appendix 1). Representative photographs are included in Figures 2.3 and 2.4. Detailed information about the grain size analysis is available in Appendix 2.

Facies associations (FA)	Texture	Thickness	Sedimentary structures	Grain size analysis	Fossil content/ bioturbation	Paleocurrents	Others
FA1	Alternation of thin layers of siltstone and thin layers of sandstone. Sharp-based sandstone layers with lateral thickness variations. The top of the sandstone is wavy. Siltstones deposited on top of the sandstone layers. No gradual transition observed. Fine to very fine sandstone with rounded grains, well to very well sorting matrix. Some layers with medium to coarse grains.	Sandstone mm up to 10 cm thick, with predominance of $1-5cm$ thicknesses. Coarser grained sandstones tend to thicker layers. Lateral variations of thickness. Centimetre scale siltstone layers, with predominance of $5cm$ thicknesses.	Siltstone lacks sedimentary structures. Sandstone layers are structureless or very thinly, asymmetrical cross-laminated (mm-cm layers).	No grain size analysis.	Scarce bioturbation, very few vertical burrows. The diameter of the burrows varies between $1-3cm$.	No paleocurrents measured.	Scarce mudclasts (up to $15cm$ long). Some sandstone layers are rich in white mica and others in organic matter. Highly weathered, samples show little to no cement.

Table 2.1: Summary of the facies associations described in the field (continued)

FA	Texture	Thickness	Sedimentary structures	GSA	Fossil/ bioturbation	Paleocurrents	Others
FA2	Alternation of thin siltstone layers and sandstone layers. Sharped-based sandstone layers with lateral thickness variations in layer thickness. Siltstones deposited on top the sandstone layers. No gradual transition observed. Fine to very fine sandstone, well to very well sorted. No information about roundness.	Sandstones thickness range from 0.1 to 30cm, with predominance of 15 − 20cm thicknesses. Lateral variations in layer thickness. Centimetre scale siltstone layers, with an average thickness of 5cm.	Siltstone layers lack sedimentary structures or display parallel lamination. Asymmetrical cross-laminated (mm-cm layers) sandstones, sometimes very thin lamination. Occasionally, thicker layers include low-angle cross-lamination and planar lamination. Abundant scour and reactivation surfaces. Erosional base of sandstone. No amalgamation of sandstone layers observed.	No grain size analysis.	Scarce bioturbation, very few vertical burrows. The diameter of the burrows varies between 1 − 3cm.	No paleocurrents measured.	Some well-cemented sandstone samples.
FA3	Sharp-based sandstones with scarce siltstone layers in between layers. The thickness of the silt layers decreases towards the top. Well to very well sorted, very fine to medium sand. Well-rounded sand.	Bed thickness: 30 − 90cm. The thickness of the sandstone beds varies cyclically. The sandstone layers are thinner right after a siltstone layer and the thickness of the sandstone layers increases progressively until the next siltstone layer. Lateral thickness variations of the sandstone layers. Siltstone layers 5 − 10cm thick.	Low angle, trough cross lamination with large wavelengths (in the meter scale and up to 8 m in some cases) with scour surfaces. The sandstone layers are amalgamated.	$N = 4$ Mean grain size $0.0625mm$ Sphericity $= 0.785$ Circularity $= 0.645$	None.	Shift from unidirectional eastward [$N = 4$, Average $95°$ $(70° − 110°)$] to predominantly south-westward [$N = 14$, Average $255°$ $(200° − 340°)$]	Occasional internal erosional surfaces with floating coarse grains. Highly weathered, samples show little to no cement.

Table 2.1: Summary of the facies associations described in the field (continued)

FA	Texture	Thickness	Sedimentary structures	GSA	Fossil/ bioturbation	Paleocurrents	Others
FA4	Very clean, very fine to medium grained sandstone layers, with sharp and often erosional bases. Round to very round grains and moderately to very well sorted. Occasional silty layers.	Individual set thicknesses varying from 10 to 50cm. Lateral thickness variations.	The sandstone layers show low-angle, trough cross stratification, sometimes looking like sub-parallel stratification, and amalgamation. The stratification is mainly unclear. Poor preservation of bottom and topsets of the cross-stratification. The silty intervals display sub-planar stratification.	$N = 3$ Mean grain size $= 0,089mm*$ Sphericity $= 0.769*$ Circularity $= 0.634*$ *Two of the samples show similar values, but one has higher mean grain size and lower sphericity and circularity.	Scarce horizontal burrows, with millimetre-scale diameter. Possible *Ophiomorpha*. Scarce broken shells.	Unidirectional westward [$N = 6$, Average 280° (290° – 5°)]	Coarser grain size with clay clasts (flat and up to 14cm long) in the contact with FA3. Very poorly cemented intervals with of concretions of different sizes. Isolated, mm-sized mud-clasts. Scarce organic matter-rich layers. Some layers are rich in white mica. Laterally discontinuous weathering profiles. Highly weathered, samples show little to no cement.
FA5	Fine to coarse-grained sandstone. Coarsening upwards trend. Moderately to very well sorted and rounded grains. Coarser sand at the bottom of some sets.	Lateral changes in thickness. Set thickness varies from 5 to 80cm, depending on the location. Decreasing set thickness towards the top.	Trough cross bedding.	$N = 3$ Mean grain size $= 0.151mm$ Sphericity $= 0.712$ Circularity $= 0.6$	*Macaronichnus segregatis*, abundant in some locations. Scarce shell fragments $(1 - 2mm)$.	Unidirectional southward [$N = 11$, Average 170° (135° – 200°)]	Rich in organic material, specially towards the top. Rich in white mica (some fragments are mm scale). Scarce, small iron concretions towards the top. Laterally discontinuous weathering profiles. Highly weathered, samples show little to no cement.
FA6	Very well to well sorted, fine to coarse-grained sandstone. Rounded grains.	Laterally discontinuous. Maximum set thickness of 10cm.	Mainly symmetrical cross-laminated. Asymmetrical cross-lamination, planar cross-stratification, or structureless sandstone locally.	No grain size analysis.	None.	No paleocurrents measured.	Highly weathered, samples show little to no cement.

Table 2.1: Summary of the facies associations described in the field (continued)

FA	Texture	Thickness	Sedimentary structures	GSA	Fossil/ bioturbation	Paleocurrents	Others
FA7	Brown coal, sandstone (fine to very fine), dark grey siltstones.	Laterally discontinuous. Bed thickness varies from 0 to 5m.		No grain size analysis.	None.	No paleocurrents measured.	Mottling and calcrete.
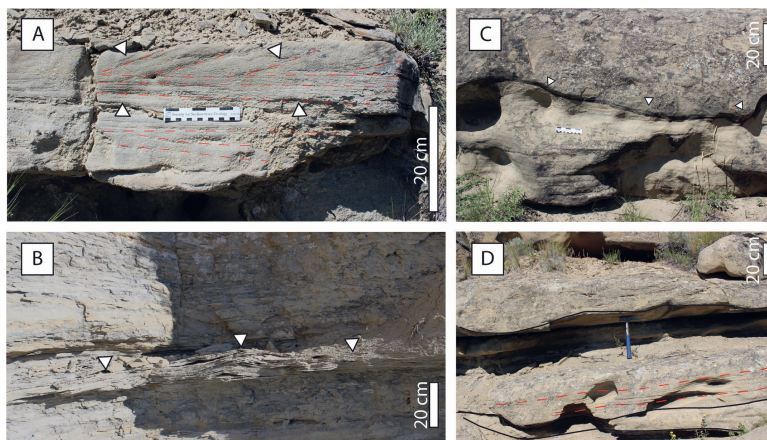
Figure 2.3: Outcrop photographs illustrating the main features from facies associations FA1 to FA3. A - Detailed image of a sandstone layer in FA2. In red discontinuous lines the internal structure of the layer: at the base, low-angle cross lamination; in the middle, planar lamination; and cross lamination in the top. B - Example of thin sandstone layer, thinly cross-laminated and lateral thickness variations in FA1. C - Example of two fine- to medium-grained sandstone layers in FA3, with a scour surface (indicated in white triangles) separating the layers. On top of the scour surface, coarse, floating grains were identified. D - Contact between sandstone layers in FA3, with low angle cross lamination within the sandstone layer (in red). Scale bar in all photographs: $20cm$.
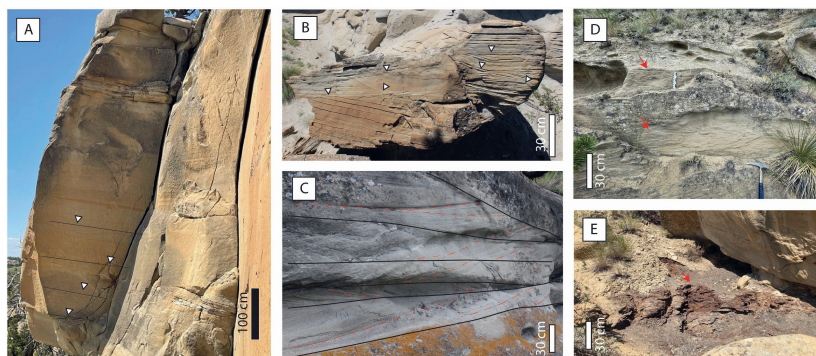
Figure 2.4: Outcrop photographs illustrating the main features from facies associations FA4 to FA7. A - View of the sub-planar stratification in the sandstone of FA4. B - Detail of the low-angle cross lamination conserved within concretions in FA4, with white triangles some of the scour surfaces are indicated. C - Outcrop example of FA5 showing the relationship between the erosion surfaces (in black) and the trough-cross stratification (in red). D - Thin and parallel cross-lamination of sandstones in FA6. E - Brown coal layer in FA7.
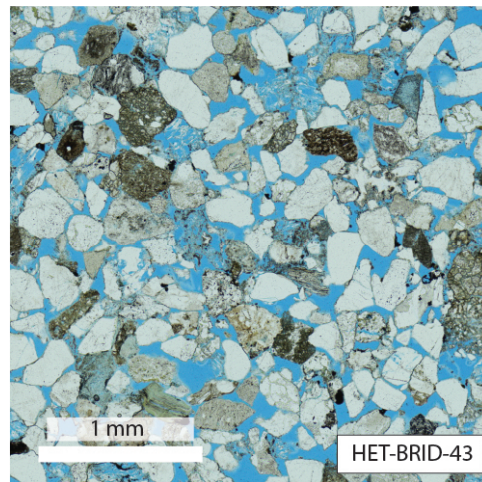
Figure 2.5: Example of a thin section from sample HET-BRID-43 in FA5. The sample porosity is filled by blue epoxy. Different types of grains can be identified, but no matrix nor cement, which characterises the thin sections analysed. White bar equals to $1mm$.

Facies association 1 (FA1): Offshore Transition

This association includes an alternation of thin layers of siltstone and sandstone, with grain sizes typically fine to very fine sand. The sandstones are sharp-based, display no internal structure or are thinly cross-laminated, and their thickness varies from some millimetres up to $10cm$ (Figure 2.3B). Some sandstone layers are composed of coarser grains, between medium and coarse sand, and tend to be thicker than the layers composed of finer grains. The sandstone layers vary in thickness laterally. Embedded in the sandstones, elongated mudclasts can be found, up to 15 cm long. Some of the sandstone layers are rich in organic material, with millimetre to centimetre scale coal fragments. Other layers are rich in white mica fragments. Structureless silt deposit occur on top of the sandstones, with abrupt transitions from the sandstone layers into the silt layers.

This facies association is interpreted to represent the alternation of deposition from suspension during fair-weather conditions and deposition of event-related sandstones during storm conditions in the offshore transition. The thin asymmetrical cross-lamination of the sandstone layers is related to the formation of ripples by oscillatory and unidirectional currents during major storms [17]. The silt layers deposited from suspension during fair-weather periods. Medium to coarse grained sandstones have also been described in this facies association. These layers could be related to sandy hyperpycnal flows or sustained, sediment-laden turbulent flows [46]. This type of flows are low-density, long-lived flows linked to river effluents. Whenever the slope of the system is continuous and without abrupt inclination

changes, the flow can travel long distances into the basin. The presence of mica and organic matter rich layers are interpreted to be related to the gravitational collapse of the suspension plumes formed during the hyperpycnal flow [46].

Bioturbation is scarce. Very few and isolated simple, vertical burrows were observed, with diameters in the centimetre scale. The bioturbation is interpreted to represent the *Skolithos* ichnofacies [47]. *Skolithos* can be found in lower shoreface to offshore depositional environments, where they opportunistically colonise sandy substrates [48]. The low diversity and scarce bioturbation in the offshore-transition depositional environments and the presence of opportunistic colonization are interpreted to represent an environment where the development of traditional offshore transition ichnofacies was hindered. Strong storm-wave effects have been proven to markedly decrease the diversity and abundance of bioturbation [49].

Facies association 2 (FA2): Distal Lower Shoreface

This association includes an alternation of thin layers of silt and sandstone layers, with grain sizes typically ranging from fine to very fine sand, which differs from FA1 in terms of the thickness of the sandstone layers and the sedimentary structures therein. The sandstones display thin, asymmetric cross-lamination, and their thickness varies from some millimetres up to $30cm$ although the majority of layers are between 15 and $20cm$ thick (Figure 2.3A). Occasionally, some of the thickest layers include low-angle cross lamination and planar lamination. Some sandstone layers are composed of coarser grains, between medium and coarse sand. The base of the sandstones varies from sharp to clearly erosional. In contrast to FA1, erosional surfaces and scours are recognised in some of the sandstone layers. The sandstone layers vary laterally in thickness. Structureless and parallel-laminated siltstones deposit occur on top of the sandstones, with abrupt transitions from the sandstone layers into the silt layers.

This facies association is interpreted to represent the alternation of deposition from suspension during fair-weather conditions and deposition of event-related sandstones during storm conditions in the distal lower shoreface [44]. In this facies association, the storm-wave related deposition is better developed, with sandstone layers that include ripple lamination and hummocky cross-stratification. Hummocky cross-stratification forms under storm-generated, waning oscillatory flows [50]. The increase in the abundance and the thickness of sandstone layers indicates a shallowing or an increased storm-activity.

Bioturbation is scarce and shows the same characteristics as in FA2, with isolated simple, vertical burrows belonging to the *Skolithos* ichnofacies. The low diversity and scarce bioturbation could be related to strong storm-wave effects in the depositional environment [49].

Facies association 3 (FA3): Proximal Lower Shoreface

This association consists of sandstone layers and scarce, thin silt layers. The sandstone layers, with grain sizes varying between very fine to medium sand, are well to very well sorted and are formed by well-rounded grains. The sandstones display low-angle cross lamination with large wavelengths (up to $8m$), and their thickness varies from $30cm$ up to $90cm$ (Figure 2.3C and 2.3D). There are also lateral thickness variations at the same wavelength as the low-angle cross lamination. The base of the sandstones are erosional surfaces. Scour surfaces are common and majority of the sandstone layers are amalgamated. Occasionally, internal erosional surfaces are observed with floating coarse grains on top of them (Figure 2.3C). Scarce layers of structureless siltstones, with abrupt transitions from the sandstone layers into the silt layers.

There are two intervals with this facies association. The lower interval displays cyclical thickness variations of the sandstone layers. The sandstone layers are thinner right on top of a silt layer and the thickness of the sandstones increases progressively until the next silt layer.

The grain size distribution and sphericity/circularity of four samples from the upper FA3 interval were analysed. The mean grain size per sample varied from 0.057 to $0.068mm$. The sphericity of the samples goes from 0.773 to 0.8 and the circularity, from 0.632 to 0.667.

The low-angle cross-stratification and lateral thickness variations of the sandstone layers are hummocky cross stratification, resulting from storm and waves generated flows [50]. This facies association is interpreted to represent proximal lower shoreface deposits, where sedimentation is controlled by oscillatory-dominated combined flows [17, 50].

Paleocurrent indicators were measured for each of the two intervals of FA3. Each interval resulted in different dominant paleocurrent direction. The lower interval is characterized by a unidirectional paleocurrent towards the east, pseudo-perpendicular to the shoreline and in the seaward direction [26]. Measurements in the upper interval vary within a $180°$ spread, with predominance of paleocurrents towards the west-southwest direction, oblique to the paleo-shoreline and directed landwards. This change in paleocurrents might indicate a change in the processes controlling deposition. Seaward directed sedimentary structures result from seawards-directed post-storm flows [50, 51]. Oblique and landwards directed paleocurrents could be related to an increasing influence of wave-induced currents as overall water depth decreases.

Facies association 4 (FA4): Middle Shoreface

This association is composed of very clean sandstone layers and scarce, thin silt layers. The sandstone layers, with grain sizes varying from very fine to medium sand, are moderately to very well sorted and are formed by rounded to well-rounded grains. The sandstones display low-angle trough cross-stratification, which in some cases appears as sub-parallel stratification (Figures 2.4A and 2.4B), and sandstone layers are amalgamated often showing sharp and erosional bases. There are cm-scale lateral thickness variations in the sandstone layers. Scour surfaces are common and all layers are amalgamated, which results in poor preservation of bottom and top-sets of the cross-stratification. The stratification is often unclear, but some internal erosional surfaces are observed (Figure 2.4B). Scarce layers of structureless siltstones occur, with abrupt transitions from the sandstone layers into the silt layers. At the contact with FA3, medium sand layers with elongated, clay clasts (flat and up to $14cm$ long) are observed. Isolated, millimetre-sized mudclasts are observed in other locations. Some layers are rich in organic matter and some others in white mica fragments.

There are two superimposed intervals of FA4. The lower interval does not exhibit evident diagenetic features, whereas the upper interval is characterized by the development of centimetre- to metre-scale concretions (Figure 2.4B). The shape of the concretions varies from rounded to elongated ellipsoids. The concretions develop locally and have been identified in the central and two northernmost stratigraphic logs. They are located at different sandstone layers within the upper interval.

The grain size distribution and sphericity/circularity of three samples from FA4 were analysed, one from the lower interval and two from the upper interval. The mean grain size per sample varied from 0.061 to $0.137mm$. The sphericity of the samples ranges from 0.735 to 0.786 and the circularity, from 0.607 to 0.652. One of the samples of the upper interval shows coarser grain size (more than double the mean diameter) and lower sphericity and circularity than the other samples. This sample is located at the southernmost log, and it was taken in a poorly cemented zone. The difference in grain size properties results from the variability within the facies association, already observed in the field, with sand varying from very fine to medium grain size.

This facies association is interpreted to represent sedimentation in the middle shoreface [49]. The low-angle cross-stratification and amalgamation of sandstone layers is characteristic of swaley cross-stratification formed due to storm reworking [50, 51]. Swaley cross-stratification forms at higher sediment transport rates than hummocky cross-stratification, in a more landward position [51].

Paleocurrent indicators were measured in the upper interval of the FA4. The results show a dominant unidirectional westward paleocurrent, pseudo-perpendicular to the

shoreline and in the landward direction [26], but with measurements spreading within a $180°$ range. In combination with the presence of swaley cross-stratification, FA4 could represent an onshore and oblique, storm-driven flow. Such features have been previously observed in Cenomanian deposits in Sao Luis Basin, northern Brazil [52]. One of the possible mechanisms suggested for these landwards-oriented features is the combination of erratic storm waves refracted to shore normal directions due to the combination of strong winds and shoaling effect [53].

Bioturbation is scarce and it is only present at the top of the upper interval of FA4. It is represented by scarce horizontal burrows, with millimetre-scale diameter. These burrows are identified as belonging to the *Ophiomorpha* ichnofacies. The low diversity and scarce bioturbation are typical for middle and upper shoreface sandstones [49].

This facies association displays a certain degree of meter- to decametre-scale lateral heterogeneity (Figure 2.6) with some outcrops showing protrusions with a cliff-forming character, while other areas are less steep and tend to be covered by debris and vegetation. The observations made in the field and samples indicate that both areas belong to the same facies association based on their sedimentological characteristics. We conclude that these features develop as the result of weathering/erosional effect due to water flow and more sustained vegetation. Samples from both areas have been collected to evaluate if the different weathering profiles also link to changes in their petrophysical properties.

Facies association 5 (FA5): Upper Shoreface

This association is composed of medium to coarse-grained sandstone layers. The sandstone layers are moderately to very well sorted and are formed by rounded grains. There is a coarsening upwards trend from the base of FA5 to the top of the grain size, from predominantly fine to medium sandstones to medium to coarse sandstones. The sandstones display multidirectional trough cross-stratification (Figures 2.4C). The coarser sand grains are located at the bottom of the sandstone sets. The thickness of the sandstone sets vary from 5 to $80cm$, and there is a general trend of upwards thinning of the sets. The sets show lateral thickness variations. This facies association also includes organic material, white mica and iron concretions. The concentration of organic material progressively increases towards the top and it is mainly deposited on the topset of the stratification. Some layers are rich on white micas, with fragments up to some millimetres long. Scarce, small iron concretions are also found close to the top of the FA5.

The grain size distribution and sphericity/circularity of three samples from FA5 were analysed. The mean grain size per sample varied from 0.145 to $0.159mm$. The sphericity of the samples goes from 0.59 to 0.79 and the circularity, from 0.592 to 0.605. FA5 is composed by the coarsest grain size from all facies

associations and displays the lowest values of sphericity and circularity. This means that these samples in FA5 are composed by grains less rounded than in other facies associations for which grain size analysis was performed. This matches with the observations made during the initial outcrop analysis. Paleocurrent indicators measured for FA5 show a spread within a $90°$ range, with a predominant unidirectional southwards paleocurrent, pseudo-parallel to the shoreline [26].

This facies association is interpreted to represent upper shoreface sedimentation [17]. The observed sedimentary structures and sandstone set thickness indicate that the flow intensity was higher than in FA1 to FA4 and resulted in the migration of three-dimensional dunes [54]. This migration would be a response to the longshore currents generated by waves during fair-weather conditions above the fair-weather wave-base [17], as supported by the paleocurrent measurements taken in the field. The presence of mm-scale mica flakes suggests the existence of a nearby and/or young continental sediment source system [55, 56].

The bioturbation in this facies association is only observe locally, and then close to the contact with FA6. Burrow clusters of *Macaronichnus segregatis* were found, indicating deposition in a high-energy environment [49]. The presence of zones with abundant *Macaronichnus segregatis*, also known as "toe-of-the-beach", is characteristic of upper shoreface and foreshore deposits and tends to develop at the transition between these two depositional environments [57].

This facies association displays a certain degree of metre- to decametre-scale lateral heterogeneity (Figure 2.6). Some outcrops areas show protrusions with a cliff-forming character, while other areas are less steep and tend to be covered by debris and vegetation. The observations made in the field and samples indicate that both areas belong to the same facies association based on their sedimentological characteristics. We conclude that these features develop as the result of weathering/erosional effect due to water flow and more sustained vegetation. It was not possible to sample the cliff-forming protrusions because of accessibility.

Facies association 6 (FA6): Foreshore

FA6 is composed of sandstones varying in grain size from fine to coarse, with very well to well sorted and rounded grains. It displays a variety of sedimentary structures, including structureless, planar cross-stratification and symmetric and asymmetric cross-lamination related to ripples (Figure 2.4D). The sedimentary structures of this facies association are not laterally continuous.

The symmetric cross-lamination is interpreted to have been formed by wave-induced oscillatory currents [58] in a foreshore environment. However, the variety of grain size and sedimentological structures described in the field indicate lateral variations of the dominant currents or depositional processes. Asymmetric cross-lamination is

related to unidirectional currents [58], structureless areas can be related to rapid deposition of sediment-laden, storm-related currents [59, 60] or liquefaction [61], and planar cross-stratification with rip currents [62]. All these processes can be laterally active in foreshore environments.
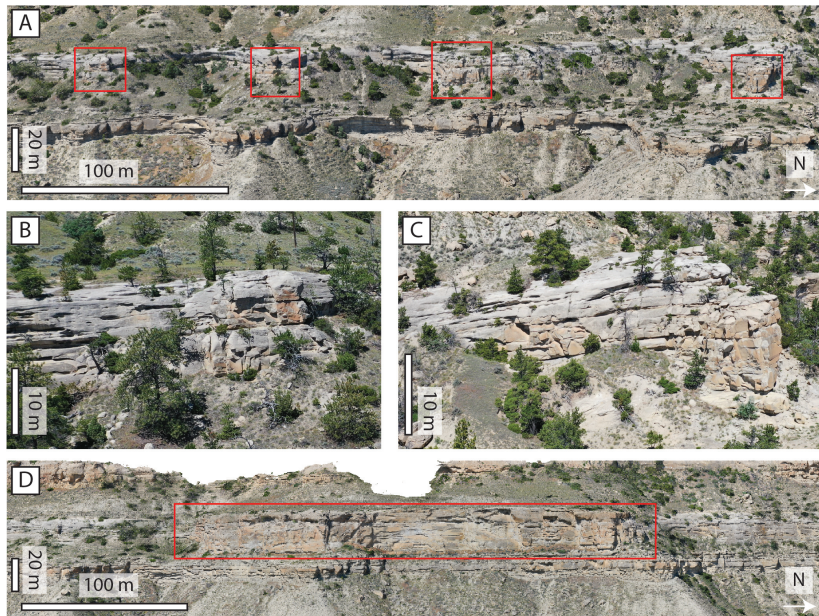
Figure 2.6: Meter-scale weathering-related, lateral heterogeneities observed in the uppermost intervals of FA4 and FA5, indicated by their protrusion, and cliff-forming character relative to the rest of the cliff. A - Overview of some of these locations, highlighted in red, with lateral extent of tens of meters. B - Detailed image of the southernmost protrusion in A. C - Detailed image of the northernmost protrusion in A. D - Overview of one of these heterogeneities, with a lateral extent of $240 m$.

Facies association 7 (FA7): Backshore- Lagoon

Facies association FA7 is composed of brown coal deposits (Figure 2.4E) and fine-grained sandstones, has maximum thickness of 5 meters, and it is not laterally continuous. It is found at the top of all logs with the exception of the northernmost one. Sand with calcretes and mottling is observed only in the central log. The presence of mottling and calcretes in the sandy deposits are indicative of pedogenetic processes.

This facies association is interpreted to represent deposition in a backshore or lagoonal depositional environment. It displays little evidence for wave and storm activity, because sandstone deposition is only observed in the area around the central log. The sediment supply is based on organic matter from vegetation,

probably developed in salt marshes or coastal plain environments, which have been previously described for the Western Interior Basin [63].

2.4.2. Stratigraphic architecture of the facies association succession

The base of the section and the contact with the underlying formation (the Claggett formation, consisting of shale) is not constrained. From literature, it is known that the contact between the Parkman Sandstone and the Claggett formation is conformable [33] and both sharp and transitional contacts have been identified in the neighbouring Bighorn basin [64]. At the study site, the contact between the Claggett Formation and the Parkman Sandstone is transitional, and due to insufficient age data for the sediments, we were unable to correlate it with the contact observed in outcrops from adjacent basins. As a result, the precise position of the formation boundary remains uncertain.

In the study area, nine distinct intervals were identified, consisting either of alternating sandstone and siltstone beds or of sandstone bedsets alone. Each facies association (FA1, FA2, FA5, FA6, and FA7) is represented by a single interval, while FA3 and FA4 occur in two separate intervals each. Based on observations of the drone images, we conclude that all vertical transitions between these intervals are gradual, with no evidence of erosional surfaces (Figures 2.7 and 2.8). Across the studied outcrop, which spans approximately 1200 meters, no lateral changes in facies associations were observed.

The vertical stacking of FA1, FA2, and the lower interval of FA3 is marked by a gradual increase in both the number and thickness of sandstone layers, accompanied by a corresponding decrease in siltstone deposition (Figure 2.7). The boundaries between these intervals are approximate and are not associated with any distinct event or marker bed. At the top of the lower FA3 interval, sandstone layers progressively merge with those of the lower FA4 interval (Figure 2.7A), indicating a lack of erosion at this transition. The contacts between the lower FA4 interval, the upper FA3 interval, and the upper FA4 interval are defined by sharp-based sandstone beds (Figure 2.8A), though no direct evidence of erosional surfaces has been observed. The transitions from the upper FA4 interval into FA5 and FA6 are more gradual, characterized by changes in sandstone thickness and sedimentary structures (Figure 2.8). The contact between FA4 and FA5 is most clearly distinguished in drone imagery, where it corresponds to a shift in the weathering profile (Figure 2.8). Finally, the boundary between FA6 and FA7 is not directly visible in the field due to surface cover by debris and vegetation.
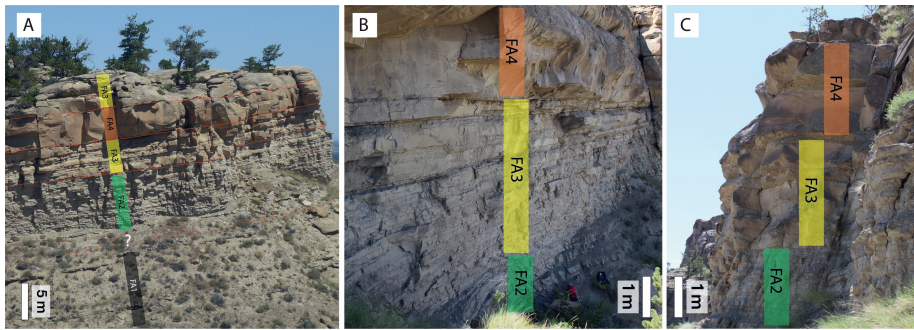
Figure 2.7: A - Overview of the lower half of the outcrop. A gradual increase in sandstone layers and in the thickness of these layers through FA1, FA2, and FA3 is observed. The contacts are all gradual and the limit between the facies associations is approximated. The contact between FA3 and FA4 is also gradual, with no erosional features observed and layers from FA3 merging into FA4. On top of FA4, there is another interval of FA3. B - Detail of the contacts between FA2, FA3, and FW4. This photograph shows the merging of layers from FA3 into FA4. C - Detail of the contacts between FA2, FA3, and FA4. The thickness of each facies association per location changes, showing the lateral variability of this type of wave-dominated systems. The scale bar is included for each case.
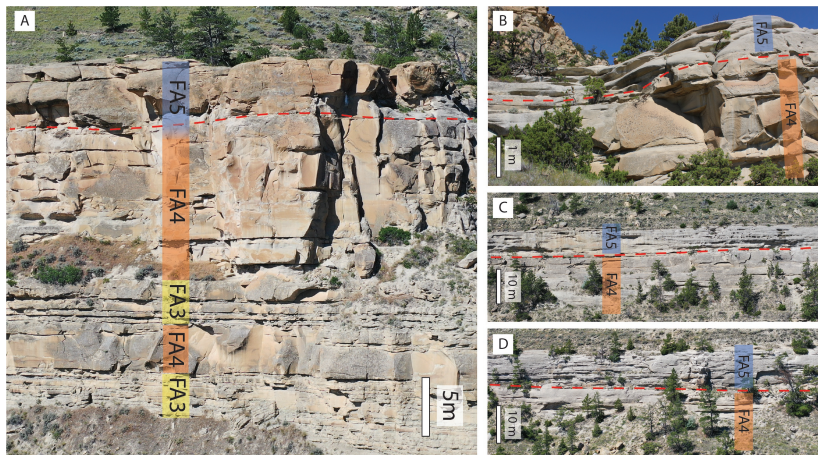
Figure 2.8: Different examples of the contact between, FA3, FA4, and FA5. In red, the contact between FA4 and FA5 is indicated. A - Only location where the contact between FA3, FA4, and FA5 is exposed. None of the contacts show erosional features. B - Outcrop image with the low-angle, trough cross bedded sandstones of the FA4 at the bottom and trough cross bedded sandstones at the top. The transition between the facies is gradual. Due to the perspective of the photo, the scale is only applicable for the central area of the image. C and D - Drone images of the contact between the FA4 and FA5. On vertical cliff areas, the contact is a line that separates two different weathering profiles. Scale bars are included for each figure.

Centimetre-scale sand layers with asymmetrical cross-lamination, along with silt layers characteristic of FA1, are observed at the top of FA7. This shift in sedimentation—from a backshore/lagoon setting to an offshore transition environment—suggests that the contact marks a flooding event, with the boundary between FA7 and FA1 representing the flooding surface.

2.4.3. Micropaleontology and palynology analysis

The micropalaeontology split samples were dominated by plant matter, and no microfossils were recovered. Consequently, no ages for the samples can be established. Similarly, the palynology split samples are dominated by plant matter, spores, and pollen (Table 2.2), which only allowed for an approximate dating. The presence of Surculosphaeridium longifurcatum, a dynoflagellate, in samples HET-BRID-64 and HET-BRID-65, at the base of log 5, indicates that the samples are not younger than Early Campanian [65]. This matches with the age of the Judith River formation, which is dated to be Campanian [25]. Palynology samples from FA1 and FA2 are interpreted to be deposited in a non-marine setting (Table 2.2). Samples HET-BRID-64 and HET-BRID-65 contain enough dinocyst specimens to suggest that they were deposited in a transitional terrestrial/marine setting. The presence of high concentrations of spores and pollen reflects that the system had a significant terrigenous influx that influenced all facies associations. The significant terrestrial influence in this otherwise wave-dominated environment suggests the presence of a river system at some distance from the study location from which siliciclastic sediment was derived through longshore current and/or an oblique wave regime, a situation not uncommon for linear wave-dominated shorelines.

Sample	Log	Location in log	Facies assoc.	Count of specimens									Dep. Environ.
				Foram	Acritar.	Botryoc.	Prasino.	Dinocy.	Fungi	Misc.pal.	Spore/pollen	Zygnema.	
HET-BRID-46	1	1 m	FA1	0	0	0	2	0	0	0	98	0	Non marine
HET-BRID-48	1	24 m	FA2	0	0	0	0	1	3	2	94	0	Non marine
HET-BRID-50	1	62 m	FA7	0	0	0	0	0	0	1	99	0	Non marine
HET-BRID-53	2	0 m	FA1	0	0	1	0	0	0	2	74	0	Non marine
HET-BRID-55	2	26 m	FA2	0	3	0	0	0	0	0	100	0	Non marine
HET-BRID-57	2	41.5 m	FA3	0	0	0	0	0	21	2	97	0	Non marine
HET-BRID-58	3	12.5 m	FA2	0	0	0	1	0	0	0	100	0	Non marine
HET-BRID-60	4	13 m	FA1	0	1	0	0	0	1	0	97	0	Non marine
HET-BRID-62	4	18 m	FA3	0	0	0	0	7	0	0	100	0	Non marine
HET-BRID-64	5	1.5 m	FA1	0	3	0	0	0	10	4	75	1	Transitional
HET-BRID-66	5	4.5 m	FA1	0	2	0	0	6	0	0	92	0	Transitional
HET-BRID-68	5	53 m	FA7	0	7	0	0	0	0	0	93	0	Non marine

Table 2.2: Summary of the palynology analysis performed on 12 loose silt samples collected at locations within the stratigraphic logs with the interpretation of the depositional environment. No microfossils were collected. The samples are dominated by spores and pollen. More information on the specific taxonomy of the specimens is available in Cuesta-Cano et al. [66].

2.4.4. Depositional environment

The following observations suggest that the depositional system was controlled by
high-energy waves and longshore drift:

1. The scarce bioturbation only found in the lower shoreface deposits (FA2 and
   FA3).

2. The amalgamation of sandstone beds with storm-related structures (hummocky
   and swaley cross stratification) (FA2, FA3, and FA4).

3. The lack of clay and silt in the sandstone layers of FA3, FA4 and FA5, resulting
   from winnowing associated with wave-reworking in the lower, middle and
   upper shoreface (cf. [67]).

4. Clear boundaries between deposits from different subenvironments, and a
   general increase in grain size from lower to upper shoreface deposits.

5. And the paleo-landwards and oblique-to-shoreline paleocurrents measure-
   ments in the upper interval of FA3, FA4 and FA5, likely related to onshore,
   storm-driven flow and longshore drift (cf. [49, 53, 68]).

Although no channelized deposits were observed on the field, hyperpycnal flows
(FA1) and layers rich in mica flakes and organic matter (FA1, FA4, FA5) have been
identified. Thus, a continental sediment source is associated with this system with a
location beyond the study area.

No tidal influence has been observed in the deposits. Tidally modulated or influenced
shorefaces are characterised by strong bioturbation in the lower shoreface, poorly
defined boundaries between shoreface subenvironments, thick foreshore intervals,
and similar grain sizes from the offshore to the upper shoreface [49, 69].

2.4.5. Stratigraphic architecture

A NW-SE oriented correlation panel has been constructed, parallel to the cliff
section, based on the five stratigraphic logs and the photogrammetry panel (Figure
2.9) covering $1.2km$. This panel is also parallel to the paleo-shoreline of the
depositional system [26]. The panel illustrates the lateral thickness variations of the
succession and the vertical stacking pattern of facies associations. The succession
is upward-coarsening with gradational boundaries between facies associations
and with a flooding surface at the top. Such stratigraphic architecture has been
previously described from wave-dominated successions in the upper Cretaceous
of the Western Interior Basin (e.g. [17, 70]). There is a minor landward shift of
facies associations recorded in each log after deposition of the lower interval of FA4

(Figure 2.9). This shift is recorded as a gradational change and it results in the deposition of another interval of FA3.

The maximum thickness of the outcrop reaches $70m$ in the northernmost part (recorded in stratigraphic log 2; Figure 2.9). Previous studies on wave-dominated systems from the upper Cretaceous in the Western Interior Basin have reported parasequences with total thicknesses ranging from 10 to 50 meters [15, 17, 44, 71]. In this study, we recorded up to $45m$ of distal lower shoreface to foreshore-lagoon/backshore deposition (not considering FA1), which exceeds the maximum values reported by Eide, Howell and Buckley [72] (up to $36m$) or the $35m$, approximately, from the 'K4' shoreface tongue [17], both studies from the Campanian Blackhawk Formation. In this study, we also record a maximum and vertically continuous mmiddle-upper shoreface complex thickness of $25m$ in logs 4 and 5a, which exceeds by, approximately, $10m$ the shoreface thickness measured in the 'K4' shoreface tongue [17, 72].

Lateral variations in thickness of the facies associations are observed throughout the outcrop. The variations for FA1 are mainly related to the lack of constraints at the base of the facies association. FA2 becomes thicker towards the north of the outcrop (Figure 2.9). This can be related to the sedimentary criteria (sandstone layer thickness, presence of basal erosional surfaces, and sedimentary structures in the sandstone layers) applied to make the distinction between the facies associations and/or a higher concentration of hyperpycnal sandstone beds and storm-beds. When combined with the 3D model, we observe that the thickness of the lower interval of FA4 varies from 1.5 to $5m$. This interval is composed of clean sandstones displaying swaley cross-stratification and it is underlain and overlain by hummocky cross-stratified sandstone intervals. Due to the genetic relationship between these two types of sedimentary structures [50, 73], the lateral and, therefore, paleoshore-parallel thickness variations, might be related to the interplay between the sedimentological processes creating the sedimentary structures. This same interplay can be responsible for the thickness variations of the upper interval of FA3 and FA4. In the case of FA5, there is a progressive increase in thickness from south to north. The thickest FA5 intervals were measured around the hectometre-scale protrusion in Figure 2.6D.

Figure 2.9: *Next page* S-N correlation panel aligned parallel to the cliff section and to the paleo-shoreline (cf. [26]). Note the varying spacing between logged sections. Dominant grain size, sedimentological structures, and bioturbation have been included. The datum for correlation is taken at the top of each log, which is interpreted as a flooding surface. Note the thickness variations of the different facies associations with FA2 showing the largest thickness variations. All facies associations are present in each log, but FA7 only in the northernmost log. No major erosional surfaces have been identified. The location of the samples has been included. Note that the location for the samples in between logs is approximate and we refer to the dataset for further details [66].
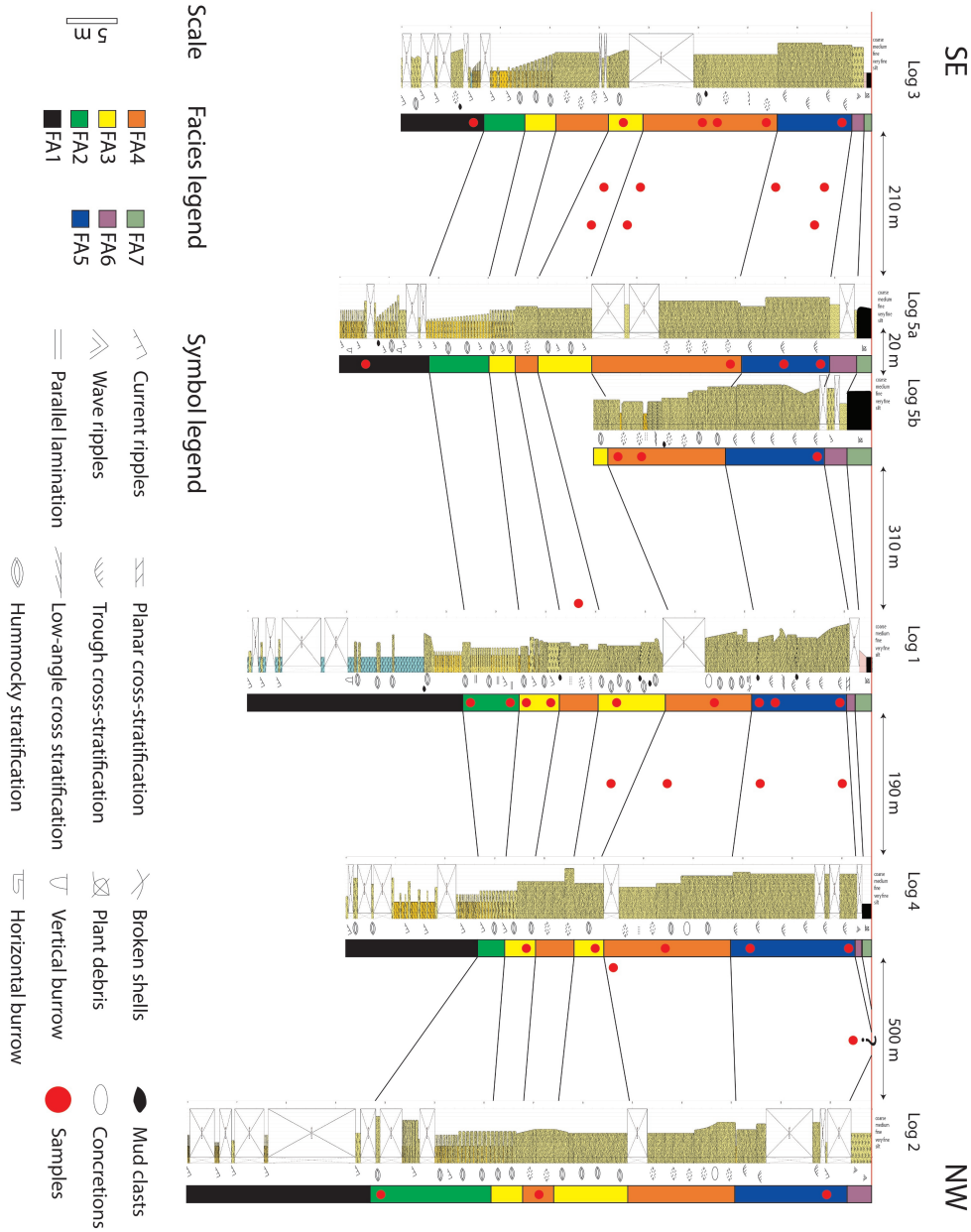
Finally, FA6 is the thickest in the northernmost log 2 (Figure 2.9), with a maximum thickness of $3m$, and it becomes thinner towards the central area of the study area, where it is barely present. Because the contact between FA6 and FA7 does not crop out, it is uncertain whether the thickness variability in FA7 is due to non-deposition or erosion. FA7, on the other hand, is the thickest in the central area, where a $2m$ thick layer brown coal is present. However, this facies is absent on the northern edge of the study area. FA6 and FA7 are thin and do not result in clear outcrop features mappable on the drone images, so the thickness and lateral extent is only based on the stratigraphic log information.

2.4.6. Petrophysical, elastic and acoustic properties

The goal of the analysis of the petrophysical, elastic, and acoustic properties is twofold. The first aim is to investigate whether the observed range of facies associations contain different property ranges by which they can be characterized and distinguished. The second aim is to evaluate if the facies associations each have a characteristic lateral or vertical property trend.

For the analysis of the properties, 44 samples from facies associations FA1 to FA5 were collected along the stratigraphic logs and in the areas between them (Figure 2.9). The upper two intervals, corresponding to the facies associations FA6 and FA7, were not sampled because of insufficient good quality outcrops that allowed for the extraction of cores or unsuitability of rock types (coal). The number of samples per facies varies from 2 to 16. Facies characterized by a cm-scale alternation of sand- and siltstone were difficult to sample, because of the lack of layers that were thick enough for the collection of cores resulting in less samples. The limited number of samples for FA4 is due to poor outcrop accessibility. Two batches of FA3 samples have been collected. Batch FA3(1) was collected from the lower FA3 interval and batch FA3(2) from the upper FA3 interval. Three batches of FA4 samples have been obtained. FA4(1) samples were collected in the lower FA4 interval, and FA4 (2) and FA4(3) were collected from the upper FA4 interval. Batch FA4(3) was collected at the cliff-forming protrusions, whilst batch FA4(2) was collected outside these areas.

Figures 10 and 11 show the property distributions of each sample batch, including the mean and standard deviation for each facies association. For more information on the measurements, we refer to Appendix 3 and the database associated to this publication [66].

The grain density is highest in the samples from FA1, FA2 and FA3(1) (Figure 2.10A), which compose the base of the section. There is a change in grain density between the deposition of FA3(1) and FA4(1) (Figure 10A), which might be related to a change of the sediment type supplied to the system. This change is supported by the contrast in grain density between the two sample batches from FA3 (Figure 2.10A), which display the same sedimentological properties, but different ranges

of grain density. A general porosity decrease from FA1 to FA4(1) is observed followed by a semi-constant porosity distribution; FA2, however, deviates from this trend (Figure 2.10B). The bulk density shows large overlap between all facies (Figure 2.10B), which is a consequence of the combination of the porosity and grain density values. Batches FA4(2) and FA4(3) show only minor differences, with largely overlapping property value ranges. Samples collected from the cliff-forming protrusions tend to display slightly higher values. However, with the current dataset, it is not possible to determine whether these differences are caused by weathering or if weathering is more pronounced in specific areas due to these subtle variations.
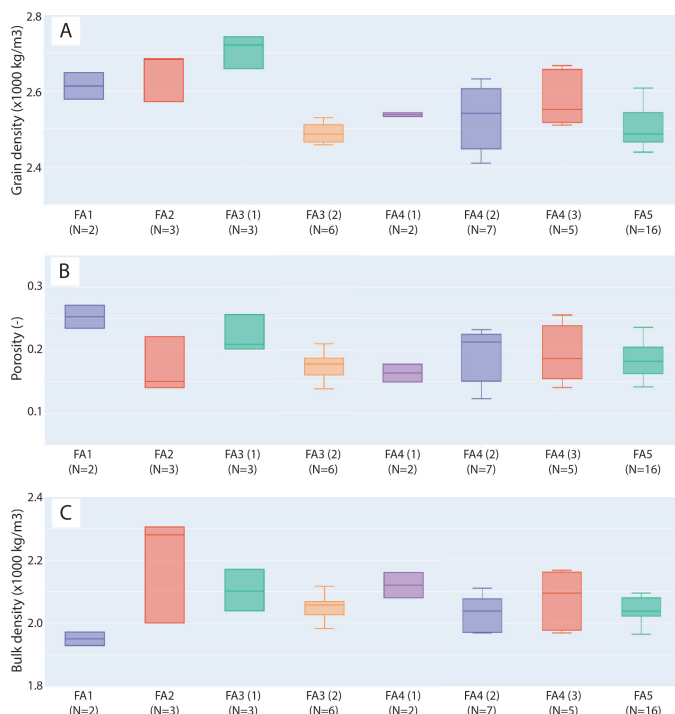

Figure 2.10: Distribution of grain density $(x1000kg/m^3)$ (A), porosity (unitless) (B), and bulk density $(x1000kg/m^3)$ (C) per sample batch. The box size equals the distribution between quartile 1 and quartile 3, the median is the horizontal line within the box, and the ranges indicated below and above the box mark the minimum and maximum value, respectively. These graphs show the overlapping values for the different properties. There is almost full overlap for the facies FA4, independent from diagenetic features or interval, and FA5.

P-wave velocity displays a general trend of velocity decrease from FA2 to FA4 (1) followed by a semi-constant velocity distribution (Figure 2.11A). FA1 does not fit this trend and is characterized by low P-wave velocity values, possibly due to the high porosity of the samples [74]. A high contrast between the values measured for FA3(1) and FA4(1) can be related to a decrease in grain density as previously

mentioned, and it is also supported by the contrast in P-wave velocity between FA3(1) and FA3(2). There is a strong overlap between the values recorded for FA1, FA3(2), FA4(2), FA4(3), and FA5 (Figure 2.11A). The same trends are observed in the data from S-wave velocity (Figure 2.11B), as it is expected from the linear relationship between P-wave and S-wave velocities reported for clastic rocks [75, 76]. For both the P-wave and the S-wave velocity, the reported values are lower than the ones observed in subsurface core samples of shoreface deposits [3]. The difference in values is related to weathering [21].
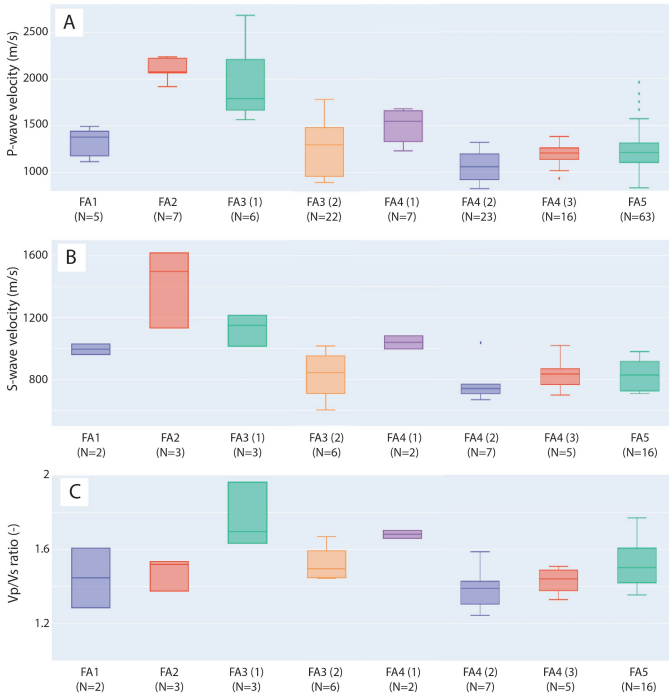

Figure 2.11: Distribution of P-wave velocity (m/s) (A), S-wave velocity (m/s) (B), and Vp/Vs ratio (unitless) (C) per facies. The box size equals the distribution between quartile 1 and quartile 3, the median is the horizontal line within the box, and the ranges indicated below and above the box mark the minimum and maximum value, respectively. These graphs show the overlapping values that are observed for the different properties. The trend between FA(1) and (2) is the same for all the properties. FA4(1) displays higher values in all properties compared to the other FA4 sample batches.

The Vp/Vs ratio varies from $1,24$ up to $1,96$ (Figure 2.11C). The Vp/Vs ration is a measurement extensively used in seismic subsurface characterization due to its ability to distinguish between rock and fluid physical properties such as lithology [75, 77] or fluid types [78, 79], among others. In this dataset we do not observe an increasing trend of Vp/Vs for higher porosity samples, as suggested by Tatham [77], who studied the measurements recorded from subsurface core samples in

publications from three laboratories.

Plotting the values of the different properties against their spatial distribution shows that no spatial trends are present. No property changes are observed close to the contacts between the facies associations or in the lateral direction.

2.4.7. Idealised facies succession of the base of the Parkman Sandstone in Bridger

The base of the Parkman Sandstone in the Bridger area is characterized by the vertical stacking of seven facies associations, indicating a progressive shallowing of depositional environments—from offshore transition (FA1) to backshore (FA7) settings (Figure 2.12). At the base, the offshore transition deposits (FA1) consist of alternating fair-weather suspension sediments (silt layers) and event-related deposits (thin sandstone layers with current-ripple cross-lamination). Above these, the distal lower shoreface (FA2) is represented by non-amalgamated sandstone layers with hummocky cross-stratification, interbedded with progressively thinner silt deposits from fair-weather conditions. The proximal lower shoreface (FA3) is marked by amalgamated hummocky cross-stratification formed by frequent storm-wave activity, with paleocurrent directions ranging from seaward-oriented to oblique relative to the paleoshoreline. The middle shoreface (FA4) comprises amalgamated sandstone layers with swaley cross-stratification, reflecting high-energy wave action and paleocurrents trending landward to oblique. The upper shoreface deposits (FA5) feature trough cross-stratification formed by migrating dunes, with paleocurrent directions displaying pseudo-parallel orientations to the paleo-coastline, indicative of longshore drift. At the top of the outcrop, foreshore sandstones (FA6) exhibit wave-ripple and parallel laminations, overlain by backshore deposits (FA7) consisting of brown coal interbedded with sand layers.

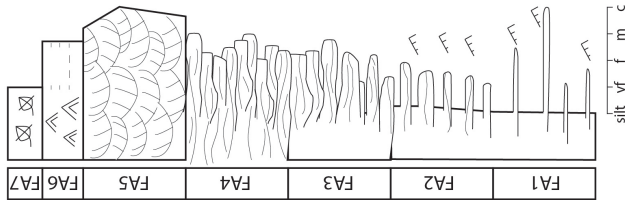|	Paleocurrent	Interpretation	Petrophysics properties	Elastic and acoustic properties
	No	Backshore	No	No
	No	Foreshore	No	No
	Unidirectional pseudo-parallel to coastline.	Upper shoreface, dune migration related to longshore drift.	Grain density (g/cm³) = 2.50 (0.05) Bulk density (g/cm³) = 2.04 (0.04) Porosity (-) = 0.18 (0.03)	Vp (m/s) = 1238.64 (196.81) Vs (m/s) = 834.92 (81.47) Vp/Vs ratio (-) = 1.52 (0.13)
	Unidirectional landward, 180° range.	Middle shoreface, swaley stratification related to strong wave-action.	Grain density (g/cm³) = 2.54 (0.01) and 2.53 (0.09) Bulk density (g/cm³) = 2.12 (0.06) and 2.03 (0.05) Porosity (-) = 0.16 (0.02) and 0.20 (0.04)	Vp (m/s) = 1512.92 (173.30) and 1030.62 (132.61) Vs (m/s) = 1040.68 (59.99) and 771.62 (121.56) Vp/Vs ratio (-) = 1.68 (0.03) and 1.39 (0.11)
	Shift from seaward to oblique to coastline.	Proximal lower shoreface, amalgamated hummocky stratification due to common event-related wave action.	Grain density (g/cm³) = 2.71 (0.04) and 2.49 (0.03) Bulk density (g/cm³) = 2.10 (0.07) and 2.05 (0.04) Porosity (-) = 0.22 (0.03) and 0.18 (0.02)	Vp (m/s) = 1951.07 (421.38) and 1270.64 (301.74) Vs (m/s) = 1127.57 (101.89) and 827.11 (166.25) Vp/Vs ratio (-) = 1.76 (0.18) and 1.52 (0.09)
	No	Distal lower shoreface. Non-amalgamated hummocky stratification from isolated event-related wave action and fair-weather sedimentation.	Grain density (g/cm³) = 2.65 (0.07) Bulk density (g/cm³) = 2.20 (0.17) Porosity (-) = 0.17 (0.04)	Vp (m/s) = 2105.12 (108.02) Vs (m/s) = 1417.11 (252.93) Vp/Vs ratio (-) = 1.48 (0.09)
	No	Offshore transition. Alternation fair-weather, suspension sedimentation and deposition of event-related sandstones.	Grain density (g/cm³) = 2.61 (0.05) Bulk density (g/cm³) = 1.95 (0.03) Porosity (-)= 0.25 (0.03)	Vp (m/s) = 1322.34 (147.05) Vs (m/s) = 996.62 (48.39) Vp/Vs ratio (-) = 1.45 (0.23)

Figure 2.12: Idealised vertical facies association succession of the studied area including facies associations, paleocurrents, interpretation of the depositional setting, and petrophysical, elastic and acoustic properties. For the petrophysical, elastic and acoustic properties the mean value of the measurements is provided together with the standard deviation, in between brackets. For each property, the units are included. For more information on the number of measurements we refer to Figures 2.10 and 2.11, Appendix 3 and the supplementary material from the associated database. Note that for FA3 and FA4, two sets of values are provided, and they result from the different sample batches from different intervals (FA3(1) and FA3(2)) in the case of FA3, and the same for FA4). FA4(3) has not been included and the data can be found in the Appendices.

2.5. Discussion

2.5.1. Relative sea level and regression of the Parkman Sandstone

The Parkman Sandstone, one of the five transgressive-regressive depositional cycles in the Claggett T-R cycle [26, 27] was deposited during a period with relatively high and stable sea level that lasted approximately $4m.y.$ [28, 29]. The stable sea level allowed for the development of a facies stacking pattern characteristic for normal regression [80, 81]). This stacking pattern reflects a gradual transition between adjacent depositional environments, recording progressive shoaling associated with the basinward migration of the coastline. The basinward displacement of the coastline was due to the continuous infill of accommodation space in the basin. Normal regression successions are commonly overlain by coastal plain deposits, in this case represented by a coal seam.

The development of normal regression can be related to different sediment supply versus accommodation space relationship, the latter expressed as relative sea level. In the study area, the Parkman Sandstone does not display any evidence of surfaces of non-deposition or erosional discontinuities interpreted to have formed by allogenic controls. Therefore, we infer that this system developed during a period of stable base level, or in a setting where sediment supply outpaced relative sea level change.

Reeves [35] recognized two normal regression events in the Parkman Sandstone in the Powder River Basin, 300 km in the SW direction from the study area (Western Wyoming). The first event is related to relative sea level lowstand and it is topped by an erosional surface, and the second event is related to a highstand normal regression. Due to the lack of chronostratigraphic controls, there are two possible correlations with the study area:

- First, the first normal regression event is interpreted to be time equivalent with the deposition of FA1, FA2, the lower intervals of FA3 and FA4. However, the relative sea level rise that followed this normal regression was related to autogenic processes at basin scale, as, like in our study area, this relative sea level fall is only represented by a minor landward shift of facies associations. The second normal regression event, topped by a maximum flooding surface, is interpreted to represent deposition of the upper interval of FA3, the upper interval of FA4, FA5, FA6, and FA7.

- Second, the first normal regression event interpreted in the Powder River Basin is time equivalent to the outcrop analysed in this study and the flooding surface observed in the top of the section corresponds to the erosional surface described by Reeves [35].

2.5.2. Depositional environment of the Parkman Sandstone

Previous research interpreted different shallow marine depositional environments for the Parkman Sandstone in the Powder River Basin, in Southeast Montana and Wyoming [32, 35, 36]. Hubbert and Rubey [32] identified evidence of strong waves and subordinate tidal currents in the lower section of the Parkman Sandstone, with lateral variations suggesting a stronger influence of tides. They also observed a predominance of landward and along-shore paleocurrent indicators, highlighting the impact of longshore drift on sedimentation, which agrees with the observations from this study. Dogan [36] interpreted the deposits from the Parkman Sandstone to represent a river-dominated delta, while Reeves [35] concluded that, in the Powder River Basin, the Parkman Sandstone built a wave-dominated delta, emphasizing changes in the balance between wave and fluvial action depending on the location. All previous studies agreed with the observations made in this study in recognizing the strong influence of wave action on deposition. The local impact of tide and particularly fluvial processes, even if not present in the study area, have also been identified in previous research, but never as the main agents controlling the sedimentation.

Wave-dominated systems of Campanian age, deposited along the western shoreline of the WIB have also been identified in New Mexico, Utah, and Colorado [71]. The Blackhawk and Castlegate formations in the Book Cliffs area, around $700km$ south of our study area, are one of the most extensively documented outcrop areas of wave-dominated shoreface systems [15, 17, 20, 44, 72, 82, 83]. These display a variety of stacking patterns that have become textbook examples of forced and normal regressive systems (e.g. [82, 84]. In the Desert-Castlegate parasequences, the shallowest marine successions show coarsening-upward cycles with gradational transitions between facies associations lacking a sharp-erosive shoreface base [85]. These systems follow dominantly low angle ascending regressive or flat-horizontal trajectories and result from increased sediment supply.

Another example of normal regression is the 'SC4' shoreface tongue of the Spring Canyon Member, in the Blackhawk Formation [82]. This prograding interval developed during the early part of a highstand systems tract and records the transition between wave-dominated shoreface to wave-influenced delta [84]. The 'SC4' includes non-depositional discontinuities in the form of intensely bioturbated horizons and minor landward facies shifts [17], that are not identified in the Parkman Sandstone section. Other wave-dominated systems with normal regressive stacking patterns in the Blackhawk formation also include non-depositional discontinuity surfaces [44].

The key difference between the wave-dominated systems in the Book Cliffs and the Parkman Sandstone outcrop in Bridger is the presence of bioturbation. The bioturbation in the distal lower shoreface, for example, of the Blackhawk formation is often described to be moderate to intense [44, 71]. Only the bioturbation in some

bedsets from the Star Point Sandstone (the lower Blackhawk Formation) display absent bioturbation [70]. In contrast, in the Parkman Sandstone—deposited in a comparable environment—bioturbation is generally absent to scarce. This difference may be attributed to the proximity of a river, which likely led to high sedimentation rates and the continental signature observed in the palynology analysis.

2.5.3. Petrophysical property distribution and outcrop trends

The petrophysical property analysis has shown that the different facies associations do not result in significantly different values and that it is not possible to recognize discrete spatial distributions of the measured properties. However, even with limited number of samples for some of the facies associations, a large range of property variations was measured. The ranges are interpreted to represent the spatial variability of the properties within each facies association. However, these samples have all been exposed to weathering, which has modified the properties of the samples versus their analogues in the subsurface [21]. Unless we are able to isolate the imprint of weathering on the properties, we cannot state that, in subsurface conditions, the samples would display such broad value ranges.

The recorded distribution of grain density values allowed for the identification of changes in sediment type in FA3 (Figure 2.10). This change seems to have an impact on the seismic velocity and Vp/Vs ratio, where a similar trend is observed (Figure 2.11). We infer that changes in grain density, even if not noticed in bulk density, might have an impact on seismic velocities. Previous research has highlighted the relationship with bulk density, but not grain density [86].

The subsurface porosity values of the Parkman Sandstone range from 0.08 to 0.21 in samples of the neighboring Powder River Basin [35, 87]. The lowest average porosity measured in the samples from this study is 0.16 and some sample batches, FA1 and FA3 (1), showed average porosity values higher than the values reported from subsurface. This elevated porosity range can be related to the weathering processes and the consequent dissolution of the cement in the samples. The Parkman sandstone in subsurface is characterized by calcite cementation [87], and this cementation has not been observed in the thin sections.

It is not the intention of this paper to compare the elastic and acoustic property values with those measured in the subsurface. As previously mentioned, the outcrop samples are affected by weathering, which has shown to modify the measured values [21]. In our case, the P-wave velocity and S-wave velocity values are lower than those normally measured in the subsurface for sandstones. As reference, we compared with the values used to perform forward seismic modelling studies on the wave-dominated systems of the Book Cliffs [3, 88], subsurface property values which were collected from comparable lithofacies in the Brent Group in the North Sea. These studies assigned values of P-wave velocity of, approximately, $3650 m/s$

to the offshore transition, $3800m/s$ to the lower shoreface and $3600m/s$ to the upper shoreface [3, 88]. These values are twice as high as the values measured in the Parkman sandstone outcrop (Figure 2.12). The bulk density values collected from the Brent Group are closer to the grain density values than to the bulk density values that we measured in the Parkman Sandstone [3]. As the bulk density is calculated based on the grain density and the porosity, this observation could be related to three scenarios: 1) for similar porosity, the grains of the Brent Group are denser than the ones in the Parkman sandstone, 2) for similar grain density, the porosity in the Brent Group is lower, and 3) the bulk density of the Brent Group is of (oil/water) saturated rocks. These discrepancies underscore the impact of weathering on rock properties—such as P-wave and S-wave velocities—as well as the variability of physical properties within similar depositional environments.

2.5.4. Implication on heterogeneity analysis in the subsurface

The Parkman Sandstone outcrop is an example of a wave-dominated shoreface system and contains deposits from offshore-shoreface transition to the backshore. Shoreface systems are generally characterized by good reservoir potential and, therefore, have been targeted in the subsurface [9–11]. The Parkman Sandstone itself is an important reservoir in Montana and Wyoming [23, 32, 33]. Part of the subsurface characterization of reservoirs depends on seismic reflection campaigns, and the vertical resolution of the collected seismic data is controlled by the depth of the target, the seismic velocity of the sediments, and the frequency [89]. For targets deeper than $2km$, layer thicknesses under $10 - 15$ meters will not be resolved in the seismic data. The contacts between thicker layers will only be visible if there is enough contrast between the acoustic properties of the layers. With the Parkman Sandstone as an example, many of the intervals in the succession are thinner than $10m$, which would make them undetectable on seismic data.

Creating seismograms out of the seismic data requires inversion workflows. In short, these workflows transform the seismic reflections data into rock-properties, such as density and P-wave velocity. Traditionally, in inversion, a constant property value is assigned per lithofacies (e.g., [90–92]). This assumption aims at representing and simplifying the complex property distribution in the subsurface. However, this assumption might not allow for the identification of intervals with different reservoir properties in wave-dominated systems. This work shows that the difference in average P-wave velocity between some sample batches is less than a 10% and that the value range per sample batch can be greater than this difference. The assignation of average bulk density or P-wave velocity values would result in some rock packages being indistinguishable, even though they have particular porosity distributions, sedimentological structures, sedimentological structures, grain size distributions, or mineral content (organic matter or mica rich). This work highlights the limitations of using averaged property values in inversion workflows, as such

simplifications can conceal heterogeneity in wave-dominated systems—potentially masking reservoir intervals with distinct rock characteristics.

2.6. Conclusions

The outcrop analysis shows that the base of the Parkman Sandstone (Middle Campanian, Cretaceous) is a normal regressive shoreface succession with a thickness of, approximately, 50 meters. This outcrop represents a paleoshore-parallel section composed by a staked succession of deposits from 7 facies associations, ranging from offshore transition to backshore. The deposits are laterally continuous and display a general coarsening upwards trend, with gradual transitions between deposits of different facies associations. From the sedimentological characterization of the facies associations, we infer that the depositional environment has a strong influence of wave-actions and longshore currents. This conclusion is in agreement with previous research on the Parkman Sandstone in neighbouring basins. Similar stacking patterns and sedimentological features have been recognized in wave-dominated systems of the Campanian Blackhawk formation, $700km$ south of the study area.

The analysis of petrophysical, acoustic, and elastic properties of samples from the outcrop indicate that the facies associations are not characterized by a specific range of values per measured property. The properties from the samples have been modified by weathering. This is evident from the comparison between porosity values of the Parkman sandstone in subsurface $(0.06 - 0.21)$ and on the outcrop (up to 0.25). Although these values have been altered by weathering, all samples exhibit a similar imprint, suggesting that the observed variation reflect the petrophysical property variability within the facies associations. The high variability within the samples from the same facies associations, having a difference of less than a 10% between the average P-velocity of some of the sample batches, and the thickness of the intervals (under $10m$ in majority of the cases) highlight the challenges of characterizing wave-dominated shoreface systems in the subsurface.

The current study did not recognize spatial patterns in the distribution of properties. This can be a consequence of insufficient sampling density or that the outcrop is parallel to the paleo-shoreline. Future research should focus on isolating the imprint of weathering on petrophysical, acoustic and elastic measurements from outcrop samples, so that the link between these properties and the sedimentology are better understood.

2.7. Data Availability statement

The three-dimensional models, together with the images and GNNS information used for their creation, can be found in an open repository [93]. Another

separate repository contains the supplementary material, high resolution figures, rock sample photos and datasets, including grain size analysis data and lab measurements for petrophysical, acoustic and elastic measurements, paleocurrent data, micropaleontological and palynology charts [66].

2.8. Acknowledgments

References

[1]   H. Braaksma, J. N. Proust, J. A. Kenter, G. G. Drijkoningen and N. Filippidou. 'Sedimentological, Petrophysical, and Seismic Characterization of an Upper Jurassic Shoreface-Dominated Shelf Margin (the Boulonnais, Northern France)'. In: *Journal of Sedimentary Research* 76 (1 Jan. 2006), pp. 175–199. ISSN: 1527-1404. DOI: 10.2110/JSR.2006.11.

[2]   N. Grasseau, C. Grélaud, M. López-Blanco and P. Razin. 'Forward seismic modeling as a guide improving detailed seismic interpretation of deltaic systems: Example of the Eocene Sobrarbe delta outcrop (South-Pyrenean foreland basin, Spain), as a reference to the analogous subsurface Albian-Cenomanian Torok-Nanushuk Delta of the Colville Basin (NPRA, USA)'. In: *Marine and Petroleum Geology* 100 (Feb. 2019), pp. 225–245. ISSN: 02648172. DOI: 10.1016/J.MARPETGEO.2018.11.010.

[3]   D. Hodgetts and J. A. Howell. 'Synthetic seismic modelling of a large-scale geological cross-section from the Book Cliffs, Utah, USA'. In: *Petroleum Geoscience* 6 (3 2000), pp. 221–229. ISSN: 13540793. DOI: 10.1144/PETGEO.6.3.221.

[4]   J. A. Howell, A. W. Martinius and T. R. Good. 'The application of outcrop analogues in geological modelling: a review, present status and future outlook'. In: *GSLSP* 387 (1 Jan. 2014), pp. 1–25. ISSN: 0305-8719. DOI: 10.1144/SP387.12.

[5]   K. Bakke, I. Kane, O. Martinsen, S. Petersen, T. Johansen, S. Hustoft, F. Jacobsen and A. Groth. 'Seismic modeling in the analysis of deep-water sandstone termination styles'. In: *AAPG Bulletin* 97 (9 2013), pp. 1395–1419. DOI: 10.1306/03041312069.

[6]   R. Sech, M. Jackson and G. Hampson. 'Three-dimensional modeling of a shoreface-shelf parasequence reservoir analog: Part 1. surface-based modeling to capture high-resolution fades architecture'. In: *American Association of Petroleum Geologists Bulletin* 93 (9 2009), pp. 1155–1181. DOI: 10.1306/05110908144.

[7]   H. Zeng, X. Zhu and R. Zhu. 'New insights into seismic stratigraphy of shallow-water progradational sequences: Subseismic clinoforms'. In: *Interpretation* 1 (1 Aug. 2013). doi: 10.1190/INT-2013-0017.1, SA35–SA51. ISSN: 2324-8858. DOI: 10.1190/INT-2013-0017.1.

[8]   C. Schmidt, B. Busch and C. Hilgers. 'Lateral variations of detrital, authigenic and petrophysical properties in an outcrop analog of the fluvial Plattensandstein, Lower Triassic, Central S-Germany'. In: *Zeitschrift der Deutschen Gesellschaft für Geowissenschaften* 172 (4 Dec. 2021), pp. 541–564. ISSN: 1860-1804. DOI: 10.1127/zdgg/2020/0234.

[9] J. Bhattacharya and R. G. Walker. 'River- and wave-dominated depositional systems of the Upper Cretaceous Dunvegan Formation, northwestern Alberta'. In: *Bulleting of Canadian Petroleum Geology* 39 (2 June 1991), pp. 165–191.

[10] N. Tyler and R. J. Finley. 'Architectural Controls on the Recovery of Hydrocarbons From Sandstone Reservoers'. In: *The Three-Dimensional Facies Architecture of Terrigenous Clastic Sediments and its Implications for Hydrocarbon Discovery and Recovery*. SEPM Society for Sedimentary Geology, 1991, pp. 1–5. DOI: 10.2110/csp.91.03.0001.

[11] P. Lis and A. Wysocka. 'Middle Miocene Deposits in Carpathian Foredeep: Facies Analysis and Implications for Hydrocarbon Reservoir Prospecting'. In: *Annales Societatis Geologorum Poloniae* 82 (2012), pp. 239–253.

[12] S. Tahir, B. Musta, J. Asis and F. Hanis. 'Wave and tide influence in Neogene paralic hydrocarbon potential reservoirs in Sabah'. In: *ASM Science Journal* 11 (2 2018), pp. 278–292.

[13] P. S. Roy, P. J. Cowell, M. A. Ferland, B. G. Thom and O. van de Plassche. 'Wave-dominated coasts'. In: *Coastal Evolution: Late Quaternary Shoreline Morphodynamics*. Cambridge University Press, 1995, pp. 121–186.

[14] J. Bhattacharya. 'Deltas'. In: *Facies Models Revisited*. Ed. by H. Posamentier and R. Walker. Vol. 84. SEPM (Society for Sedimentary Geology), Jan. 2006, pp. 237–292. DOI: 10.2110/pec.06.84.0237.

[15] G. J. Hampson. 'Sediment dispersal and quantitative stratigraphic architecture across an ancient shelf'. In: *Sedimentology* 57 (1 Jan. 2010), pp. 96–141. ISSN: 00370746. DOI: 10.1111/j.1365-3091.2009.01093.x.

[16] R. L. Kieft, C. A.-L. Jackson, G. J. Hampson and E. Larsen. 'Sedimentology and sequence stratigraphy of the Hugin Formation, Quadrant 15, Norwegian sector, South Viking Graben'. In: *Geological Society, London, Petroleum Geology Conference Series* 7 (1 Jan. 2010), pp. 157–176. ISSN: 2047-9921. DOI: 10.1144/0070157.

[17] G. J. Hampson and J. E. A. Storms. 'Geomorphological and sequence stratigraphic variability in wave-dominated, shoreface-shelf parasequences'. In: *Sedimentology* 50 (4 Aug. 2003), pp. 667–701. ISSN: 0037-0746. DOI: 10.1046/j.1365-3091.2003.00570.x.

[18] K. G. Taylor, R. L. Gawthorpe, C. D. Curtis, J. D. Marshall and D. N. Awwiller. 'Carbonate Cementation in a Sequence-Stratigraphic Framework: Upper Cretaceous Sandstones, Book Cliffs, Utah-Colorado'. In: *Journal of Sedimentary Research* 70 (2 Mar. 2000), pp. 360–372. ISSN: 1527-1404. DOI: 10.1306/2DC40916-0E47-11D7-8643000102C1865D.

[19] J. M. Ketzer, S. Morad, R. Evans and I. S. Al-Aasm. 'Distribution of Diagenetic Alterations in Fluvial, Deltaic, and Shallow Marine Sandstones Within a Sequence Stratigraphic Framework: Evidence from the Mullaghmore Formation (Carboniferous), NW Ireland'. In: *Journal of Sedimentary Research* 72 (6 Nov. 2002), pp. 760–774. ISSN: 1527-1404. DOI: 10.1306/042202720760.

[20] T. Sømme, J. Howell, G. Hampson and J. Storms. 'Genesis, Architecture, and Numerical Modeling of Intra-Parasequence Discontinuity Surfaces In Wave-Dominated Deltaic Deposits: Upper Cretaceous Sunnyside Member, Blackhawk Formation, Book Cliffs, Utah, U.S.A.' In: *Recent Advances in Models of Siliciclastic Shallow-Marine Stratigraphy* (2008), pp. 421–441. DOI: 10.2110/PEC.08.90.0421.

[21] A. Grippa, A. Hurst, G. Palladino, D. Iacopini, I. Lecomte and M. Huuse. 'Seismic imaging of complex geometry: Forward modeling of sandstone intrusions'. In: *Earth and Planetary Science Letters* 513 (2019), pp. 51–63. DOI: 10.1016/j.epsl.2019.02.011.

[22] H. S. Hussein, O. Bábek, H. Mansurbeg and S. Shahrokhi. 'Outcrop-to-subsurface correlation and sequence stratigraphy of a mixed carbonate–siliciclastic ramp using element geochemistry and well logging; Upper Cretaceous Kometan Formation, Zagros Foreland, NE Iraq'. In: *Sedimentary Geology* 459 (Jan. 2024), p. 106547. ISSN: 00370738. DOI: 10.1016/j.sedgeo.2023.106547.

[23] R. Johnson, T. Finn, D. Taylor and V. Nuccio. *Stratigraphic Framework, Structure, and Thermal Maturity of Cretaceous and Lower Tertiary Rocks in Relation to Hydrocarbon Potential, Crazy Mountains Basin, Montana*. Tech. rep. U.S. Geological Survey Scientific Investigations, 2005, pp. 1–95.

[24] D. Lopez. *Geologic Map of the Bridger 30' x 60' Quadrangle, Montana*. 2000.

[25] S. Vuke, K. Porter, J. Loon and D. Lopez. *Geologic Map of Montana*. 2007.

[26] J. R. Gill and W. A. Cobban. *Stratigraphy and geologic history of the Montana group and equivalent rocks, Montana, Wyoming, and North and South Dakota*. Tech. rep. 1973. DOI: 10.3133/pp776.

[27] E. Kauffman. 'Paleobiogeography and evolutionary response dynamic in the Cretaceous Western Interior Seaway of North America'. In: *Geological Association of Canada Special Paper* 27 (1984), pp. 273–306.

[28] R. Lynds and J. Slattery. *Correlation of the Upper Cretaceous Strata of Wyoming*. Tech. rep. Wyoming State Geological Survey, 2017.

[29] R. Weimer. 'Relation of Unconformities, Tectonics, and Sea Level Changes, Cretaceous of the Denver Basin and Adjacent Areas'. In: *Mesozoic Paleogeography of the West-Central United States*. Ed. by M. Reynolds and E. Dolly. SEPM, Rocky Mountain Section Special Publication, 1983, pp. 359–376.

[30] I. Niezgodzki, G. Knorr, G. Lohmann, J. Tyszka and P. J. Markwick. 'Late Cretaceous climate simulations with different CO2 levels and subarctic gateway configurations: A model-data comparison'. In: *Paleoceanography* 32 (9 Sept. 2017), pp. 980–998. ISSN: 0883-8305. DOI: 10.1002/2016PA003055.

[31] L. Burgener, E. Hyland, E. Griffith, H. Mitášová, L. E. Zanno and T. A. Gates. 'An extreme climate gradient-induced ecological regionalization in the Upper Cretaceous Western Interior Basin of North America'. In: *GSA Bulletin* 133 (9-10 Sept. 2021), pp. 2125–2136. ISSN: 0016-7606. DOI: 10.1130/B35904.1.

[32] M. K. Hubbert and W. W. Rubey. 'Role of fluid pressure in mechanics of overthrust faulting: I. Mechanics of fluid-filled porous solids and its application to overthrust faulting'. In: *GSA Bulletin* 70 (2 Feb. 1959), pp. 115–166.

[33] D. Lichtner, R. Toner, J. Wrage and R. Lynds. *Upper Cretaceous Strata in the Powder River Basin: Formation Tops Database, Structure and Thickness Contour Maps, and Associated Well Data*. Tech. rep. Wyoming State Geological Survey, Sept. 2020, pp. 1–50.

[34] E. Rich. 'Stratigraphic Relation of Latest Cretaceous Rocks in Parts of Powder River, Wind River, and Big Horn Basins, Wyoming'. In: *AAPG Bulletin* 42 (10 Oct. 1958), pp. 2424–2443. ISSN: 0149-1423. DOI: 10.1306/0BDA5BDC-16BD-11D7-8645000102C1865D.

[35] L. Reeves. *Geologic evaluation of the Parkman Sandstone Powder Basin, Wyoming*. 2021.

[36] A. Dogan. 'Stratigraphy, Petrology, Depositional and Post-depositional Histories and Their Effects Upon Reservoir Properties of the Parkman Formation of the Mesaverde Group, Powder River Basin, Wyoming'. PhD thesis. University of Iowa, 1984.

[37] C. J. Wilson. 'Revision of Stratigraphy of Dry Creek and Golden Structures, Carbon County, Montana: GEOLOGICAL NOTES'. In: *AAPG Bulletin* 22 (1 Jan. 1938), pp. 106–108.

[38] E. Merewether. *Stratigraphy and tectonic implications of Upper Cretaceous rocks in the Powder River basin, northeastern Wyoming and southeastern Montana*. Tech. rep. U. S. Geol. Survey Bull., 1996, pp. 1–92. DOI: 10.3133/b1917T.

[39] D. Hodgetts, T. Seers, W. Head and B. Burnham. 'High Performance Visualisation of Multiscale Geological Outcrop Data in Single Software Environment'. In: June 2015. DOI: 10.3997/2214-4609.201412862.

[40] Z. Sylvester. *segmenteverygrain*. 2024.

[41] A. Kirillov, E. Mintun, N. Ravi, H. Mao, C. Rolland, L. Gustafson, T. Xiao, S. Whitehead, A. C. Berg, W.-Y. Lo, P. Dollár and R. Girshick. 'Segment Anything'. In: *2023 IEEE/CVF International Conference on Computer Vision (ICCV)*. IEEE, Oct. 2023, pp. 3992–4003. ISBN: 979-8-3503-0718-4. DOI: 10.1109/ICCV51070.2023.00371.

[42] M. Li, D. Wilkinson and K. Patchigolla. 'Comparison of Particle Size Distributions Measured Using Different Techniques'. In: *Particulate Science and Technology* 23 (3 July 2005), pp. 265–284. ISSN: 0272-6351. DOI: 10.1080/02726350590955912.

[43] P. K. Kaj, H. Abels, A. Barnhoorn, L. V. Meleza and P. Vardon. *Database of Experimental Data on Three Geothermal Plays in the Netherlands from the ProperBase Project*. 2024.

[44] K. Charvin, G. J. Hampson, K. L. Gallagher and R. Labourdette. 'Intra-parasequence architecture of an interpreted asymmetrical wave-dominated delta'. In: *Sedimentology* 57 (3 Apr. 2010), pp. 760–785. ISSN: 00370746. DOI: 10.1111/j.1365-3091.2009.01118.x.

[45] G. J. Hampson. 'Discontinuity Surfaces, Clinoforms, and Facies Architecture in a Wave-Dominated, Shoreface-Shelf Parasequence'. In: *Journal of Sedimentary Research* 70 (2 Mar. 2000), pp. 325–340. ISSN: 1527-1404. DOI: 10.1306/2DC40914-0E47-11D7-8643000102C1865D.

[46] C. Zavala. 'Hyperpycnal (over density) flows and deposits'. In: *Journal of Palaeogeography* 9 (1 Dec. 2020), p. 17. ISSN: 2524-4507. DOI: 10.1186/s42501-020-00065-x.

[47] L. A. Buatois and M. G. Mángano. *Ichnology: Organism-Substrate Interactions in Space and Time*. Cambridge University Press, Aug. 2011. ISBN: 978-0-521-85555-6. DOI: 10.1017/CBO9780511975622.

[48] S. M. Vossler and S. G. Pemberton. 'Skolithos in the Upper Cretaceous Cardium Formation: an ichnofossil example of opportunistic ecology'. In: *Lethaia* 21 (4 Oct. 1988), pp. 351–362. ISSN: 0024-1164. DOI: 10.1111/j.1502-3931.1988.tb01763.x.

[49] S. G. Pemberton, J. A. MacEachern, S. E. Dashtgard, K. L. Bann, M. K. Gingras and J.-P. Zonneveld. 'Shorefaces'. In: 2012, pp. 563–603. DOI: 10.1016/B978-0-444-53813-0.00019-8.

[50] R. Dott and J. Bourgeois. 'Hummocky stratification: Significance of its variable bedding sequences.' In: *GSA Bulletin* 93 (8 1982), pp. 663–680.

[51] S. Dumas and R. Arnott. 'Origin of hummocky and swaley cross-stratification— The controlling influence of unidirectional current strength and aggradation rate'. In: *Geology* 34 (12 2006), p. 1073. ISSN: 0091-7613. DOI: 10.1130/G22930A.1.

[52] D. de Fátima Rossetti. 'Internal architecture of mixed tide- and storm-influenced deposits: an example from the Alcântara Formation, northern Brazil'. In: *Sedimentary Geology* 114 (1-4 Dec. 1997), pp. 163–188. ISSN: 00370738. DOI: 10.1016/S0037-0738(97)00067-5.

[53] W. Duke and A. Prave. 'Storm- and Tide-Influenced Prograding Shoreline Sequences in the Middle Devonian Mahantango Formation, Pennsylvania'. In: *Clastic Tidal Sedimentology*. Ed. by D. Smith, G. Reinson, B. Zaitlin and R. Rahmani. Vol. Memoir 16. CSPG Special Publications, 1991, pp. 349–369.

[54] S. J. Boggs. *Principles of Sedimentology and Stratigraphy*. 4th ed. Pearson Education Inc., 2006, pp. 1–662.

[55] J. Dias, O. Pilkey and V. Heilweil. 'Detrital Mica: Environmental significance in North Portugal Continental Shelf Sediments'. In: *Comm. Serv. Geol. Portugal* 70 (1 1984), pp. 93–101.

[56] E. Garzanti, S. Andò and G. Vezzoli. 'Grain-size dependence of sediment composition and environmental bias in provenance studies'. In: *Earth and Planetary Science Letters* 277 (3-4 Jan. 2009), pp. 422–432. ISSN: 0012821X. DOI: 10.1016/j.epsl.2008.11.007.

[57] B. K. Vakarelov, R. B. Ainsworth and J. A. MacEachern. 'Recognition of wave-dominated, tide-influenced shoreline systems in the rock record: Variations from a microtidal shoreline model'. In: *Sedimentary Geology* 279 (Nov. 2012), pp. 23–41. ISSN: 00370738. DOI: 10.1016/j.sedgeo.2011.03.004.

[58] O. Evans. 'The Classification of Wave-formed Ripple Marks'. In: *SEPM Journal of Sedimentary Research* 11 (1 1941). ISSN: 1527-1404. DOI: 10.1306/D42690DF-2B26-11D7-8648000102C1865D.

[59] H. Olsen, N. A. Briedis and D. Renshaw. 'Sedimentological analysis and reservoir characterization of a multi-darcy, billion barrel oil field – The Upper Jurassic shallow marine sandstones of the Johan Sverdrup field, North Sea, Norway'. In: *Marine and Petroleum Geology* 84 (June 2017), pp. 102–134. ISSN: 02648172. DOI: 10.1016/j.marpetgeo.2017.03.029.

[60] A. E. V. Yperen, J. M. Holbrook, M. Poyatos-Moré and I. Midtkandal. 'Coalesced Delta-front Sheet-like Sandstone Bodies from Highly Avulsive Distributary Channels: The Low-accommodation Mesa Rica Sandstone (Dakota Group, New Mexico, U.S.A.)' In: *Journal of Sedimentary Research* 89 (7 July 2019), pp. 654–678. ISSN: 1527-1404. DOI: 10.2110/jsr.2019.27.

[61] P. Alfaro, J. Delgado, A. Estévez, J. Molina, M. Moretti and J. Soria. 'Liquefaction and fluidization structures in Messinian storm deposits (Bajo Segura Basin, Betic Cordillera, southern Spain)'. In: *International Journal of Earth Sciences* 91 (3 May 2002), pp. 505–513. ISSN: 1437-3254. DOI: 10.1007/s00531-001-0241-z.

[62] K. Yagishita. 'Planar cross-bedding associated with rip currents of Upper Cretaceous formations, northeast Japan'. In: *Sedimentary Geology* 93 (3-4 Nov. 1994), pp. 155–163. ISSN: 00370738. DOI: 10.1016/0037-0738(94)90002-7.

[63] L. N. R. Roberts and M. A. Kirschbaum. *Paleogeography and the Late Cretaceous of the Western Interior of middle North America; coal distribution and sediment accumulation*. Tech. rep. 1995. DOI: 10.3133/pp1561.

[64] P. Richards. *Geology of the Bighorn Canyon-Hardin area, Montana and Wyoming*. Tech. rep. U.S. Geological Survey, 1955. DOI: 10.3133/b1026.

[65] P. K. Bijl. 'DINOSTRAT: a global database of the stratigraphic and paleolatitudinal distribution of Mesozoic–Cenozoic organic-walled dinoflagellate cysts'. In: *Earth System Science Data* 14 (2 Feb. 2022), pp. 579–617. ISSN: 1866-3516. DOI: 10.5194/essd-14-579-2022.

[66] A. Cuesta-Cano, J. Storms, G. Rongier and A. Martinius. *Supplementary material: Characterising reservoir heterogeneity in a wave-dominated system: sedimentological, stratigraphic, and petrophysical analysis of a field analogue (Judith River Formation, Late Cretaceous)*. 2025.

[67] B. J. Willis and H. Tang. 'Three-Dimensional Connectivity of Point-Bar Deposits'. In: *Journal of Sedimentary Research* 80 (5 2010), pp. 440–454. ISSN: 1527-1404.

[68] R. Selley. 'A Classification of Paleocurrent Models'. In: *The Journal of Geology* 76 (1 1968), pp. 99–110.

[69] S. E. Dashtgard, J. A. MacEachern, S. E. Frey and M. K. Gingras. 'Tidal effects on the shoreface: Towards a conceptual framework'. In: *Sedimentary Geology* 279 (Nov. 2012), pp. 42–61. ISSN: 00370738. DOI: 10.1016/j.sedgeo.2010.09.006.

[70] G. J. Hampson, M. R. Gani, K. E. Sharman, N. Irfan and B. Bracken. 'Along-Strike and Down-Dip Variations in Shallow-Marine Sequence Stratigraphic Architecture: Upper Cretaceous Star Point Sandstone, Wasatch Plateau, Central Utah, U.S.A.' In: *Journal of Sedimentary Research* 81 (3 Mar. 2011), pp. 159–184. ISSN: 1527-1404. DOI: 10.2110/jsr.2011.15.

[71] M. V. Cappelle, G. J. Hampson and H. D. Johnson. 'Spatial and Temporal Evolution of Coastal Depositional Systems and Regional Depositional Process Regimes: Campanian Western Interior Seaway, U.S.A.' In: *Journal of Sedimentary Research* 88 (8 Aug. 2018), pp. 873–897. ISSN: 1527-1404. DOI: 10.2110/jsr.2018.49.

[72] C. H. Eide, J. A. Howell and S. J. Buckley. 'Sedimentology and reservoir properties of tabular and erosive offshore transition deposits in wave-dominated, shallow-marine strata: Book Cliffs, USA'. In: *Petroleum Geoscience* 21 (1 Feb. 2015), pp. 55–73. ISSN: 1354-0793. DOI: 10.1144/petgeo2014-015.

[73] W. L. Duke. 'Hummocky cross-stratification, tropical hurricanes, and intense winter storms'. In: *Sedimentology* 32 (2 Apr. 1985), pp. 167–194. ISSN: 0037-0746. DOI: 10.1111/j.1365-3091.1985.tb00502.x.

[74] D. Lin, Y. Bu, H. Liu, C. Lu, S. Guo and H. Xu. 'An experimental study of the correlation between P-wave velocity and the physical properties of weakly cemented formations'. In: *Scientific Reports* 13 (1 Dec. 2023), p. 21966. ISSN: 2045-2322. DOI: 10.1038/s41598-023-48783-1.

[75] J. P. Castagna, M. L. Batzle and R. L. Eastwood. 'Relationships between compressional-wave and shear-wave velocities in clastic silicate rocks'. In: *GEOPHYSICS* 50 (4 Apr. 1985), pp. 571–581. ISSN: 0016-8033. DOI: 10.1190/1.1441933.

[76] T. A. Sabrian, R. Saad, M. Saidin, S. B. Muhammad and R. Yusoh. 'Empirical Approach in Developing Vs/Vp Ratio for Predicting S-Wave Velocity, Study Case; Sungai Batu, Kedah'. In: *Journal of Physics: Conference Series* 995 (Apr. 2018), p. 012089. ISSN: 1742-6588. DOI: 10.1088/1742-6596/995/1/012089.

[77] R. H. Tatham. 'Vp/Vs and lithology'. In: *Geophysics* 47 (3 Mar. 1982), pp. 336–344. ISSN: 0016-8033. DOI: 10.1190/1.1441339.

[78] N. Brantut and E. C. David. 'Influence of fluids on VP/VS ratio: increase or decrease?' In: *Geophysical Journal International* 216 (3 Mar. 2019), pp. 2037–2043. ISSN: 0956-540X. DOI: 10.1093/gji/ggy518.

[79] J. P. Castagna and M. M. Backus. *Offset-Dependent Reflectivity—Theory and Practice of AVO Analysis*. Vol. 8. Society of Exploration Geophysicists, Jan. 1993. ISBN: 978-1-56080-059-0. DOI: 10.1190/1.9781560802624.

[80] A. Plint and R. Walker. 'Cardium Formation 8. Facies and environments of the Cardium shoreline and coastal plain in the Kakwa field and adjacent areas, northwestern Alberta.' In: *Bulletin of Canadian Petroleum Geology* 35 (1 1987), pp. 48–64.

[81] R. Walker and A. Plint. 'Wave-and Storm-Dominated Shallow Marine Systems'. In: *Facies Models: Response to Sea Level Change*. Ed. by R. Walker and N. James. Geological Association of Canada, 1992, pp. 219–238.

[82] J. C. V. Wagoner, R. M. Mitchum, K. M. Campion and V. D. Rahmanian. *Siliciclastic Sequence Stratigraphy in Well Logs, Cores, and Outcrops*. American Association of Petroleum Geologists, 1990. ISBN: 0-89181-657-7. DOI: 10.1306/Mth7510.

[83] S. A. Pattison. 'Using classic outcrops to revise sequence stratigraphic models: Reevaluating the Campanian Desert Member (Blackhawk Formation) to lower Castlegate Sandstone interval, Book Cliffs, Utah and Colorado, USA'. In: *Geology* 47 (1 Jan. 2018), pp. 11–14. ISSN: 0091-7613. DOI: 10.1130/G45592.1.

[84]   D. L. Kamola and J. C. V. Wagoner. 'Stratigraphy and Facies Architecture of Parasequences with Examples from the Spring Canyon Member, Blackhawk Formation, Utah'. In: *Sequence Stratigraphy of Foreland Basin Deposits‹subtitle›Outcrop and Subsurface Examples from the Cretaceous of North America‹/subtitle›*. Ed. by J. V. Wagoner and G. Bertram. American Association of Petroleum Geologists, 1995. DOI: 10.1306/M64594C3.

[85]   S. A. J. Pattison. 'Sediment-supply-dominated stratal architectures in a regressively stacked succession of shoreline sand bodies, Campanian Desert Member to Lower Castlegate Sandstone interval, Book Cliffs, Utah–Colorado, ‹scp›USA‹/scp›'. In: *Sedimentology* 67 (1 Jan. 2019), pp. 390–430. ISSN: 0037-0746. DOI: 10.1111/sed.12647.

[86]   G. H. F. Gardner, L. W. Gardner and A. R. Gregory. 'Formation velocity and density — the diagnostic basics for stratigraphic traps'. In: *GEOPHYSICS* 39 (6 Dec. 1974), pp. 770–780. ISSN: 0016-8033. DOI: 10.1190/1.1440465.

[87]   D. Wheeler. 'Discovery and Development of Savageton Field, Powder River Basin, Wyoming'. In: *WGA Sixty-First Conference Guidebook, Unconventional Energy Resources*. Ed. by L. Fletcher. 2010, pp. 15–38.

[88]   D. Tetyukhina, S. M. Luthi and D. Gisolf. 'Acoustic nonlinear full-waveform inversion on an outcrop-based detailed geological and petrophysical model (Book Cliffs, Utah)'. In: *AAPG Bulletin* 98 (1 Jan. 2014), pp. 119–134. ISSN: 0149-1423. DOI: 10.1306/05251311162.

[89]   Ö. Yilmaz. *Seismic Data Analysis*. Society of Exploration Geophysicists, 2001.

[90]   M. Cardiff and P. K. Kitanidis. 'Bayesian inversion for facies detection: An extensible level set framework'. In: *Water Resources Research* 45 (10 Oct. 2009). ISSN: 0043-1397. DOI: 10.1029/2008WR007675.

[91]   D. Grana. 'Joint Inversion of Facies and Reservoir Properties'. In: *81st EAGE Conference and Exhibition 2019*. European Association of Geoscientists & Engineers, 2019, pp. 1–5. DOI: 10.3997/2214-4609.201901298.

[92]   F. Roncarolo and D. Grana. 'Improved Reservoir Characterization Integrating Seismic Inversion, Rock Physics Model, and Petroelastic Log Facies Classification: A Real Case Application'. In: *SPE Annual Technical Conference and Exhibition*. SPE, Sept. 2010. DOI: 10.2118/134919-MS.

[93]   A. Cuesta-Cano, J. Storms, G. Rongier and A. Martinius. *3D model of a clastic, shallow marine outcrop in the Western Interior Basin (Parkman Sandstone, Judith River Formation, Cretaceous)*. 2024.

Appendixes

Appendix 1. Paleocurrent analysis

Rose diagrams compiling the paleocurrent measurements for each facies association.

FA3 Family 1 (N=4)

FA3 Family 2 (N=14)

FA4 (N=6)

FA5 (N=11)
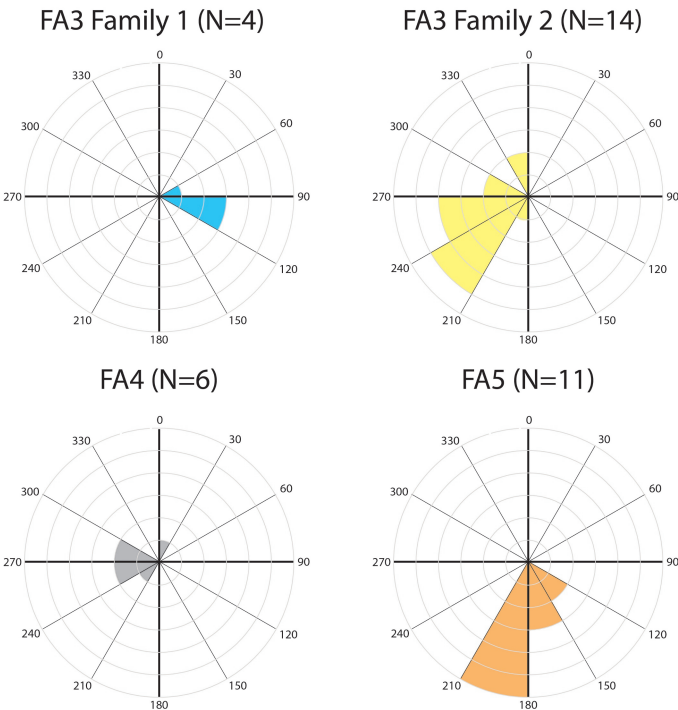
Appendix 2. Grain analysis

Detailed information of the grain size analysis for ten thin sections. Here, we include the summary of the mean grain size, standard deviation of the grain size, sphericity, and circularity per sample (Table 2.3), together with the exact location of each sample and the total number of grains that were measured per sample. The averaged grain size distribution data, and the percentage frequency for circularity and sphericity data for each sample and subsamples are publicly accessible in Cuesta-Cano *et al.* [1].

FA3 and FA4 have a similar grain size distribution, with the exception of sample HET-BRID-25, which was collected in the southernmost stratigraphic log. The mean grain size of these samples varies from 0.57 to 0.66, and standard deviations from 0.019 to 0.024 (Table 2.3). Sample 25 is composed by coarser grains. Sample 25 includes three subsamples for which the fine material seems to not be adequately measured because their grain size curve deviates from the other subsamples. When removing these three samples from the analysis, the new average grain size is 0.11 mm with a standard deviation of 0.065 (sphericity and circularity statistics are not affected).

For FA5, there is a wider range of mean grain size and standard deviations (Table 2.3). Samples 9 and 25, even if they belong to the same interval of FA4, have very different mean grain size values and standard deviations. This agrees with the observations made in the field, where grain sizes from very fine to medium were identified. The values from sample 9 better match to those of the samples in FA3 and FA4 (Table 2.3). In general, we observe a constant grain size distribution for the samples from the lower shoreface and middle shoreface, with a slight coarsening upwards, depicted by the increase in mean grain size from samples 18 and 21 to samples in FA3(2) and FA4(2). The main coarsening occurs from FA4 to FA5, with the change from middle to upper shoreface.

The sphericity and circularity values show similar trends as observe for the grain size distribution, where the coarser samples also are formed by the more angular grains. The sphericity varies from mean values of 0.773 to 0.8 and the circularity, from 0.632 to 0.667 for samples in FA3 and FA4. Samples belonging to facies FA5 show sphericities ranging from 0.704 to 0.718 and circularities in the range of 0.592 to 0.605. Once again, sample 25 is an outlier, with values closer to those of facies FA5, especially for circularity.

Sample	Facies	Subsamples	Total grains	Mean GS	Stand. dev.	Sphericity	Circularity
HET-BRID-9	FA4 (2)	10	11912	0.069 mm	0.026	0.786	0.652
HET-BRID-16	FA3 (2)	10	11940	0.066 mm	0.023	0.777	0.640
HET-BRID-18	FA3 (2)	11	15309	0.059 mm	0.024	0.800	0.667
HET-BRID-21	FA4 (1)	8	11701	0.061 mm	0.022	0.787	0.644
HET-BRID-25	FA4 (2)	11	6648	0.137 mm	0.085	0.735	0.607
HET-BRID-27	FA3 (2)	11	13826	0.068 mm	0.023	0.773	0.632
HET-BRID-35	FA5	10	2663	0.149 mm	0.060	0.718	0.605
HET-BRID-37	FA3 (2)	10	15865	0.057 mm	0.019	0.790	0.641
HET-BRID-43	FA5	11	3091	0.159 mm	0.079	0.704	0.592
HET-BRID-45	FA5	11	3300	0.145 mm	0.059	0.713	0.604

Table 2.3: Summary of the analysed samples, including the total number of subsamples for which grains could be segmented, the total number of grains detected during the grain size analysis, the mean grain size (in mm) value, the standard deviation, the mean sphericity (unitless), and the mean circularity (unitless) values. The facies information has also been included. For those facies associations where there are two intervals, the number indicates if the sample is from the lower (1) or upper (2) interval. The grain size analysis of those samples belonging to the FA5 facies include a significant lower amount of grains. This is related to the general greater grain size compared to the other samples.

Appendix 3. Petrophysical, elastic and acoustic properties

In this appendix, we include a summary of the mean values and the standard deviation, in between brackets, obtained for every facies association and every property. More details on the measurements are available in Cuesta-Cano *et al.* [1]

Sample batch	Number samples	Number density, Vs measurements	Number Vp measurements	Grain density (g/cm^3)	Bulk density (g/cm^3)	Porosity $(-)$	P-wave velocity (m/s)	S-wave velocity (m/s)	Vp/Vs ratio $(-)$
FA1	2	2	5	2.61 (0.05)	1.95 (0.03)	0.25 (0.03)	1322.34 (147.05)	996.62 (48.39)	1.45 (0.23)
FA2	3	3	7	2.65 (0.07)	2.20 (0.17)	0.17 (0.04)	2105.12 (108.02)	1417.11 (252.93)	1.48 (0.09)
FA3 (1)	3	3	6	2.71 (0.04)	2.10 (0.07)	0.22 (0.03)	1951.07 (421.38)	1127.57 (101.89)	1.76 (0.18)
FA3 (2)	6	6	22	2.49 (0.03)	2.05 (0.04)	0.18 (0.02)	1270.64 (301.74)	827.11 (166.25)	1.52 (0.09)
FA4 (1)	2	2	7	2.54 (0.01)	2.12 (0.06)	0.16 (0.02)	1512.92 (173.30)	1040.68 (59.99)	1.68 (0.03)
FA4 (2)	7	7	23	2.53 (0.09)	2.03 (0.05)	0.20 (0.04)	1030.62 (132.61)	771.62 (121.56)	1.39 (0.11)
FA4 (3)	5	5	16	2.58 (0.07)	2.08 (0.09)	0.19 (0.04)	1188.24 (119.77)	822.50 (106.10)	1.43 (0.07)
FA5	16	16	63	2.50 (0.05)	2.04 (0.04)	0.18 (0.03)	1238.64 (196.81)	834.92 (81.47)	1.52 (0.13)

Table 2.4: Distribution of number of samples per facies association and number of measurements performed. For density, only one measurement per sample was taken. For seismic velocities, some of the samples were divided into smaller subsamples due to size limitations and, thus, more than one measurement per sample was performed. Mean values and standard deviation (in brackets) for all the properties measured and calculated per facies association.

3

Introduction to stratigraphic forward modelling

3.1. Introduction

In this thesis, I aim to analyse the seismic response of metre-scale, stratigraphic heterogeneities that develop in clastic, wave-dominated shallow marine environments. These metre-scale stratigraphic heterogeneities in wave-dominated environments result from (1) erosional surfaces and the consequent abrupt change of lithologies [1], and (2) gradual transitions between lithologies or gradual changes of rock property, including porosity [2–4]. In the field of reservoir characterisation, the analysis and interpretation of stratigraphic heterogeneities is sometimes based on the application of forward seismic modelling tools to site specific outcrop analogue data [5–8]. However, the number of good-quality, laterally extensive outcrops that allow for 3D observations is limited. This makes it challenging to characterise stratigraphic heterogeneities in a reservoir by only using outcrops. Therefore, in this chapter, I explore a different path to characterise reservoir heterogeneities by using geologically-sound forward stratigraphic simulations that can be used as input for the forward seismic modelling.

In nature, the formation of stratigraphic heterogeneities, at any scale, occurs as a combination of the interaction between sedimentological processes, the characteristics of the depositional environment and the post-depositional processes, such as diagenesis or fracturing. In depositional environments dominated by clastic sediments, sedimentological processes include, for instance, erosion, transport, and deposition of sediment at the surface. After deposition, the heterogeneities might be affected by other processes, such as compaction, dissolution, or cement precipitation. To understand and predict the effects of sediment erosion, transport, and deposition, a wide variety of Stratigraphic Forward Modelling (SFM) methods and tools have been developed over the past decades (e.g. [9–12]). SFM tools mimic some of the sedimentological processes to generate geological simulations that include synthetic stratigraphy and distribution of sedimentological properties, e.g. grain size distribution. These tools rely on mathematical formulae that mimic sedimentological processes or reproduce the deposit geometries to generate geologically plausible synthetic stratigraphy [13, 14]. Depending on the temporal and spatial scales of the desired model output, the methods may include a refined physics-based description or a more simplified process-mimicking description of sediment erosion, transport and sedimentation, either formulated in 2D or 3D. The general idea behind forward stratigraphic modelling is that they suffice to general geological principles such as Walther's law, and that they represent the effects of autogenic and allogenic forcings on the simulated stratigraphy. This means that in general Forward Stratigraphic Models can be useful tools simulate the formation of stratigraphic heterogeneities.

In this project, I require a SFM tool that is able to generate fine-scale, stratigraphic heterogeneities in a wave-dominated, shallow marine depositional environment. To decide which SFM tool fits best with the project, I have set a series of conditions based on the objectives and needs of the future steps. These conditions are:

1. The required outputs: Because I want to apply stratigraphic forward modelling, I need to make sure that I can link one or several of the outputs of the SFM tool with petrophysical properties. This means that the SFM tool should compute porosity or the grain size distribution, so I can calculate porosity in a later stage.

2. The nature and dimensions of the heterogeneities: The stratigraphic heterogeneities should be at metre scale in the vertical direction. Horizontal scale of $10-20m$ or lower is a plus.

3. The processes acting in the depositional environment of interest: wave action and longshore drift are some of the processes present in wave-dominated systems and they should be included in the simulation.

4. The computational expense: A computationally inexpensive SFM tool allows the generation of many simulations in short time. As mentioned in 1, the parallel project applies machine learning techniques for the identification of fine-scale heterogeneities, and requires the generation of extensive training data.

5. Spatial dimensions: this project does not required 3D geological simulations.

3.2. Stratigraphic modelling types

To simulate stratigraphy using a SFM tool, we need to decide on what temporal scale are most relevant for the specific application. How should we model sediment flows that take minutes or hours when modelling the formation of stratigraphy over e.g. millions of years? How should we model the grain distribution at a specific location when we are also interested in the infill of an entire sedimentary basin? All the correct mathematical models that build the stratigraphy could be defined and combined to predict their result, given enough computing power.

Due to the complexity of simulating the actual sedimentological processes that build stratigraphy, different stratigraphic forward modelling (SFM) tools apply different approaches to represent simplified sedimentological processes [15], finding a balance between physical accuracy and computational efficiency. Depending on which approach they use, a distinction can be made between process-based and process-mimicking SFM tools [13, 16]. Process-based models (also referred to as physics-based models) aim at numerically modelling the physics of water flow and sediment transport. Process-mimicking models do not resolve the physics but aim to reproduce the general behaviour of the processes, which are captured in rules [13, 14, 16].

Process-based SFM simulations rely on methods such as sediment diffusion, in which transport and deposition of sediment is a function of potential gradient [9, 10,

17, 18], or hydraulic equations, which resolve shallow water equations, simplified version of Navier Stokes equations, and they combine them with bed-load transport equations that model the sediment transport and deposition [18–22]. From empirical studies, it is known that the Navier-Stokes equations work well in modelling fluid flow [12, 23, 24]. Thus, the strength of process-based models is that they, to some extent, are based on physical laws and, therefore, they have the potential to simulate meaningful stratigraphic heterogeneities [14, 25]. Yet, process-based models have a greater number of initial and boundary conditions that have to be defined versus other model types, and they have a high computational cost, even if they still depend on approximations or simplifications of the physical processes responsible to build the stratigraphy.

Instead of resolving the processes, process-mimicking (or rule-based) models use rules that aim to capture the essence of the actual processes to simulate a depositional environment and the associated thickness and geometry of the deposits [11, 15, 26–28]. Some of these tools are based on the relationship between sediment shape, volume of sediment supply, rate of subsidence, type of sediment, etc. Rule-based models vary greatly from one to another depending on the complexity of the rules that they apply [25]. The process-mimicking models are able to generate in seconds or minutes stratigraphic sections based on, for instance, accommodation change and sediment supply and they can simulate meaningful, metre-scale, stratigraphic heterogeneity.

In case of rule-based and process-based SFM tools, the resulting synthetic stratigraphy will depend on the type of tool that the modeller chooses and the set of boundary conditions and parameters that the modeller inputs. Depending on the rules or the processes used in every specific modelling tool, the boundary conditions and parameters that need to be adjusted might vary. In case of clastic depositional environments, the combination of the tool, the initial and boundary conditions, and the parameter values control the way sediment is eroded, transported, and deposited within the simulation. However, some of the parameters are common to many tools. This is the case of, for instance, sediment input or sea level variation.

It is important to highlight that it can be difficult to draw the line between process-based and process-mimicking SFM tools. Process-mimicking tools can incorporate complex rules that mimic depositional events and their results, while all process-based tools rely on simplifications of the fluid flow processes. Then, the question that arises is: when does a simplification become a complex rule?

3.3. Stratigraphic forward modelling tools for wave-dominated systems

There is a plethora of research dealing with the processes that shape clastic, wave-dominated, shallow marine depositional environments [29–37]. And there

are tools available specifically for the stratigraphic forward modelling of these environments [11, 38–43].

For this project, I have reviewed the characteristics of some SFM tools that could meet the requirements defined earlier. In this section, I present three SFM tools, both open source and commercial, that I analysed and that might fulfil the requirements: DionisosFlow, SedSim, and BarSim. Other SFM tools specific for coastal depositional environments, such as SimClast, Sedapp v2021, or SIMSAFADIM-CLASTIC, are not applicable to this project because their vertical resolution is too coarse or because they focus on the interaction between fluvial and deltaic processes instead of wave action [18, 20, 44].

3.3.1. DionisosFlow

DionisosFlow is a SFM software suite developed and commercially distributed by Beicip [45]. It performs simulations in time, from kiloyears up to millions of years, and space, from tens to hundreds of kilometres [46], in a three-dimensional space. This tool was developed for basin-scale basin infill studies [45–47]. The input parameters are: subsidence maps for specific ages, initial bathymetry map, location and intensity history of sediment sources (with different grain size classes and ratios), sea-level history, sediment transport parameters, and compaction and flexure parameters [45, 47].

DionisosFlow accounts for four different processes that contribute to stratigraphy building: sea level change, tectonics, sediment supply, and sediment transport [45]. These processes are resolved using gravity- and water-driven diffusion equations, which allows the simulation of sediment transport at geological time scales in continental and marine environments [47]. Additionally, mass conservation principles are applied to each grain size fraction [45].

The software is able to create horizontal layers, small-scale oblique features and clinoform geometries [48]. The horizontal resolution of the model will depend on the simulated grid size. The minimal horizontal grid size that the software can handle is $50x50m$, however the recommended highest resolution is $100x100m$ cell size. The vertical resolution in the simulation depends on the sedimentation rate and the time steps (S. Bou Daher, personal communication, 26th March 2021). For low sedimentation rates and short time steps, the vertical resolution can be on the centimetre scale.

This model is mainly used to quantify the interaction between tectonic and sedimentary processes, test different interpretations of seismic data based on geological scenarios and reduce uncertainty in interpretation of stratigraphic architecture [45]. The typical workflow includes the generation of different scenarios based on a trial-and-error approach, until finding the best match with the available

seismic data for a certain subsurface target [45].

I ran some simulations to understand the impact of the input parameters in the system and the suitability of the modelling tool for my project. DionisosFlow meets the condition of required outputs, by providing grain size and porosity distribution maps (Figure 3.1). DionisosFlow incorporates wave action but not longshore drift, the main sediment supply in wave-dominated systems. This means that the sediment input always happens through a continental source through a fluvial system (Figure 3.1). DionisosFlow does not meet the requirements regarding the dimensions of the heterogeneities as the recommended horizontal resolution is $100m$. On the computational expense, simple runs can be solved in less than a day, but they required access MySQL database to store data and it runs in multiprocessor. All in all, DionisosFlow is not a good candidate for the study of heterogeneities in wave-dominated shoreface systems at the metre scale.
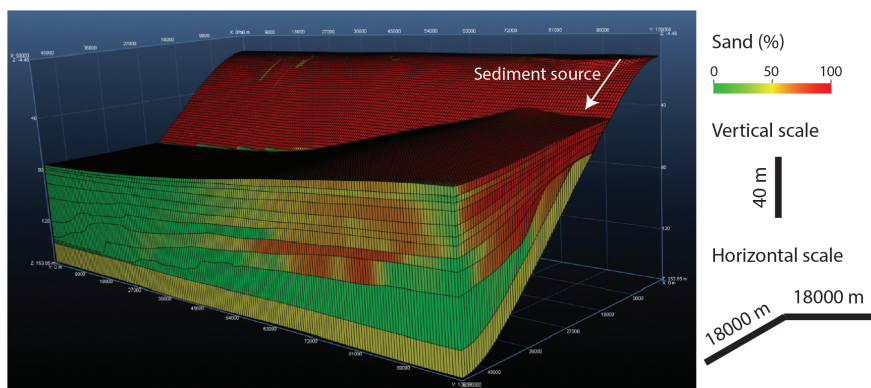

Figure 3.1: Example of DionisosFlow simulation displaying the percentage of sand per cell. The thickness of the layers vary from 5 to $40m$. The horizontal grid size is $500m$. The location of the sediment source and direction of the sediment input is indicated with a white arrow. Simulation's run time: $27h$.

3.3.2. SedSim

Sedimentary Simulator or SedSim is a three-dimensional stratigraphic modelling tool to analyse the formation of basins at geological and engineering time scales [49]. This tool has been in continuous development since the 80s [12, 43, 50] and a number of studies have demonstrated that SedSim is able to predict sediment distribution in different depositional environments from the decimetre to the kilometre scale [12, 19, 50, 51].

The core program runs flow and sedimentation simulations. The simulation of the fluid flow is based on an approximation to the Navier-Stoke equations [19]. The

transport and deposition of sediment is based on the principle of mass conservation. The user adds modules to the core program to incorporate more processes into the simulation. Some available modules are wave transport, subsidence, relative sea level change, carbonate sedimentation, etc.

The required input parameters will depend on the modules that the user includes. Some of the minimal input parameters are initial topography, relative sea or lake-level curves, sediment source location and input rates, simulation time, grid size, sediment components and their properties, etc. The output file includes the fraction of each grain size class per cell, facies distribution, and the porosity. SedSim is able to simulate bedforms and layers whose thickness is under $1m$ [50, 52].

The modules of SedSim are extensively discussed in the literature [49, 53–55]. For the analysis of heterogeneities in wave-dominated, shallow marine environments, SedSim includes a module that simulates the effect of wave action in the sediment transport and deposition [43]. This module can be activated independent from fluvial or tidal action, isolating the effect of waves on the redistribution of sediment. In order to model the effect of wave action over geologic periods of time, the most basic known principles of wave motion are used [50]. However, the module lacks the option of longshore sediment input.

From the test runs done for the project, I saw that SedSim meets the output requirements by providing grain size (Figure 3.2) and porosity distribution. The vertical scale requirement is also met, with heterogeneities in the metre-scale, however, the horizontal scale requirement is not met, as the simulations of a grid $50x50m$ resulted in error. SedSim includes storm and wave action as separate modules and the effect of these processes can be simulated independently from fluvial sediment input (Figure 3.2). However, even if there are tricks to include longshore currents into the simulation, SedSim is not able to include longshore drift processes. The only solution is to make a two-step simulation in which, first, I activate the input of sediment on the side of the grid (Figure 3.2A), and, second, stop the input and activate the redistribution of the sediment by shore-parallel currents (Figure 3.2B). Regarding the computational expense, running a simple simulation on a laptop could take longer than a couple of days. All in all, the limitations of SedSim do not make it a good fit for the project.

3.3.3. BarSim

BarSim is an event-based, process-mimicking model that simulates the long-term coastal evolution and stratigraphic architecture through time of wave-dominated coastal systems [11, 56, 57]. This model is based on a simple approximation of a 2D cross-shore profile and simulates the deposition of individual storm beds, with thickness values that go down to the centimetre scale [56, 57]. BarSim applies mass conservation principles to erosion, transport, and deposition of multiple grain
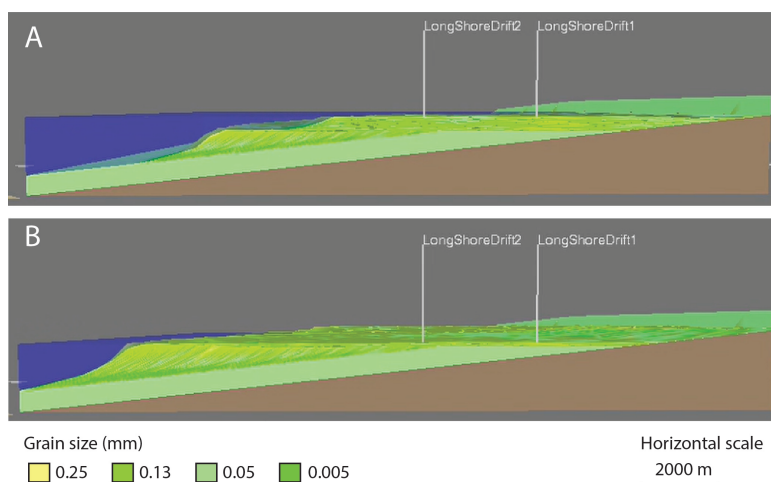
Figure 3.2: Example of SedSim simulation displaying the dominant grain size per cell. A.-
Deposition of sediment on the side of the simulation during a stage of no wave
nor other current action. B.- Redistribution of the sediment by shore-parallel
currents, mimicking longshore drift, waves and storm action. This simulation
takes over 24 hours.

size classes along a 2D profile at surface conditions [56–58]. This means that
sediment that is eroded at any location on the shoreface due to the action of
waves is transported and deposited at other locations in the 2D profile, where
accommodation is available. Sediment input into and out of the model occurs as
along-shore transport, which is defined as net sediment input by the user [11].

The input variables are (1) model parameters controlling sediment erosion, transport,
and deposition (wave efficiency, rate of erosion, characteristic travel distances),
(2) time-dependent variables (sea level, sediment budget), (3) and variables that
define the initial conditions (grain size distributions, littoral drift, wave-base depth,
substrate slope) [11]. The output includes sedimentological information (fraction of
the different grain size classes, mean grain size, sorting, facies) for all the grid cells
[59].

There is a recent implementation of BarSim, called pyBarSim, which speeds up
the simulation process to generate the geological simulations [60]. pyBarsim is a
Python package that also allows the interpolation of the simulated sediment layers
onto a regular vertical grid.

Considering the requirements for the choice of SFM set at the beginning of the
chapter, BarSim meets them all. As an output, I obtain ratio of the grain size classes
used in the simulations (Figure 3.3), data that I can use to calculate porosity and
make the connection to petrophysical and acoustic properties. The heterogeneities
that BarSim generates are centimenter to metre-scale in the vertical direction and

can be interpolated into a regular grid defined by the user, and $50m$ in the horizontal direction, perpendicular to shoreline. From the analysed SFM tools, BarSim is the only one that simulates grid sizes below $100m$ in the horizontal direction. BarSim is specifically designed to simulate wave-dominated shorelines, so it includes the effect of wave action and longshore drift. With the pyBarSim version, simulations take only a few seconds and can be run locally in any type of machine.
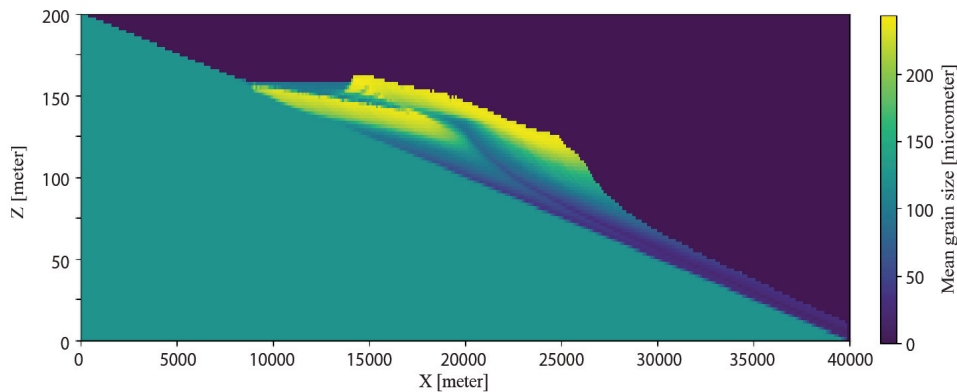

Figure 3.3: Example of BarSim simulation displaying the mean grain size distribution. The cell size is uniformised to $50x2m$. Running one simulation using the pyBarSim version takes a couple of seconds.

3.4. Conclusions

Each stratigraphic forward modelling tool is designed to fit specific goals when analysing the development of stratigraphic heterogeneities and, depending on these goals, the modeler shall choose a different SFM tool. Here, I am looking for tools that allow the analysis of metre-scale heterogeneities in wave-dominated shoreface environments and I have set some conditions that the preferred SFM tool should meet to fit in the project. A summary of the properties for each tool analysed can be found in Table 3.1.

Applying the conditions listed at the beginning of this chapter to each SFM tools (Table 3.2), I conclude that BarSim is the most suitable SFM tool for this project. Even though, BarSim lacks porosity as an output, this parameter can be approximated based on the grain size distribution [61]. However, BarSim is the only SFM tool that includes longshore drift processes in the simulations, which run in seconds.

	DionisosFlow	SedSim	BarSim
SFM tool type	Process-based (Diffusion)	Process-based (Approximation Navier-Stokes)	Process-mimicking
Dimensionality	3D	3D	2 and 2,5D
Minimum vertical grid cell size	$< 1m$*	Dm-scale	Cm-scale
Minimum grid cell size (other dimensions)	$100m x 100m$	$> 100m$	$50m$
Minimum timestep	Kiloyear	Year	Year
Depositional environment	Multiple	Multiple	Single

Table 3.1: Summary of some of the properties of DionisosFlow, SedSim, and BarSim. * DionisosFlow is only able to simulate grid cells that are under the $1m$ mark in vertical direction under very specific conditions, typical of deep sea depositional environments.

	DionisosFlow	SedSim	BarSim
Output: porosity	Yes	Yes	No
Output: grain size distribution	Yes	Yes	Yes
Heterogeneity: metre scale	No	Yes	Yes
Processes: longshore drift	No	No	Yes
Processes: wave action	Yes	Yes	Yes
Computational expense: low	Hours/simulation	Hours-days/simulation	Seconds/simulation

Table 3.2: Selection criteria for the SFM tool: Requirements for this project and their alignment with the three SFM tools discussed in the previous section.

References

[1] G. J. Hampson and J. E. A. Storms. 'Geomorphological and sequence stratigraphic variability in wave-dominated, shoreface-shelf parasequences'. In: *Sedimentology* 50 (4 Aug. 2003), pp. 667–701. ISSN: 0037-0746. DOI: 10.1046/j.1365-3091.2003.00570.x.

[2] K. G. Taylor, R. L. Gawthorpe, C. D. Curtis, J. D. Marshall and D. N. Awwiller. 'Carbonate Cementation in a Sequence-Stratigraphic Framework: Upper Cretaceous Sandstones, Book Cliffs, Utah-Colorado'. In: *Journal of Sedimentary Research* 70 (2 Mar. 2000), pp. 360–372. ISSN: 1527-1404. DOI: 10.1306/2DC40916-0E47-11D7-8643000102C1865D.

[3] J. M. Ketzer, S. Morad, R. Evans and I. S. Al-Aasm. 'Distribution of Diagenetic Alterations in Fluvial, Deltaic, and Shallow Marine Sandstones Within a Sequence Stratigraphic Framework: Evidence from the Mullaghmore Formation (Carboniferous), NW Ireland'. In: *Journal of Sedimentary Research* 72 (6 Nov. 2002), pp. 760–774. ISSN: 1527-1404. DOI: 10.1306/042202720760.

[4] T. Sømme, J. Howell, G. Hampson and J. Storms. 'Genesis, Architecture, and Numerical Modeling of Intra-Parasequence Discontinuity Surfaces In Wave-Dominated Deltaic Deposits: Upper Cretaceous Sunnyside Member, Blackhawk Formation, Book Cliffs, Utah, U.S.A.' In: *Recent Advances in Models of Siliciclastic Shallow-Marine Stratigraphy* (2008), pp. 421–441. DOI: 10.2110/PEC.08.90.0421.

[5] D. A. Armitage and L. Stright. 'Modeling and interpreting the seismic-reflection expression of sandstone in an ancient mass-transport deposit dominated deep-water slope environment'. In: *Marine and Petroleum Geology* 27 (1 Jan. 2010), pp. 1–12. ISSN: 0264-8172. DOI: 10.1016/J.MARPETGEO.2009.08.013.

[6] K. Bakke, I. Kane, O. Martinsen, S. Petersen, T. Johansen, S. Hustoft, F. Jacobsen and A. Groth. 'Seismic modeling in the analysis of deep-water sandstone termination styles'. In: *AAPG Bulletin* 97 (9 2013), pp. 1395–1419. DOI: 10.1306/03041312069.

[7] E. Pemberton, L. Stright, S. Fletcher and S. Hubbard. 'The influence of stratigraphic architecture on seismic response: Reflectivity modeling of outcropping deepwater channel units'. In: *Interpretation* 6 (3 2018), T783–T808. DOI: 10.1190/INT-2017-0170.1.

[8] H. Zeng, X. Zhu and R. Zhu. 'New insights into seismic stratigraphy of shallow-water progradational sequences: Subseismic clinoforms'. In: *Interpretation* 1 (1 Aug. 2013). doi: 10.1190/INT-2013-0017.1, SA35–SA51. ISSN: 2324-8858. DOI: 10.1190/INT-2013-0017.1.

[9]   D. Granjeon. '3D forward modelling of the impact of sediment transport and base level cycles on continental margins and incised valleys'. In: *From Depositional Systems to Sedimentary Successions on the Norwegian Continental Margin*. Wiley, Aug. 2014, pp. 453–472. DOI: 10.1002/9781118920435.ch16.

[10] J. C. Rivenæs. 'Application of a dual-lithology, depth-dependent diffusion equation in stratigraphic simulation'. In: *Basin Research* 4 (2 June 1992), pp. 133–146. ISSN: 0950-091X. DOI: 10.1111/j.1365-2117.1992.tb00136.x.

[11] J. Storms, G. Weltje, J. V. Duke, C. Geel and S. Kroonenberg. 'Process-response modeling of wave-dominated coastal systems: Simulating evolution and stratigraphy on geological timescales'. In: *Journal of Sedimentary Research* 72 (2 2002), pp. 226–239. DOI: 10.1306/052501720226.

[12] D. Tetzlaff and J. Harbaugh. *Simulating Clastic Sedimentation*. 1st ed. Springer New York, 1989, pp. 1–202.

[13] P. M. Burgess. 'A brief review of developments in stratigraphic forward modelling, 2000–2009'. In: *Phanerozoic Regional Geology of the World*. Elsevier, 2012, pp. 378–404. DOI: 10.1016/B978-0-444-53042-4.00014-5.

[14] X. Huang, C. M. Griffiths and J. Liu. 'Recent development in stratigraphic forward modelling and its application in petroleum exploration'. In: *Australian Journal of Earth Sciences* 62 (8 Nov. 2015), pp. 903–919. ISSN: 14400952. DOI: 10.1080/08120099.2015.1125389.

[15] D. N. Christie, F. J. Peel, G. M. Apps and D. " Stanbrook. 'Forward Modelling for Structural Stratigraphic Analysis, Offshore Sureste Basin, Mexico'. In: *Frontiers in Earth Science* 9 (Dec. 2021). ISSN: 2296-6463. DOI: 10.3389/feart.2021.767329.

[16] C. Paola. 'Quantitative models of sedimentary basin filling'. In: *Sedimentology* 47 (SUPPL. 1 Feb. 2000), pp. 121–178. ISSN: 1365-3091. DOI: 10.1046/J.1365-3091.2000.00006.X.

[17] E. W. Hutton and J. P. Syvitski. 'Sedflux 2.0: An advanced process-response model that generates three-dimensional stratigraphy'. In: *Computers & Geosciences* 34 (10 Oct. 2008), pp. 1319–1337. ISSN: 00983004. DOI: 10.1016/j.cageo.2008.02.013.

[18] J. Li, P. Liu, S. Sun, Z. Sun, Y. Zhou, L. Gong, J. Zhang and D. Du. 'Sedapp v2021: a nonlinear diffusion-based forward stratigraphic model for shallow marine environments'. In: *Geoscientific Model Development* 14 (8 Aug. 2021), pp. 4925–4937. ISSN: 1991-9603. DOI: 10.5194/gmd-14-4925-2021.

[19] C. M. Griffiths, C. Dyt, E. Paraschivoiu and K. Liu. 'Sedsim in Hydrocarbon Exploration'. In: 2001, pp. 71–97. DOI: 10.1007/978-1-4615-1359-9_5.

[20] O. Gratacós, K. Bitzer, L. Cabrera and E. Roca. 'SIMSAFADIM-CLASTIC: A new approach to mathematical 3D forward simulation modelling for terrigeneous and carbonate marine sedimentation'. In: *Geologica Acta* 7 (3 2009).

[21] R. Basani, M. Janocko, M. J. Cartigny, E. W. Hansen and J. T. Eggenhuisen. 'MassFLOW-3D ^{TM} as a simulation tool for turbidity currents'. In: *From Depositional Systems to Sedimentary Successions on the Norwegian Continental Margin*. Wiley, Aug. 2014, pp. 587–608. DOI: 10.1002/9781118920435.ch20.

[22] F. A. Trentin, E. L. C. Lavina, A. S. da Silveira, V. E. da Silva, S. R. X. Lopes, A. A. de Oliveira Lopes and J. E. Faccion. '3D stratigraphic forward modeling of an ancient transgressive barrier system: A case study of accuracy and sensitivity'. In: *Marine and Petroleum Geology* 109 (Nov. 2019), pp. 675–686. ISSN: 02648172. DOI: 10.1016/j.marpetgeo.2019.06.013.

[23] W. Graf. *Hydraulics of Sediment Transport*. Water Resources Publication, 1984, pp. 1–513.

[24] D. Simons and F. Şentürk. *Sediment transport technology: water and sediment dynamics*. Water Resources Publication, 1992, pp. 1–897.

[25] M. J. Pyrcz, R. P. Sech, J. A. Covault, B. J. Willis, Z. Sylvester and T. Sun. 'Stratigraphic rule-based reservoir modeling'. In: *Bulletin of Canadian Petroleum Geology* 63 (4 Dec. 2015), pp. 287–303. ISSN: 0007-4802. DOI: 10.2113/GSCPGBULL.63.4.287.

[26] M. J. Pyrcz, T. McHargue, J. Clark, M. Sullivan and S. Strebelle. 'Event-Based Geostatistical Modeling: Description and Applications'. In: (2012), pp. 27–38. DOI: 10.1007/978-94-007-4153-9_3.

[27] Z. Sylvester, A. Cantelli and C. Pirmez. 'Stratigraphic evolution of intraslope minibasins: Insights from surface-based model'. In: *AAPG Bulletin* 99 (06 June 2015), pp. 1099–1129. ISSN: 0149-1423. DOI: 10.1306/01081514082.

[28] N. Yan, L. Colombera, G. I. Cosgrove and N. P. Mountney. 'A 3D forward stratigraphic model of aeolian dune evolution for prediction of lithofacies heterogeneity'. In: *Computers & Geosciences* 187 (May 2024), p. 105594. ISSN: 00983004. DOI: 10.1016/j.cageo.2024.105594.

[29] N. Kumar and J. E. Sanders. 'Characteristics of shoreface storm deposits; modern and ancient examples'. In: *Journal of Sedimentary Research* 46 (1 Mar. 1976), pp. 145–162. ISSN: 1527-1404. DOI: 10.1306/212F6EDD-2B24-11D7-8648000102C1865D.

[30] M. E. Field and P. S. Roy. 'Offshore transport and sand-body formation; evidence from a steep, high-energy shoreface, southeastern Australia'. In: *Journal of Sedimentary Research* 54 (4 Dec. 1984), pp. 1292–1302. ISSN: 1527-1404. DOI: 10.1306/212F85C1-2B24-11D7-8648000102C1865D.

[31] O. Madsen. 'Mechanics of Cohesionless Sediment Transport in Coastal Waters'. In: *Proc. Coastal Sediments* ASCE (1991), pp. 15–27.

[32] D. Swift, P. S. and J. Thorne. 'Sedimentation on continental margins, IV. Lithofacies and depositional systems.' In: *Shelf Sand and Sandstone Bodies*. Ed. by D. Swift, G. Oertel, R. Tillman and J. Thorne. Vol. 14. Int. Assoc. Sedimentol. Spec. Publ., 1991, pp. 89–152.

[33] T. R. Keen, R. L. Slingerland, S. J. Bentley, Y. Furukawa, W. J. Teague and J. D. Dykes. 'Sediment Transport on Continental Shelves: Storm Bed Formation and Preservation in Heterogeneous Sediments'. In: *Sediments, Morphology and Sedimentary Processes on Continental Shelves* (Jan. 2012), pp. 295–310. DOI: 10.1002/9781118311172.CH14.

[34] E. J. Anthony. 'Storms, shoreface morphodynamics, sand supply, and the accretion and erosion of coastal dune barriers in the southern North Sea'. In: *Geomorphology* 199 (Oct. 2013), pp. 8–21. ISSN: 0169-555X. DOI: 10.1016/J.GEOMORPH.2012.06.007.

[35] J. Backstrom, D. Jackson, A. Cooper and C. Loureiro. 'Contrasting geomorphological storm response from two adjacent shorefaces'. In: *Earth Surface Processes and Landforms* 40 (15 Dec. 2015), pp. 2112–2120. ISSN: 1096-9837. DOI: 10.1002/ESP.3788.

[36] E. J. Anthony and T. Aagaard. 'The lower shoreface: Morphodynamics and sediment connectivity with the upper shoreface and beach'. In: *Earth-Science Reviews* 210 (Nov. 2020), p. 103334. ISSN: 0012-8252. DOI: 10.1016/J.EARSCIREV.2020.103334.

[37] N. C. Mitchell and Z. Zhao. 'Effects of currents and waves on the morphologies of coastal sandy clinoforms: sediment mobility calculations based on current meter and wave data from Southern California, U.S.A.' In: *Journal of Sedimentary Research* 93 (7 July 2023), pp. 488–501. ISSN: 1527-1404. DOI: 10.2110/JSR.2023.002.

[38] A. Ashton, A. B. Murray and O. Arnoult. 'Formation of coastline features by large-scale instabilities induced by high-angle waves'. In: *Nature* 414 (6861 Nov. 2001), pp. 296–300. ISSN: 0028-0836. DOI: 10.1038/35104541.

[39] L. Laigle, P. Joseph, G. D. Marsily and S. Violette. '3-D process modelling of ancient storm-dominated deposits by an event-based approach: Application to Pleistocene-to-modern Gulf of Lions deposits.' In: *Marine Geology* 335 (2012), pp. 177–199. DOI: 10.1016/j.margeo.2012.11.007.

[40] J. H. Nienhuis and J. Lorenzo-Trueba. 'Simulating barrier island response to sea level rise with the barrier island and inlet environment (BRIE) model v1.0'. In: *Geoscientific Model Development* 12 (9 Sept. 2019), pp. 4013–4030. ISSN: 1991-9603. DOI: 10.5194/gmd-12-4013-2019.

[41] M. Poff, I. Georgiou, M. Kulp, M. Leadon, G. Thomson and D. Walstra. *2017 Coastal Master Plan Modeling: Attachment C3-4: Barrier Island Model Development (BIMODE)*. Tech. rep. Coastal Protection and Restoration Authority, 2017, pp. 1–128.

[42] A. Quiquerez, P. Allemand, G. Dromart and J.-P. Garcia. 'Impact of storms on mixed carbonate and siliciclastic shelves: insights from combined diffusive and fluid-flow transport stratigraphic forward model'. In: *Basin Research* 16 (4 2004), pp. 431–449. ISSN: 0950-091X. DOI: https://doi.org/10.1111/j.1365-2117.2004.00247.x.

[43] D. M. Tetzlaff. 'Modelling Coastal Sedimentation through Geologic Time'. In: *Journal of Coastal Research* 21 (3 (213) May 2005), pp. 610–617. ISSN: 0749-0208. DOI: 10.2112/04-704A.1.

[44] X. D. Meijer. 'Modelling the drainage evolution of a river–shelf system forced by Quaternary glacio-eustasy'. In: *Basin Research* 14 (3 Sept. 2002), pp. 361–377. ISSN: 0950-091X. DOI: 10.1046/j.1365-2117.2002.00187.x.

[45] I. Csato, D. Granjeon, O. Catuneanu and G. Baum. 'A three-dimensional stratigraphic model for the Messinian crisis in the Pannonian Basin, eastern Hungary'. In: *Basin Research* 25 (2 2013), pp. 121–148. DOI: 10.1111/j.1365-2117.2012.00553.x.

[46] D. Granjeon and P. Joseph. 'Concepts and Applications of A 3-D Multiple Lithology, Diffusive Model in Stratigraphic Modeling'. In: *Numerical Experiments in Stratigraphy⟨subtitle⟩Recent Advances in Stratigraphic and Sedimentologic Computer Simulations⟨/subtitle⟩* (Oct. 1999). DOI: 10.2110/PEC.99.62.0197.

[47] X. Yin, S. Lu, K. Liu, S. Jiang and B. Sun. 'Non-uniform subsidence and its control on the temporal-spatial evolution of the black shale of the Early Silurian Longmaxi Formation in the western Yangtze Block, South China'. In: *Marine and Petroleum Geology* 98 (2018), pp. 881–889. DOI: 10.1016/j.marpetgeo.2018.05.011.

[48] A. Balázs, D. Granjeon, L. Matenco, O. Sztanó and S. Cloetingh. 'Tectonic and Climatic Controls on Asymmetric Half-Graben Sedimentation: Inferences From 3-D Numerical Modeling'. In: *Tectonics* 36 (10 2017), pp. 2123–2141. DOI: 10.1002/2017TC004647.

[49] C. Griffiths. *Sedsim Stratigraphic Forward Modelling*. 2003.

[50] P. Martinez and J. Harbaugh. 'Simulating Nearshore Environments'. In: *Computer Methods in Geosciences*. Vol. 12. 1993, pp. 1–265.

[51] C. Griffiths and E. Paraschivoiu. 'Three-Dimensional Forward Stratigraphic Modelling of Early Cretaceous Sedimentation on the Leveque and Yampi Shelves, Browse Basin'. In: *The APPEA Journal* 38 (1 1998), pp. 147–158. ISSN: 1326-4966. DOI: 10.1071/AJ97008.

[52] D. Tetzlaff, J. Tveiten, P. Salomonsen, A. Christ, W. Athmer, H. Borgos, L. Sonneland, C. Martinez and M. Raggio. 'Geologic Process Modeling'. In: *IX Conference of Hydrocarbon Exploration and Development*. Oct. 2014.

[53]   F. Li, C. Dyt and C. Griffiths. '3D modelling of flexural isostatic deformation'. In: *Computers & Geosciences* 30 (9-10 Nov. 2004), pp. 1105–1115. ISSN: 00983004. DOI: 10.1016/j.cageo.2004.08.005.

[54]   F. Li, C. Dyt and C. Griffiths. 'Multigrain sedimentation/erosion model based on cross-shore equilibrium sediment distribution: Application to nourishment design'. In: *Estuarine, Coastal and Shelf Science* 67 (4 May 2006), pp. 664–672. ISSN: 02727714. DOI: 10.1016/j.ecss.2006.01.006.

[55]   T. Salles, E. Marchès, C. Dyt, C. Griffiths, V. Hanquiez and T. Mulder. 'Simulation of the interactions between gravity processes and contour currents on the Algarve Margin (South Portugal) using the stratigraphic forward model Sedsim'. In: *Sedimentary Geology* 229 (3 Aug. 2010), pp. 95–109. ISSN: 00370738. DOI: 10.1016/j.sedgeo.2009.05.007.

[56]   J. Storms. 'Event-based stratigraphic simulation of wave-dominated shallow-marine environments'. In: *Marine Geology* 199 (1-2 2003), pp. 83–100. DOI: 10.1016/S0025-3227(03)00144-0.

[57]   J. Storms and D. Swift. 'Shallow-marine sequences as the building blocks of stratigraphy: Insights from numerical modelling'. In: *Basin Research* 15 (3 2003), pp. 287–303. DOI: 10.1046/j.1365-2117.2003.00207.x.

[58]   K. Charvin, G. J. Hampson, K. L. Gallagher, J. E. Storms and R. Labourdette. 'Characterization of Controls on High-Resolution Stratigraphic Architecture in Wave-Dominated Shoreface–Shelf Parasequences Using Inverse Numerical Modeling'. In: *Journal of Sedimentary Research* 81 (8 Aug. 2011), pp. 562–578. ISSN: 1527-1404. DOI: 10.2110/JSR.2011.48.

[59]   J. Storms and G. Hampson. 'Mechanisms for forming discontinuity surfaces within shoreface-shelf parasequences: Sea level, sediment supply, or wave regime?' In: *Journal of Sedimentary Research* 75 (1 2005), pp. 67–81. DOI: 10.2110/jsr.2005.007.

[60]   G. Rongier, J. E. Storms and A. Cuesta-Cano. *pyBarSim*. 2023.

[61]   D. C. Beard and P. K. Weyl. 'Influence of Texture on Porosity and Permeability of Unconsolidated Sand'. In: *AAPG Bulletin* 57 (2 Feb. 1973), pp. 349–369. ISSN: 0149-1423. DOI: 10.1306/819A4272-16C5-11D7-8645000102C1865D.

4

Discretization of small-scale, stratigraphic heterogeneities and its impact on the seismic response: lessons from the application of process-based modelling.

Andrea Cuesta Cano, A. Karimzadanzabi, J.E.A. Storms, G. Rongier, D.J. Verschuur and A. W. Martinius

Reducing the uncertainty of reservoir characterisation requires to better identify the small-scale structures of the subsurface from the available data. Studying the seismic response of metre-scale, stratigraphic heterogeneities typically relies on the generation of reservoir models based on outcrop examples and their forward seismic modelling. To bridge geological information and seismic modelling, these methods allocate values of acoustic properties, such as mass-density and P-wave velocity, according to discretised properties like layer-type lithology or facies units.

This strategy matches the current workflow in seismic data inversion in industry, where modelling workflows are based on lithofacies distributions. However, from stratigraphic modelling, we know that metre-scale heterogeneities occur within certain facies and lithologies.

Here, we evaluate the difference on the seismic response between allocating acoustic properties in a grain-size-based, semi-continuous manner versus discretised manners based on lithology and facies classifications. To do so, we generate a reference geological simulation that we populate with acoustic properties, mass-density and P-wave velocity, using three different strategies: (1) based on grain-size distribution, (2) based on facies distribution, and (3) based on lithology. The method we propose includes the generation of realistic geological simulations based on stratigraphic modelling and the transformation of its output into acoustic properties, honouring the intra-lithology and intra-facies, small-scale structures. We, then, generate seismic data by applying a forward seismic modelling workflow. The synthetic data show that the grain size-based simulation allows the identification of small-scale, stratigraphic heterogeneities, such as beds with strong density and velocity contrasts. These stratigraphic structures are smoothed or may completely disappear in the facies and lithology discretised simulations and, therefore, not (well) represented in the synthetic seismic data.

Recognising metre-scale, stratigraphic heterogeneities is relevant for the characterisation of the fluid flow in the reservoir. However, current discrete and lithology-based strategies in seismic inversion are not able to resolve such heterogeneities, because real subsurface properties are not discrete properties, but continuous, unless there are stratigraphic discontinuities such as erosional surfaces or faults. This research works towards a better understanding of the relationship between changes in these continuous properties and the observed seismic data, by introducing greater complexity into the discretised geological simulations. Here, we use synthetic seismic images with the goal of eventually aiding in fine-tuning seismic inversion methodologies applied to real seismic data. One pathway is to foster the development of inversion approaches than can leverage stratigraphic modelling to get stronger geological priors, and replace the standard but inadequate multigaussian prior.

4.1. Introduction

Understanding multiscale, spatial sedimentary and stratigraphic architecture of reservoirs and the variability of associated discrete and continuous properties is crucial for the advancement of subsurface projects, such as storing CO_2 or H_2, groundwater or exploring for mineral resources [2, 3]. One of main techniques to study the subsurface and the structures herein is seismic reflection data acquisition. The resolution of seismic data is controlled by two main factors that define the size of the observable structures: the frequency of acquisition and the depth of the reservoir to be characterised [4]. Under perfect conditions, the vertical resolution is one fourth of the wavelength, which depends on the average velocity of the rocks and the acquisition frequency. However, the wavelength increases with depth due to attenuation processes, which means that the vertical resolution decreases [4, 5]. The lateral resolution is also a function of depth and wavelength [5, 6]. Considering that stratigraphic heterogeneities, both discrete and continuous, occur at spatial scales ranging from millimetres to 10th of metres, heterogeneities will be present below the vertical seismic resolution [7–9]. Examples of discrete heterogeneities include channels encased in fine-grained deposits or the stacking of different depositional facies (a facies is a rock type deposited under particular environmental conditions and that, therefore, has similar lithological characteristics such as a gradational porosity change). Examples of continuous heterogeneities, and the focus of this paper, include gradual changes in grain size distribution and, thus, porosity. These features cannot always be interpreted on seismic reflection data, even though they affect subsurface fluid flow [10–13].

Seismic forward modelling tools have been used to better understand the seismic response of metre-scale, stratigraphic heterogeneities that are close to the resolution limits of seismic data [14–21]. These studies mainly focus on analysing the seismic response of heterogeneities of deep-water channel and lobe deposits [9, 22, 23] and deltaic clinoform geometries [7, 24–26]. The typical workflow combines collecting outcrop data (architecture, lithology and/or facies) for the purpose of creating a geological model of the outcrop and, subsequently, convert this model into synthetic seismograms, often deploying different seismic frequencies [18, 22, 23, 26, 27]. Thereafter, the outcrop-based synthetic seismic model is used to inform and improve the construction of a subsurface reservoir model.

An essential step in forward seismic modelling is to populate a geological reservoir model with petrophysical and acoustic properties (mass-density and P-wave velocity). In addition, also S-wave velocity needs to be defined in case of full elastic seismic modelling. Most commonly, those properties come from measurements in the borehole and from core plugs [15, 18, 20, 28–30]. Other studies developed and applied experimental equations that relate shale volume, density, porosity or clay content to calculate acoustic properties [14, 22, 27, 31, 32]. No matter whether core or experimental data are used, these studies allocate only one value of each property to all the cells of the model with the same lithology or facies [15, 18, 23, 27,

30]. The allocation of single values matches with the workflows applied in seismic data inversion, where constant values are used to simplify geological modelling [33–36].

However, relying upon outcrop data and the allocation of single property values per lithology or facies for the analysis of small-scale heterogeneities poses two challenges. First, the number of good-quality outcrops, laterally extensive and that allow 3D observation is limited, and so it is the variability of heterogeneities that is represented on them. And second, continuous, sedimentological and petrophysical properties, such as grain size or porosity, vary within the same lithology and facies [10]. Therefore, allocating a single property value to individual lithology/facies might not honour the internal variability within certain facies and lithologies.

This paper evaluates the impact on the seismic response of allocating petrophysical and acoustic properties based on a continuous property, such as grain size, and, consequently, considering the internal variations within different facies and lithologies. We compare the results to the seismic response that allocating the properties based on lithology and facies produces. Using lithology and facies represent coarser discretisation levels, and, as previously mentioned, is the common strategy to populate geological models. For this purpose, we have designed a method that does not depend on outcrop data for the generation of the geological models, but on stratigraphic modelling tools, and that handles the allocation of petrophysical and acoustic properties beyond lithology/facies resolution and based on grain size distribution.

We focus on metre-scale heterogeneities, here referred as small-scale heterogeneities, present in a 2D simulation of a wave-dominated shallow marine system. Wave-dominated shallow marine systems are characterised by clean sand and gravel, often well sorted and abraded [37], and have been targeted in the subsurface because of their promising reservoir potential [38–41]. Metre-scale heterogeneities in wave-dominated systems are associated with (1) erosional surfaces and abrupt or gradual transitions between diverse lithologies [42], and (2) gradual rock property changes, including porosity [43–45]. The formation of such heterogeneities and the processes of deposition, transport and erosion that control their formation is understood and can be predicted, as they are based on sedimentological processes that were previously studied. In the case of wave-dominated shoreface environments, we refer to Kumar and Sanders [46], Field and Roy [47], Madsen [48], Swift, S. and Thorne [49], Keen *et al.* [50], Anthony [51], Backstrom *et al.* [52], Anthony and Aagaard [53] and Mitchell and Zhao [54]. This knowledge is the basis for focused stratigraphic modelling tools that simulate the sedimentological processes to generate synthetic stratigraphy. Some of these tools also include the modelling of processes from wave-dominated shoreface environments [55–60]. For our research, we base the stratigraphic modelling on the tool presented by Storms *et al.* [56].

Stratigraphic modelling tools have been previously used in combination with forward

stratigraphic modelling to evaluate the influence of sedimentary processes at basin and sub-basin scale In this paper, we explore the impact on the seismic response of assigning acoustic properties based on different levels of discretisation. To do so, we define a workflow based on stratigraphic forward modelling to create a synthetic geological simulation, at a cell-size of $2x2m$, that we will use as reference model for our research. Each cell includes information about grain size, facies, and lithology. These three data types are used to generate three different scenarios, where the distribution of acoustic properties, mass-density and P-wave velocity, depend on different data types. The distribution based on grain size includes the greater level of detail, while the lithology-based represents the greatest discretisation level. By applying numerical seismic modelling and inversion, we obtain synthetic seismic data for each scenario. The observations on the seismic data demonstrate that some of the stratigraphic heterogeneities of our simulation can be still observed in the grain-size based scenario, while they are vaguely represented or, even, erased for the lithology- and facies-based discretisation scenarios.

4.2. Methodology: from stratigraphic modelling to synthetic seismic data

Because we limit ourselves to wave-dominated shoreface models, we can assume our geologic structures to have a so-called 2.5D characteristic, meaning that we do not expect large variations in the along-shore direction. Therefore, we can limit our studies to 2D cross-sections of the models. In addition, this paper aims in demonstrating the effect of transferring the detailed geologic models to a discretized version suitable for seismic data analysis. Although the Earth – of course – is an elastic medium, we limit ourselves to the recording of P-wave data via a water layer that is put on top of our subsurface models. In addition, we mainly look at the structural seismic images, therefore, we can limit ourselves with acoustic seismic data modelling, neglecting the effect of S-wave velocity variations as well as S-waves in the seismic measurements.

The method we apply to evaluate the impact on the seismic data of the discretisation of small-scale, stratigraphic heterogeneities is based on three steps (Figure 4.1). The first step is the use of a stratigraphic modelling tool to create a 2D geological simulation that includes architectural features at different scales. The output includes grain size distribution (ratio of every grain size class and mean grain size), lithology, and facies data for each grid cell. The second step consists of converting the grain size distribution data into acoustic parameters – mass-density, and P-wave velocity. Finally, we perform seismic forward modelling followed by migration to generate a structural seismic image. Since we sum the contribution of all angles into a single structural image, angle-dependent imaging is not directly highlighted.
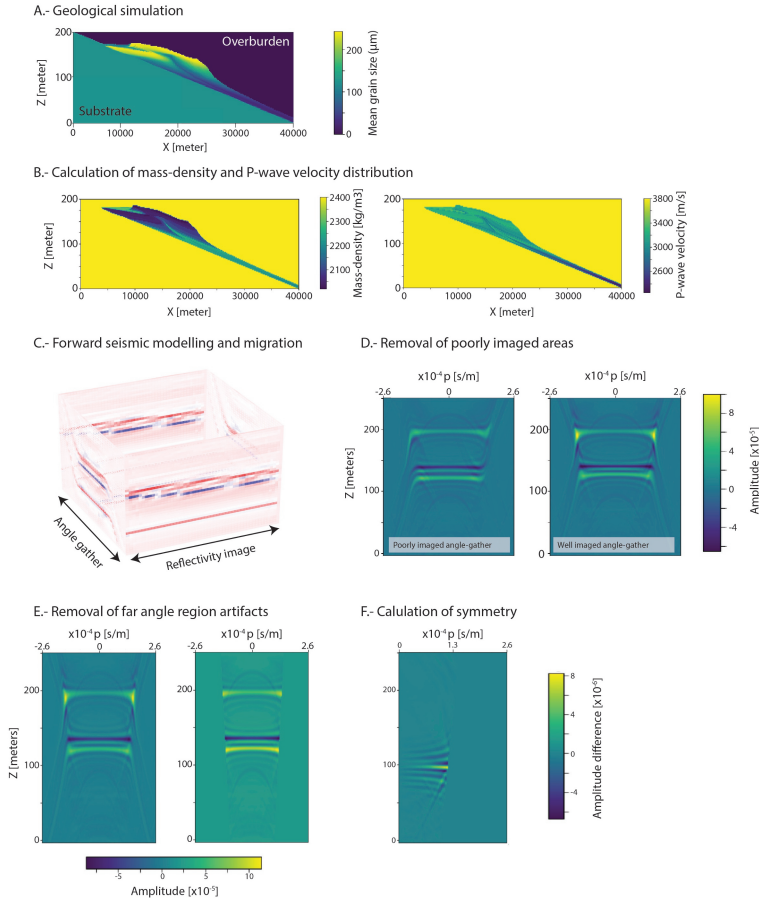
Figure 4.1: Methodology to generate the synthetic seismic data, composed of three steps. Step 1 (blue) is the generation of geological simulations. Step 2 (yellow) is the processes to populate the simulations with acoustic parameters – mass-density, and P-wave velocity– based on grain size distribution. Step 3 (green) consists of the application of seismic forward modelling techniques and migration to obtain the seismic subsurface image. The final output is the seismic image.

4.2.1. Step 1: Generation of geological simulations using stratigraphic modelling tools

Forward stratigraphic modelling (FSM) mimics the processes of erosion and deposition we observe in nature to distribute sediment and create synthetic stratigraphic architectures. Compared to other modelling tools (see [61] for more details on this topic), FSM has two main advantages: (1) it mimics the rules of physics and hydrodynamics that result in patterns of deposition that follow Walthers'

law; (2) it deals with the issue of preservation potential, where erosion will remove part of the strata in a predictable manner.

There are many different FSM tools available with various degrees of complexity and accessibility [61]. For this study, we defined three requirements that the FSM tool must meet. First, the FSM tool must be able to simulate the formation of sedimentary heterogeneities at metre scale, in the vertical direction, and in the order of tens of metres in the horizontal direction. Secondly, the FSM tool must have a low computational cost, allowing the generation of several scenarios within limited run-time on a laptop/desktop machine. Third, the FSM tool should provide grain size distribution data or sediment grain size proportion as output, because the acoustic property allocation procedure is based on grain size, as explained in the following subsection. Preferably, the FSM tool should also be open-source, so the code can be adapted to fit the workflow.

BarSim, a process-response approach that simulates the long-term coastal evolution and stratigraphic architecture through time of wave-dominated coastal systems [56, 57, 62], meets all those requirements. This model is based on a simple approximation of a 2D cross-shore profile and simulates the deposition of individual storm beds, with thickness values that go down to the centimetre scale [57, 62]. BarSim applies mass conservation principles to erosion, transport, and deposition of multiple grain size classes along a 2D profile at surface conditions [57, 62, 63]. This means that sediment that is eroded at any location on the shoreface due to the action of waves is transported and deposited at other locations in the 2D profile, where accommodation is available. Sediment input into and out of the model occurs as along-shore transport, which is defined as net sediment input by the user [63].

The input variables are (1) model parameters controlling sediment erosion, transport, and deposition(wave efficiency, rate of erosion, characteristic travel distances), (2) time-dependent variables (sea level, sediment budget), (3) and variables that define the base conditions (grain size distributions, littoral drift, wave-base depth, substrate slope) [56]. The time-dependent variables and the variables that define the base conditions of the model can be modified to create a variety of outputs. The output includes sedimentological information (fraction of the different grain size classes, mean grain size, sorting, facies) for all the grid cells [64].

We use an implementation of BarSim, called pyBarSim, to generate the geological simulations [65]. pyBarsim is a recently-developed Python package, which speeds up the simulation process. This package also allows the interpolation of the simulated sediment layers onto a regular grid.

For this study, lithology is derived from the grain size distributions. To do so, we assume that the simulation is solely composed of quartz grains. The cells are labelled as siltstone or sandstone based on the proportion of the different grain size classes. For our set-up, when the grain size classes corresponding to 5 and $50\mu m$ show a proportion of 50% or higher, the cell is identified as siltstone [66–68]. The

cells for which the proportion is under 50% are defined as sandstone.

At the end of this step, every cell of the grid has three associated properties: grain size distribution (as proportion of each grain size class), facies (as a label), and lithology (as a label).

4.2.2. Step 2: Population of acoustic property values

From the geological simulations, we obtain, for each cell, grain size distributions at surface conditions. In step two, we will transform that data into acoustic properties (mass-density and P-wave velocity) at certain depth. During this transformation, we will use intermediate parameters such as sorting, initial porosity, and final porosity.

Firstly, the sorting is calculated as a weighted standard deviation of the grain size distribution. Then, we use the relationships from Friedman [69] to convert the sorting parameter from standard deviation to Trask coefficients [70]. With mean grain size and sorting distribution we can assign initial porosity, following empirical relationships described in literature [71–74]. To do so, we apply an interpolation to each cell based on the relationship between initial porosity, mean grain size, and sorting reported by Beard and Weyl [73] for wet, unconsolidated mixtures. Lastly, we define the overburden and calculate the final porosity. To calculate the final porosity a porosity loss function is applied, following the trends defined in the look-up table from SedSim [59, 75] based on Wendebourg and Harbaugh [74].

Once the final porosity value is obtained, density is calculated under two assumptions: (1) the grains are pure quartz, and (2) the porosity is water saturated. For the calculation of P-wave velocity, the empirical equation proposed by Eberhart-Phillips, Han and Zoback [32] is used:

$$V_p(km/s) = 5.77 - 6.94\phi - 1.73\sqrt{C} + 0.446(P_e - e^{(-16.7P_e)}) \qquad (4.1)$$

where φ is porosity (dimensionless), C is clay content (dimensionless), and Pe is effective pressure ($kbar$). The resulting P-wave velocity is in km/s. The clay content is directly obtained from the grain size distribution produced by pyBarSim. The effective pressure is user-defined and it must match the characteristics of the applied overburden.

Following this method, we can create simulations where the acoustic properties are derived from grain size distribution. To populate the facies-based and lithology-based simulations, we extract the acoustic property values for each facies/lithology class and we calculate the average. The resulting average value is, then, assigned to all the cells with the same label. This way, we ensure that the values from the grain size-, facies-, and lithology-based simulations are related to each other.

4.2.3. Step 3: Forward seismic modelling and migration

Forward seismic modelling: finite difference approach

Using geological models that capture the physical properties of the subsurface to replicate seismic field experiments is known as forward numerical modelling of seismic data. Several forward modelling techniques are available, and choosing one is based on a balance between model complexity, accuracy, and computing time. Two of the most popular approaches are the ray and wave-equation methods. Ray methods rely on the decomposition of the seismic wavefield into independent elementary waves that propagate along rays [76]. The rays are resolved individually, which simplifies the calculations. Ray tracing methods provide solutions that are accurate within a localized region or along specific ray paths, rather than globally across the entire model. Consequently, ray methods struggle to handle strong and small-scale velocity variation in the medium [77–79]. Wave equations do not have the same limitation, as they approach the propagation problem over the entire model as a numerical solution of partial differential equations [79, 80]. Therefore, wave equations are able to resolve accurate travel-times and amplitudes even in complex media [79].

Within wave propagation approaches, the finite-difference, time-domain method is a robust numerical approach with a strong ability to model seismograms even in complex and heterogeneous media [81]. This method is used to create the synthetic seismograms for this paper due to the stratigraphical complexity that the simulations display. Finite-difference techniques can incorporate all wave phenomena, including multiples, and diffractions, and they offer precise numerical solutions [82]. The only constraint on finite difference methods is the computing time [83].

In finite-difference techniques, seismic wave equations are represented as partial differential equations with spatial and temporal derivatives that are used to explain seismic wave propagation in the subsurface. As an example, one-dimensional acoustic wave propagation is represented by:

$$\frac{\partial^2 p(x,t)}{\partial x^2} = \frac{1}{v^2}\frac{\partial^2 p(x,t)}{\partial t^2} \tag{4.2}$$

where p and v are wavefield pressure and propagation velocity, respectively, x is distance, and t is time. To calculate temporal derivatives, one often uses the 2nd-order finite difference. And by considering the pressure wave-field to be a function of grid size and time-step, respectively shown by Δx and Δt, the equation expands as follows (Eq.3):

$$\frac{\partial^2 p(x,t)}{\partial t^2} = \lim_{\tau \to 0} \frac{p_{j,m-1} - 2p_{j,m} + p_{j,m+1}}{\Delta t^2} \tag{4.3}$$

where j and m represent grid number in both directions, such that $p_{j,m} \equiv p(j\Delta x, m\Delta t)$.

For a spatial derivative, which will require the wavefield values at the current grid cell and its two neighbouring cells, at a given time step, an equation akin to Eq.3 can also be constructed. A graphical representation of such scenario can be found in Liu and Sen [80]. We can create a recursion formula for solving the 1D wave equation inserting Eq.4.3 into Eq.4.2 and substituting a (2N)th-order finite difference formula for the 2nd-order spatial derivative and rearranging that to

$$p_{j,m+1} = 2p_{j,m} - p_{j,m-1} + \frac{\Delta t^2 v^2}{\Delta x^2} \left[c_0 p_{j,m} + \sum_{n=1}^{N} c_n \left(p_{j-n,m} + p_{j+n,m} \right) \right]. \tag{4.4}$$

The wave field values at two successive time steps, $t = 0$ and $t = \Delta t$, are known at the start of the recursion. The final equation (Eq.4.4) is used to calculate the wavefield values at each spatial location at a future time step. After the calculation of the wavefield, values at each spatial location for a future time step, the finite-difference time-domain (FDTD) method continues iteratively, advancing the solution through time to simulate the entire seismic wave propagation $p_{j,m}$.

Note that for the FDTD modelling in this paper, we use the 2D acoustic wave equation, where pressure is a function of space and depth, and also density variations are taken into account. In FDTD, receivers are strategically placed within the model to capture the seismic wavefield at specific locations as the waves propagate through the subsurface. These receivers record the time-dependent wavefield values, which are used to construct synthetic seismograms.

Full-wavefield migration in angle-dependent mode

In the following step, the output from the seismic modelling is migrated to construct the final reflectivity image. Figure 4.2 represents the block diagram for the full-wavefield migration (FWM) that we apply here following Davydenko and Verschuur [84]. This inversion scheme consists of different blocks of data comparison, adjoint forward model, model update and the forward operator. In the data comparison, the modelled data and the measured data are being compared. In the adjoint forward model, this procedure translates the residual from the data domain to the model domain and generates the model update. In the next block of model update, the model space is refreshed by scaling the update computed in the previous step and adding it to the current model. Finally, the forward model

computes new data using the updated model space, which is then used for the subsequent iteration of data comparison [84].

The primary feature of this FWM method is its forward model, which generates comprehensive reflection data [85]. This imaging process benefits from the inversion-based approach. Additionally, its forward model can incorporate angle-dependent reflection information. To achieve such goal, the imaging at each depth level should be carried out in angle-dependent mode: for every lateral location, the down going wavefield should be cross-correlated with a back-propagated residual that is shifted in space by several spatial lags, creating a spatial reflectivity operator for each grid point in the image domain. Subsequently, a 2D Radon transformation is applied to each reflectivity operator, decomposing the spatial reflectivity operator into reflection properties per angle of incidence. After the FWM-angle dependency generates the image-angle gathers for all lateral locations, the information is summed along the angle axis. This results in a structural reflectivity image created from all angles of incidence, thereby enhancing the overall image information [84]. Such method differs from the conventional FWM, which does not leverage spatial lag and Radon transformation and results in the final image primarily reflecting information from normal incidents [84].
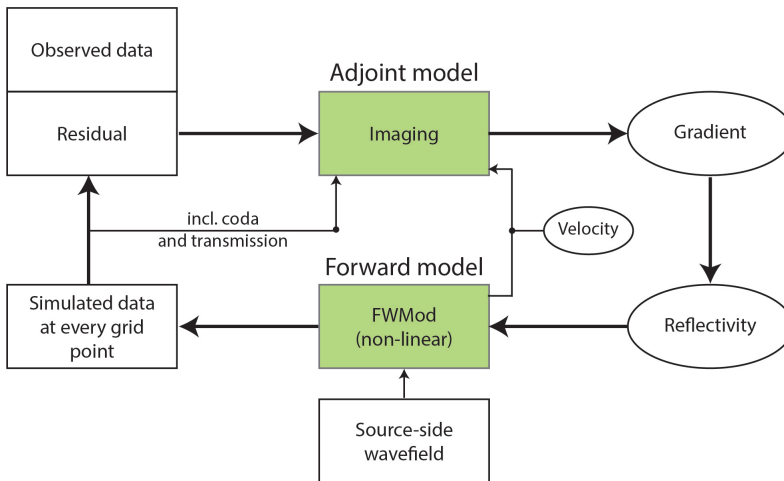

Figure 4.2: Schematic representation of the full-wavefield migration method. Adapted from Davydenko and Verschuur [84]

4.3. Modelling

4.3.1. Reference geological simulation

We perform the forward stratigraphic modelling using pyBarSim to generate a 2D reference geological simulation that will be used throughout this study. This simulation records the sedimentation and synthetic stratigraphy for a system with four grain size classes ($250\mu m$, $125\mu m$, $50\mu m$, $5\mu m$) and that experiences a relative sea level fall, rise and fall. The simulation results in a target structure that is $40000m$ long and $200m$ thick. The grid cell is $2x2m$ to capture the stratigraphic heterogeneities within each facies and lithology. We added $100m$ of underburden and $1100m$ of overburden, including a 100 m-thick seawater layer on top. Cells have been added to each side of the simulation, equivalent to $2500m$ in each case, to ensure adequate illumination of every part of the target area during the forward seismic modelling.

The output of the forward stratigraphic modelling includes facies distribution (Figure 4.3A), grain size distribution (in Figure 4.3B represented as mean grain size), and lithology distribution (Figure 4.3C), all of them including only part of the overburden . Within the facies distribution (Figure 4.3A), we identify six different facies based on depositional environment: lagoon, barrier island, upper shoreface, lower shoreface, and offshore. The outputs related to the grain size distribution include the ratio per cell of each grain size class and the mean grain size (Figure 4.3B). For this simulation, there are four grain size classes. The finest, simulated grain size class is $5\mu m$, corresponding to fine silt. The coarsest grain size class is $250\mu m$, corresponding to the limit between medium and fine sand. Thus, the lithology distribution includes three labels (Figure 4.3C): sandstone, siltstone, and underburden and overburden together.

These three outputs - grain size, facies, and lithology - are used to create different distributions of mass-density and P-wave velocity at different levels of discretisation. The most detailed labels are those of grain size-based simulation, with unique values for every cell of $2x2m$. A more discretised property distribution is based on the facies distribution, with five labels within the simulation. The greatest level of discretisation is achieved when using the lithology for the distribution of petrophysical and acoustic properties, with two labels within the simulation. The acoustic property distribution method is described in subsection 4.2.2. Table 4.1 includes the average values of mass-density and P-wave velocity calculated for each lithology and facies label. The resulting P-wave velocity and mass-density distributions are displayed on Figure 4.4.

The properties of the overburden and underburden are the same for the three simulations.

Due to computational limitations, the reference simulation of over $40km$ on the

horizontal dimension had to be divided into segments. 7 segments of $7600m$ and a smaller 8th segment were created. To ensure the full imaging of all the areas on the simulation, there is an overlap of $1800m$ between segments.
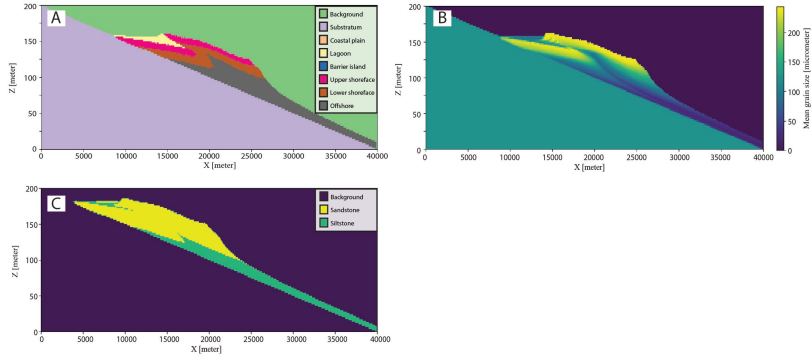

Figure 4.3: Reference geological simulation generated by pyBarSim. The output files include the facies distribution (A), mean grain size (B), and lithology distribution (C). Lithology is assigned applying the conditions described in subsection 4.2.1. Z indicates the thickness of the simulated reservoir model and X, the lateral extent. Here, only a partial part of the overburden is included, to better appreciate the small-scale, stratigraphic heterogeneities.

Label	Mass-density (kg/m^3)	P-wave velocity (m/s)
Lithology		
Sandstone	2078	3149
Siltstone	2226	2937
Facies		
Lagoon	2225	3199
Barrier island	2035	3123
Upper shoreface	2047	3146
Lower shoreface	2084	3164
Offshore	2205	2984

Table 4.1: Average values of mass-density (kg/m^3) and P-wave velocity (m/s) calculated based on the grain size-based simulation for all the categories within the lithology and facies simulations. All grid cells of the grain size-based simulation have a lithology and a facies label. By considering all the cells with the same label, the average mass-density and P-wave velocity values are calculated.
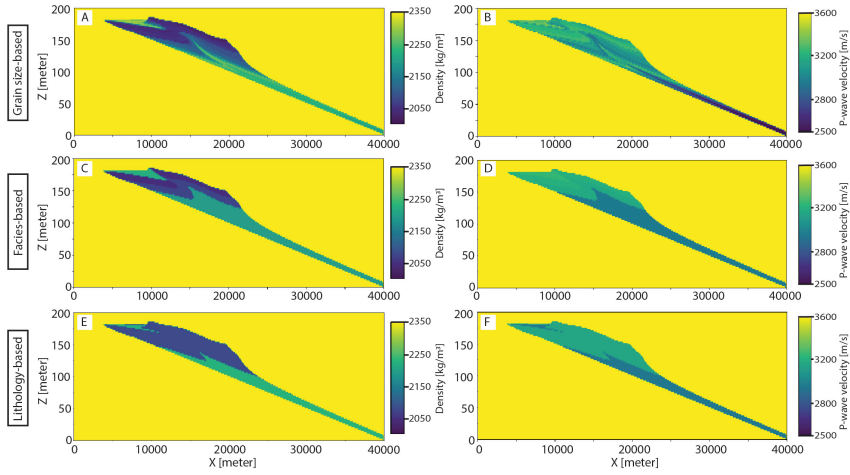
Figure 4.4: Mass-density (kg/m^3) and P-wave velocity (m/s) distributions for the simulations: grain size distribution-based, method (A - mass-density; B – P-wave velocity), facies-based discretised (C – mass-density; D – P-wave velocity), and lithology-based discretised (E – mass-density; F – P-wave velocity). Note that the same colour scale has been used for all the subfigures of the same property. Z indicates the thickness of the simulation and X, the lateral extent, both in m. Note that only part of the overburden is included in the figure.

4.3.2. Input parameters for forward seismic modelling and migration

Once the P-wave velocity and mass-density simulations are obtained, the time-domain finite difference method, based on first-order acoustic wave equations, as explained in subsection 4.2.3, is used for forward modelling, including the target area and the full overburden. The source wavelet is a Ricker source. For the data acquisition plan, we employ a fixed spread scheme: all receivers are positioned at the surface, covering the entire range of the model at intervals of $2m$. All sources are also positioned at the surface, covering the entire range of the model at intervals of $10m$. The time sampling rate is $0.002s$, and the recording length is $1.2s$. For the FWM-angle dependent, the source sampling and the receiver sampling are chosen as $10m$ and $2m$, respectively. The frequency range is compatible with the modelling frequency range of 5 to $150Hz$. A smooth velocity model, the maximum and minimum velocity ranges are also derived from the forward modelling velocity models to be used in the migration step. Considering the average model's velocity, and the maximum frequency used for the seismic modelling, it is our observation that the minimum layer thickness that can be distinguished in the reservoir model is $14m$.

4.4. Results and interpretation

4.4.1. P-velocity and density contrast

This section explores the difference in properties between the three simulations. On average, the mass-density values are 8% higher for the grain size-based distribution when compared to the facies-based discretisation, with the differences varying between -5% and $+10\%$. There is a greater range of variation for P-wave velocity. The mean difference in P-wave values is 3%, with higher values for the facies-based simulation. The range goes from $+23\%$ to -15%. Within the facies-based simulation, some of the labels show very similar velocity and density values (Table 4.1).

When considering the difference in mass-density values between the grain size-based distribution and the lithology-based discretisation, the mean difference is 1%, with higher values when using lithology-based discretisation. This difference varies between -9% and $+9\%$. On average, the P-wave velocity values are 6% lower for the discretised model, with a range of difference that goes from -13% to $+23\%$.

With the information about the variation of mass-density and P-wave velocity, we can calculate the expected variations in the impedance. Taking into account the average percentage difference in the case of lithology-based discretisation, the impedance variation is 11% and, for the facies-based discretisation, 7%. However, if we consider the maximum variations observed in the acoustic properties, we can expect changes in impedance of 35% for the lithology-based and 34% for the facies-based. In both cases, the resulting reflection coefficient is around 0.15.

4.4.2. Mapping the difference in seismic response

This study focuses on the most relevant differences of the seismic data between the three discretisation levels. Those differences are concentrated in two locations (Figure 4.5). The first location is associated with a high-density and high-velocity area that develops at the top left of the geologic simulation (Figure 4.5, red square). This location is partially related to the lagoon facies and it is composed of sandstone and siltstone (Figure 4.3). The second location is a stratigraphic structure composed by high-density and high-velocity sediments and that results from the increase in relative sea level (Figure 4.5, black square). This location is composed of sediments from the offshore, lower shoreface, and upper shoreface facies and it is composed of sandstone and siltstone (Figure 4.3).

With the current input parameters, in those areas where the target is thinner than $14m$, only the reflectors of the top and the bottom of the target are observed. This thickness threshold is reached in segment 6.
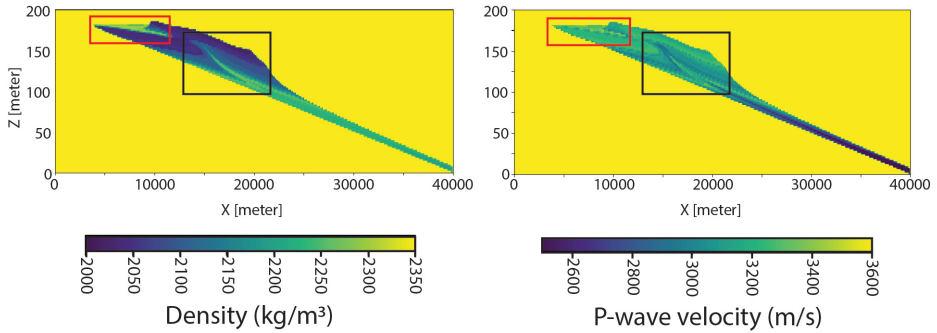
Figure 4.5: Acoustic property distribution for the grain size-based simulation showing the two areas where the main differences between discretisation levels are observed. The red square highlights location one and the black square, location two. More detailed images and analysis of the differences between discretised levels in Figures 4.6 and 4.7 and subsections 4.4.2 and 4.4.2. Note that only part of the overburden is included in the figure.

Location one

The first major contrast on seismic response is located on the upper left side of the simulation (Figure 4.5, red square). On the blowup image, we observe a high-density and high-velocity area for the grain size-based simulation (Figure 4.6A). For the facies-based simulation, the density contrast is still high, but the velocity distribution shows smooth transitions between facies. For the lithology-based simulation, there is an alternation of lower and higher density/velocity areas. These differences on the distribution of acoustic properties translate into two major distinctions on the seismic response, here labelled as zone A and zone B (Figure 4.6B).

Zone A marks the contact between the high-density, high-velocity area and an area with lower density and velocity values (Figure 4.6A). It is also related to a shift of facies and a change of lithology. But the main changes in properties occur with different property contrasts and at slightly different locations around zone A (Figure 4.6A). The particular geometry of each change affects the continuity, thickness, and amplitude values of reflection 1 (Figure 4.6B). This area develops due to the contrasting sedimentological characteristics of the lagoon (greater ratio of fine sediment) and the upper shoreface (greater ratio of coarser sediment) (Figure 4.3). As result of the implemented methodology for the allocation of acoustic properties, areas with greater proportion of fine sediments lose more porosity during compaction than areas dominated by coarser sediments, which results in higher mass-density values (Figure 4.6A).

Because the contrasting properties are associated to changes in facies, we find more similarities between the seismic response of the grain size-based and facies-based simulations (Figure 4.6B). The lithology-based simulation does not

capture this changes adequately. We also observe that the contact between upper shoreface and lagoon does not fit with the main changes in mass-density and P-wave velocity variations, which actually occur within the lagoon facies, resulting in different thickness of the reflection 1 (Figure 4.6B).

Zone B marks the variation of acoustic property values in the vertical direction throughout the simulations (Figure 4.6A). The location and the intensity of the changes on density and velocity vary from one level of discretisation to another. This translates into different thickness and amplitude values of reflection 2 and the amplitude distribution of reflection 3 (Figure 4.6B). The behaviour in amplitude values of reflection 3 is of special interest. This reflection is characterized by a very low and constant amplitude value for the whole highlighted region in the lithology-based simulation, which matches with the mass-density and P-wave velocity distributions, where the only difference is related to local cells labelled as silt, responsible to the transition from reflection 2 to 3 (Figure 4.6B). Reflection 3 is also represented by a smooth distribution of amplitude values for the facies-based simulation, with lower values towards the contact with the lowermost reflection that represents the base of the target. This smooth distribution is related to the smooth changes in P-wave velocity and mass-density, that result from applying a single, averaged value per facies (Figures 4.4 and 4.6). However, in the grain size-based simulation, the amplitude value distribution is more spotty, which relates to local changes in grain size distributions and the consequent local changes in P-wave velocity and mass-density (Figure 4.6). It is also observable that the distribution of properties within the upper and lower shoreface facies is almost as constant as in the facies-based simulation (Figures 4.3, 4.4 and 4.6).

Location two

A second significant contrast in the seismic response is located in the central part of the simulations (Figure 4.5, black square). A high-density and high-velocity area for the grain size-based simulation is located in the middle, surrounded by lower density and velocity values, that merges with a second high-density and high-velocity layer at the bottom of the simulation (Figure 4.7A). For the facies-based discretisation, both the density and velocity contrasts are high between the offshore and lower shoreface facies. For the lithology-based discretisation, there is contrast between siltstone and sandstone in density/velocity. These contrasts of acoustic properties are reflected on the seismic response of three zones (Figure 4.7B, labelled as zones C, D and E), that spread throughout almost the whole simulation. The architecture observed in the distribution of properties is related to a relative sea level rise, which forces a migration of the facies and, in general, the deposition of coarser sediments towards the land, and a following, progressive, relative sea level fall.
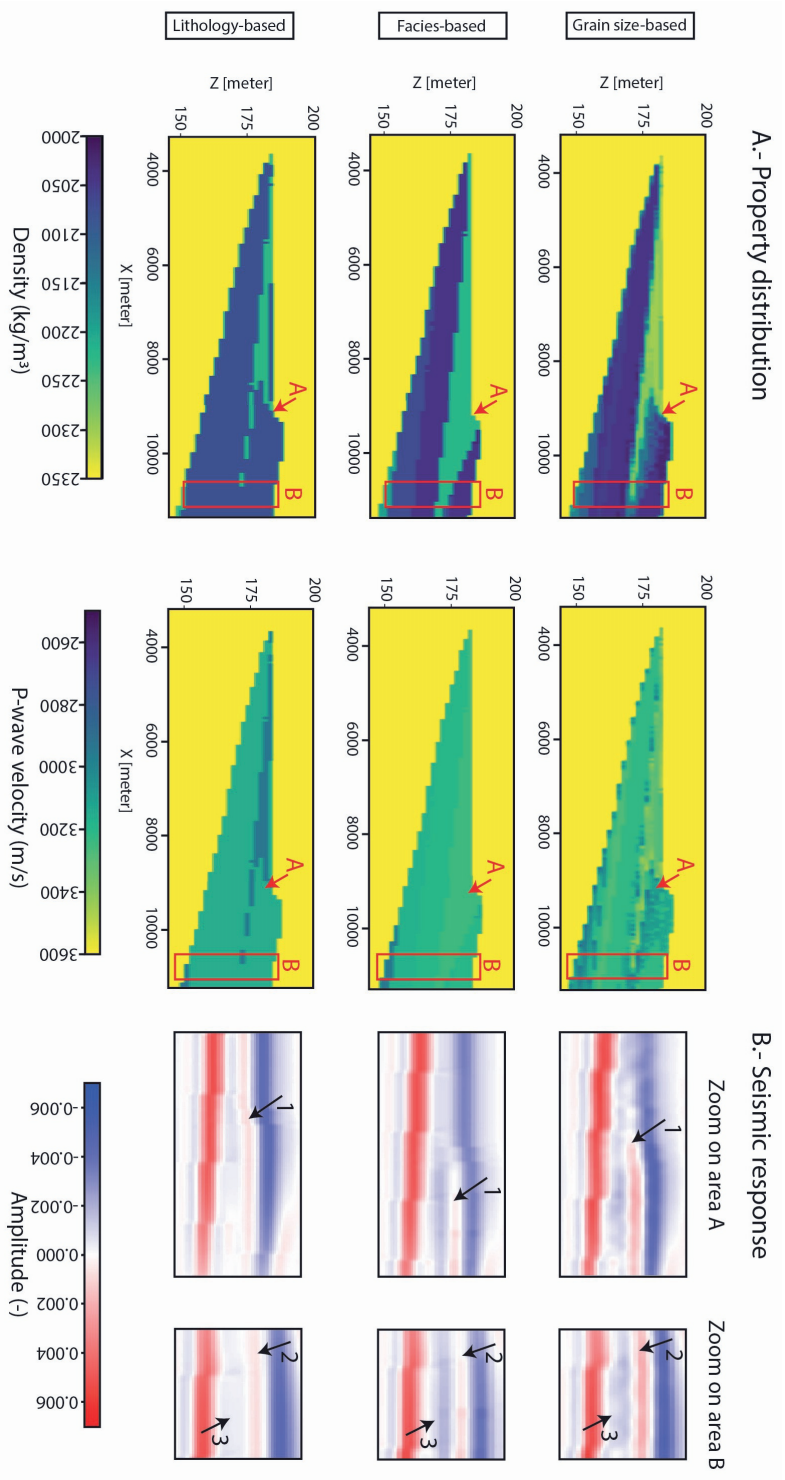
Figure 4.6: A.- Blowup of the location one indicated in Figure 4.5 with the density (kg/m^3), and P-wave velocity (m/s) distributions for each discretisation level. A and B indicate the areas where the seismic response differences are observed. B.- Blowup of the seismic response (in amplitude, unitless) of areas A and B. The main differences have been indicated with numbers from 1 to 3 to aid the comparison between simulations.

Zone C is characterised by a higher density and lower velocity layer on the grain size-based simulation (Figure 4.7A). This layer is not registered in the lithology-based discretisation, because the changes in grain size distributions do not imply a change in lithology (Figure 4.3). On the facies-based discretisation, the facies show a trend that matches with the orientation of the layer but with lower contrasts (Figure 4.7), that results from allocating averaged values of mass-density and P-wave velocity. These distinctions can also be observed on the seismic data with changes in continuity, thickness and amplitude intensity on reflection 4 and reflection 5 (Figure 4.7B). The general geometry of the layer that we observe in the grain size-based simulation is also observable on the seismic response of the facies-based simulation, where reflection 5 has a notable lateral change of the amplitude value (Figure 4.7B), but the lateral extent of the structure is not fully captured.

Zone D is characterized by two features: (a) a progressive mass-density and P-wave velocity change in the vertical direction on the grain size-based simulation; (b) the merging of the high velocity and density layer that crosses the simulation with another high velocity and density layer at the bottom of the target (Figure 4.7A). This structure is only registered as one facies change for the facies-based simulation and one lithology alternation for the lithology-based simulation (Figure 4.7A). The seismic response for the facies- and lithology-based simulations is a parallel alternation of reflections, with a slight change in the thickness and amplitude intensity, especially of reflection 7 (Figure 4.7B). When comparing to the grain size-based simulation, it is observed that the blue reflection (6 and 8), which was continuous for the other simulations, is here discontinuous and showing significant thickness variations. The seismic response is dominated by the shape and distribution of reflection 7, which represents the high density and velocity layer mentioned above. Reflection 7 also controls the thickness and continuity of the blue reflections above and below.

Zone E shows the lateral thinning of the target and the internal heterogeneity (Figure 4.7A). For the lithology- and facies-based simulations, there is only one change in lithology and one in facies, respectively. The complexity is higher for the grain size-based simulation, with the appearance of a low velocity/density area in between the high velocity and density layers mentioned in the previous paragraph (Figure 4.7A). This contrast has an impact on the continuity and geometry of reflection 9 versus the blue reflection (Figure 4.7B). The strong contrast in P-wave velocity and density registered at the bottom of the grain size-based simulation enhances the lateral continuity of the blue reflection and the merging of the two red reflections. This observation opposes the geometry of the reflections in the lithology- and facies-based simulations.
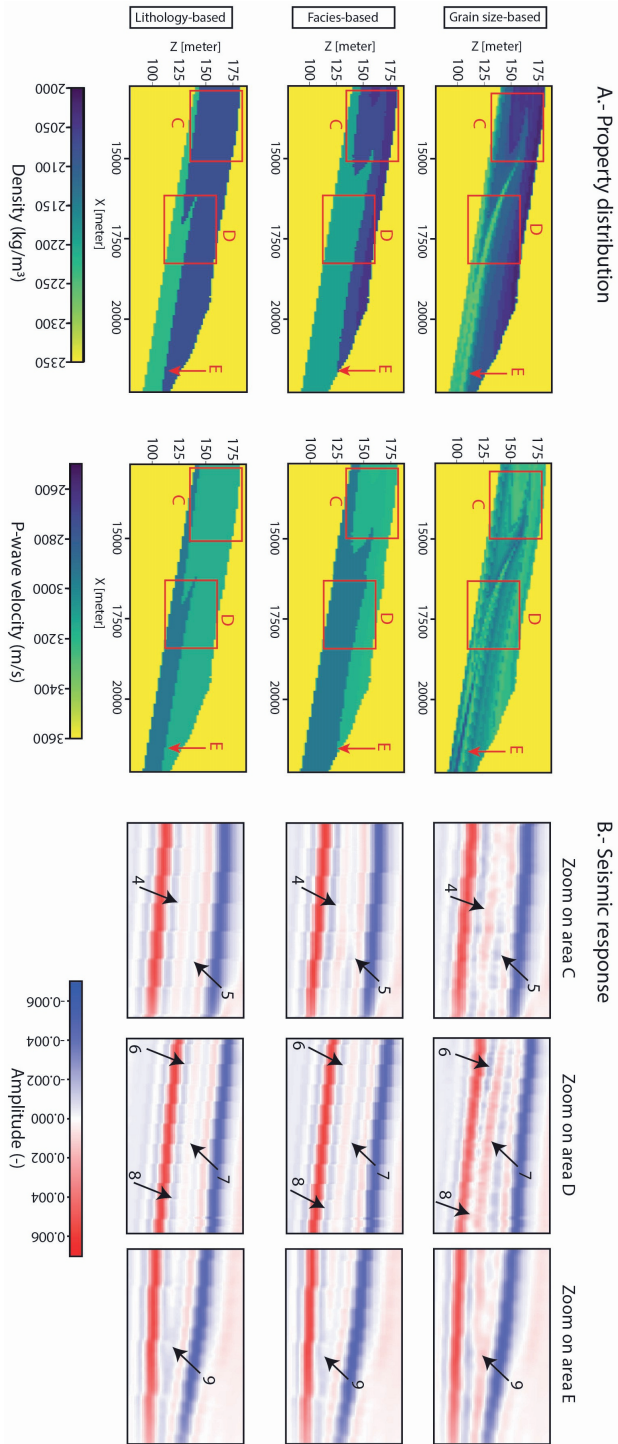
Figure 4.7: Blowup of the location two indicated in Figure 4.5 with the density (kg/m^3), and P-wave velocity (m/s) distributions for each discretisation level. C, D, and E indicate the areas where the seismic response differences are observed. B.- Blowup of the seismic response (in amplitude, unitless) of areas C, D, and E. The main differences have been indicated with numbers from 4 to 9 to aid the comparison between simulations.

4.5. Discussion

4.5.1. Gibbs' phenomenon: why are there reflections where there is no property contrast?

When spatial discontinuities occur, they require infinite frequency content to be fully characterised. But in practice, seismic measurements have a finite bandwidth, partly by the acquisition devices, but mostly due to absorption in the Earth during wave propagation [4, 86]. This limitation will cause ringing artifacts in the imaged reflectivities, leading to unwanted echoes in or edge distortion in our images [87]. The phenomenon responsible for these unwanted echoes is known as the Gibbs' Phenomenon, and occurs when a band-limited signal is reflected at a sharp contrasts, resulting in high-frequency oscillations and inaccuracies near the discontinuities.

As depicted in Figure 4.8, there are some changes in the seismic amplitude (Figure 4.8G, H, and I, black arrows) that are not link to changes in mass-density nor P-wave velocity (Figure 4.8A to F). These ringing effects will interfere with the reflections that are related to acoustic property changes (Figures 4.8A and B, and related, red arrows). Because of this interference, the change in reflection coefficients is not the sole factor influencing the generation of patterns in reflectivity images. This can pose challenges for interpretation, by giving the false impression about the existence of sublayers with contrasting acoustic properties. We only observed this phenomenon in our facies-based and lithology-based simulations.

There are several methods available to mitigate these artifacts to some extent, by imposing extra constraints or weights during the imaging process, but none of them were applied in our workflow [87, 88].

4.5.2. Impact of discretisation on the small-scale, stratigraphic heterogeneities

The data depicted in Figures 4.6 and 4.7 show that the level of discretisation has an impact on the seismic response. Creating simulations that are based on stratigraphic modelling and where the acoustic properties are assigned based on grain size distributions preserves the representation of small-scale, stratigraphic heterogeneities within specific facies or lithologies (Figures 4.6 and 4.7). Table 4.2 includes a compilation of the described zones and the specific improvements in the imaging for this specific case of wave-dominated, shoreface systems. The observed structures sometimes develop in different depositional environments and are composed of different lithologies (Figure 4.5 to 4.7). When allocating a single value to one facies/lithology, these structures are no longer represented and,

therefore, it is not possible to recognise them in the seismic response.
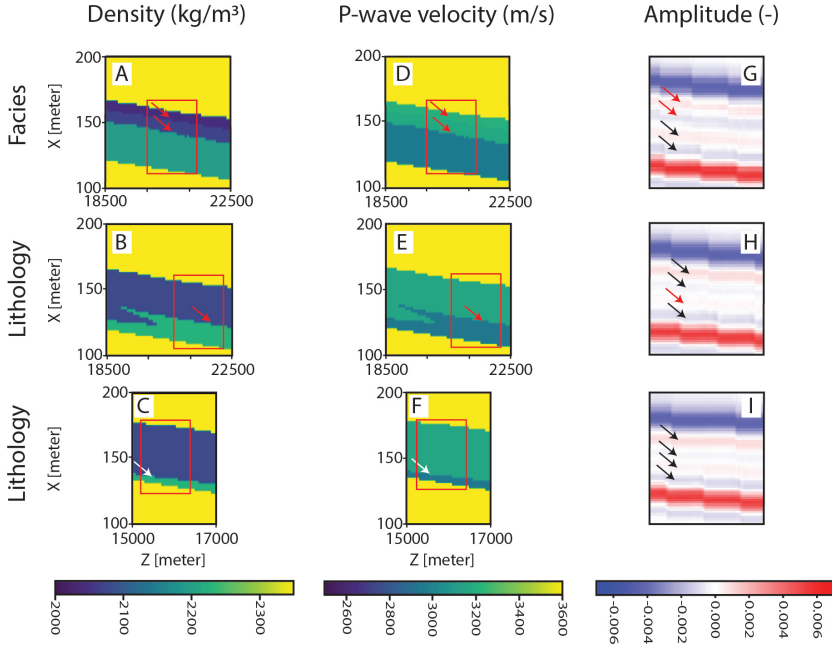

Figure 4.8: Examples of locations in our models with only one (B, C, E, F) or two (A, D) changes in acoustic properties but where four reflections (G, H, I) are generated in the synthetic seismic data (black arrows). The density (kg/m^3), P-wave velocity (m/s), and a blowup of the amplitude values of the seismic data (unitless) are included. Arrows in red indicate the changes in density and P-wave velocity (A, B, D, E) and where they can be observed in the seismic response (G, H). On the lowermost example, the change cannot be observed because the thickness of the layer is below the resolution threshold (white arrows) (C, F, I). The generation of these reflections is linked to the Gibbs' phenomenon (G,H, I).

Being able to distinguish small-scale, stratigraphic heterogeneities with strong velocity and/or density contrast and isolate their location from the surrounding sediments will help understand how the fluid flow might behave inside the reservoir. In our method, the calculation of mass-density and P-wave velocity is strongly dependent on the porosity. This means that high velocity and density layers are also characterised by lower porosity values. In grain size classes varying from silt to medium sand, lower porosity values tend to relate to lower permeability [89]. The opposite occurs with layers with high porosity values. For subsurface locations where the relationship between porosity and permeability are well understood, this method can help identify areas with higher or lower permeability values, which will behave as pathways or barriers for the fluid flow. Our method has shown that the use of stratigraphic modelling can capture the presence of these heterogeneities and they can be recognised in synthetic seismic data.

Zone	Lithology	Facies	Improvement
A	Sandstone and siltstone	Lagoon	–Accurate imaging of the contact between the high density/ velocity and the low density/velocity area within the lagoon. –Better definition of the lateral extend of the low density/velocity layer related to upper shoreface deposits.
B	Sandstone	Lagoon, upper and lower shoreface	–Better definition of the thickness of the upper shoreface area on top of the lagoon. –Detailed imaging of the density/velocity changes within the upper and lower shoreface.
C	Sandstone	Upper and lower shoreface, offshore	–Detailed definition of the structure and density/velocity variations resulting from the relative sea level rise.
D	Sandstone and siltstone	Lower shoreface, offshore	–Detailed imaging of the structure and density/velocity variations resulting from the relative sea level rise.
E	Sandstone and siltstone	Lower shoreface, offshore	–Better definition of layer pinch-out towards offshore deposition.

Table 4.2: Summary of the improvements in the seismic imaging that have been observed for each zone when applying the grain size-based distribution of acoustic properties. For each zone, we include the lithologies, and facies involved, and a short description of the structures that are better imaged.

In this paper the acoustic property values from the grain size-based simulation were used to calculate the corresponding values for the facies- and lithology-based simulations. The values were calculated by averaging all the cells with the same lithology or facies label, as explained. This method of averaging, but with core data, has also been used in other forward seismic modelling papers [30]. In other cases, they have referred to typical velocity and density values for stratigraphic units in particular sedimentary basins [19, 29], what we assumed to be averaged values as well. In the case of the facies-based simulation, applying averaging techniques for the calculation of properties smooths the internal contrast within the facies and results in similar values for acoustic properties for different facies, except for the offshore and the mass-density of the lagoon (Table 4.1). Therefore, the transition between some of the facies is not clearly observed in the seismic data (Figure 4.6, area B).

When comparing the different discretisation levels, some resemblance between the seismic responses of the three simulations is observed. First, the geometry of the seismic response of the facies- and grain size-based simulations are similar for areas A and C (Figures 4.6 and 4.7). However, there is strong contrast in the amplitude variations and, particularly for area A, in the lateral extent of the reflections (Figure 4.6). Second, the seismic response of the lithology- and the facies-based simulations for areas D and E are similar (Figure 4.7). These seismic responses are characterised by a rhythmical alternation of reflections for area D, and the merging of two blue reflections in area E (Figure 4.7). However, the seismic response of the grain size- and lithology-based simulations do not show resemblance for any of the highlighted cases. Consequently, for the case of wave-dominated, shoreface systems, the use of lithology-based simulations when analysing small-scale, stratigraphic heterogeneities will result in the least precise characterisation of the subsurface target.

4.5.3. Implications on seismic inversion and geological modelling

In this paper, we have shown that the way we discretise the acoustic properties of the subsurface have an impact on the seismic response, and that, if we allocate properties based on lithology or facies classifications, some small-scale, stratigraphic heterogeneities will be erased from our seismic data. These findings have an impact on the way inversion of seismic data is traditionally performed. Seismic inversion aims at transforming seismic data from the subsurface into elastic properties, which can then be used in petrophysical and geological modelling to build 3D models of other valuable properties for reservoir characterisation [90–93]. A key challenge is to quantify the uncertainty due in part to the lack of resolution of seismic data, which blurs small-scale heterogeneities.

Owing to their unique mathematical properties, (multivariate) Gaussian distributions have become a cornerstone of inversion workflows to capture uncertainties in the spatial variations of subsurface properties [35, 94, 95]. But the results of this study show that the application of Gaussian distributions is not able to resolve the architectural features observed in the geological simulations.

In the case of properties such as porosity, the available data to condition the posterior distribution are based on well log and core data. From those data, an autocovariance or a semi-variogram model is traditionally used to capture the spatial variability of those properties in the subsurface. But variations of sea level and sediment supply lead to elongated, curved, and non-stationary structures whose properties are discontinuous along erosional surfaces, all features that cannot be represented based on a single covariance model [96].

However, our results highlight that small-scale, stratigraphic heterogeneities that develop at scales below lithology or facies have an impact on the seismic response. So modelling properties as constant values for each facies or lithology – as is sometimes done to simplify geological modelling based on lithofacies, lithotypes or litho/fluid distributions [33, 34, 97–100] – leads to ignoring valuable information available in the data. At the same time, the resolution of seismic data is rarely high enough to unambiguously characterise those heterogeneities. In that context, a covariance model is too weak as a geological prior to compensate for the lack of data. This raises the question of the true predictive power of the models obtained through inversion based on multivairate Gaussian distributions.

In recent years, researchers have tried to overcome the limitations of the Gaussian assumption by developing other approaches for the definition of the prior and posterior distributions [[95], and references herein]. Elongation, curvature, and more generally non-stationary can be captured in Gaussian simulations but only using advanced approaches with a higher modelling cost [101–103]. Multiple-point approaches provide a more straightforward solution to use more geologically

plausible priors [104–106], although the geological structures are rarely perfectly preserved.

We consider that the current approach of seismic inversion workflows should be reconsidered to better captured small-scale, stratigraphic heterogeneities. Some studies that include geological conditioning in the inversion process have shown its impact on the quantitative risking of reservoir's prospectivity, especially in areas with limited well information [105, 107], and on CO_2 monitoring [36]. Here, we suggest adding the use of forward stratigraphic modelling to the workflow for seismic data inversion. This way we can account for the changes in properties and the resulting small-scale, stratigraphic heterogeneities that occur below facies or lithology scale. For this, it is necessary to develop fast and flexible stratigraphic modelling tools and procedures to generate acoustic properties that fit the targets in the subsurface.

This paper focuses on wave-dominated, shoreface environments and stratigraphic heterogeneities that develop in such depositional environments. Future work can apply the same method to other depositional environments. To do so, it is necessary to evaluate the available forward stratigraphic modelling tools for other depositional environments and their compatibility with the method used for this study. There are stratigraphic modelling tools for deep-water channels [108], fluvial systems [109], and tide- and/or fluvial-dominated shallow marine environments [SedSim, [59, 75]].

4.5.4. Methodology limitations

The method used to create the grain size-based simulations has a series of limitations. First, the selection of the stratigraphic modelling tool is limited to those that are able to generate small-scale stratigraphic heterogeneities at metre scale and that provide grain size distribution data as output, typically in the form of proportion of different grain size classes. There are different types of stratigraphic modelling tools, and within rule-based tools, two of the main drawbacks is the limitation for log data conditioning and the limitation to simulate different depositional environments in the same tool [61]. On this regard, rule-based modelling tools approximate the physical processes that control erosion and deposition to a series of rules, rules that are specific for each depositional environment and that represent processes that are active in each environment. Further effort is required to develop more robust tools that can handle different ruling for different depositional environments within the same simulation [61]. There are also process-based modelling tools where the resulting property distributions are based on physical laws that control the erosion, transport and deposition of sediment [61]. However, this type of tools tend to resolve diffusion equations that approximate the real processes active in nature to be able to handle modelling through large areas for long modelling time (from thousands to millions of years) [75, 110, 111].

Second, for the calculation of the acoustic properties, a number of assumptions

are made. In the proposed method, allocation of initial porosity depends on the experimental values obtained by Beard and Weyl [73], who used fluvial sand samples to relate initial porosity, mean grain size, and sorting. Those measurements did not account for variations in roundness and sphericity of the grains. However, roundness and sphericity change from one depositional environment to another [112]. Roundness and sphericity impact the packing of the grains and, in consequence, the porosity [73, 113, 114]. Thus, we cannot confirm that, for the same mean grain size and sorting relationships, we would obtain the same initial porosity values in a wave-dominated coastal environment.

In our method, we have calculated the final porosity by implementing a porosity loss constant [74]. This is necessary because pyBarSim simulates sedimentation at surface conditions, but rocks in the subsurface experience compaction and, in many cases, diagenetic processes that change the arrangement of grains and the porosity [115]. Porosity loss curves are lithology and basin dependent [116] and there are other equations that can be used to calculate the final porosity [116–120]. Diagenetic processes, such as cementation, might also affect specific facies or areas above others, creating velocity and density contrast that might not be related to grain size variations alone.

For the calculation of mass-density, values for the density of the grains and the density of the fluid filling the pore space are required. We assumed that the sediment is only composed by quartz particles, a simplification of the sediment composition in siliciclastic systems, and that the porosity is water saturated. However, the sediment composition of wave-dominated shoreface systems can vary from mainly quartz to calcite dominated, with many other accessory minerals and possible combinations. These parameters can be modified to better fit sediment and fluid compositions observed in subsurface data and analyse the impact of these changes on the seismic response.

For the calculation of P-wave velocity, we use an empirical equation that relates porosity, clay content, and effective pressure [32]. Here, the finest grain size class used as input for BarSim has a diameter of $5\mu m$ and is classified as fine silt [121]. Therefore, we assumed that the clay content equals the proportion of fine silt. We have also assumed the effective pressure to be equivalent to $1000m$ depth. There are other empirical equations that explore the relationship between clay content, and porosity [31], but they do not take effective pressure into account, and so they were discarded. It is also worth noting that the empirical equations are based on lab sample measurements and that no upscaling methods have been applied to the acoustic properties. Research has shown that the impact of the properties controlling the wave velocities at laboratory scale might decrease in presence of other structural features [122].

There are also some limitations in the numerical seismic modelling and migration process that have an impact in the vertical resolution of the synthetic seismic data. The vertical resolution depends on the frequency content of the seismic waves and

the subsurface velocity model [5]. Assuming a maximum frequency of $150Hz$, and an average P-wave velocity of $3600m/s$ in the target area, the detection resolution, which is normally approximated to $1/4$ of the wavelength, is $6m$, and the resolution to distinguish the presence of stratigraphic features, which is approximated to $1/10$ of the wavelength, is around $2,5m$ [4].

Also note that by limiting ourselves to 2D and acoustic modelling, we have still made simplifications of the reality, which is a 3D elastic Earth. However, it is our believe and expectation that the conclusions we made on discretization of the geologic models and the link to seismic resolution will not change by making all modelling more realistic. But strictly speaking, this has to be proven still in follow-up research.

On a final note, this research still uses a discretised distribution of properties, a discretisation based on a continuous property. Lithology and facies are labels used to simplify the complexity of the subsurface, where the heterogeneities are the result of the change in continuous properties, such as grain size. In our simulations, the 2x2 cells result from the interpolation of grain size changes within that area and it is already able to add more detail to the simulations. The finer our grid is, the better we could capture the real distribution of the properties in subsurface. However, we have shown that avoiding the discretisation based on lithology or facies already brings improvement to the imaging of the stratigraphic architecture of the target area. And this seems to be the right path to fine-tune seismic inversion methodologies applied to real seismic data.

4.6. Conclusion

This paper shows that simulated metre-scale, stratigraphic heterogeneities of grain-size distributions have an impact on the synthetic seismic response. To analyse these heterogeneities, we introduce a method that links the generation of geological simulations using stratigraphic modelling and the allocation of acoustic properties based on grain size distribution. Even with its limitations, this method enables improved observations of stratigraphic heterogeneities in the seismic response versus the simulations with discretised acoustic properties. The imprint of these heterogeneities is modified or disappears when we classify the detailed grain-size distributions data into facies and, especially, into lithology, as this results in a single, averaged values of acoustic properties per facies and/or lithology class.

Our results also highlight the limitations of the conventional, lithology-based seismic inversion workflows and Gaussian-based uncertainty analysis. We have proven that discretising simplifies the complexity contained within certain facies or lithology and fails to capture the impact of gradual changes of density and P-wave velocity and that are related to gradual porosity and grain size distribution changes. The grain size-based simulation better captures the curved architecture and property changes that result from relative sea level variations.

For the case of clastic, wave-dominated shoreface environments and under the input parameters that we set, we have observed the impact of discretising mass-density and P-wave velocity in three situations: (1) the property changes within the sediments that constitute the lagoon area; (2) the architecture and property contrast between lower shoreface, upper shoreface and offshore after a relative sea level rise and the subsequent sediment deposition during sea level fall; (3) the architecture and property distribution in the lower shoreface to offshore transition and the reservoir thinning.

References

[1]   A. Cuesta-Cano, A. Karimzadanzabi, J. E. A. Storms, G. Rongier, D. J. Verschuur and A. W. Martinius. 'Discretization of small-scale, stratigraphic heterogeneities and its impact on the seismic response: Lessons from the application of process-based modelling'. In: *Geophysical Prospecting* (Mar. 2025). ISSN: 0016-8025. DOI: 10.1111/1365-2478.70015.

[2]   J. de Jager. *Handbook: Risk and Volume Assessment*. Tech. rep. De Jager Geological Consulting, 2021, pp. 1–124.

[3]   M. Simmons, A. Davies and L. Cowliff. 'Plausible Characterisation of Subsurface Geology is Essential for the Energy Transition'. In: *First Break* 41 (6 June 2023), pp. 69–74. ISSN: 0263-5046. DOI: 10.3997/1365-2397.fb2023045.

[4]   Ö. Yilmaz. *Seismic Data Analysis*. Society of Exploration Geophysicists, 2001.

[5]   D. R. Cox, A. M. Newton and M. Huuse. 'An introduction to seismic reflection data: acquisition, processing and interpretation'. In: *Regional Geology and Tectonics: Principles of Geologic Analysis*. Elsevier, 2020, pp. 571–603. DOI: 10.1016/B978-0-444-64134-2.00020-1.

[6]   S. Chopra, J. Castagna and O. Portniaguine. 'Seismic resolution and thin-bed reflectivity inversion'. In: *CSEG RECORDER* (Jan. 2006), pp. 19–25.

[7]   H. Zeng, X. Zhu and R. Zhu. 'New insights into seismic stratigraphy of shallow-water progradational sequences: Subseismic clinoforms'. In: *Interpretation* 1 (1 Aug. 2013). doi: 10.1190/INT-2013-0017.1, SA35–SA51. ISSN: 2324-8858. DOI: 10.1190/INT-2013-0017.1.

[8]   T. Klausen, J. Torland, C. Eide, B. Alaei, S. Olaussen and D. Chiarella. 'Clinoform development and topset evolution in a mud-rich delta – the Middle Triassic Kobbe Formation, Norwegian Barents Sea'. In: *Sedimentology* 65 (4 2018), pp. 1132–1169. DOI: 10.1111/sed.12417.

[9]   A. Jackson, A. Jackson, L. Stright, S. Hubbard and B. Romans. 'Static connectivity of stacked deep-water channel elements constrained by high-resolution digital outcrop models'. In: *AAPG Bulletin* 103 (12 2019), pp. 2943–2973. DOI: 10.1306/03061917346.

[10] J. A. Howell, A. Skorstad, A. MacDonald, A. Fordham, S. Flint, B. Fjellvoll and T. Manzocchi. 'Sedimentological parameterization of shallow-marine reservoirs'. In: *Petroleum Geoscience* 14 (1 2008), pp. 17–34. DOI: 10.1144/1354-079307-787.

[11] M. Jackson, G. Hampson and R. Sech. 'Three-dimensional modeling of a shoreface-shelf parasequence reservoir analog: Part 2. geologic controls on fluid flow and hydrocarbon recovery'. In: *American Association of Petroleum Geologists Bulletin* 93 (9 2009), pp. 1183–1208. DOI: 10.1306/05110908145.

[12] R. Sech, M. Jackson and G. Hampson. 'Three-dimensional modeling of a shoreface-shelf parasequence reservoir analog: Part 1. surface-based modeling to capture high-resolution fades architecture'. In: *American Association of Petroleum Geologists Bulletin* 93 (9 2009), pp. 1155–1181. DOI: 10.1306/05110908144.

[13] P. Ringrose and M. Bentley. *Reservoir Model Design A Practitioner's Guide*. Springer, 2015.

[14] M. W. Shuster and T. Aigner. 'Two-Dimensional Synthetic Seismic and Log Cross Sections from Stratigraphic Forward Models'. In: *AAPG Bulletin* 78 (3 Mar. 1994), pp. 409–431. ISSN: 0149-1423. DOI: 10.1306/BDFF90C8-1718-11D7-8645000102C1865D.

[15] D. Hodgetts and J. A. Howell. 'Synthetic seismic modelling of a large-scale geological cross-section from the Book Cliffs, Utah, USA'. In: *Petroleum Geoscience* 6 (3 2000), pp. 221–229. ISSN: 13540793. DOI: 10.1144/PETGEO.6.3.221.

[16] K. Bakke, J. Gjelberg and S. A. Petersen. 'Compound seismic modelling of the Ainsa II turbidite system, Spain: Application to deep-water channel systems offshore Angola'. In: *Marine and Petroleum Geology* 25 (10 Dec. 2008), pp. 1058–1073. ISSN: 02648172. DOI: 10.1016/j.marpetgeo.2007.10.009.

[17] M. Tomasso, R. Bouroullec and D. Pyles. 'The use of spectral recomposition in tailored forward seismic modeling of outcrop analogs'. In: *American Association of Petroleum Geologists Bulletin* 94 (4 2010), pp. 457–474. DOI: 10.1306/08240909051.

[18] K. Bakke, I. Kane, O. Martinsen, S. Petersen, T. Johansen, S. Hustoft, F. Jacobsen and A. Groth. 'Seismic modeling in the analysis of deep-water sandstone termination styles'. In: *AAPG Bulletin* 97 (9 2013), pp. 1395–1419. DOI: 10.1306/03041312069.

[19] I. Anell, I. Lecomte, A. Braathen and S. J. Buckley. 'Synthetic seismic illumination of small-scale growth faults, paralic deposits and low-angle clinoforms: A case study of the Triassic successions on Edgeøya, NW Barents Shelf'. In: *Marine and Petroleum Geology* 77 (Nov. 2016), pp. 625–639. ISSN: 02648172. DOI: 10.1016/j.marpetgeo.2016.07.005.

[20] O. Rabbel, O. Galland, K. Mair, I. Lecomte, K. Senger, J. B. Spacapan and R. Manceda. 'From field analogues to realistic seismic modelling: A case study of an oil-producing andesitic sill complex in the Neuquén Basin, Argentina'. In: *Journal of the Geological Society* 175 (4 July 2018), pp. 580–593. ISSN: 00167649. DOI: 10.1144/JGS2017-116.

[21] L. Wan, S. Hurter, V. Bianchi, P. Li, J. Wang and T. Salles. 'The roles and seismic expressions of turbidites and mass transport deposits using stratigraphic forward modeling and seismic forward modeling'. In: *Journal of Asian Earth Sciences* 232 (July 2022), p. 105110. ISSN: 13679120. DOI: 10.1016/j.jseaes.2022.105110.

[22]   D. A. Armitage and L. Stright. 'Modeling and interpreting the seismic-reflection expression of sandstone in an ancient mass-transport deposit dominated deep-water slope environment'. In: *Marine and Petroleum Geology* 27 (1 Jan. 2010), pp. 1–12. ISSN: 0264-8172. DOI: 10.1016/J.MARPETGEO.2009.08.013.

[23]   E. Pemberton, L. Stright, S. Fletcher and S. Hubbard. 'The influence of stratigraphic architecture on seismic response: Reflectivity modeling of outcropping deepwater channel units'. In: *Interpretation* 6 (3 2018), T783–T808. DOI: 10.1190/INT-2017-0170.1.

[24]   N. Holgate, G. Hampson, C.-L. Jackson and S. Petersen. 'Constraining uncertainty in interpretation of seismically imaged clinoforms in deltaic reservoirs, Troll field, Norwegian North Sea: Insights from forward seismic models of outcrop analogs'. In: *AAPG Bulletin* 98 (12 2014), pp. 2629–2663. DOI: 10.1306/05281413152.

[25]   N. Holgate, C.-L. Jackson, G. Hampson and T. Dreyer. 'Seismic stratigraphic analysis of the Middle Jurassic Krossfjord and Fensfjord formations, Troll oil and gas field, northern North Sea'. In: *Marine and Petroleum Geology* 68 (2015), pp. 352–380. DOI: 10.1016/j.marpetgeo.2015.08.036.

[26]   N. Grasseau, C. Grélaud, M. López-Blanco and P. Razin. 'Forward seismic modeling as a guide improving detailed seismic interpretation of deltaic systems: Example of the Eocene Sobrarbe delta outcrop (South-Pyrenean foreland basin, Spain), as a reference to the analogous subsurface Albian-Cenomanian Torok-Nanushuk Delta of the Colville Basin (NPRA, USA)'. In: *Marine and Petroleum Geology* 100 (Feb. 2019), pp. 225–245. ISSN: 02648172. DOI: 10.1016/J.MARPETGEO.2018.11.010.

[27]   R. Feng, S. Luthi, D. Gisolf and S. Sharma. 'Obtaining a high-resolution geological and petrophysical model from the results of reservoir-orientated elastic wave-equation-based seismic inversion'. In: *Petroleum Geoscience* 23 (3 2017), pp. 376–385. DOI: 10.1144/petgeo2015-076.

[28]   A. Bourgeois, P. Joseph and J. C. Lecomte. 'Three-dimensional full wave seismic modelling versus one-dimensional convolution: the seismic appearance of the Grès d'Annot turbidite system'. In: *Geological Society Special Publication* 221 (2004), pp. 401–417. ISSN: 03058719. DOI: 10.1144/GSL.SP.2004.221.01.22.

[29]   O. Falivene, P. Arbués, J. Ledo, B. Benjumea, J. A. Muñoz, O. Fernández and S. Martínez. 'Synthetic seismic models from outcrop-derived reservoir-scale three-dimensional facies models: The Eocene Ainsa turbidite system (southern Pyrenees)'. In: *AAPG Bulletin* 94 (3 Mar. 2010), pp. 317–343. ISSN: 0149-1423. DOI: 10.1306/08030908157.

[30] A. Grippa, A. Hurst, G. Palladino, D. Iacopini, I. Lecomte and M. Huuse. 'Seismic imaging of complex geometry: Forward modeling of sandstone intrusions'. In: *Earth and Planetary Science Letters* 513 (2019), pp. 51–63. DOI: 10.1016/j.epsl.2019.02.011.

[31] D. H. Han, A. Nur and D. Morgan. 'Effects of porosity and clay content on wave velocities in sandstones'. In: *Geophysics* 51 (11 Nov. 1986), pp. 2093–2107. ISSN: 0016-8033. DOI: 10.1190/1.1442062.

[32] D. Eberhart-Phillips, D. H. Han and M. D. Zoback. 'Empirical relationships among seismic velocity, effective pressure, porosity, and clay content in sandstone'. In: *GEOPHYSICS* 54 (1 Feb. 1989), pp. 82–89. ISSN: 00168033. DOI: 10.1190/1.1442580.

[33] M. Cardiff and P. K. Kitanidis. 'Bayesian inversion for facies detection: An extensible level set framework'. In: *Water Resources Research* 45 (10 Oct. 2009). ISSN: 0043-1397. DOI: 10.1029/2008WR007675.

[34] M. Kemper and J. Gunning. 'Joint Impedance and Facies Inversion – Seismic inversion redefined'. In: *First Break* 32 (9 Sept. 2014). ISSN: 0263-5046. DOI: 10.3997/1365-2397.32.9.77968.

[35] J. Pendrel and H. Schouten. 'Facies — The drivers for modern inversions'. In: *The Leading Edge* 39 (2 Feb. 2020), pp. 102–109. ISSN: 1070-485X. DOI: 10.1190/tle39020102.1.

[36] C. Barajas-Olalde, A. Mur, D. C. Adams, L. Jin, J. He, J. A. Hamling and C. D. Gorecki. 'Joint impedance and facies inversion of time-lapse seismic data for improving monitoring of CO2 incidentally stored from CO2 EOR'. In: *International Journal of Greenhouse Gas Control* 112 (Dec. 2021), p. 103501. ISSN: 17505836. DOI: 10.1016/j.ijggc.2021.103501.

[37] P. S. Roy, P. J. Cowell, M. A. Ferland, B. G. Thom and O. van de Plassche. 'Wave-dominated coasts'. In: *Coastal Evolution: Late Quaternary Shoreline Morphodynamics*. Cambridge University Press, 1995, pp. 121–186.

[38] J. Bhattacharya and R. G. Walker. 'River- and wave-dominated depositional systems of the Upper Cretaceous Dunvegan Formation, northwestern Alberta'. In: *Bulleting of Canadian Petroleum Geology* 39 (2 June 1991), pp. 165–191.

[39] N. Tyler and R. J. Finley. 'Architectural Controls on the Recovery of Hydrocarbons From Sandstone Reservoers'. In: *The Three-Dimensional Facies Architecture of Terrigenous Clastic Sediments and its Implications for Hydrocarbon Discovery and Recovery*. SEPM Society for Sedimentary Geology, 1991, pp. 1–5. DOI: 10.2110/csp.91.03.0001.

[40] P. Lis and A. Wysocka. 'Middle Miocene Deposits in Carpathian Foredeep: Facies Analysis and Implications for Hydrocarbon Reservoir Prospecting'. In: *Annales Societatis Geologorum Poloniae* 82 (2012), pp. 239–253.

[41] S. Tahir, B. Musta, J. Asis and F. Hanis. 'Wave and tide influence in Neogene paralic hydrocarbon potential reservoirs in Sabah'. In: *ASM Science Journal* 11 (2 2018), pp. 278–292.

[42] G. J. Hampson and J. E. A. Storms. 'Geomorphological and sequence stratigraphic variability in wave-dominated, shoreface-shelf parasequences'. In: *Sedimentology* 50 (4 Aug. 2003), pp. 667–701. ISSN: 0037-0746. DOI: 10.1046/j.1365-3091.2003.00570.x.

[43] K. G. Taylor, R. L. Gawthorpe, C. D. Curtis, J. D. Marshall and D. N. Awwiller. 'Carbonate Cementation in a Sequence-Stratigraphic Framework: Upper Cretaceous Sandstones, Book Cliffs, Utah-Colorado'. In: *Journal of Sedimentary Research* 70 (2 Mar. 2000), pp. 360–372. ISSN: 1527-1404. DOI: 10.1306/2DC40916-0E47-11D7-8643000102C1865D.

[44] J. M. Ketzer, S. Morad, R. Evans and I. S. Al-Aasm. 'Distribution of Diagenetic Alterations in Fluvial, Deltaic, and Shallow Marine Sandstones Within a Sequence Stratigraphic Framework: Evidence from the Mullaghmore Formation (Carboniferous), NW Ireland'. In: *Journal of Sedimentary Research* 72 (6 Nov. 2002), pp. 760–774. ISSN: 1527-1404. DOI: 10.1306/042202720760.

[45] T. Sømme, J. Howell, G. Hampson and J. Storms. 'Genesis, Architecture, and Numerical Modeling of Intra-Parasequence Discontinuity Surfaces In Wave-Dominated Deltaic Deposits: Upper Cretaceous Sunnyside Member, Blackhawk Formation, Book Cliffs, Utah, U.S.A.' In: *Recent Advances in Models of Siliciclastic Shallow-Marine Stratigraphy* (2008), pp. 421–441. DOI: 10.2110/PEC.08.90.0421.

[46] N. Kumar and J. E. Sanders. 'Characteristics of shoreface storm deposits; modern and ancient examples'. In: *Journal of Sedimentary Research* 46 (1 Mar. 1976), pp. 145–162. ISSN: 1527-1404. DOI: 10.1306/212F6EDD-2B24-11D7-8648000102C1865D.

[47] M. E. Field and P. S. Roy. 'Offshore transport and sand-body formation; evidence from a steep, high-energy shoreface, southeastern Australia'. In: *Journal of Sedimentary Research* 54 (4 Dec. 1984), pp. 1292–1302. ISSN: 1527-1404. DOI: 10.1306/212F85C1-2B24-11D7-8648000102C1865D.

[48] O. Madsen. 'Mechanics of Cohesionless Sediment Transport in Coastal Waters'. In: *Proc. Coastal Sediments* ASCE (1991), pp. 15–27.

[49] D. Swift, P. S. and J. Thorne. 'Sedimentation on continental margins, IV. Lithofacies and depositional systems.' In: *Shelf Sand and Sandstone Bodies*. Ed. by D. Swift, G. Oertel, R. Tillman and J. Thorne. Vol. 14. Int. Assoc. Sedimentol. Spec. Publ., 1991, pp. 89–152.

[50] T. R. Keen, R. L. Slingerland, S. J. Bentley, Y. Furukawa, W. J. Teague and J. D. Dykes. 'Sediment Transport on Continental Shelves: Storm Bed Formation and Preservation in Heterogeneous Sediments'. In: *Sediments, Morphology and Sedimentary Processes on Continental Shelves* (Jan. 2012), pp. 295–310. DOI: 10.1002/9781118311172.CH14.

[51] E. J. Anthony. 'Storms, shoreface morphodynamics, sand supply, and the accretion and erosion of coastal dune barriers in the southern North Sea'. In: *Geomorphology* 199 (Oct. 2013), pp. 8–21. ISSN: 0169-555X. DOI: 10.1016/J.GEOMORPH.2012.06.007.

[52] J. Backstrom, D. Jackson, A. Cooper and C. Loureiro. 'Contrasting geomorphological storm response from two adjacent shorefaces'. In: *Earth Surface Processes and Landforms* 40 (15 Dec. 2015), pp. 2112–2120. ISSN: 1096-9837. DOI: 10.1002/ESP.3788.

[53] E. J. Anthony and T. Aagaard. 'The lower shoreface: Morphodynamics and sediment connectivity with the upper shoreface and beach'. In: *Earth-Science Reviews* 210 (Nov. 2020), p. 103334. ISSN: 0012-8252. DOI: 10.1016/J.EARSCIREV.2020.103334.

[54] N. C. Mitchell and Z. Zhao. 'Effects of currents and waves on the morphologies of coastal sandy clinoforms: sediment mobility calculations based on current meter and wave data from Southern California, U.S.A.' In: *Journal of Sedimentary Research* 93 (7 July 2023), pp. 488–501. ISSN: 1527-1404. DOI: 10.2110/JSR.2023.002.

[55] C. Paola. 'Quantitative models of sedimentary basin filling'. In: *Sedimentology* 47 (SUPPL. 1 Feb. 2000), pp. 121–178. ISSN: 1365-3091. DOI: 10.1046/J.1365-3091.2000.00006.X.

[56] J. Storms, G. Weltje, J. V. Duke, C. Geel and S. Kroonenberg. 'Process-response modeling of wave-dominated coastal systems: Simulating evolution and stratigraphy on geological timescales'. In: *Journal of Sedimentary Research* 72 (2 2002), pp. 226–239. DOI: 10.1306/052501720226.

[57] J. Storms. 'Event-based stratigraphic simulation of wave-dominated shallow-marine environments'. In: *Marine Geology* 199 (1-2 2003), pp. 83–100. DOI: 10.1016/S0025-3227(03)00144-0.

[58] A. Quiquerez, P. Allemand, G. Dromart and J.-P. Garcia. 'Impact of storms on mixed carbonate and siliciclastic shelves: insights from combined diffusive and fluid-flow transport stratigraphic forward model'. In: *Basin Research* 16 (4 2004), pp. 431–449. ISSN: 0950-091X. DOI: https://doi.org/10.1111/j.1365-2117.2004.00247.x.

[59] D. M. Tetzlaff. 'Modelling Coastal Sedimentation through Geologic Time'. In: *Journal of Coastal Research* 21 (3 (213) May 2005), pp. 610–617. ISSN: 0749-0208. DOI: 10.2112/04-704A.1.

[60] L. Laigle, P. Joseph, G. D. Marsily and S. Violette. '3-D process modelling of ancient storm-dominated deposits by an event-based approach: Application to Pleistocene-to-modern Gulf of Lions deposits.' In: *Marine Geology* 335 (2012), pp. 177–199. DOI: 10.1016/j.margeo.2012.11.007.

[61] M. J. Pyrcz, R. P. Sech, J. A. Covault, B. J. Willis, Z. Sylvester and T. Sun. 'Stratigraphic rule-based reservoir modeling'. In: *Bulletin of Canadian Petroleum Geology* 63 (4 Dec. 2015), pp. 287–303. ISSN: 0007-4802. DOI: 10.2113/GSCPGBULL.63.4.287.

[62] J. Storms and D. Swift. 'Shallow-marine sequences as the building blocks of stratigraphy: Insights from numerical modelling'. In: *Basin Research* 15 (3 2003), pp. 287–303. DOI: 10.1046/j.1365-2117.2003.00207.x.

[63] K. Charvin, G. J. Hampson, K. L. Gallagher, J. E. Storms and R. Labourdette. 'Characterization of Controls on High-Resolution Stratigraphic Architecture in Wave-Dominated Shoreface–Shelf Parasequences Using Inverse Numerical Modeling'. In: *Journal of Sedimentary Research* 81 (8 Aug. 2011), pp. 562–578. ISSN: 1527-1404. DOI: 10.2110/JSR.2011.48.

[64] J. Storms and G. Hampson. 'Mechanisms for forming discontinuity surfaces within shoreface-shelf parasequences: Sea level, sediment supply, or wave regime?' In: *Journal of Sedimentary Research* 75 (1 2005), pp. 67–81. DOI: 10.2110/jsr.2005.007.

[65] G. Rongier, J. E. Storms and A. Cuesta-Cano. *pyBarSim*. 2023.

[66] M. D. Picard. 'Classification of fine-grained sedimentary rocks'. In: *Journal of Sedimentary Research* 41 (1 Mar. 1971), pp. 179–195. ISSN: 1527-1404. DOI: 10.1306/74D7221B-2B21-11D7-8648000102C1865D.

[67] R. Merriman, D. Highley and D. Cameron. 'Definition and characteristics of very-fine grained sedimentary rocks : clay, mudstone, shale and slate'. In: (2003).

[68] J. H. Schön. 'Rocks—Their Classification and General Properties'. In: *Handbook of Petroleum Exploration and Production* 8 (Jan. 2011), pp. 1–16. ISSN: 1567-8032. DOI: 10.1016/S1567-8032(11)08001-3.

[69] G. M. Friedman. 'On sorting, Sorting Coefficients, and the Lognormality of the Grain-Size Distribution of Sandstones'. In: *The Journal of Geology* 70 (6 1962), pp. 737–753. URL: http://www.journals.uchicago.edu/t-and-c.

[70] P. D. Trask. 'Mechanical analysis of sediments by centrifuge'. In: *Economic Geology* 25 (6 Sept. 1930), pp. 581–599.

[71] R. L. Folk and W. C. Ward. 'Brazos River bar [Texas]; a study in the significance of grain size parameters'. In: *Journal of Sedimentary Research* 27 (1 Mar. 1957), pp. 3–26. ISSN: 1527-1404. DOI: 10.1306/74D70646-2B21-11D7-8648000102C1865D.

[72] J. J. Rogers and W. B. Head. 'Relationships between Porosity, Median size, and Sorting Coefficients of Synthetic Sands'. In: *Journal of Sedimentary Petrology* 31 (3 1961), pp. 467–470.

[73] D. C. Beard and P. K. Weyl. 'Influence of Texture on Porosity and Permeability of Unconsolidated Sand'. In: *AAPG Bulletin* 57 (2 Feb. 1973), pp. 349–369. ISSN: 0149-1423. DOI: 10.1306/819A4272−16C5−11D7−8645000102C1865D.

[74] J. Wendebourg and J. Harbaugh. 'Chapter 4 Endowing simulated sequences with petrophysical flow properties'. In: *Computer Methods in the Geosciences*. Ed. by W. J. and H. J.W. Vol. 16. Pergamon, Jan. 1997, p. 81. DOI: 10.1016/S1874−561X(97)80005−3.

[75] D. Tetzlaff and J. Harbaugh. *Simulating Clastic Sedimentation*. 1st ed. Springer New York, 1989, pp. 1–202.

[76] V. Červený, L. Klimeš and I. Pšenčík. 'Seismic ray method: Recent developments'. In: *Advances in Wave Propagation in Heterogenous Earth*. Ed. by R.-S. Wu, V. Maupin and R. Dmowska. Vol. 48. Elsevier, 2007, pp. 1–126. DOI: 10.1016/S0065−2687(06)48001−8.

[77] V. Červený. *Seismic Ray Theory*. Cambridge University Press, 2001.

[78] R. Wang, X. Jia and T. Hu. 'The precise finite difference method for seismic modeling'. In: *Applied Geophysics* 1 (2 Oct. 2004), pp. 69–74. ISSN: 1672-7975. DOI: 10.1007/s11770−004−0001−5.

[79] N. Rawlinson, J. Hauser and M. Sambridge. 'Seismic ray tracing and wavefront tracking in laterally heterogeneous media'. In: *Advances in Geophysics* 49 (Jan. 2008), pp. 203–273. ISSN: 0065-2687. DOI: 10.1016/S0065−2687(07)49003−3.

[80] Y. Liu and M. Sen. 'Advanced Finite-Difference Methods for Seismic Modeling'. In: *Geohorizons* 14 (2009), pp. 5–16.

[81] O. Holberg, J. Pajchel, P. Riste and H. B. Helle. 'Comparison of ray tracing and finite-difference modeling'. In: *SEG Technical Program Expanded Abstracts 1990*. Society of Exploration Geophysicists, Jan. 1990, pp. 1037–1041. DOI: 10.1190/1.1889901.

[82] S. W. Fagin. *Seismic Modeling of Geologic Structures : Applications to Exploration Problems*. Society of Exploration Geophysicists, Jan. 1991. ISBN: 978-1-56080-050-7. DOI: 10.1190/1.9781560802754.

[83] K. R. Kelly, R. W. Ward, S. Treitel and R. M. Alford. 'Synthetic seismograms—a finite difference approach'. In: *Geophysics* 41 (1 Feb. 1976), pp. 2–27. ISSN: 0016-8033. DOI: 10.1190/1.1440605.

[84] M. Davydenko and D. Verschuur. 'Full-wavefield estimation of angle-dependent reflectivity and migration velocity'. In: *Proceedings of the 87th Annual International Meeting*. SEG, 2017, pp. 5631–5635. DOI: 10.1190/segam2017−17782606.1.

[85] A. (Berkhout. 'Review Paper: An outlook on the future of seismic imaging, Part I: forward and reverse modelling'. In: *Geophysical Prospecting* 62 (5 Sept. 2014), pp. 911–930. ISSN: 0016-8025. DOI: 10.1111/1365-2478.12161.

[86] K. Aki and P. Richards. *Quantitative Seismology*. 2nd ed. CA: Univ. Sci. Books, 2002, pp. 1–700.

[87] J. Chhoa. *An Adaptive Approach to Gibbs' Phenomenon*. 2020.

[88] S. Abolhassani and D. J. Verschuur. 'Efficient preconditioned least-squares wave-equation migration'. In: *GEOPHYSICS* 89 (3 May 2024), S275–S288. ISSN: 0016-8033. DOI: 10.1190/geo2023-0048.1.

[89] G. V. Chilingar. 'Relationship Between Porosity, Permeability, and Grain-Size Distribution of Sands and Sandstones'. In: *Developments in Sedimentology* 1 (1964), pp. 71–75. DOI: 10.1016/S0070-4571(08)70469-2.

[90] W. J. Ostrander. 'Plane-wave reflection coefficients for gas sands at nonnormal angles of incidence'. In: *GEOPHYSICS* 49 (10 Oct. 1984), pp. 1637–1648. ISSN: 0016-8033. DOI: 10.1190/1.1441571.

[91] R. T. Shuey. 'A simplification of the Zoeppritz equations'. In: *GEOPHYSICS* 50 (4 Apr. 1985), pp. 609–614. ISSN: 0016-8033. DOI: 10.1190/1.1441936.

[92] N. S. Neidell. 'Amplitude variation with offset'. In: *The Leading Edge* 5 (3 Mar. 1986), pp. 47–51. ISSN: 1070-485X. DOI: 10.1190/1.1439241.

[93] R. E. Sheriff and L. P. Geldart. *Exploration Seismology*. Cambridge University Press, Aug. 1995. ISBN: 978-0-521-46282-2. DOI: 10.1017/CBO9781139168359.

[94] M. Jullum and O. Kolbjørnsen. 'A Gaussian-based framework for local Bayesian inversion of geophysical data to rock properties'. In: *GEOPHYSICS* 81 (3 May 2016), R75–R87. ISSN: 0016-8033. DOI: 10.1190/geo2015-0314.1.

[95] D. Grana. 'Joint facies and reservoir properties inversion'. In: *GEOPHYSICS* 83 (3 May 2018), pp. M15–M24. ISSN: 0016-8033. DOI: 10.1190/geo2017-0670.1.

[96] A. G. Journel. 'Beyond Covariance: The Advent of Multiple-Point Geostatistics'. In: 2005, pp. 225–233. DOI: 10.1007/978-1-4020-3610-1_23.

[97] G. D. Merletti and C. Torres-Verdín. 'Accurate Detection and Spatial Delineation of Thin-Sand Sedimentary Sequences via Joint Stochastic Inversion of Well Logs and 3D Prestack Seismic Amplitude Data'. In: *All Days*. SPE, Sept. 2006. DOI: 10.2118/102444-MS.

[98] F. Roncarolo and D. Grana. 'Improved Reservoir Characterization Integrating Seismic Inversion, Rock Physics Model, and Petroelastic Log Facies Classification: A Real Case Application'. In: *SPE Annual Technical Conference and Exhibition*. SPE, Sept. 2010. DOI: 10.2118/134919-MS.

[99] A. Mur and K. Waters. 'Play scale seismic characterization: Using basin models as an input to seismic characterization in new and emerging plays'. In: *SEG Technical Program Expanded Abstracts 2018*. Society of Exploration Geophysicists, Aug. 2018, pp. 555–559. DOI: 10.1190/segam2018-2992809.1.

[100] D. Grana. 'Joint Inversion of Facies and Reservoir Properties'. In: *81st EAGE Conference and Exhibition 2019*. European Association of Geoscientists & Engineers, 2019, pp. 1–5. DOI: 10.3997/2214-4609.201901298.

[101] J. B. Boisvert, J. G. Manchuk and C. V. Deutsch. 'Kriging in the Presence of Locally Varying Anisotropy Using Non-Euclidean Distances'. In: *Mathematical Geosciences* 41 (5 July 2009), pp. 585–601. ISSN: 1874-8961. DOI: 10.1007/s11004-009-9229-1.

[102] D. F. Machuca-Mory and C. V. Deutsch. 'Non-stationary Geostatistical Modeling Based on Distance Weighted Statistics and Distributions'. In: *Mathematical Geosciences* 45 (1 Jan. 2013), pp. 31–48. ISSN: 1874-8961. DOI: 10.1007/s11004-012-9428-z.

[103] F. Fouedjio. 'Second-order non-stationary modeling approaches for univariate geostatistical data'. In: *Stochastic Environmental Research and Risk Assessment* 31 (8 Oct. 2017), pp. 1887–1906. ISSN: 1436-3240. DOI: 10.1007/s00477-016-1274-y.

[104] Y. Liu, A. Harding, W. Abriel and S. Strebelle. 'Multiple-point simulation integrating wells, three-dimensional seismic data, and geology'. In: *AAPG Bulletin* 88 (7 July 2004), pp. 905–921. ISSN: 0149-1423. DOI: 10.1306/02170403078.

[105] E. F. Gonzalez, S. Gesbert and R. Hofmann. 'Adding geologic prior knowledge to Bayesian lithofluid facies estimation from seismic data'. In: *Interpretation* 4 (3 Aug. 2016), SL1–SL8. ISSN: 2324-8858. DOI: 10.1190/INT-2015-0220.1.

[106] K. S. Cordua, T. M. Hansen and K. Mosegaard. 'Monte Carlo full-waveform inversion of crosshole GPR data using multiple-point geostatistical a priori information'. In: *GEOPHYSICS* 77 (2 Mar. 2012), H19–H31. ISSN: 0016-8033. DOI: 10.1190/geo2011-0170.1.

[107] J. L. Crepaldi, L. P. de Figueiredo, A. Zerilli, I. S. Oliveira and J. P. Sinnecker. 'Bayesian joint inversion of seismic and electromagnetic data for reservoir lithofluid facies, including geophysical and petrophysical rock properties'. In: *GEOPHYSICS* 89 (3 May 2024), K1–K16. ISSN: 0016-8033. DOI: 10.1190/geo2022-0546.1.

[108] M. J. Pyrcz, T. McHargue, J. Clark, M. Sullivan and S. Strebelle. 'Event-Based Geostatistical Modeling: Description and Applications'. In: (2012), pp. 27–38. DOI: 10.1007/978-94-007-4153-9_3.

[109] B. J. Willis and H. Tang. 'Three-Dimensional Connectivity of Point-Bar Deposits'. In: *Journal of Sedimentary Research* 80 (5 2010), pp. 440–454. ISSN: 1527-1404.

[110] J. Harbaugh. 'Simulating Sedimentary Basins: An Overview of the SEDSIM Model and its Relevance to Sequence Stratigraphy'. In: *Geoinformatics* 4 (3 1993), pp. 123–126.

[111] D. Granjeon and P. Joseph. 'Concepts and Applications of A 3-D Multiple Lithology, Diffusive Model in Stratigraphic Modeling'. In: *Numerical Experiments in Stratigraphy‹subtitle›Recent Advances in Stratigraphic and Sedimentologic Computer Simulations‹/subtitle›* (Oct. 1999). DOI: 10.2110/PEC.99.62.0197.

[112] B. Patro and B. K. Sahu. 'Factor analysis of sphericity and roundness data of clastic quartz grains: Environmental significance'. In: *Sedimentary Geology* 11 (1 May 1974), pp. 59–78. ISSN: 00370738. DOI: 10.1016/0037-0738(74)90005-0.

[113] G.-C. Cho, J. Dodds and J. C. Santamarina. 'Particle Shape Effects on Packing Density, Stiffness, and Strength: Natural and Crushed Sands'. In: *Journal of Geotechnical and Geoenvironmental Engineering* 132 (5 May 2006), pp. 591–602. ISSN: 1090-0241. DOI: 10.1061/(ASCE)1090-0241(2006)132:5(591).

[114] H. S. Suh, K. Y. Kim, J. Lee and T. S. Yun. 'Quantification of bulk form and angularity of particle with correlation of shear strength and packing density in sands'. In: *Engineering Geology* 220 (Mar. 2017), pp. 256–265. ISSN: 00137952. DOI: 10.1016/j.enggeo.2017.02.015.

[115] K. Bjørlykke and K. Høeg. 'Effects of burial diagenesis on stresses, compaction and fluid flow in sedimentary basins'. In: *Marine and Petroleum Geology* 14 (3 May 1997), pp. 267–276. ISSN: 0264-8172. DOI: 10.1016/S0264-8172(96)00051-7.

[116] P. Allen and J. Allen. *Basin Analysis: Principles and Applications*. Blackwell Scientific Publications, 1990.

[117] M. K. Hubbert and W. W. Rubey. 'Role of fluid pressure in mechanics of overthrust faulting: I. Mechanics of fluid-filled porous solids and its application to overthrust faulting'. In: *GSA Bulletin* 70 (2 Feb. 1959), pp. 115–166.

[118] J. G. Sclater and P. A. F. Christie. 'Continental stretching: An explanation of the Post-Mid-Cretaceous subsidence of the central North Sea Basin'. In: *Journal of Geophysical Research: Solid Earth* 85 (B7 July 1980), pp. 3711–3739. ISSN: 0148-0227. DOI: 10.1029/JB085iB07p03711.

[119] B. Baldwin and C. Butler. 'Compaction Curves'. In: *AAPG bulletin* 69 (4 1985), pp. 622–626.

[120] M. Giles. *Diagenesis: A Quantitative Perspective. Implications for Basin Modelling and Rock Property Prediction*. 1997, pp. 1–526.

[121] R. Folk. 'The Distinction between Grain Size and Mineral Composition in Sedimentary-Rock Nomenclature'. In: *The Journal of Geology* 62 (1954), pp. 344–359.

[122] C. Bailly, J. Fortin, M. Adelinet and Y. Hamon. 'Upscaling of Elastic Properties in Carbonates: A Modeling Approach Based on a Multiscale Geophysical Data Set'. In: *Journal of Geophysical Research: Solid Earth* 124 (12 Dec. 2019), pp. 13021–13038. ISSN: 2169-9313. DOI: 10.1029/2019JB018391.

Appendixes

Appendix 1. Input parameters geological simulation

This section includes the values of input parameters used to generate the reference geological simulation. The modelled time is 30000 years. Figure 4.9. shows the relative sea level and sediment input applied at different modelling times. Other input parameters remain constant during the modelling time and are included in Table A1.1. All input parameters are within the range suggested in Rongier, Storms and Cuesta-Cano [2].
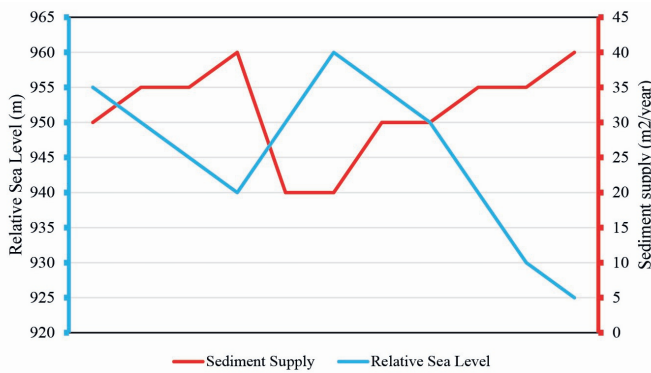

Figure 4.9: Relative sea level (in blue, in m) and sediment supply variations (in red, in $m^2/year$) used as input for the simulation run.

Parameter	Values
System slope	$0.05\%(0.29°)$
Horizontal spacing of nodes	$100m$
Vertical spacing of nodes	$2m$
Fair weather wave height	$1.5m$
Storm wave height	$6m$
Erodibility	0.4
Grain size classes	$5\mu m, 50\mu m, 125\mu m, 250\mu m$
Sediment fraction of input sediment	$0.25, 0.25, 0.25, 0.25$
Substratum thickness	$100m$
Sediment fraction of substratum	$0.2, 0.2, 0.3, 0.3$

Table 4.3: Values of the main input parameters for the simulation. For explanation on the parameter description and recommended value ranges, we refer to the recommendation in Rongier, Storms and Cuesta-Cano [2].

Appendix 2. Segment subdivision of the simulation

Due to computational limitations, the geological simulation had to be divided into smaller segments (Figure 4.10). Each segment is $7600m$ long, except for the last segment, number 8, which is $4400m$ long. To ensure that every location within the simulation is properly imaged, there is an overlap of $1800m$ between the different segments. There is a segment number 8, but the thickness of the target only allows for the observation of the reflectors of the top and the bottom of the target.
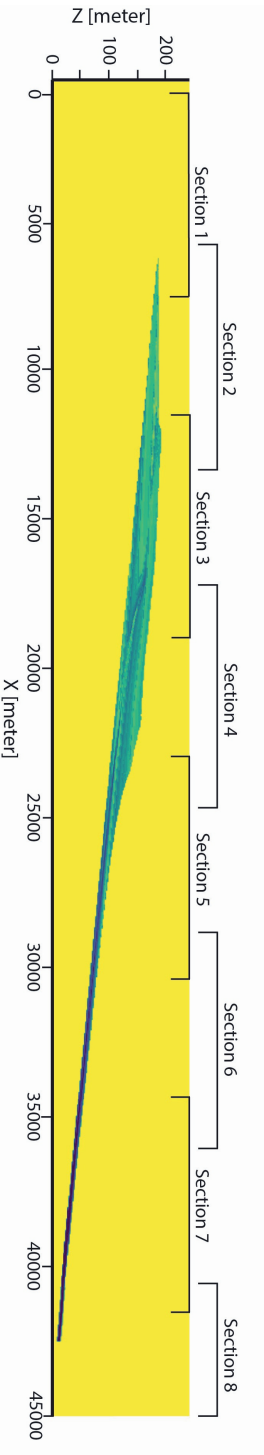
Figure 4.10: Subdivision in segments of the simulation. Each segment is $7600m$ long, except for segment 8. There is an overlapping of $1800m$ between the segments to ensure the adequate imaging of the whole model.

5

Characterizing Subsurface Acoustic Heterogeneity Through Angle-Gather Asymmetry Analysis

This study explores the potential of angle-dependent seismic data to detect and characterize lateral variations in subsurface acoustic properties, with an emphasis on P-wave velocity and mass-density. Nine geologically plausible synthetic models representing wave-dominated shoreface systems were constructed using stratigraphic forward modelling. Seismic responses were generated using finite-difference time-domain forward modelling followed by angle-dependent Full Wavefield Migration (FWM), which preserves the angular variation of reflected wavefields.

To assess the relationship between acoustic property variation and angle-gather responses, we computed a suite of statistical descriptors that quantify both the asymmetry in angle-gather data and the spatial heterogeneity in acoustic parameters. Our statistical analyses revealed moderate but complex, non-linear correlations, particularly between P-wave velocity variations and asymmetry metrics such as standard deviation and the sum of absolute differences of absolute amplitude distributions. Visual inspection confirmed that asymmetry features in angle-gather panels consistently highlight sharp lateral onsets and internal discontinuities in reservoir structures, demonstrating sensitivity to metre-scale contrasts in P-wave velocity. This sensitivity is consistent with the established understanding that wave velocity plays a predominant role in controlling the kinematics of wave propagation.

The study identified asymmetry artifacts resulting from inadequate subsurface

illumination — primarily due to acquisition geometry and data processing strategies — as well as artifacts associated with fixed-grid synthetic modelling, highlighting the importance of accounting for these effects in practical applications.

Overall, our findings stress the diagnostic value of angle-gather asymmetry for resolving metre-scale heterogeneities. Despite using simplified statistical descriptors, meaningful patterns were identified, supporting the potential of extracting valuable information about small-scale heterogeneities from angle gathers. Future work should expand to higher-dimensional acoustic models and leverage advanced statistical and machine learning techniques to fully capture the complex patterns within angle-dependent seismic data.

5.1. Introduction

The de-risking and sustainability of subsurface activities related to the energy transition benefit from our ability to identify and quantify changes in acoustic and elastic properties associated with geological heterogeneities [1, 2]. Relevant subsurface activities include CO_2 and H_2 storage, groundwater production, and mineral resource exploration. The heterogeneities—whether smooth or abrupt—can occur in any direction, at any scale, and often influence subsurface fluid flow [3–5], as it is known from outcrop analogues and subsurface analysis (e.g. [6–8]).

While core plug data can directly characterize heterogeneities in one dimension, they provide little to no information about the property distribution between cores—thus lacking insight into the full 3D subsurface variability. In contrast, seismic reflection is one of the primary tools used by the energy sector to investigate subsurface structures in 3D. However, seismic resolution is limited. The smallest features detectable in seismic data are controlled by acquisition frequency, reservoir depth, and average propagation velocity [9–11]. For typical seismic frequencies ranging from 20 to $60Hz$, P-wave velocities in sedimentary formations between 2000 and $3000m/s$, and depths of approximately 1000 to $2000m$, the achievable vertical resolution is on the order of 10 to $20m$.

Because heterogeneities range from millimetres to tens of metres in scale, many fall below the resolution of seismic data [12–14]. Consequently, researchers have developed methods to extract sub-seismic-scale features from seismic datasets [12, 15–17]. These approaches often rely on geological scenarios derived from outcrop analogues, combined with forward seismic modelling and inversion techniques (e.g. [4, 6, 12, 15]). Some studies employ simplified geological models incorporating sub-seismic heterogeneities, using synthetic seismic data and machine-learning approaches to correlate seismic responses with variations in acoustic properties such as mass density and P-wave velocity [16–18].

Synthetic angle-dependent seismic data are typically generated using angle-dependent Full Wavefield Migration (FWM) [19]. This workflow follows the structure of traditional inversion schemes, including data comparison, adjoint forward modelling, model updating, and seismic forward modelling [20]. The key innovation in angle-dependent FWM versus traditional FWM lies in the forward modelling step [21], where angle dependence is preserved. To obtain the angle-dependent data, at each lateral location, the down-going wavefield is cross-correlated with a back-propagated residual, spatially shifted via a 2D lag. A 2D Radon transform is then applied to the reflectivity operators, and stacking across frequencies generates an angle-dependent image volume, or angle-gather block [19]. These angle gathers organize seismic reflections by incidence angle at a subsurface point and are typically separated into positive and negative angles [19, 22, 23].

Angle-dependent seismic data obtained through the application of angle-dependent FWM have shown potential to encode metre-scale heterogeneities in acoustic

properties [20, 23–25]. However, the potential diagnostic use of asymmetry between positive and negative incidence angles in angle gathers has not yet been explored. In laterally homogeneous media, these gathers appear symmetric; in contrast, heterogeneities lead to asymmetric responses [19]. This asymmetry arises from the physics of wave interactions at geological boundaries, where conservation of energy and momentum leads to reflection, transmission, and conversion phenomena—all of which alter amplitude [9].

Traditionally, angle gathers have been used in Amplitude Versus Offset/Angle (AVO/AVA) analysis to infer properties like saturation and lithology, using the Zoeppritz equations or their approximations [26, 27]. Additionally, they are employed in migration velocity model updates, based on gather curvature [28]. These uses typically reduce the gather to two parameters: intercept (zero-angle amplitude) and gradient (amplitude variation with angle).

This paper instead explores the direct use of angle-gather data for characterizing variations in acoustic properties, without reducing the data to intercept and gradient values. Rather than simplifying the data, we preserve the full angle-dependence by generating a separate subsurface image for each incidence angle [29]. This approach enables the capture of variations in energy arrival associated with different angles of incidence. Such variations arise from ray bending effects dictated by Snell's Law, which lead to asymmetries in amplitude distributions between positive and negative incidence angles [29].

To achieve this, we conduct a statistical and visual analysis of the relationship between angle gather asymmetry and variations in acoustic properties, specifically P-wave velocity and mass-density. Our workflow integrates stratigraphic forward modelling and seismic forward modelling, applied to a suite of synthetic geological models based on wave-dominated shoreface systems [30]. From these models, we generate corresponding angle gather datasets and compute statistical descriptors of gather asymmetry.

Although the Earth is an elastic and 3D medium, this study focuses solely on acoustic parameters—P-wave velocity and mass density—and simplifies the analysis to 2D, as an initial step towards understanding the potential of angle-gather asymmetry in characterizing subsurface heterogeneity.

5.2. Methodology

5.2.1. Data generation and processing

We employ a multi-step methodology adapted from Cuesta-Cano *et al.* [30] to investigate metre-scale stratigraphic heterogeneities in geological subsurface settings. This generic approach can be applied to various depositional settings by

modifying the input stratigraphic model. In this study, we apply it to heterogeneities developed in wave-dominated, shoreface systems. Compared to traditional lithofacies-based methods, this workflow more accurately captures the seismic response of metre-scale heterogeneities [30].

The methodology consists of three main steps. First, a stratigraphic forward modelling tool, here BarSim [31], is used to generate 2D geological simulations that include architectural features at different scales (Figure 5.1A). The output of BarSim includes grain size distribution data with cells of $2m$ in the vertical direction and $50m$ in the horizontal. These simulations are the basis for the construction of geological models that include a reservoir area, overburden and a water layer on top. More information on BarSim and pyBarSim, the python implementation of the modelling tool, can be found in Appendix 1. The second step involves converting the grain size data into acoustic parameters – mass-density and P-wave velocity – through the application of empirical equations (Figure 1B). Here, the equation suggested by Eberhart-Phillips et al. (1989) is applied for the calculation of P-wave velocity. For the calculation of mass-density, we assume that the grain fraction is composed solely by quartz grains and the porosity is water-saturated. The grid of the models is then linearly interpolated to a 2x2m cell grid. The third step consists of the application of seismic forward modelling based on the finite-difference time-domain method and the following application of full-wavefield migration in angle-dependent mode.

In both the seismic modelling and the migration, we used the same input parameters as in Cuesta-Cano *et al.* [30]. The migration generates image-angle gathers for all the lateral locations (Figure 5.1C). When summed along the angle axis, we obtain the structural reflectivity image. At each horizontal location in the simulation, the angle-gather data form a two-dimensional space, where the vertical axis represents depth and the horizontal axis corresponds to the ray parameter, which is dependent on the angle of incidence.

The angle-gather panels located at the edges of each section exhibit poor imaging quality due to unbalanced energy arrival caused by edge effects. These edge effects result from limited subsurface illumination and reduced wavefield coverage at the section boundaries. As a result, these panels were excluded from the analysis of angle-gather asymmetry, mass density, and P-wave velocity (Figure 5.1D). These poorly imaged areas account for $1200m$ at each end of the section. Additionally, common artifacts observed in synthetic data in the outermost parts of the far-angle range were removed from the angle-gather data (Figure 5.1E).
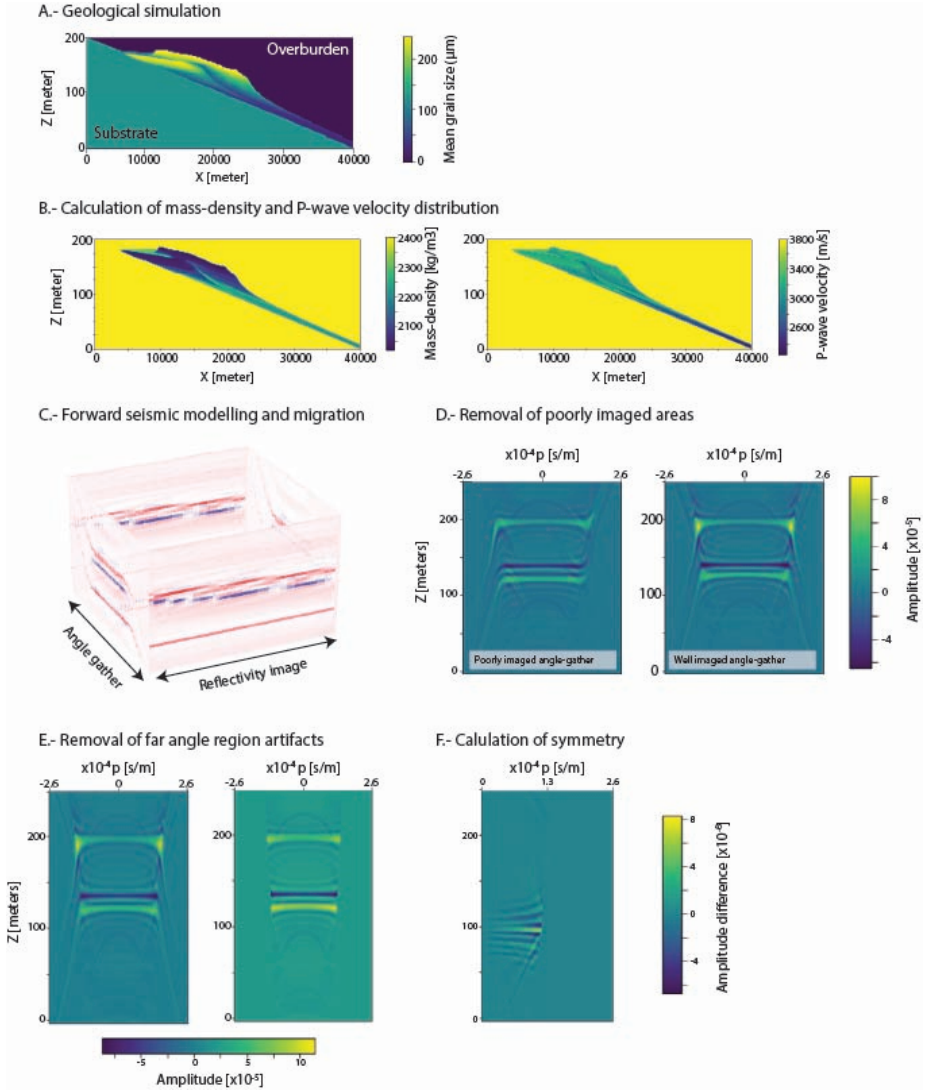
Figure 5.1: Methodology to generate the dataset analysed in this paper. A.- First, we use BarSim, a stratigraphic forward modelling tool, to generate geological simulations with heterogeneities at a $50x2m$ scale. BarSim outputs grain size distribution data, here represented as mean grain size (μm). For more information about BarSim, we refer to Appendix 1. B.- From the grain size distribution, we calculate mass-density (kg/m^3) and P-wave velocity (m/s). C.- Then, we apply forward seismic modelling and migration techniques to obtain the reflectivity images and the angle-gather data. From the angle gather data, (D) we remove the poorly imaged angle gathers on the side of the simulations and (E) the artifacts on the far angle region. F.- Finally, we calculate the asymmetry of each angle gather by subtracting one half to the other one.

To analyse the asymmetry of the angle-gather data, we split the axis representing the ray-parameter data into two halves, mirror them and calculate the difference as a subtraction (Figure 5.1F). For every location, we calculate the maximum difference value, the minimum difference value, the mean difference value, the absolute mean difference value, and the standard deviation. We have also defined three extra parameters that might capture the asymmetry better than more classical statistical parameters:

- The total sum of the absolute difference of the absolute amplitudes,

- The total sum of the absolute difference of the amplitudes, and

- The total sum of the difference of the absolute amplitudes.

For each location, we calculate the mean and standard deviation of P-wave velocity and mass density, as well as identify the presence of sharp lateral discontinuities. These discontinuities are defined as locations where a distinct contact occurs between the reservoir and the surrounding background medium along vertical planes. Given the grid structure, these lateral discontinuities manifest over vertical extents of approximately $2m$, corresponding to the height of individual grid cells. Such sharp contacts are observed at both the top and bottom boundaries of the reservoir (Figure 5.2). To detect these discontinuities, we analyse each column by comparing the first and last appearance of the reservoir with those in the adjacent column. If the first appearance of the reservoir differs from that of the neighbouring column, it indicates a step at the top surface of the reservoir, which is assigned a value of 1. Similarly, if the last appearance differs, this is also considered a step, this time at the bottom of the reservoir, and assigned a value of 2.
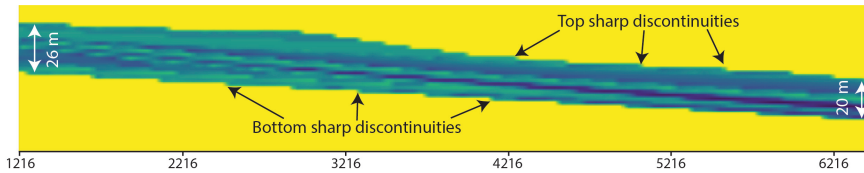

Figure 5.2: Example of some of the locations where we can find sharp lateral discontinuities at reservoir level, both at the top and the bottom boundaries. These discontinuities result in abrupt property contrast and they are related to the grid structure of the scenarios.

The statistical properties describing angle-gather asymmetry and the evolution of acoustic parameters are compared—both visually and, where applicable, quantitatively—to each other. Additionally, the location of lateral discontinuities is compared to the angle-gather asymmetry to assess potential correlations between spatial heterogeneities and variations in seismic response.

5.2.2. Methodology for data analysis

This study employs two types of comparison methods. The first is a numerical comparison, which involves calculating correlation coefficients between statistical parameters derived from angle-gather asymmetry and acoustic properties. The aim is to quantify both the strength and the direction (positive or negative) of the relationship between pairs of variables. Four correlation metrics are used: Pearson's correlation coefficient (r), Spearman's rank correlation (ρ), Kendall's Tau (τ), and distance correlation (DC). Each method is suited to detecting different types of relationships.

Pearson's correlation measures linear relationships between continuous variables, assuming normal distribution and homogeneity of variance, but is sensitive to outliers ([32], and references therein). Spearman's rank correlation assesses monotonic relationships based on the ranked values of variables. It does not require normality and can capture non-linear monotonic trends, though it is still sensitive to outliers ([32], and references therein). Kendall's Tau also evaluates monotonic relationships based on rankings but is better suited to small sample sizes, handles tied ranks more effectively, and is less sensitive to outliers than both Pearson's and Spearman's methods ([32], and references therein). Distance correlation, on the other hand, can identify both linear and non-linear dependencies, including non-monotonic relationships, and is similarly robust to outliers ([33], and references therein). This makes distance correlation particularly valuable for detecting complex relationships that may be missed by the other methods.

Since the nature of the relationships between the variables is not known a priori, all four correlation measures are computed and compared. Differences between the values of the correlation coefficients can provide insight into the type (linear or non-linear, monotonic or non-monotonic) and strength of the relationships. To further assess the robustness of these correlations, scatter plots are used to visualize the parameter pairs with the highest and lowest correlation coefficients.

The second approach is a visual comparison. Here, the statistical parameters derived from the angle-gather asymmetry data are plotted against the mean values of the acoustic properties. This analysis is intended to identify patterns in the evolution of the asymmetry-related statistical measures and how these patterns relate to variations in acoustic properties.

5.3. Data generation

Nine geological models were generated and grouped into three categories based on their similarities (Figure 5.3). All models include a $100m$-thick seawater layer at the top and an overburden of $1100m$. Due to computational limitations associated with forward seismic modelling and migration, the models, which exceeding $40km$ in

the horizontal direction, were divided into sections. Specifically, each model was split into seven sections of $7600m$, along with a smaller eighth section. To ensure complete imaging coverage, adjacent sections overlap by $1800m$.

Each group represents different types of stratigraphic heterogeneity, which are caused by varying interactions between relative sea-level fluctuations and sediment supply. Group 1 models are based on simulations reflecting a fall–rise–fall relative sea-level (Figure 5.3 – Model Group 1), with minor differences between models due to small differences in sea-level variation rate. The main distinction among the 1.1, 1.2, and 1.3 models lies in the development of a high P-wave velocity zone that traverses the model, which appears as a continuous feature only in model 1.2.

Group 2 models simulate sedimentation associated with a rise–fall–rise sea-level cycle (Figure 5.3 – Model Group 2), again with small differences in sea-level variation rate across models. The primary differences among the 2.1, 2.2, and 2.3 models include the position of a top-surface protrusion and the geometry of a high P-wave velocity region located beneath it.

Group 3 uses the same relative sea-level variations as Group 1 but assumes reduced sediment input, resulting in thinner models (Figure 5.3 – Model Group 3). The most significant difference between the 3.1, 3.2, and 3.3 models is the formation of a low P-wave velocity zone near the centre of the model.
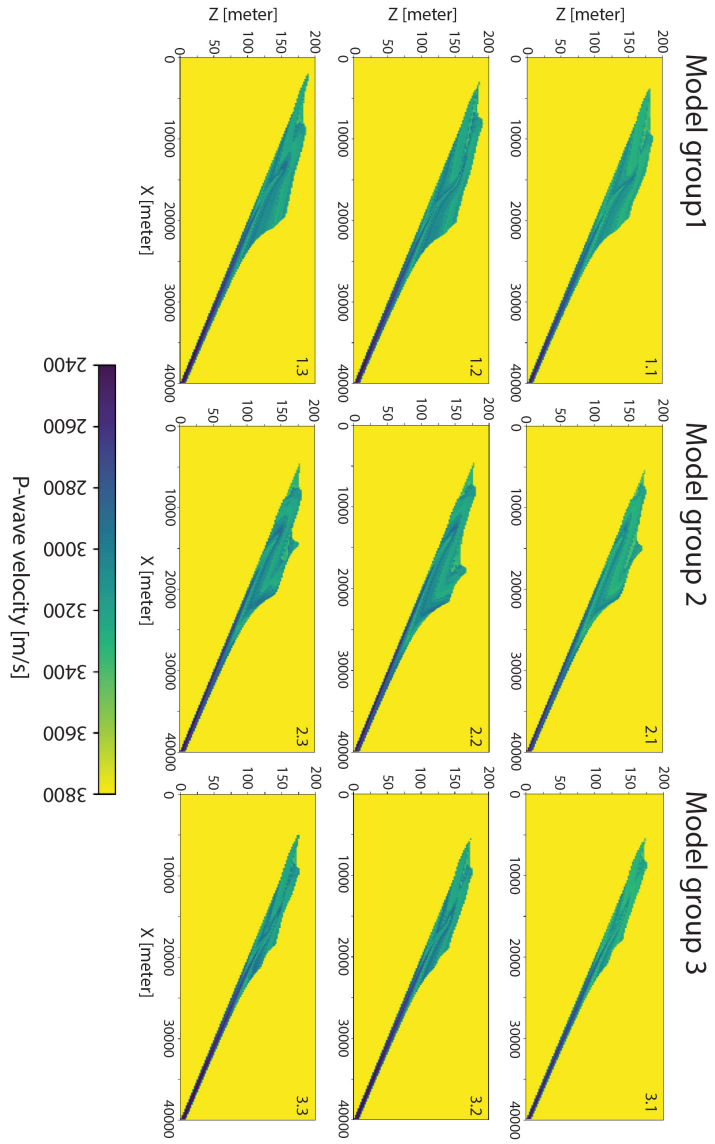
Figure 5.3: P-wave velocity (m/s) distribution of the reservoir area for the nine models used for this research. The overburden has been removed so the P-wave velocity distribution within the reservoir is properly imaged. The models are organised in three groups, based on the similarity between them. Note that the same colour bar has been used for all the subfigures. Z indicates the thickness of the model and X, the lateral extent, both in m.

5.4. Results and interpretation

5.4.1. Correlation coefficients between the asymmetry of angle-gather data and acoustic properties

The correlation coefficient analysis between the statistical properties calculated for the asymmetry on the angle-gather data and the acoustic properties includes correlation coefficients of four methods: Pearson's, Spearman's, Kendall's (Figure 5.4), and distance correlation (Figure 5.5). In general, the Pearson's coefficient shows weak correlation between the acoustic and angle gather related variables, with coefficients rarely deviating from the range -0.3 to 0.3 (Figure 5.4). Moderate positive correlation is observed between the standard deviation of P-wave velocity and the maximum values standard deviation of the angle gather asymmetry and the sum of absolute difference of (absolute) amplitudes. The standard deviation of P-wave velocity also displays a moderate, but negative, correlation with the minimum values of the angle gather asymmetry. Spearman's correlation agrees with the results from the Pearson's correlation (Figure 5.4), and it displays a stronger correlation between the standard deviation of the P-wave velocity and the angle gather asymmetry related variables. Compared to Pearson's correlation, Spearman's correlation coefficient shows notably higher values when assessing the relationship between the absolute mean angle gather asymmetry and both the mean mass density and mean P-wave velocity. Kendall's correlation coefficients are, in general, lower than those obtained for the Pearson's correlation, with the exception of the absolute mean angle gather asymmetry and the mean P-wave velocity (Figure 5.4), in agreement with the Spearman's coefficients. The distance correlation (DC) coefficients agree on the moderate correlations between the P-wave velocity standard deviation and various angle gather asymmetry statistical parameters, for which the highest coefficients are obtained for standard deviation and the sum of absolute difference of (absolute) amplitudes, DC coefficients 0.67 and 0.7 respectively (Figure 5.5). Distance correlation also calculates moderate correlation coefficients between all the acoustic property-related statistical measures and the maximum values, minimum values and standard deviation of the angle gather asymmetry, with DC coefficients above 0.4.
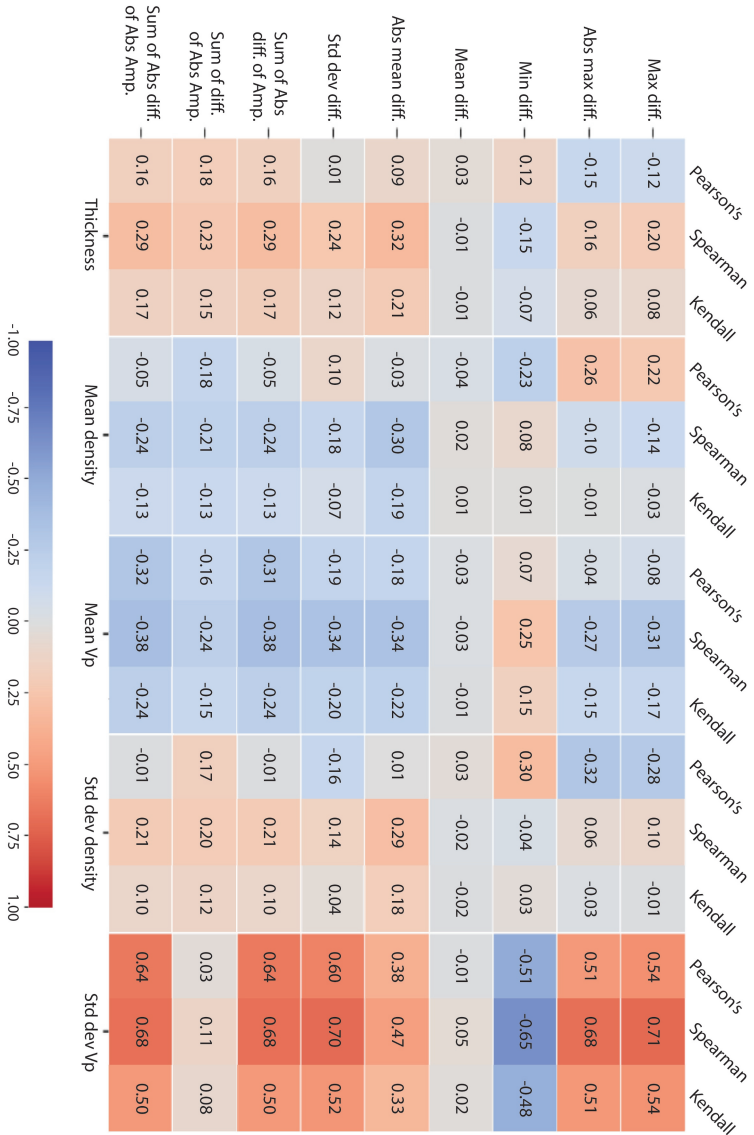
	Thickness			Mean density			Mean Vp			Std dev density			Std dev Vp		
	Pearson's	Spearman	Kendall	Pearson's	Spearman	Kendall	Pearson's	Spearman	Kendall	Pearson's	Spearman	Kendall	Pearson's	Spearman	Kendall
Max diff	-0.12	0.20	0.08	0.22	-0.14	-0.03	-0.08	-0.31	-0.17	-0.28	0.10	-0.01	0.54	0.71	0.54
Abs max diff	-0.15	0.16	0.06	0.26	-0.10	-0.01	-0.04	-0.27	-0.15	-0.32	0.06	-0.03	0.51	0.68	0.51
Min diff	0.12	-0.15	-0.07	-0.23	0.08	0.01	0.07	0.25	0.15	0.30	-0.04	0.03	-0.51	-0.65	-0.48
Mean diff	0.03	-0.01	-0.01	-0.04	0.02	0.01	-0.03	-0.03	-0.01	0.03	-0.02	-0.02	-0.01	0.05	0.02
Abs mean diff	0.09	0.32	0.21	-0.03	-0.30	-0.19	-0.18	-0.34	-0.22	0.01	0.29	0.18	0.38	0.47	0.33
Std dev diff	0.01	0.24	0.12	0.10	-0.18	-0.07	-0.19	-0.34	-0.20	-0.16	0.14	0.04	0.60	0.70	0.52
Sum of Abs diff. of Amp.	0.16	0.29	0.17	-0.05	-0.24	-0.13	-0.31	-0.38	-0.24	-0.01	0.21	0.10	0.64	0.68	0.50
Sum of diff. of Abs Amp.	0.18	0.23	0.15	-0.18	-0.21	-0.13	-0.16	-0.24	-0.15	0.17	0.20	0.12	0.03	0.11	0.08
Sum of Abs diff. of Abs Amp.	0.16	0.29	0.17	-0.05	-0.24	-0.13	-0.32	-0.38	-0.24	-0.01	0.21	0.10	0.64	0.68	0.50

Colour scale: -1.00, -0.75, -0.50, -0.25, 0.00, 0.25, 0.50, 0.75, 1.00

Figure 5.4: Results for Pearson's, Spearman, and Kendall, between the asymmetry of the angle-gather data and the mass-density and P-wave velocity statistical parameters. Here, the correlation between angle-gather data has not been included. The strongest correlations are observed between the standard deviation of the P-wave velocity and the maximum values, minimum values, standard deviation of the angle gather asymmetry and the sum of the absolute difference of (absolute) amplitudes. The mean asymmetry displays weak correlation values in all the cases.

The correlation coefficients show that there could be a moderate dependency (values ranging from 0.40 to 0.67) from the maximum values, minimum values, standard deviation from the angle gather asymmetry data and the sum of difference with both the standard deviation and the mean values of mass-density and P-wave velocity. However, the lower Pearson's, Spearman's and Kendall's correlation indicate that, in case of an existing relationship, this would be nonlinear and non-monotonic. The exception is the variable pairs including the standard deviation of the P-wave velocity, which shows the strongest correlation coefficients across all measures, indicating a possible strong complex correlation, possibly monotonic (due to the high Spearman coefficients) and with a linearity component (due to the values of the Pearson coefficient) with the angle gather asymmetry data.

The lowest correlation coefficients are those from variable pairs including the mean value (from 0.01 to 0.05, in negative and positive, Figure 5.4) of the asymmetry of angle gather, which also display low DC coefficients (Figure 5.5). There are some parameter pairs, for instance sum of absolute difference of absolute amplitudes versus standard deviation of mass-density, that display very low Pearson's correlation coefficients, indicating a nonlinear relationship, but the distance correlation is moderate (coefficient 0.38), which could indicate a monotonic correlation, due to the higher Spearman coefficients.

Scatter plots have been generated to evaluate the nature of the possible relationships between parameters (Figure 5.6). For the plots including parameter pairs with high DC values, the data points often form distributions with shapes resembling arcs and cluster gradients. The relationships are not linear, which is supported by the Pearson's coefficients (Figure 5.4), but show certain consistency where increasing X tends to increase or decrease Y in a predictable way. However, there is variability along the Y-axis for each X-value, meaning that there is dispersion (Figure 5.6A). The high DC plots also show wide vertical spreads in specific X-ranges, implying local regions of strong non-linearity of heterogeneity. In contrast, scatter plots with low DC coefficients display diffuse and unstructured distributions, characterized by a wide range of Y-values for each X-value and an absence of any clear trend (Figure 5.6B). These cases imply weak or negligible statistical dependence between the measures.

These statistical analyses reveal that while many variable pairs show weak correlations, especially those involving mean asymmetry values, others—particularly those including the standard deviation of P-wave velocity—exhibit moderate to strong relationships. The structured patterns observed in the scatterplots further support the presence of non-linear but consistent dependencies. These results help clarify which parameters are most relevant to asymmetry behaviour. This understanding will guide the visual comparisons to assess whether the observed correlations can be used to characterise acoustic property heterogeneities in the metre-scale.
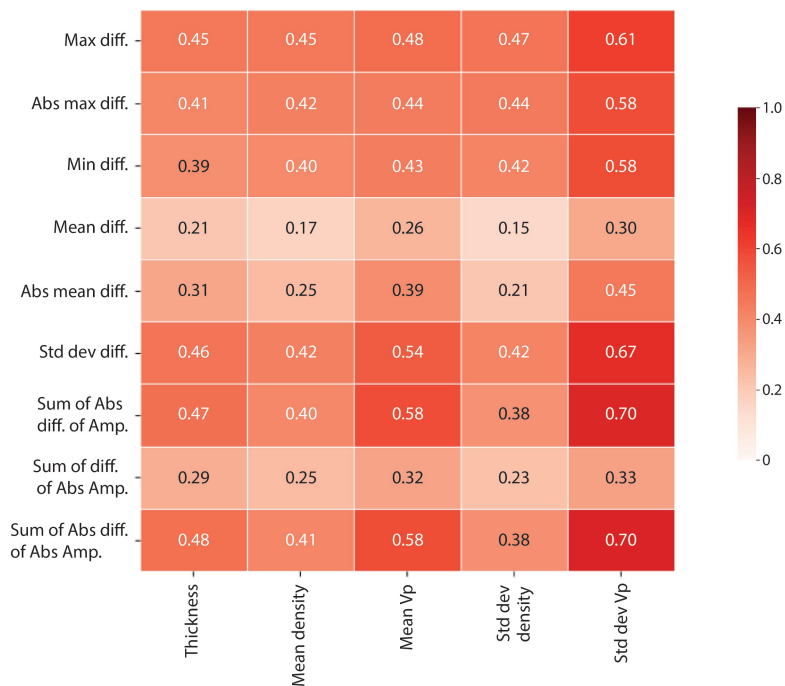
Figure 5.5: Distance correlation coefficients between the asymmetry of the angle-gather data and the mass-density and P-wave velocity statistical measures. Here, the correlation among angle-gather data parameters has not been included. The strongest correlations are observed between the standard deviation of the P-wave velocity and the standard deviation of the angle-gather asymmetry and the sum of the absolute difference of the (absolute) amplitudes. The mean asymmetry displays weak correlation values in all the cases.

5.4.2. Visual correlation of the asymmetry of the angle gathers and acoustic properties

Visual correlation between statistical parameters defining angle-gather asymmetry

The sum of absolute differences of absolute amplitudes and the sum of absolute differences of amplitudes — two parameters developed to investigate how best to characterize the asymmetry of angle-gather data — are highly correlated, exhibiting a Pearson's correlation coefficient of 0.9997. In addition to their strong mutual correlation, both parameters are also strongly correlated with the standard deviation of the asymmetry, each showing a Pearson's coefficient of 0.95.

A visual comparison between the sum of absolute differences of absolute amplitudes

and the standard deviation further illustrates this relationship (Figure 5.7), with both parameters displaying similar overall trends. However, discrepancies between the two are evident at certain locations. In Figure 5.7, red arrows indicate areas where the standard deviation more effectively captures asymmetry through distinct peaks or bulges not reflected in the sum-of-differences signal. Conversely, black arrows highlight areas where the sum-of-differences metric reveals peaks or bulges absent in the standard deviation.
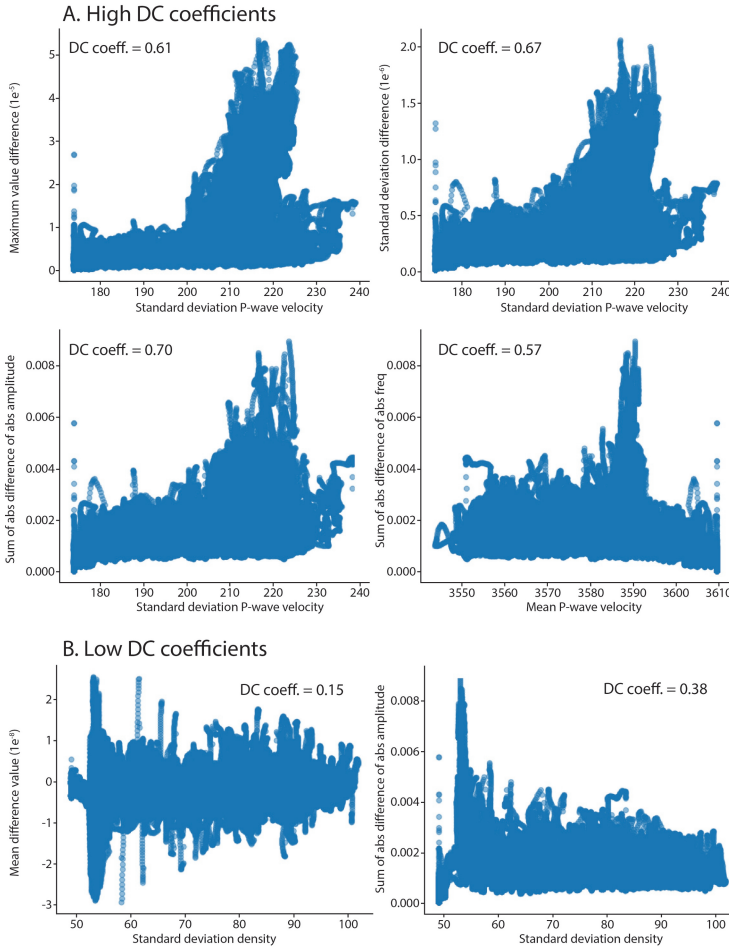
Figure 5.6: Scatterplots display pairs of statistical measures with both the highest and some of the lowest distance correlation (DC) coefficients. Each plot includes the corresponding DC coefficient value. In general, a broader range of Y-axis values is observed for each X-axis value when DC coefficients are low. In contrast, for pairs with high DC coefficients, the widest Y-axis value ranges tend to be concentrated within specific intervals of the X-axis.

Consequently, if the objective of the angle-gather asymmetry analysis is to identify regions of highest asymmetry, either parameter would be sufficient, as both effectively capture the main trends—as confirmed by both numerical and visual correlation. In this context, the standard deviation is the preferred choice due to its widespread availability in statistical libraries and programming packages, which facilitates standardization of the analysis. However, if a more detailed investigation of angle-gather asymmetry is required, these parameters can be both analysed, since each may respond to different aspects of the underlying acoustic properties, potentially offering complementary insights into reservoir characteristics.
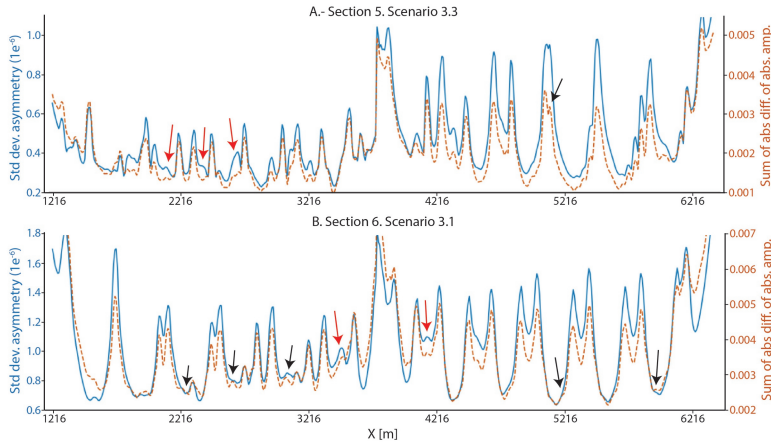
Figure 5.7: Two examples of the comparison between the standard deviation of the asymmetry of angle gather data (blue) and the sum of the absolute difference of absolute amplitudes (orange). These graphs highlight the similarities between both statistical measures. The red arrows point at the locations where the standard deviation displays a more detailed response. The black arrows point at the locations where the sum of absolute difference of the absolute amplitudes show more complex trends.

Indications of poor illumination in angle-gather data

A trend unrelated to acoustic property variations is identified at the beginning of the models, prior to the onset of the reservoir. This trend is characterized by fluctuations in angle-gather asymmetry occurring in regions where no changes in P-wave velocity or mass density are observed (Figure 5.8). Figure 5.8 presents data from Section 1 of Scenario 1.1 and Scenario 2.1, where variations in the maximum, minimum, mean, and standard deviation of the angle-gather asymmetry are evident, despite the absence of corresponding changes in the statistical indicators of acoustic properties.
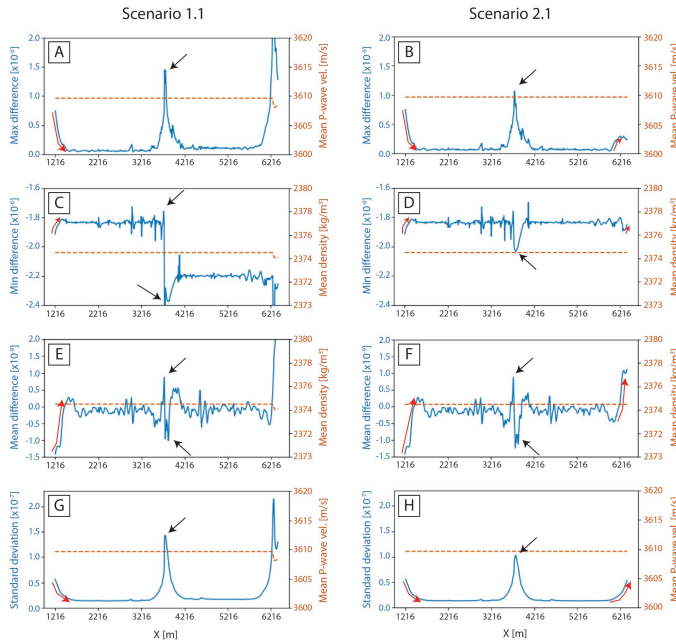
Figure 5.8: Distributions of the maximum values, minimum values, mean, and standard deviation of the angle asymmetry data for Section 1 of 1.1 and 2.1 (blue curves). The orange curves indicate the mean P-wave velocity and mass density, depending on the respective graph. Variations in the angle-gather asymmetry data are observed even in regions where acoustic properties remain constant. Red arrows mark the trends at the beginning and end of the sections, while black arrows highlight the central peaks in the angle-gather data.

At the right end of the graphs for Scenario 1, some variations in acoustic properties are present. Although the overall trends are similar between the two scenarios, the exact values differ. These trends typically involve increasing or decreasing patterns at both ends of the sections, along with one or two peaks in the central area, depending on the specific statistical measure. For instance, the maximum values show a decreasing trend at the left end, an increasing trend at the right end, and a central peak, forming a well-defined maximum (Figures 5.8A and 5.8B). A similar pattern is observed for the standard deviation (Figures 5.8G and 5.8H). In contrast, the mean and minimum values tend to rise at both ends and form two peaks in the central portion of the section (Figures 5.8C–5.8F), although in some cases these peaks are not well defined.

The observed trends in the asymmetry of the angle-gather data are attributed to poor illumination. The edges of the sections were not adequately illuminated, and due to memory limitations, each section had to be divided in the middle for the processing, introducing an additional area of reduced illumination at the centre. As a result, the experimental setup was unable to achieve complete illumination

across the sections. Thus, both lateral and central regions of the sections are unsuitable for analysing the correlation between parameters. These observations also demonstrate that poor illumination has a significant and clear effect on the asymmetry observed in the angle-gather data.

Similar signs of poor illumination are evident across all sections in each geological model. Additional examples can be found in Appendix 2, where red arrows highlight artifacts caused by poor illumination at the edges of the models, and black arrows indicate those occurring in the central areas.

Reservoir detection based on acoustic property variations

A clear trend is observed in the statistical parameters of the asymmetry of the angle-gather data, which can be directly linked to changes in mass density and P-wave velocity (Figure 5.9). The geological simulations used in this analysis include some border areas without reservoir presence. Section 1 corresponds to models from Group 1, and Section 2 corresponds to models from Groups 2 and 3; both sections cover the rightmost edge of the reservoir. The beginning of the reservoir is indicated by a decrease in the mean values of P-wave velocity and mass density (Figure 5.9, orange line). At this same location, an increase is seen in the amplitude of the maximum and minimum values, as well as in the mean and standard deviation of the asymmetry (Figure 5.9). This suggests that the statistical parameters calculated from the asymmetry of the angle gathers are capable of detecting changes in acoustic properties and, therefore, can identify the presence of the reservoir.

Sharp lateral discontinuities in acoustic data

For this analysis, the locations of sharp lateral discontinuities were compared with two variables: the distribution of mean P-wave velocity and the spatial variations in angle-gather asymmetry. These discontinuities arise from the underlying grid structure and span $2m$ in the vertical direction, corresponding to the vertical dimension of the grid cells. Moreover, these locations also represent changes in reservoir thickness, typically where the reservoir becomes one cell thicker or thinner.

Three primary patterns are observed in the comparison between mean P-wave velocity and the presence of sharp lateral discontinuities (Figure 5.10), defined in section 2.1 (Figure 5.2). In many cases, the discontinuities are situated adjacent to the onset of increasing or decreasing P-wave velocities, or at local maxima or minima in velocity (indicated by green arrows in Figure 5.10). Conversely, there are locations where variations in mean P-wave velocity occur without any nearby discontinuities (red arrows in Figure 5.10). In these cases, the observed
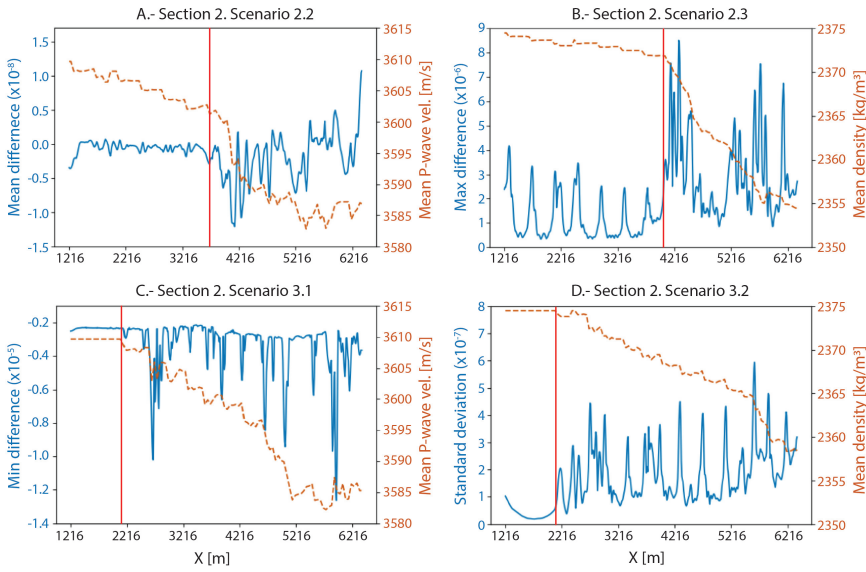
Figure 5.9: Distribution of mean values (A), maximum values (B), minimum values (C), and standard deviation (D) of the angle gather asymmetry data at section 2 of different models. The location where the reservoir starts is indicated by a decrease in the P-wave velocity and mass-density mean values (in orange). At the same location, the amplitude of the angle gather data increases significantly (in blue), proving that the asymmetry of the angle gather data is sensitive to the presence of acoustic property variations.

velocity changes are entirely attributable to internal variations within the reservoir. In contrast, when velocity variations align with sharp discontinuities, they result from a combination of velocity heterogeneities within the reservoir and changes in reservoir thickness at those locations. There are some other cases that the sharp lateral discontinuities are not associated to remarkable velocity changes (black arrows in Figure 5.10). In this case, the change in velocity that is happening within the reservoir is compensated by the change in thickness.

From the comparison between the location of the sharp lateral discontinuities and the sum of absolute difference of the absolute amplitude of the angle-gather data, a parameter defined to measure asymmetry on the angle-gather data, a correlation emerges. This correlation is most clearly expressed in geological model sections 5 and 6, where variations in P-wave velocity within the reservoir are predominantly associated with sharp lateral discontinuities (Figure 5.11). In these sections, peaks in the angle-gather asymmetry parameter often coincide with the presence of sharp vertical discontinuities, even in the absence of pronounced velocity contrasts (highlighted in red in Figure 5.11). In other instances, the asymmetry peaks do not align precisely with the discontinuities themselves but rather with inflection points in the P-wave velocity trends or with locations where the velocity gradient
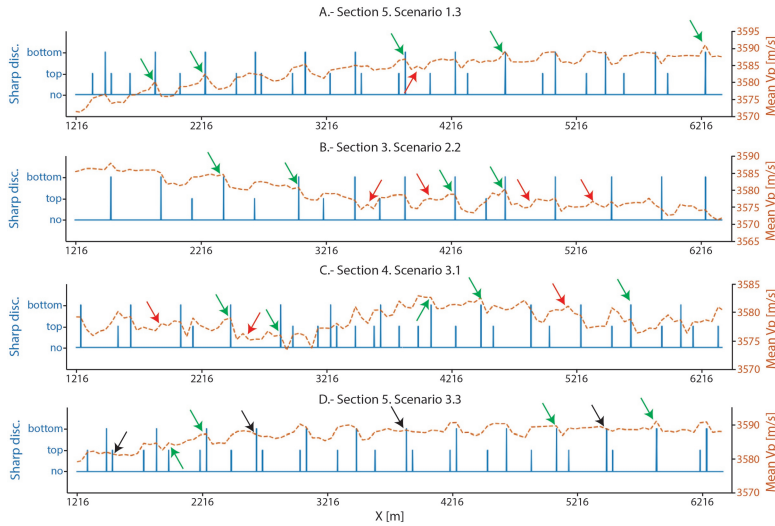
Figure 5.10: Distribution of the mean P-wave velocity (m/s) and location of sharp lateral discontinuities across various sections of different scenarios. Green markers indicate locations where discontinuities coincide with P-wave velocity peaks or the onset of velocity increases or decreases. Red markers denote locations where changes in P-wave velocity do not align with the positions of the identified discontinuities. Black markers highlight sharp lateral discontinuities without associated mean P-wave velocity change.

is most abrupt (highlighted in green in Figure 5.11). Additionally, some velocity transitions associated with lateral discontinuities give rise to dual peaks in the asymmetry measure, as observed in the purple-shaded areas of Figure 5.11. By contrast, regions located away from such discontinuities—characterized by smoother and more gradual velocity transitions—tend to exhibit lower asymmetry values, reinforcing the sensitivity of angle-gather asymmetry to sharp lateral changes in acoustic properties.

For other sections, many asymmetry maxima are linked to inflexion points on the variation trends of the P-wave velocity or internal sharp velocity changes (Figure 5.12). Those internal sharp velocity changes can be located at any depth within the reservoir. However, there is no visual link between the amplitude of the asymmetry peaks and the velocity variations and, whenever more than one abrupt variation happens along the same 1D location, it does not seem to result in higher peak amplitude of the asymmetry. As previously mentioned when defining the sharp lateral discontinuities along the top and bottom surfaces of the reservoir, the abrupt internal velocity variations also display the geometry of the grid on the geological model, with $2m$, vertical contacts. Appendix 3 includes other examples.
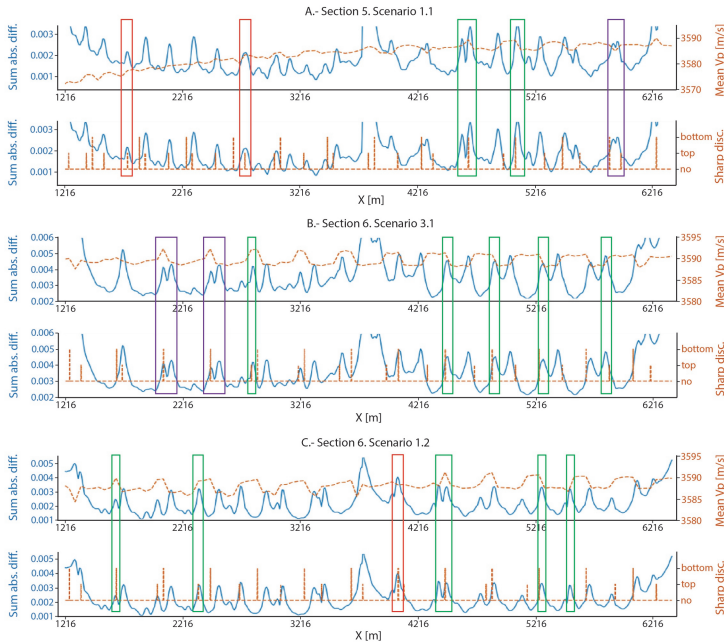
Figure 5.11: Comparison of the angle-gather data asymmetry, mean velocity variations (m/s), and location of sharp lateral discontinuities for three examples from sections 5 (A) and 6 (B and C) in different geological scenarios. Some of the asymmetry peaks match with the location of discontinuities (in red). Some other asymmetry peaks match with the consequences in the velocity trends linked to the presence of discontinuities, either with the inflexion points or the steepest velocity changes (in green) or a double-peaked asymmetry response linked to some velocity change peaks next to discontinuities (in purple).

5.5. Discussion

5.5.1. The influence of P-wave velocity on angle-gather data asymmetry and its implications

Quantitative and visual analyses of the correlation between acoustic properties and angle-gather asymmetry reveal a stronger association with P-wave velocity than with other parameters. This observation aligns with the fundamental physics of seismic wave propagation, where wave velocity plays a dominant role in governing the kinematics of wave travel, including travel times, ray bending, and reflection angles [34]. In contrast, mass density primarily influences reflection amplitudes rather than the geometrical paths of the rays. As asymmetry in angle-gather data increases, even small variations in P-wave velocity can cause distortions in the angle-dependent behaviour of seismic reflections. These effects are amplified in

regions with sharp lateral or vertical velocity contrasts, which can induce changes in the direction and curvature of ray paths.
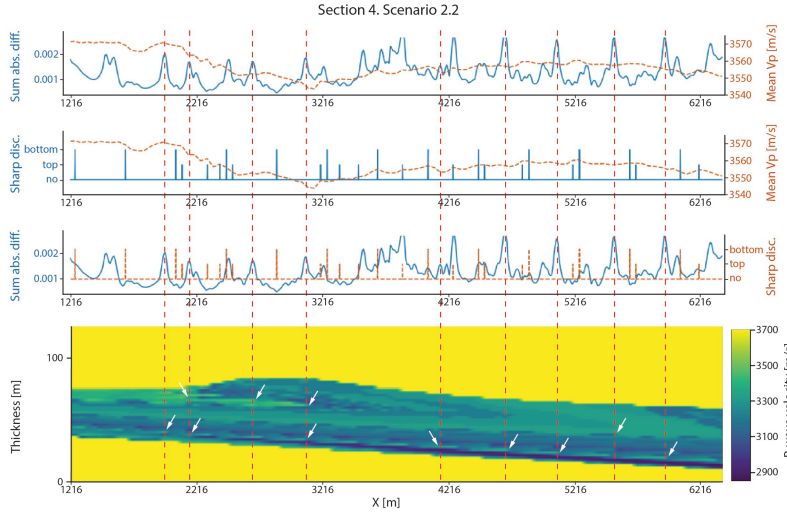
Figure 5.12: Comparison of the distribution of angle-gather data – sum of the absolute difference of the absolute amplitudes –, location of sharp lateral discontinuities along the top and bottom surfaces of the reservoir, mean P-wave velocity distribution, and the P-wave velocity distribution within the reservoir area. The red vertical lines indicate areas where we see peaks of high asymmetry explained by the internal, strong velocity variations indicated with the white arrows.

Moreover, velocity heterogeneity has a direct impact on the wavefield geometry, which in turn affects the inversion processes used in seismic imaging and attribute analysis [35, 36]. Because velocity perturbations modify the travel paths of waves, they result in a stronger influence on kinematic attributes, such as travel-time residuals and angular asymmetry, than do comparable density variations. Consequently, any localized P-wave velocity contrast within the subsurface—such as those arising from lithological changes, stratigraphic discontinuities, or reservoir boundaries—is likely to cause asymmetry in the angle-gather data.

This study demonstrates that even subtle variations in P-wave velocity, occurring within $2m$ grid cells, can be associated with peaks in the statistical parameters used to quantify angle-gather asymmetry, including those detected within the reservoir zone itself. These findings highlight the high sensitivity of angle-gather asymmetry to fine-scale velocity contrasts and their potential as a diagnostic tool for detecting such contrasts. On the other hand, the weaker correlation observed with mass density underscores its relatively limited impact on angle-dependent kinematic responses, suggesting that its influence on asymmetry may be secondary or indirect.

Building on these results, the identified role of metre-scale P-wave velocity variations

reinforces the importance of accurate and high-resolution velocity modelling in seismic interpretation workflows. Effective imaging of reservoir-scale heterogeneity therefore requires detailed spatial mapping of P-wave velocity to avoid smoothing out intra-lithofacies variations or introducing artificial sharp contacts between lithofacies [30] that would impact the asymmetry of the angle-gather data.

5.5.2. Sharp lateral discontinuities: a limitation of synthetic data and new possibilities for angle-gather data applications

The observations presented in this study pointed at a clear relationship between variations in acoustic properties—particularly P-wave velocity—and the asymmetry observed in angle-gather seismic data. This correlation emphasizes the sensitivity of angle-dependent seismic responses to even subtle heterogeneities in subsurface velocity fields. However, these findings also expose important limitations associated with the use of synthetic data and numerical models constructed on fixed-resolution grids, typically defined at the metre scale.

Grid-based discretization is a fundamental requirement of numerical modelling in seismic analysis. In most practical applications, particularly those involving deep reservoirs, the grid resolution does not extend below the metre scale due to constraints in vertical seismic resolution and computational feasibility. While necessary, this gridding approach introduces artifacts, especially sharp lateral contrasts or discontinuities in acoustic properties aligned with vertical grid planes. These artificial discontinuities, resulting from the stepwise representation of continuous property variations, will influence the simulated seismic response as shows in Section 4. Specifically, forward-modelled, seismic synthetic data often exhibit elevated levels of angle-gather asymmetry at or around locations where these abrupt lateral transitions occur—whether at the top, bottom, or within the reservoir interval. A possible option to tackle this problem is performing grid size sensitivity analyses that would provide insight into the extent to which the observed asymmetry patterns arise from discretization artifacts. Nevertheless, the use of finer grids entails an increased computational cost, which may be mitigated by implementing irregular, target-oriented gridding strategies designed to improve the resolution of specific subsurface heterogeneities.

Furthermore, the results of this study indicate that angle-gather asymmetry is highly sensitive to lateral variations in acoustic properties, even when such changes occur over relatively small spatial extents. This characteristic points to the potential of angle-gather asymmetry as a diagnostic attribute for detecting metre-scale geological features, such as small-offset faults or localized stratigraphic heterogeneities. The insights gained here suggest that incorporating angle-gather asymmetry into interpretation workflows may provide a physics-based complement

to traditional methods, enhancing the resolution and reliability of, for instance, subsurface fault detection.

5.5.3. Possible applications of angle-gather asymmetry data and future research

In this study, we have computed a set of basic statistical parameters to quantify the asymmetry of angle-gather data and the variation in acoustic properties. Specifically, for each horizontal location, the vertical distribution of acoustic properties was condensed into a single representative value, while the complex two-dimensional asymmetry patterns observed in the angle-gather panels were summarized using a single representative value for each of the statistical parameters. Although this dimensionality reduction leads to a loss of detail, it enables the identification of moderate statistical dependencies between angle-gather asymmetry metrics and acoustic properties—most notably, P-wave velocity. These dependencies are generally non-linear, non-monotonic, and often complex, thereby proving traditional linear regression approaches insufficient to capture the underlying relationships.

While this parameterization offers initial results, it does not exploit the full spatial data embedded within the 2D asymmetry panels. The potential to interpret or classify specific asymmetry geometries associated with geological features remains unexplored. Previous research investigating the use of angle-gather data to detect metre-scale heterogeneities has focused on machine learning methods applied to synthetic data generated from simplified geological models containing metre-scale variability [16–18]. These studies have demonstrated that angle-gather data can reveal heterogeneity in both 1D vertical profiles [16, 17] and laterally across adjacent traces [18, 37], thereby contributing additional constraints to AVA inversion problems and reducing the appearance of artificial discontinuities between traces.

The present work provides a new perspective to the potential of the angle-gather data by highlighting its added value for identifying lateral variations in acoustic properties, even at metre-scale resolution. However, to fully exploit this potential, more comprehensive studies are required—ones that preserve and analyse the full 2D or even 3D character of both the acoustic property distributions and their corresponding angle-gather asymmetry responses. Such analyses would involve significantly more complex and voluminous data, thereby posing challenges in terms of both computational cost and interpretive tractability. In this context, machine learning techniques—particularly those capable of handling high-dimensional, non-linear relationships—offer a promising pathway. As demonstrated in prior work (e.g., [38]), these methods can help detect subtle dependencies between P-wave velocity, mass density, and asymmetry metrics in a way that is not feasible with traditional statistical tools.

Importantly, before any automated interpretation or inversion strategy using

angle-gather asymmetry is deployed, it is essential to account for acquisition-related artifacts, particularly those caused by poor subsurface illumination. This study has demonstrated that reduced illumination from specific directions and angles can lead to artificial asymmetry in angle-gather data. These artifacts are caused by uneven ray coverage and are not indicative of true geological features. If left unrecognized, such illumination-related asymmetries may be misinterpreted as indicators of abrupt lateral changes in acoustic properties. Fortunately, our analysis shows that these artifacts can be diagnosed by their spatial distribution—specifically, a systematic decrease in asymmetry values towards the centre of the study area, where illumination is complete. Accurate identification and removal of such artifacts is a prerequisite for the reliable use of angle-gather asymmetry in any geological interpretation or data-driven modelling workflow.

Looking ahead, future studies may expand the scope of this analysis by incorporating S-wave velocity into the modelling and interpretation frameworks, enabling the implementation of full elastic inversion approaches. This would allow for a more complete characterization of subsurface mechanical properties and could improve sensitivity to features such as lithological boundaries or fractures. Together, these future developments could improve the reliability and interpretability of angle-gather-based analyses in both synthetic and field seismic datasets.

5.6. Conclusions

This study has explored the potential of angle-dependent seismic data to detect and characterize lateral variations in subsurface acoustic properties. To achieve this, nine geologically plausible synthetic models were constructed, and seismic data were generated using finite-difference time-domain forward modelling, followed by full-wavefield migration in angle-dependent mode. A suite of statistical parameters was then computed to quantify both the asymmetry in angle-gather data and the spatial variation in acoustic properties.

Through visual and statistical correlation analyses, we evaluated the relationships between asymmetry features in the angle-gather panels and acoustic parameters—specifically mass density and P-wave velocity. The results revealed moderate, yet complex, non-linear and non-monotonic correlations, particularly between angle-gather asymmetry and P-wave velocity. The strongest dependencies were found between the standard deviation of P-wave velocity and statistical descriptors of asymmetry, including the standard deviation and the sum of absolute differences of amplitudes. The high correlation coefficients are supported by the data distribution trends on scatterplots.

Visual inspection of the asymmetry maps highlighted that angle-gather asymmetry is capable of detecting the lateral onset of reservoir structures and sharp lateral discontinuities in P-wave velocity, whether occurring at the top, bottom, or within the

reservoir. These results demonstrate the method's sensitivity to metre-scale velocity contrasts, even when simplified statistical descriptors are used.

However, the study also identified the presence of asymmetry artifacts attributable to poor subsurface illumination, resulting from the experimental acquisition geometry. These artifacts, unrelated to true acoustic variations, underline the necessity of identifying and correcting for illumination effects before asymmetry attributes are used for geological interpretation or other applications.

Overall, our findings underscore the diagnostic value of angle-gather asymmetry as a tool for identifying lateral heterogeneities in P-wave velocity. While density exhibited weaker correlations, the results suggest that P-wave velocity is the primary control on angle-dependent kinematic responses, in accordance with theoretical principles of seismic wave propagation. Despite the dimensionality reduction inherent in the statistical approach adopted here, meaningful patterns and dependencies were still recoverable. Future research should move beyond scalar descriptors and focus on capturing the full spatial complexity of 2D and 3D acoustic property variations and their influence on angle-gather asymmetry. This will likely require the use of advanced machine learning techniques capable of handling large, high-dimensional datasets and learning non-linear and non-monotonic relationships.

References

[1] J. de Jager. *Handbook: Risk and Volume Assessment*. Tech. rep. De Jager Geological Consulting, 2021, pp. 1–124.

[2] M. Simmons, A. Davies and L. Cowliff. 'Plausible Characterisation of Subsurface Geology is Essential for the Energy Transition'. In: *First Break* 41 (6 June 2023), pp. 69–74. ISSN: 0263-5046. DOI: 10.3997/1365–2397.fb2023045.

[3] T. Sømme, J. Howell, G. Hampson and J. Storms. 'Genesis, Architecture, and Numerical Modeling of Intra-Parasequence Discontinuity Surfaces In Wave-Dominated Deltaic Deposits: Upper Cretaceous Sunnyside Member, Blackhawk Formation, Book Cliffs, Utah, U.S.A.' In: *Recent Advances in Models of Siliciclastic Shallow-Marine Stratigraphy* (2008), pp. 421–441. DOI: 10.2110/PEC.08.90.0421.

[4] R. Sech, M. Jackson and G. Hampson. 'Three-dimensional modeling of a shoreface-shelf parasequence reservoir analog: Part 1. surface-based modeling to capture high-resolution fades architecture'. In: *American Association of Petroleum Geologists Bulletin* 93 (9 2009), pp. 1155–1181. DOI: 10.1306/05110908144.

[5] P. Ringrose and M. Bentley. *Reservoir Model Design A Practitioner's Guide*. Springer, 2015.

[6] D. Hodgetts and J. A. Howell. 'Synthetic seismic modelling of a large-scale geological cross-section from the Book Cliffs, Utah, USA'. In: *Petroleum Geoscience* 6 (3 2000), pp. 221–229. ISSN: 13540793. DOI: 10.1144/PETGEO.6.3.221.

[7] M. Jackson, G. Hampson and R. Sech. 'Three-dimensional modeling of a shoreface-shelf parasequence reservoir analog: Part 2. geologic controls on fluid flow and hydrocarbon recovery'. In: *American Association of Petroleum Geologists Bulletin* 93 (9 2009), pp. 1183–1208. DOI: 10.1306/05110908145.

[8] N. Grasseau, C. Grélaud, M. López-Blanco and P. Razin. 'Forward seismic modeling as a guide improving detailed seismic interpretation of deltaic systems: Example of the Eocene Sobrarbe delta outcrop (South-Pyrenean foreland basin, Spain), as a reference to the analogous subsurface Albian-Cenomanian Torok-Nanushuk Delta of the Colville Basin (NPRA, USA)'. In: *Marine and Petroleum Geology* 100 (Feb. 2019), pp. 225–245. ISSN: 02648172. DOI: 10.1016/J.MARPETGEO.2018.11.010.

[9] Ö. Yilmaz. *Seismic Data Analysis*. Society of Exploration Geophysicists, 2001.

[10] S. Chopra, J. Castagna and O. Portniaguine. 'Seismic resolution and thin-bed reflectivity inversion'. In: *CSEG RECORDER* (Jan. 2006), pp. 19–25.

[11] D. R. Cox, A. M. Newton and M. Huuse. 'An introduction to seismic reflection
      data: acquisition, processing and interpretation'. In: *Regional Geology and
      Tectonics: Principles of Geologic Analysis*. Elsevier, 2020, pp. 571–603. DOI:
      10.1016/B978-0-444-64134-2.00020-1.

[12] H. Zeng, X. Zhu and R. Zhu. 'New insights into seismic stratigraphy
      of shallow-water progradational sequences: Subseismic clinoforms'. In:
      Interpretation 1 (1 Aug. 2013). doi: 10.1190/INT-2013-0017.1, SA35–SA51.
      ISSN: 2324-8858. DOI: 10.1190/INT-2013-0017.1.

[13] T. Klausen, J. Torland, C. Eide, B. Alaei, S. Olaussen and D. Chiarella.
      'Clinoform development and topset evolution in a mud-rich delta – the Middle
      Triassic Kobbe Formation, Norwegian Barents Sea'. In: *Sedimentology* 65 (4
      2018), pp. 1132–1169. DOI: 10.1111/sed.12417.

[14] A. Jackson, A. Jackson, L. Stright, S. Hubbard and B. Romans. 'Static
      connectivity of stacked deep-water channel elements constrained by
      high-resolution digital outcrop models'. In: *AAPG Bulletin* 103 (12 2019),
      pp. 2943–2973. DOI: 10.1306/03061917346.

[15] K. Bakke, I. Kane, O. Martinsen, S. Petersen, T. Johansen, S. Hustoft,
      F. Jacobsen and A. Groth. 'Seismic modeling in the analysis of deep-water
      sandstone termination styles'. In: *AAPG Bulletin* 97 (9 2013), pp. 1395–1419.
      DOI: 10.1306/03041312069.

[16] A. Karimzadanzabi, A. Cuesta-Cano and E. Verschuur. 'Geologic
      stratigraphic scenario testing via deep learning: towards imaging beyond
      seismic resolution'. In: *84th EAGE Annual Conference & Exhibition*.
      European Association of Geoscientists & Engineers, 2023, pp. 1–5. DOI:
      10.3997/2214-4609.2023101151.

[17] A. Karimzadanzabi, A. Cuesta-Cano and E. Verschuur. 'Analyzing Angle-
      Gather Spectograms: Going Beyond Seismic Resolution'. In: *85th EAGE
      Annual Conference & Exhibition*. European Association of Geoscientists &
      Engineers, 2024, pp. 1–5. DOI: 10.3997/2214-4609.202410931.

[18] P. Wang, Y.-A. Cui, L. Zhou, J.-Y. Li, X.-P. Pan, Y. Sun and J.-X. Liu. 'Multi-task
      learning for seismic elastic parameter inversion with the lateral constraint of
      angle-gather difference'. In: *Petroleum Science* 21 (6 Dec. 2024), pp. 4001–
      4009. ISSN: 19958226. DOI: 10.1016/j.petsci.2024.06.010.

[19] M. Davydenko. 'Full wavefield migration: Seismic imaging using multiple
      scattering effects'. PhD thesis. TU Delft, 2016. DOI: 10.4233/uuid:
      1cda75d5-8998-49fe-997e-b38c9b7f8b8b.

[20] M. Davydenko and D. Verschuur. 'Full-wavefield estimation of angle-
      dependent reflectivity and migration velocity'. In: *Proceedings of the
      87th Annual International Meeting*. SEG, 2017, pp. 5631–5635. DOI:
      10.1190/segam2017-17782606.1.

[21] A. (Berkhout. 'Review Paper: An outlook on the future of seismic imaging, Part I: forward and reverse modelling'. In: *Geophysical Prospecting* 62 (5 Sept. 2014), pp. 911–930. ISSN: 0016-8025. DOI: 10.1111/1365-2478.12161.

[22] B. Biondi and W. W. Symes. 'Angle-domain common-image gathers for migration velocity analysis by wavefield-continuation imaging'. In: *GEOPHYSICS* 69 (5 Sept. 2004), pp. 1283–1298. ISSN: 0016-8033. DOI: 10.1190/1.1801945.

[23] H. Hammad and D. Verschuur. 'Slowness and Reflection Coefficient Curves for Laterally Heterogeneous Media'. In: *81st EAGE Conference and Exhibition 2019*. European Association of Geoscientists & Engineers, 2019, pp. 1–5. DOI: 10.3997/2214-4609.201901538.

[24] N. Chemingui, S. Arasanipalai, C. Reiser, S. Crawley, M. Gherasim, J. Ramos-Martinez and G. Huang. 'Application of Simultaneous Inversion of Velocity and Angle-Dependent Reflectivity in Frontier Exploration'. In: *First Break* 42 (7 July 2024), pp. 79–83. ISSN: 0263-5046. DOI: 10.3997/1365-2397.fb2024061.

[25] H. Jin, S. Luo, Q. Liao, X. Shen, G. Xia, M. Vyas and C. Williams. 'FWI Derived Reflectivity Angle Gathers'. In: *85th EAGE Annual Conference & Exhibition*. European Association of Geoscientists & Engineers, 2024, pp. 1–5. DOI: 10.3997/2214-4609.202410524.

[26] K. Aki and P. Richards. *Quantitative Seismology: Theory and Methods*. University Science Books, 1981.

[27] R. T. Shuey. 'A simplification of the Zoeppritz equations'. In: *GEOPHYSICS* 50 (4 Apr. 1985), pp. 609–614. ISSN: 0016-8033. DOI: 10.1190/1.1441936.

[28] F. Li, J. Gao, Z. Gao, C. Li, W. Zhang and W. Sun. 'Angle domain common image gathers from reverse time migration by combining the Poynting vector with directional decomposition'. In: *Geophysical Prospecting* 69 (4 May 2021), pp. 799–820. ISSN: 0016-8025. DOI: 10.1111/1365-2478.13064.

[29] B. Biondi. *3D Seismic Imaging*. Society of Exploration Geophysicists, 2006.

[30] A. Cuesta-Cano, A. Karimzadanzabi, J. E. A. Storms, G. Rongier, D. J. Verschuur and A. W. Martinius. 'Discretization of small-scale, stratigraphic heterogeneities and its impact on the seismic response: Lessons from the application of process-based modelling'. In: *Geophysical Prospecting* (Mar. 2025). ISSN: 0016-8025. DOI: 10.1111/1365-2478.70015.

[31] J. Storms. 'Event-based stratigraphic simulation of wave-dominated shallow-marine environments'. In: *Marine Geology* 199 (1-2 2003), pp. 83–100. DOI: 10.1016/S0025-3227(03)00144-0.

[32] N. Chok. 'Pearson's versus Spearman's and Kendall's correlation coefficients for continuous data'. PhD thesis. University Pittsburgh, 2010.

[33]   J. Hou, X. Ye, W. Feng, Q. Zhang, Y. Han, Y. Liu, Y. Li and Y. Wei. 'Distance correlation application to gene co-expression network analysis'. In: *BMC Bioinformatics* 23 (1 Dec. 2022), p. 81. ISSN: 1471-2105. DOI: 10.1186/s12859-022-04609-x.

[34]   V. Červený. *Seismic Ray Theory*. Cambridge University Press, 2001.

[35]   A. Guitton. 'On the Velocity-density Ambiguity in Acoustic Full-waveform Inversion'. In: 2014. DOI: 10.3997/2214-4609.20141082.

[36]   J. Yang, Y. Liu and L. Dong. 'Simultaneous estimation of velocity and density in acoustic multiparameter full-waveform inversion using an improved scattering-integral approach'. In: *GEOPHYSICS* 81 (6 Nov. 2016), R399–R415. ISSN: 0016-8033. DOI: 10.1190/geo2015-0707.1.

[37]   P. Wang, X. Chen, J. Li and B. Wang. 'Lateral Constrained Prestack Seismic Inversion Based on Difference Angle Gathers'. In: *IEEE Geoscience and Remote Sensing Letters* 18 (12 Dec. 2021), pp. 2177–2181. ISSN: 1545-598X. DOI: 10.1109/LGRS.2020.3014815.

[38]   S. L. Pintea, S. Sharma, F. C. Vossepoel, J. C. van Gemert, M. Loog and D. J. Verschuur. 'Seismic inversion with deep learning'. In: *Computational Geosciences* 26 (2 Apr. 2022), pp. 351–364. ISSN: 1420-0597. DOI: 10.1007/s10596-021-10118-2.

Appendixes

Appendix 1. Understanding BarSim: a short guide

BarSim is a process-response stratigraphic forward modelling tool designed to simulate the long-term evolution and internal architecture of wave-dominated coastal systems [3–5]. It operates on a simplified 2D cross-shore profile and models the deposition of individual storm beds down to the centimetre scale. BarSim applies mass conservation principles to simulate erosion, transport, and deposition of multiple grain-size classes along the profile. Eroded material is redistributed according to transport dynamics, and sediment is input/output via user-defined net alongshore transport.

Model inputs include:

- Process parameters: model parameters controlling sediment erosion, transport, and deposition – wave efficiency, erosion rate, and transport distances;

- Time-dependent variables – sea-level changes and sediment supply (Figure 5.13A);

- Base conditions – grain-size distribution, wave-base depth, littoral drift, and slope.

Outputs consist of detailed sedimentological properties (e.g., grain-size fractions, mean grain size, sorting, facies, and lithology) for each grid cell (Figure 5.13B). The resulting stratigraphic architectures vary depending on input parameters (Figure 5.14).

We use pyBarSim, a Python-based implementation of BarSim [2], which accelerates simulations and enables interpolation of results onto a regular grid. Its computational efficiency supports rapid scenario generation, capturing metre-scale vertical heterogeneities using standard computing resources.
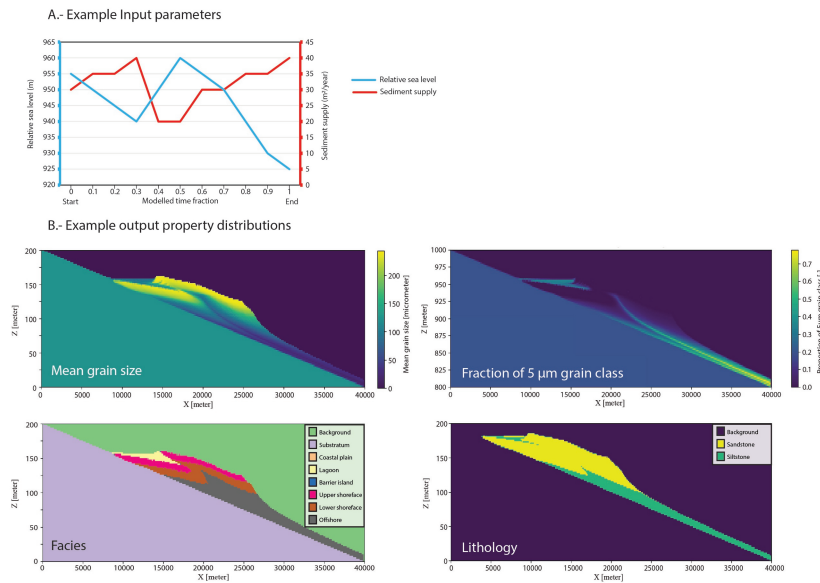
Figure 5.13: Example of BarSim input parameters and resulting outputs. The input parameters include relative sea-level variation and sediment supply rates, each specified over different time intervals. These two parameters typically follow opposing trends. BarSim outputs include detailed sedimentological properties such as mean grain size, the proportion of different grain-size classes, as well as facies and lithological classifications for each grid cell in the model domain.
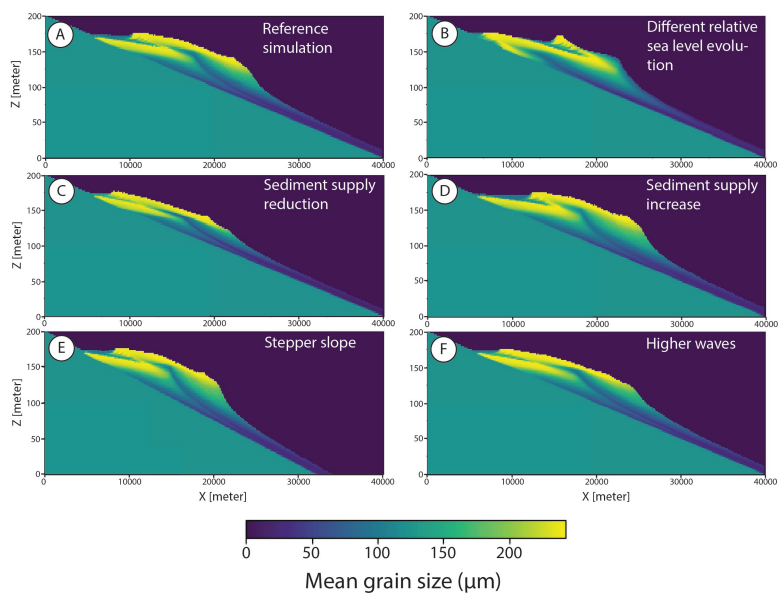
Figure 5.14: Examples of the effects of varying individual input parameters on the simulation of stratigraphic architecture and sedimentological property distribution using BarSim. Subfigure A shows the reference simulation. In subfigures B to F, each simulation retains the input parameters of the reference model, except for the specific parameter indicated in the respective subfigure. These variations illustrate how changes in individual parameters influence the resulting sedimentary architecture and grain-size distribution.

Appendix 2. Poor illumination indicators

A second indicator of poor subsurface illumination is found in the distribution of mean values derived from the angle-gather asymmetry data. Across all models, these mean values consistently exhibit a characteristic stepwise increase at both the beginning and end of each section—regardless of the underlying acoustic property distribution (Figure 5.15). This edge-related trend is particularly evident in sections 3, 4, and 5 across all models, as well as in section 2 for models where reservoir thickness exceeds $10m$. A weaker expression of this trend is also observed in section 6, suggesting that decreased reservoir thickness may mitigate the development of these edge effects.

Additionally, some sections show a repetitive pattern of alternating positive and negative peaks in the central part of the section (Figure 5.15B–E). This central undulation is consistently observed in section 3 across all models and in section 4 for model groups 1 and 2. Although this pattern occasionally appears in section 5, its presence is less distinct due to greater variability in the mean values within that section (Figure 5.15F).

A third indicator of poor illumination is found in the distribution of the standard deviation of angle-gather asymmetry data. Regardless of the underlying P-wave velocity and mass-density distributions, the standard deviation often exhibits a consistent trend: a decrease at the beginning of the section and an increase at the end (Figure 5.16). This pattern is also observed in section 6 for models with a reservoir thickness of $8m$.

Typically, the decreasing trend at the start of the section consists of an initial steep drop followed by a more gradual decline. Conversely, the increasing trend at the end is marked by a gentle rise followed by a steeper ascent. In most cases, the magnitude of the standard deviation variation appears to be correlated with the steepness of the change—sharper transitions are associated with larger variations in standard deviation.

A very similar pattern is observed in the distribution of the sum of absolute differences of absolute amplitudes. Specifically, the beginning of the section is characterised by a steep decrease in the sum values, while the end shows a corresponding steep increase (Figure 5.17). Additionally, the central part of the section displays anomalously high sum values. These central anomalies are interpreted as artifacts resulting from poor illumination, further indicating the influence of acquisition geometry on the angle-gather data.
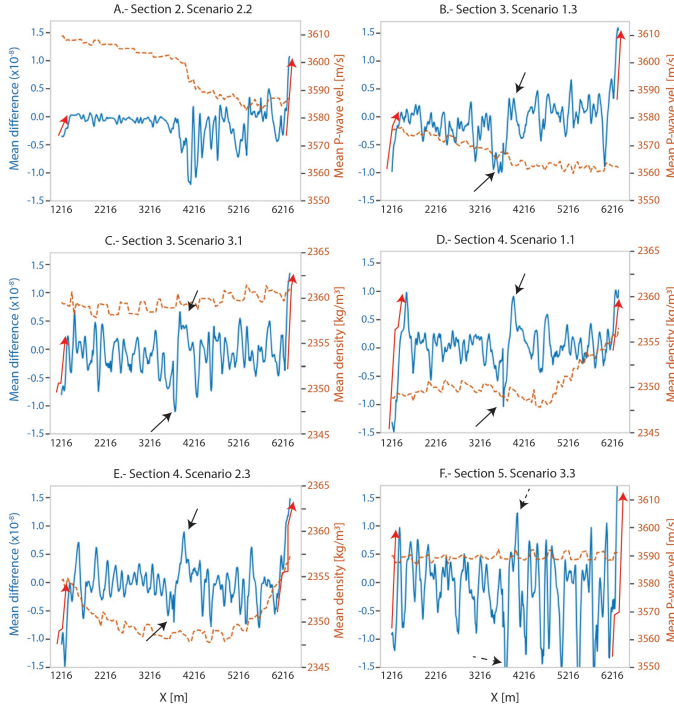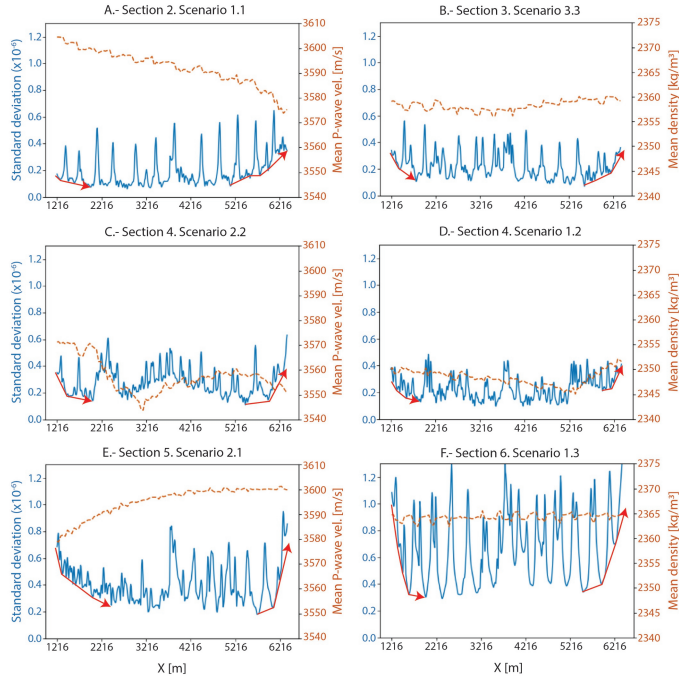
Figure 5.15: Distribution of the mean values of the angle gather asymmetry data versus the mean P-wave velocity or mass-density, depending on the graph, for different models and different sections. In all cases, independent from the acoustic property variations, the mean values display an increasing trend both at the start and end of the section. Sections 3 and 4 also display a two-peak sequence in the central area of the section that does not related to the acoustic property variation (B, C, D and E). In some cases, this sequence can also be interpreted in section 5 (F).

Figure 5.16: Distribution of the standard deviation values of the angle gather asymmetry data versus the mean P-wave velocity or mass-density, depending on the graph, for different models and different sections. In all cases, independent from the acoustic property variations, the standard deviation displays a decreasing trend in values at the start of the section and an increasing trend at the end, indicated in red arrows. These trends are divided into two parts, one steeper and another one gentler.
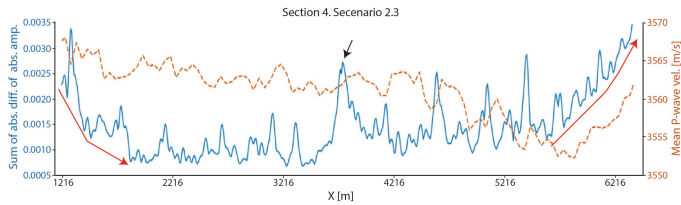
Figure 5.17: Distribution of the standard deviation values of the sum of absolute difference of absolute amplitudes versus the mean P-wave velocity. This example showcases the increased asymmetry towards the edges of the section due to poor illumination (in red). In the central area, there is a peak of asymmetry also related to illumination issues (in black).

Appendix 3. Additional example internal velocity changes linked to asymmetry peaks

This appendix includes an additional example where we compare the asymmetry of the angle-gather data – here represented as the sum of the absolute difference of the absolute amplitude of the angle gather data – with the presence of sharp lateral discontinuities, changes in mean P-wave velocity, and the internal velocity structure within the reservoir (Figure 5.18). This example highlights three locations for which peaks in the asymmetry of the angle-gather are recognised in areas where no sharp lateral discontinuities are recorded nor strong mean velocity variations. For each of those three areas, we have recognised a series of abrupt velocity changes within the reservoir and whose shape is linked to the presence of the grid structure.
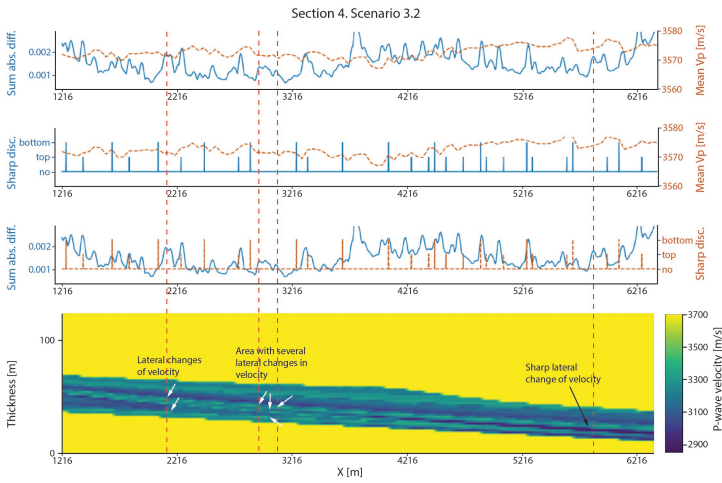
Figure 5.18: Example of locations where the peaks of asymmetry do not coincide with the presence of sharp lateral discontinuities nor variations on the mean P-wave velocity. However, there are internal changes of velocity that might be responsible for the increased asymmetry values.

6

Conclusion and Outlook

In this chapter, I summarise the most relevant findings from previous chapters in relation with the research objectives. As mentioned in 1, the goal of this thesis is to explore new methodologies to characterise the seismic response of metre-scale heterogeneities, which are often considered as sub-seismic scale heterogeneities in subsurface depths $> 2000m$. This chapter will also introduce recommendations for future research based on the findings of this thesis to enhance the characterisation of metre-scale stratigraphic heterogeneities.

6.1. Conclusions

In Chapter 2, fieldwork data from a clastic, wave-dominated shoreface outcrop analogue in Bridger, Montana, USA, are presented. This analogue is part of the Parkman Sandstone and dates to the Middle Campanian (Cretaceous). The objective of this chapter is to characterize the vertical dimensions and nature of stratigraphic heterogeneities and to analyse the distribution of petrophysical, acoustic, and elastic properties. Outcrop analysis reveals that this analogue is characterized by gradual transitions between deposits from different depositional environments, ranging from the offshore transition zone to the backshore. The thickness of deposits associated with each environment is typically less than $10m$. Measurements of petrophysical, acoustic, and elastic properties indicate no distinct value ranges for specific depositional environments. Instead, the data exhibit high variability, even among samples from the same environment. Furthermore, differences in average property values—such as P-wave velocity—between different depositional environments are often minimal, typically less than 10%. Despite these findings, the study was unable to identify clear spatial patterns in the distribution of these properties.

In Chapter 3, I provide a brief review of stratigraphic forward modelling and the available tools. To identify a modelling tool suitable for the method developed in this thesis, I established a set of key requirements. I then evaluated three tools — DionisosFlow, SedSim, and BarSim — against these criteria and concluded that BarSim is the most suitable stratigraphic forward modelling tool.

In Chapter 4, I present a method for characterizing metre-scale stratigraphic heterogeneities, specifically those found in wave-dominated shoreface depositional systems. This approach integrates stratigraphic forward modelling outputs —synthetic stratigraphic architecture and grain-size distribution data — with forward seismic modelling and inversion techniques. The method includes a series of steps to convert grain-size data into acoustic properties, such as mass density and P-wave velocity. These steps involve calculating initial and final porosity based on sorting, mean grain size, and burial depth. I assessed the impact of modelling seismic responses based on grain size compared to traditional workflows, which typically derive acoustic properties from lithology or depositional facies. The study highlights the limitations of conventional lithology-based seismic inversion workflows and Gaussian-based uncertainty analysis. Discretization oversimplifies the complexity within certain facies

or lithologies, failing to capture the effects of gradual acoustic property changes. Moreover, the grain size-based approach more accurately represents the curved stratigraphic architecture and property variations driven by relative sea level fluctuations observed in wave-dominated shorefaces.

In Chapter 5, I evaluated the potential of angle-dependent seismic data for characterizing variations in acoustic properties. This analysis involved both numerical and visual correlations between statistical measures that describe angle-gather asymmetry, mass density, P-wave velocity, and reservoir thickness. The dataset consists of nine geological scenarios generated using the methodology outlined in Chapter 4. The correlation coefficients derived from different correlation algorithms revealed moderate dependencies between P-wave velocity and angle-gather asymmetry, though the relationship is non-linear and non-monotonic. Visual correlations showed that certain trends in the statistical measures of angle-gather asymmetry match thickness variations and others do not correspond to changes in acoustic properties, stemming from illumination limitations on the forward-seismic-modelling algorithms. This study confirms the potential of angle-gathers for detecting acoustic property variations but also emphasizes the limitations of synthetic data generation.

This thesis presents a novel method for the analyse of synthetic data including metre-scale stratigraphic heterogeneities formed in wave-dominated shoreface systems. This method allows the connection between geological, petrophysical, and seismic data for a detailed representation of complex stratigraphic heterogeneities. Unlike traditional approaches for the analysis of metre-scale heterogeneities, this method does not rely on outcrop data collection for geological model generation and utilizes grid cells smaller than the vertical resolution of conventional seismic acquisition surveys. While the method is based on certain assumptions, it demonstrates the feasibility of combining stratigraphic forward modelling with forward seismic modelling to better understand the seismic response of stratigraphic heterogeneities in synthetic data. Additionally, this research highlights key knowledge gaps that need to be addressed to facilitate a more seamless integration and transition between different data types.

6.2. Future Outlook

This section is organized around two key topics that require further research to enhance the characterization of metre-scale stratigraphic heterogeneities. The first addresses the methodological assumptions outlined in Chapter 4 — particularly those concerning the relationships between geological, petrophysical, and seismic properties. For each assumption, alternative strategies are proposed, along with preliminary evaluations and recommendations for future investigation. The second topic explores the steps necessary to establish the proposed workflow as a reliable tool for analysing stratigraphic heterogeneities in real-world subsurface data.

6.2.1. Suggested improvements to the workflow for the characterisation of sub-seismic scale heterogeneities

The method presented in this thesis integrates geological insights from stratigraphic forward modelling with forward seismic modelling to characterise heterogeneities in synthetic data. The stratigraphic modelling output provides data on the distribution of different grain-size classes across the simulation area. To conduct seismic modelling, the grain-size distribution data must be converted into acoustic properties, such as mass-density and P-wave velocity, which is achieved through the calculation of porosity. From porosity, we derive P-wave velocity and mass-density values (Fig. 6.1). However, these calculations are based on certain assumptions. Ideally, these assumptions should be minimized or replaced with data-driven approaches.
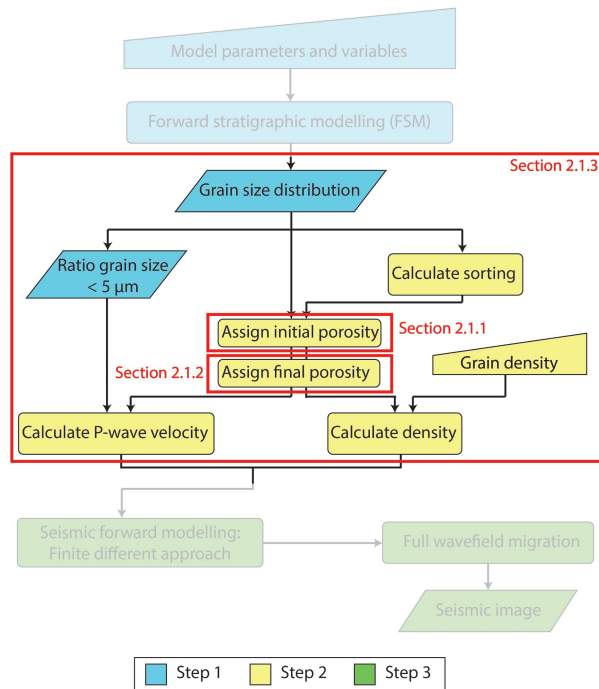
Figure 6.1: Methodology to generate synthetic seismic data including metre-scale stratigraphic heterogeneities. Steps 1 and 3 are based on modelling tools available in the literature. Step 2 is based on a series of sub-steps linking grain size distribution, sorting, porosity and acoustic properties. To refine the methodology, further research is required in the assignation of initial porosity based on grain size, the calculation of final porosity and the general link between grain size and acoustic properties. Modified from [6].

To enhance the method, I identify three areas where improvements could be made (Fig. 6.1): the assignment of initial porosity (section 6.2.1), the calculation of final

porosity (section 6.2.1), and the determination of mass-density and P-wave velocity directly from grain size data (section 6.2.1). Here I explore these assumptions in detail and discuss potential alternatives to refine the workflow.

Different methods to assign initial porosity

Our geological simulations are generated using BarSim, which outputs the ratio of each grain-size class per cell. The latest release of BarSim also includes sorting data [2], a parameter that describes the distribution of grain sizes within the sediment. Research has explored the relationship between grain-size distribution and porosity [7–9], revealing that sorting, rather than grain size itself, is the primary factor controlling the porosity of sand packs [7].

A challenge in using sorting is that different researchers have defined and calculated it in various ways [10–12]. One of the most commonly used definitions is the sorting coefficient introduced by Trask [12], which is calculated as the square root of the ratio between the first and third quartiles of the grain-size distribution. The Trask sorting coefficient helps classify the degree of sorting within a grain mixture. Well-sorted sediments consist mainly of grains of similar size, while poorly sorted sediments contain a wide range of grain sizes.

Friedman [11] examined the relationships between various sorting classifications and proposed a unified approach. In our method, the first assumption is defining sorting as the standard deviation of the grain-size distribution, following the unified method suggested by Friedman [11]. The correlations presented in Table 6.1 have been used to convert the sorting coefficient outputted by BarSim into the Trask coefficient.

Sorting class	Standard dev.	Trask coeff.
Very well sorted	< 0.35	$1.00 - 1.17$
Well sorted	$0.35 - 0.50$	$1.17 - 1.20$
Moderately well sorted	$0.50 - 0.80$	$1.20 - 1.35$
Moderately sorted	$0.80 - 1.40$	$1.35 - 1.87$
Poorly sorted	$1.40 - 2.00$	$1.87 - 2.75$
Very poorly sorted	$2.00 - 2.60$	> 2.75
Extremely poorly sorted	> 2.60	-

Table 6.1: Relationship between sorting classes and the value ranges assigned according to standard deviation and to the Trask coefficient. From Friedman [11].

Once the sorting coefficient is determined, along with its possible conversions, it can be used to estimate the initial porosity. Initial porosity refers to the pore space between grains in a rock immediately or shortly after deposition. Our method follows the approach of Beard and Weyl [7], which establishes a relationship between mean grain size and the Trask sorting coefficient to calculate initial porosity. Based on

the values reported by Beard and Weyl [7], we have defined porosity ranges that depend on both sorting and mean grain size. Since Beard and Weyl [7] provided only a single porosity value for each combination of sorting and mean grain size, we expanded this by using values from adjacent sorting levels within the same grain size category to create upper and lower boundaries for each range. A porosity value is then assigned proportionally based on both mean grain size and sorting.

The dataset used by Beard and Weyl [7] to analyse the relationship between sorting, grain size, and porosity was limited in size and derived solely from a fluvial depositional system. These measurements did not account for variations in grain roundness and sphericity, which can differ across depositional environments [13]. Since roundness and sphericity influence grain packing, they also affect porosity [7, 14, 15]. Despite these limitations, the experiments conducted by Beard and Weyl [7] allowed for the development of an equation that establishes a relationship between initial porosity and sorting:

$$\varphi = 20.91 + \frac{22.9}{S_t} \tag{6.1}$$

where S_t is the Trask sorting coefficient and φ is porosity in percentage. This equation has a R value of 0.97 [9].

Based on the sorting values obtained from BarSim and their corresponding Trask sorting coefficient equivalents, and by applying Equation 6.1, we can calculate the initial porosity for each cell. Since we also know the R value from the equation, we can even introduce noise into the simulation, generating a plausible initial porosity distribution whose relationship to sorting is not fully linear. Figure 6.2. presents examples of initial porosity calculations using two different methods: Method 1, which relies on predefined porosity ranges (currently implemented in the code), and Method 2, which is based on Equation 6.1. The simulations reveal differences of up to 20% (Figure 6.2).

Up to this point, all relationships between grain-size distribution and initial porosity have been derived from the experiments conducted by Beard and Weyl [7]. However, an alternative approach could be explored using Discrete Element Methods (DEM). DEM is a family of numerical techniques designed to analyse the microstructure of granular materials and has previously been used to study the relationship between porosity and grain-size distribution [16, 17]. However, existing research using DEM primarily focuses on systems that have reached mechanical equilibrium, where granular materials achieve their most compact packing. To reach mechanical equilibrium, certain degree of stress must be applied. In nature, this condition does not align with the concept of initial porosity. Nevertheless, these studies provide a valuable foundation for developing new DEM simulations that do not assume mechanical equilibrium. Open-source tools like MigFlow (https://www.migflow.be) offer the capability to simulate grain-fluid interactions and could be applied to this

research.

Impact on acoustic and elastic properties

Exploring alternative methods for calculating the initial porosity in a more realistic manner, while avoiding assumptions, is only meaningful if these approaches lead to differences in the distribution of acoustic and elastic properties within the simulations. Observing such differences would suggest that the seismic response of heterogeneities is influenced by the method used to calculate initial porosity and research should work to obtain initial porosity values as realistic as possible.

Given time constraints, this study focuses solely on evaluating the impact of these methods on the properties required for seismic modelling. To do this, I calculate the initial porosity for the same geological simulation using two approaches: one based on the relationships from Beard and Weyl [7] and the other applying Equation 6.1. The final porosity is then derived using the porosity loss equation from Rubey and Hubbert [18]:

$$\varphi = \varphi_0 e^{-0.39D} \tag{6.2}$$

where φ is final porosity (dimensionless), φ_0 is initial porosity (dimensionless) and D is depth (in km).

Once the final porosity is obtained, we calculate mass-density assuming that the grains are quartz and that the sample is water-saturated. We calculate P-wave velocity using the empirical equation from Eberhart-Phillips, Han and Zoback [19]:

$$V_p = 5.77 - 6.94\varphi - 1.73\sqrt{C} + 0.446 \left(P_e - e^{-16.7P_e} \right) \tag{6.3}$$

where φ is porosity (dimensionless), C is clay content (dimensionless), and P_e is effective pressure ($kbar$).

The relative differences between the two methods have been calculated for three geological simulations (Figure 6.3). In some cases, the difference in final porosity reaches up to 20%. The observed difference in mass-density exceeds 3%, while the difference in P-wave velocity reaches up to 15%.

We present the example with $700m$ of overburden. Since effective pressure at the target level varies with overburden depth, so does porosity loss. As a result, the impact of using different strategies for calculating initial porosity may be either amplified or reduced.

Future research should analyse how different strategies for assigning or calculating

initial porosity affect the seismic response of stratigraphic heterogeneities. This analysis will help determine whether the choice of strategy has a significant impact on seismic interpretation. If substantial variations in seismic response are observed, I recommend to develop porosity assignment tables derived from Discrete Element Method (DEM) simulations. These tables should incorporate grain-size distribution parameters — such as sorting and skewness — as well as grain shape characteristics, including sphericity and angularity.
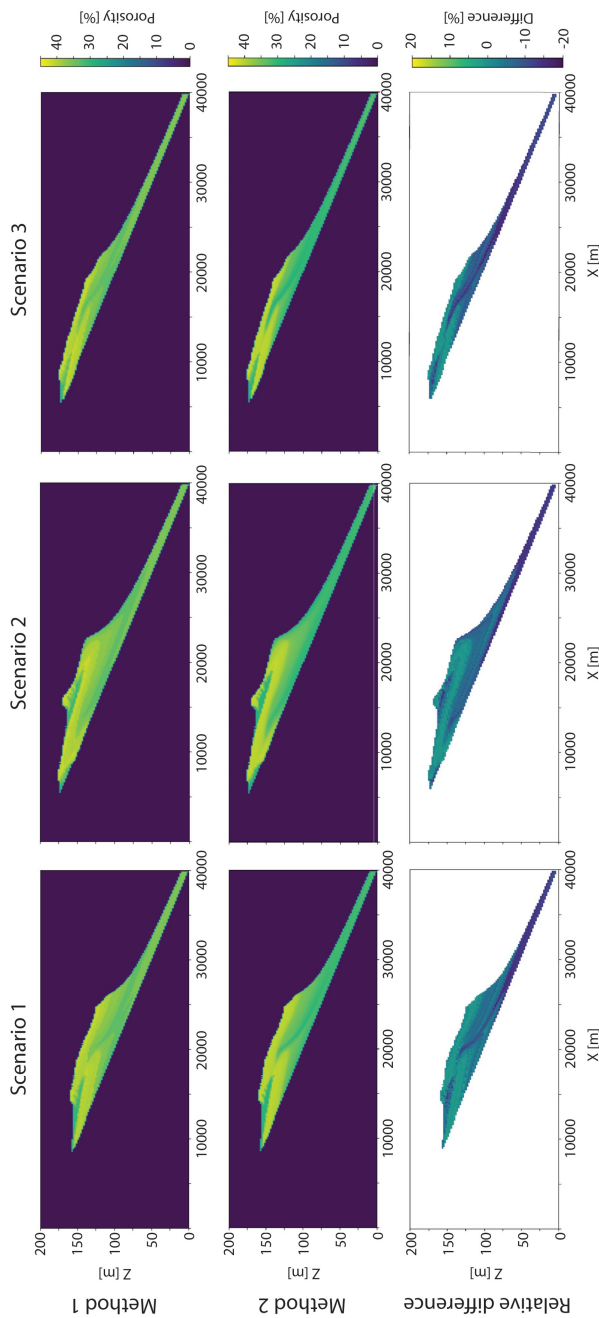
Figure 6.2: Three geological simulations generated with BarSim, each using a different method to calculate initial porosity. Method 1 applies the porosity ranges reported by Beard and Weyl [7], which are currently implemented in the method introduced in this thesis, while Method 2 is based on Equation 6.1. The initial porosity differences between the two methods can reach up to 20%. Porosity graphs share the same colour bar. Each scenario has its own "Difference" scale bar.

Figure 6.3: The relative difference (%) in final porosity, mass-density, and P-wave velocity values between the two methods used for the assignment of initial porosity, at $700\,m$ depth. The differences reach up to 20% for final porosity, 3% for mass density, and 15% for P-wave velocity. Note that each panel uses a different scale bar.
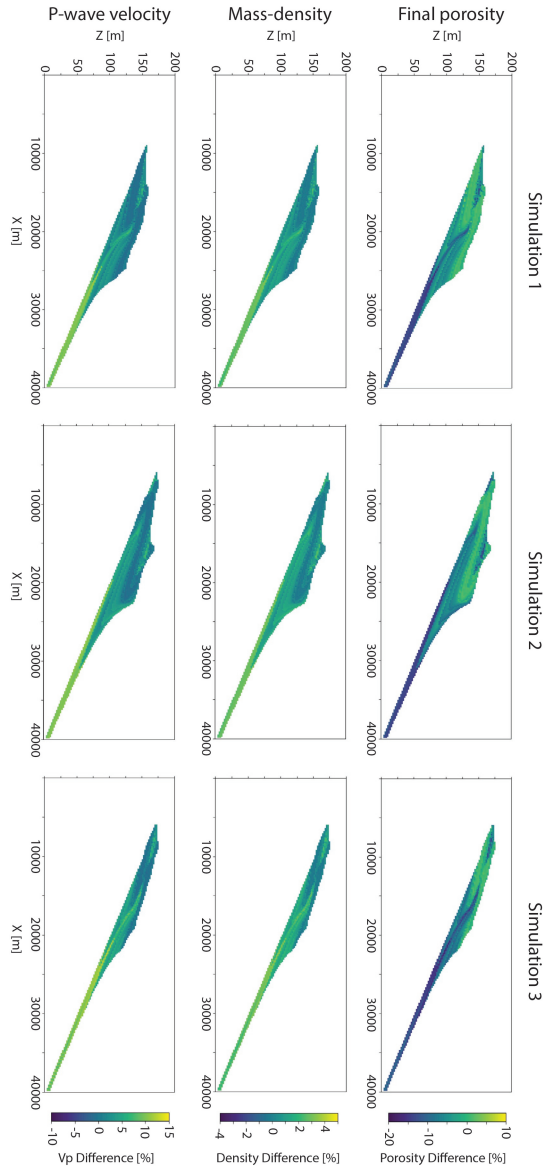
Different methods to calculate final porosity

Once the initial porosity for each cell is determined, the next step is to calculate the final porosity, which accounts for porosity loss as loose sediment undergoes burial. Our current method applies a porosity loss percentage to each cell based on effective pressure and the fine-grain fraction ratio [20]. This approach is similar to the method used in SedSim, one of the stratigraphic forward modelling tools evaluated in 3. SedSim incorporates a look-up table of final porosity values based on fine-grain fraction ratio and effective pressure. We have adapted this approach by computing porosity loss percentages at each step and defining porosity loss ranges (Table 6.2). Our method calculates the final porosity by determining the porosity loss percentage proportionally to the effective pressure and applying it on the initial porosity.

The calculation of porosity loss as a function of depth or effective pressure is a widely studied topic in the literature [18, 21–24]. Researchers have investigated how porosity evolves with depth across different materials, however, porosity loss is highly specific to each basin and/or location [23]. As a result, no single generalized equation can accurately represent all settings. Despite this, here, we evaluate the impact that different methods might have on the seismic response of heterogeneities. To do so, five porosity loss equations have been compiled (Table 6.3). These equations establish relationships between initial porosity, effective pressure (or depth), and final porosity [23]. These equations are applicable for the estimation of porosity loss in normally pressurized sandstones and siltstones.

To assess the impact of the different porosity loss equations, we generated a single initial porosity scenario and calculated the final porosity using each equation, assuming an overburden of $700m$ (Figure 6.4). The difference in final porosity reaches 50% when comparing the method currently implemented in the code with some of these alternative equations. Among the porosity loss equations themselves, the maximum difference observed is 25%, specifically between the results of Method 2 and Method 4 (Table 6.3).

In the calculation of final porosity, effective pressure is a key factor controlling porosity loss, and it is directly influenced by the burial depth of the system. To properly evaluate the impact of different porosity loss equations, it is necessary to consider a range of burial depths. Here, I applied the same initial porosity scenario across various depths and compared the results obtained using Method 2 and Method 4 (Figure 6.5). The difference between these two approaches increases with greater effective pressure. This trend is consistent across all comparisons of final porosity values, with some differences exceeding 40%. These findings highlight the importance of carefully selecting the porosity loss equation, particularly for deeper targets. A notable observation is that the current method tends to overestimate final porosity, with over-predictions reaching up to 90% at depths of $3000m$.

Fine grain fraction	Effective pressure (MPa)					
	0-10	**10-20**	**20-30**	**30-40**	**40-50**	**50-60**
0 – 0.05	0-7.7	7.7-10.3	10.3-12.8	12.8-15.4	15.4-17.9	17.9-19
0.05 – 0.1	0-8.3	8.3-13.9	13.9-16.7	16.7-18.1	18.1-19.4	19.4-21
0.1 – 0.15	0-8.8	8.8-17.6	17.6-20.6	20.6-23.5	23.5-26.5	26.5-29.5
0.15 – 0.2	0-16.4	16.4-31.3	31.3-34.3	34.3-37.3	37.3-40.3	40.3-43
0.2 – 0.25	0-28.6	28.6-40	40-45.7	45.7-48.6	48.6-51.4	51.4-54
0.25 – 0.3	0-27.8	27.8-44.4	44.4-50	50-55.6	55.6-61.1	61.1-67
0.3 – 0.4	0-30.8	30.8-46.2	46.2-56.4	56.4-61.5	61.5-66.7	66.7-71
0.4 – 0.5	0-27.9	27.9-44.2	44.2-58.1	58.1-62.8	62.8-72.1	72.1-80
0.5 – 0.65	0-29.2	29.2-43.8	43.8-54.2	54.2-62.5	62.5-70.8	70.8-77
0.65 – 0.85	0-26.4	26.4-41.5	41.5-54.7	54.7-60.4	60.4-67.9	67.9-75
0.85 – 1	0-24.1	24.1-39.7	39.7-53.4	53.4-62.1	62.1-67.2	67.2-72
1	0-23	23-39.3	39.3-52.5	52.5-60.7	60.7-67.2	67.2-74

Table 6.2: Minimum and maximum percentage (%) of porosity loss per combination of effective pressure (in MPa) and fine-to-coarse ratio (from SedSim, adapted from Wendebourg and Harbaugh [20]). We calculate ethe porosity loss percentage proportionally to the effective pressure.

Reference	Equation
Method 1 [23]	$\varphi = \varphi_0 e^{-0.39D}$
Method 2 [24]	$\varphi = \varphi_0 e^{-0.27D}$
Method 3 [23]	$\varphi = \varphi_0 / (1 + 1.53D\varphi_0)$
Method 4 [21]	$\varphi = \varphi_0 / (1 + 2.18D\varphi_0)$
Method 5 [23]	$\varphi = \varphi_0 e^{-\sigma_{\text{eff}}/33.5}$

Table 6.3: Compilation of porosity loss equations for normally pressurised sandstones and siltstones [23]. φ is final porosity, φ_0 is initial porosity, D is depth (in km), and σ_{eff} is effective pressure (in mPa). All coefficients are in km^{-1}.
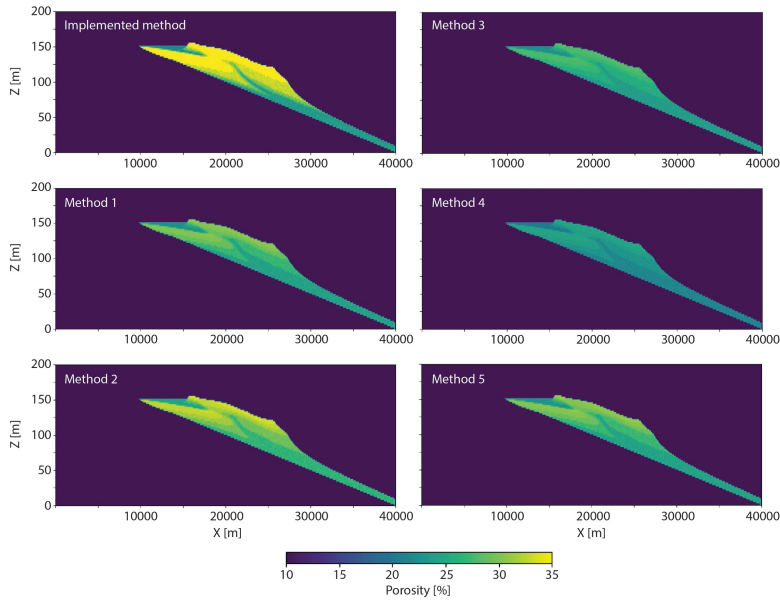
Figure 6.4: For the same initial porosity simulation, the final porosity is calculated based on the method defined in this thesis and five porosity loss equations from literature (Table 6.3). An overburden of $700m$ has been applied to all of the simulations. Note that all simulations share the scale bar. The difference between the final porosity calculated with our method and other porosity loss equations reach 50%.
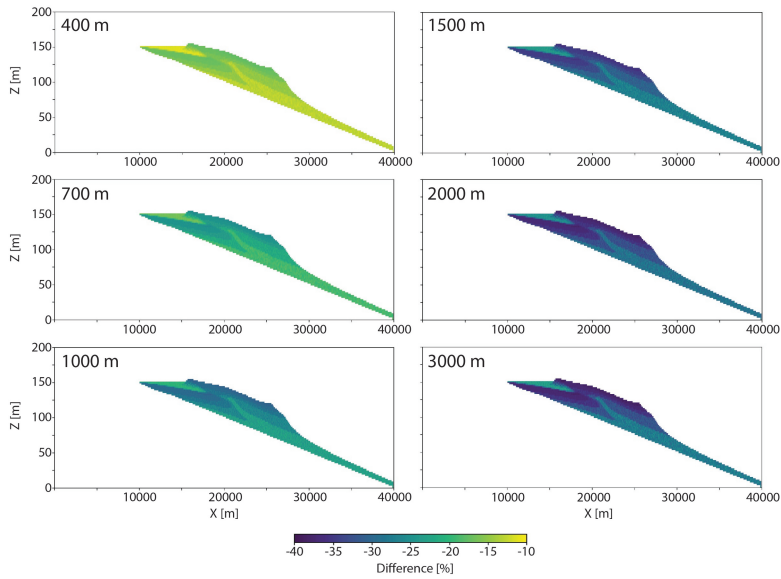
Figure 6.5: For the same initial porosity scenario, difference (%) between the final porosities calculated applying Method 2 and Method 4 (Table 6.3), the ones displaying the greatest difference between the final porosity, for different overburden settings. All simulations share the same scale bar. The difference between the results of final porosity increase with increasing overburden.

Impact on acoustic and elastic properties

The purpose of exploring these alternative approaches is to assess how different methods for calculating final porosity influence the seismic response. As a first step, we examine their effect on the acoustic properties required for seismic modelling—specifically, mass-density and P-wave velocity. Mass-density is calculated under the assumptions that the grains are composed of quartz and the sample is water-saturated. P-wave velocity is estimated using the empirical equation from Eberhart-Phillips, Han and Zoback [19]. For a scenario with an overburden of $700m$, we compute acoustic properties based on the final porosities derived from each method (Table 6.3). The results show differences in mass-density exceeding 6% (Figure 6.6) and variations in P-wave velocity greater than 17% (Figure 6.7).

Since final porosity is directly linked to burial depth and effective pressure — and acoustic properties are derived from final porosity — it's important to assess how these properties vary with depth. To do this, I compared the contrasts in mass-density and P-wave velocity across different overburden thicknesses: 400, 1000, 1500, 2000, and $3000m$. The comparison with the currently implemented method is excluded here, as it significantly overestimates porosity, leading to relative differences of up to 20% in density and up to 40% in P-wave velocity. Focusing on the equations from
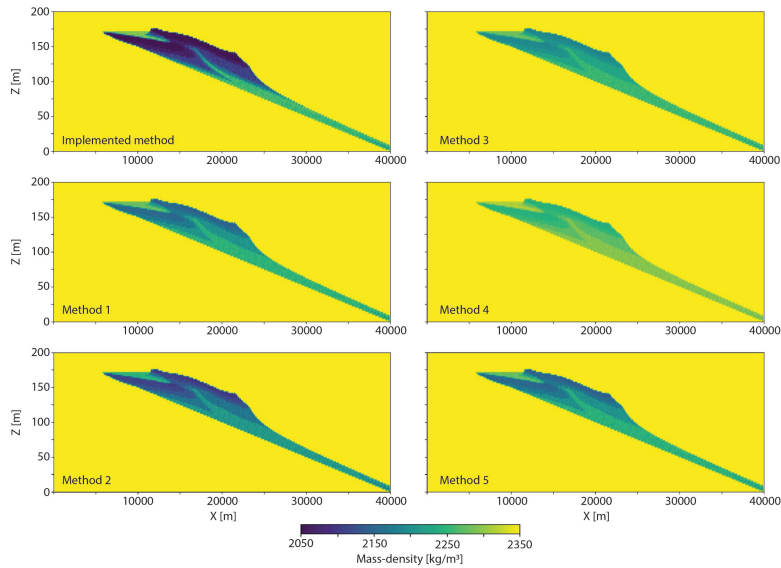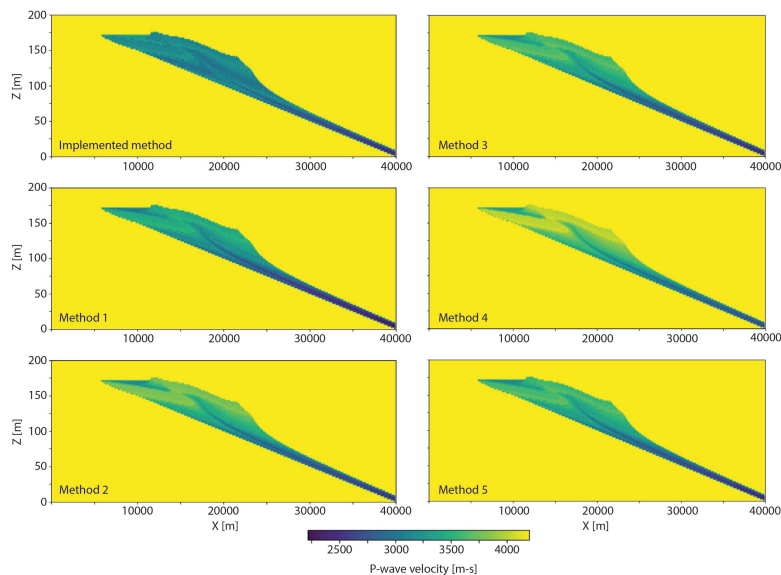
Figure 6.6: Mass-density (kg/m^3) distributions for a simulation with same initial porosity distribution and final porosity calculation based on the currently implemented method and other five porosity loss equations (Table 6.3). All simulations assume an overburden of $700m$. All simulations share the same scale bar. The results show differences in mass-density exceeding 6%.

Table 6.3, the relative difference in mass-density between methods reaches up to 4% at $400m$ overburden and decreases to a maximum of 2% at $3000m$. In contrast, P-wave velocity is more sensitive to porosity changes. The relative differences remain relatively consistent across all depths, ranging from approximately $1 - 7\%$ at shallower depths to $0 - 10\%$ at greater overburden.

Future research should investigate how these variations in mass density and P-wave velocity influence the seismic response. Additionally, it should quantify the effect of applying different porosity loss curves on this response. Such an analysis would help determine whether basin-specific porosity loss curves are necessary for accurately capturing stratigraphic heterogeneities in the subsurface. If the seismic response is significantly affected by property differences resulting from the use of various curves, then tailored, basin-specific models may be required. Conversely, if the impact is minimal, more general porosity loss curves may suffice for reservoir characterization.

Correlation between grain size, petrophysical, acoustic and elastic properties

The final improvement that could be made to the methodology presented in this thesis is to develop a strategy for directly relating grain size distribution to mass-

Figure 6.7: P-wave velocity (m/s) distributions for a simulation with same initial porosity distribution and final porosity calculation based on the currently implemented method and other five porosity loss equations (Table 6.3). All simulations assume an overburden of $700m$. All simulations share the same scale bar. The results show variations in P-wave velocity greater than 17%.

density and P-wave velocity. This would eliminate the need for intermediate porosity calculations, which are currently based on assumptions and have already been discussed along with potential alternatives. To begin exploring the assignment of acoustic properties based on grain size distribution, I conducted a preliminary analysis using samples collected during this project, as well as additional measurements provided by colleagues.

During the summer 2022 field campaign in Montana (2), we collected 45 sandstone samples from an outcrop. Laboratory analyses were conducted to measure grain density, bulk density, P-wave velocity, S-wave velocity, the P/S velocity ratio, and porosity. The primary objective was to identify potential spatial trends within the outcrops that could inform the conversion of grain size distribution data from stratigraphic modelling into petrophysical and elastic properties. However, no spatial trends were identified (2). We also measured grain size distribution-related properties for nine samples. Our main goal was identifying correlations between grain size distribution characteristics and elastic properties. We assessed the robustness of these correlations using bootstrapping techniques. The analysis revealed strong internal correlations within the grain size–related parameters, as well as among the seismic velocity measurements (Figure 6.8). A strong positive correlation was also observed between grain density and skewness. However, no other significant

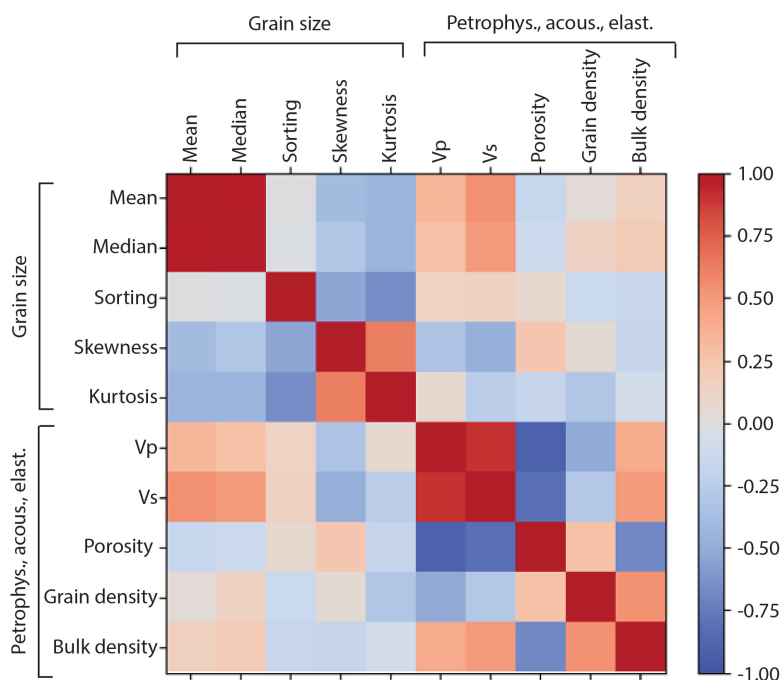correlation was found between grain size distribution properties and the acoustic or elastic properties.
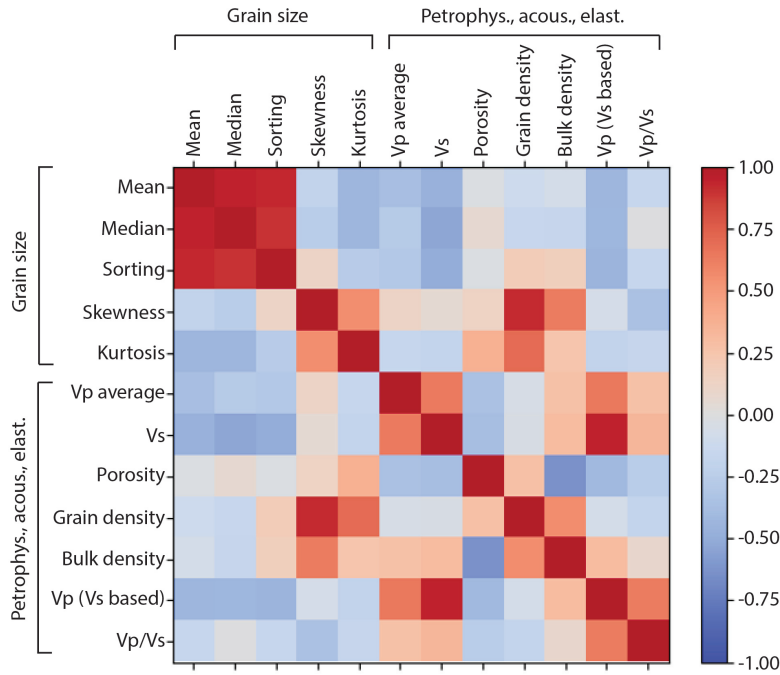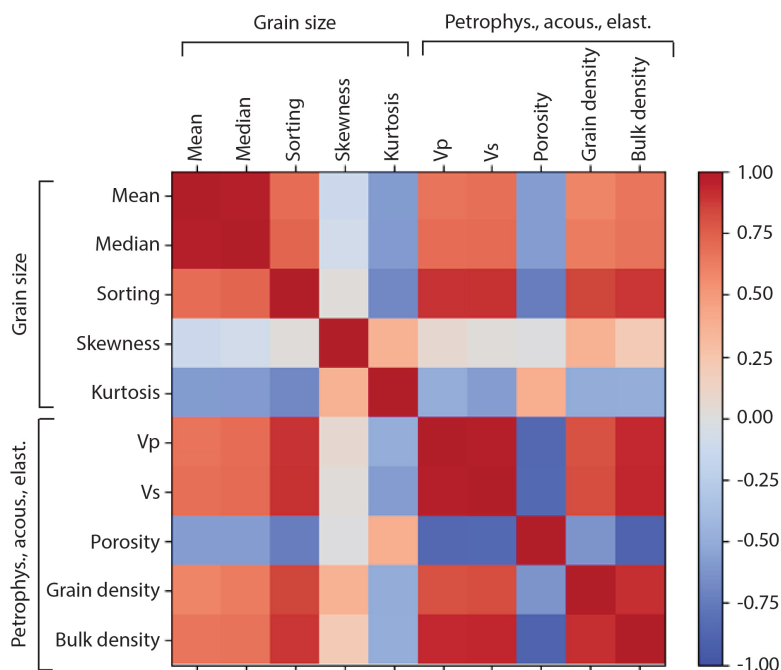

Figure 6.8: Correlation results (Pearson's correlation) between grain size and petrophysical/acoustic/elastic properties for the samples from the field ($N = 9$). Darker colours represent stronger correlations. Strong correlations are only measured among grain size related properties, among seismic velocities and grain density-skewness.

Our dataset ($N = 9$) is limited. To expand it, we incorporated an additional 9 core samples provided by a fellow PhD candidate [25]. Upon analysing the correlations and their statistical significance for the core data, the only strong and reliable correlation identified was between seismic velocities and sample porosity (Figure 6.9).

When combining both the field and core samples, the correlation analysis reveals a greater number of stronger relationships than when each dataset is considered separately (Figure 6.10). Notably, sorting now shows strong correlations with several key properties, including P-wave velocity, S-wave velocity, porosity, bulk density, and grain density. These findings are particularly promising for our project, as sorting is a direct output from geological modelling. If we can establish a reliable link between sorting and the acoustic and elastic properties (directly from the subsurface) required for seismic modelling, many of the assumptions and intermediate steps currently used in our method could potentially be eliminated. However, it is important to acknowledge that these conclusions are drawn from a limited dataset of just 18

Figure 6.9: Correlation results (Pearson's correlation) between grain size and petrophysical/acoustic/elastic properties for the samples from core data ($N = 9$). Darker colours represent stronger correlations. Strong correlations are only measured among grain size related properties and among seismic velocities.

samples and, thus, more research is needed.

Core analysis databases often contain measurements of properties such as grain density, bulk density, P-wave and S-wave velocities, and thermal characteristics, among others. If consistent correlations exist among these properties, it would enable our method to directly convert parameters like porosity into density and seismic velocities. Investigating these relationships could support a more targeted and data-driven assignment of properties in geological simulations, reducing reliance on empirical equations such as those proposed by Eberhart-Phillips, Han and Zoback [19].

Future research should focus on examining the correlations between grain size distribution parameters, such as sorting, skewness, and kurtosis, and seismic properties. With a comprehensive database that includes both grain size-related and petrophysical/elastic properties, it may eventually be possible to directly convert the output from BarSim into the parameters needed for numerical seismic modelling. Such direct conversion would avoid the need for assumptions. However, such a conversion will likely be reservoir-specific, given the variability in grain composition

and the distinct diagenetic histories of different reservoirs.

Figure 6.10: Correlation results (Pearson's correlation) between grain size and petrophysical/acoustic/elastic properties for the combination of all data points ($N = 18$). Darker colours represent stronger correlations. Strong correlations are now measured among grain size related properties, among seismic velocities, and sorting with all petrophysical, acoustic and elastic properties.

6.2.2. Consolidation and validation of the workflow

This thesis takes a theory-driven approach, aiming to establish a foundation for integrating geological and seismic data in the study of sub-seismic scale stratigraphic heterogeneities. For this reason, the seismic modelling and angle-dependent seismic analysis were conducted using geologically simple scenarios, involving basic environmental variations and short simulation durations. To fully demonstrate the workflow's potential, progressively more complex simulations are needed — by increasing both the simulation duration and the number of depositional environments involved in the simulations. To generate simulations that include multiple depositional environments, other stratigraphic forward modelling tools should be incorporated or new tools capable of generating realistic geological scenarios across multiple depositional environments simultaneously should be developed. Such tools should not only replicate heterogeneity development at or below the metre-scale but also

be computationally efficient to allow for the generation of large scenario datasets at low computational cost.

Future studies should expand the scope to investigate the effects of varying both the composition of the clastic particles and the nature of the pore fluids, as well as the role of diagenetic processes. Of particular interest is the analysis of reservoirs containing multiple fluid types. Understanding how different fluids interact with stratigraphic heterogeneities is crucial for interpreting the seismic response. In such cases, fluid distribution models should account for the sensitivity of each fluid type to the magnitude and scale of heterogeneity.

For the consolidation of the methodology, we have to establish a robust relationship between sedimentological, petrophysical, and acoustic properties. This relationship will, most likely, be reservoir-specific and will enable the generation of simulations that adequately capture the heterogeneities in the subsurface. As discussed in subsection 6.2.1, the definition of a connection between grain size distribution-related properties and acoustic properties may allow for the direct translation of stratigraphic forward model outputs (e.g., from BarSim) into parameters required for seismic modelling, reducing the need for intermediate porosity assumptions.

To validate the reliability of the proposed method, analogue analysis is recommended. For wave-dominated shoreface systems, outcrops from the Book Cliffs have already been matched with BarSim simulations [26] and can be used as reference. These simulations could be used to create a range scenarios in which the petrophysical and acoustic properties are assigned using: 1) the methodology presented in this thesis, 2) alternative strategies presented in the future outlook, 3) direct sampling in the field, and 4) subsurface data matched based on lithology, grain size, and diagenesis. These scenarios can be used to generate synthetic seismic data. It is also recommended to collect in situ seismic data from the outcrops, following the approach of Bailly *et al.* [27], to validate the outcomes.

As part of the effort to characterise the stratigraphic heterogeneities, angle gather data and other advanced visualization techniques should be further explored for their ability to detect sub-resolution features [28]. Machine learning methods are promising for extracting subtle variations in acoustic and elastic properties from seismic datasets. Current models, including those developed in this thesis, remain based on simplified, synthetic data, but they have already shown the limitations of synthetic modelling (Chapter 5). For now, ensuring proper data pre-processing and minimizing artifacts introduced by imaging techniques is essential. Bridging the gap to real-world applications will require more sophisticated simulations across a broader range of depositional settings to serve as training data.

The final objective is to enable machine learning algorithms to simultaneously differentiate between depositional settings and the types of heterogeneities present. If this task proves too complex, an alternative approach could involve a two-stage approach. In the first stage, the depositional environment is identified, followed by

a second stage that focuses on characterizing heterogeneities within that specific context. The initial stage may involve a general neural network trained to recognize the key features of various depositional settings and provide a preliminary classification. Alternatively, this classification can be performed by geoscientists, who are often able to quickly and reliably identify the depositional environment based on their expertise. In the second stage, heterogeneities at the metre-scale are analysed using a neural network specifically trained on data associated with the identified depositional environment. This targeted approach allows the machine learning model to detect heterogeneities that may elude human observation, enabling a more detailed reservoir characterization.

In this thesis, the influence of a complex overburden on the seismic response of metre-scale heterogeneities was not investigated. Instead, a simplified, layer-like overburden model was employed. However, in realistic geological settings, complexity within the overburden can attenuate seismic energy and distort wavefronts, thereby degrading the focus and illumination of the subsurface target. Consequently, the imaging quality achieved in Chapters 4 and 5 may not be representative of more geologically complex scenarios. In such cases, the application of target-oriented imaging techniques or borehole-based seismic methods—such as Vertical Seismic Profiling (VSP), crosswell seismic, or Distributed Acoustic Sensing (DAS)—may be necessary to obtain higher-resolution images of the subsurface target zone. Future research should evaluate whether the variations in seismic response observed in this study remain consistent when such acquisition and imaging methodologies are employed.

Ultimately, if this method were to be integrated into industry seismic data workflows, several key questions would need to be addressed: At which stage of the seismic analysis does the characterisation of metre-scale heterogeneities provide the most value? How can reservoir-specific rock physics models be incorporated into the approach? To what extent does the method enhance reservoir characterisation and reduce associated uncertainty? And, importantly, is the improvement significant enough to justify the additional time and resources required for its implementation? The answers to these questions can only be obtained through further research, but the method shows strong potential to enhance reservoir characterization and reduce uncertainty in seismic interpretation.

References

[1] A. Cuesta-Cano, J. Storms, G. Rongier and A. Martinius. *Supplementary material: Characterising reservoir heterogeneity in a wave-dominated system: sedimentological, stratigraphic, and petrophysical analysis of a field analogue (Judith River Formation, Late Cretaceous)*. 2025.

[2] G. Rongier, J. E. Storms and A. Cuesta-Cano. *pyBarSim*. 2023.

[3] J. Storms, G. Weltje, J. V. Duke, C. Geel and S. Kroonenberg. 'Process-response modeling of wave-dominated coastal systems: Simulating evolution and stratigraphy on geological timescales'. In: *Journal of Sedimentary Research* 72 (2 2002), pp. 226–239. DOI: 10.1306/052501720226.

[4] J. Storms. 'Event-based stratigraphic simulation of wave-dominated shallow-marine environments'. In: *Marine Geology* 199 (1-2 2003), pp. 83–100. DOI: 10.1016/S0025-3227(03)00144-0.

[5] J. Storms and D. Swift. 'Shallow-marine sequences as the building blocks of stratigraphy: Insights from numerical modelling'. In: *Basin Research* 15 (3 2003), pp. 287–303. DOI: 10.1046/j.1365-2117.2003.00207.x.

[6] A. Cuesta-Cano, A. Karimzadanzabi, J. E. A. Storms, G. Rongier, D. J. Verschuur and A. W. Martinius. 'Discretization of small-scale, stratigraphic heterogeneities and its impact on the seismic response: Lessons from the application of process-based modelling'. In: *Geophysical Prospecting* (Mar. 2025). ISSN: 0016-8025. DOI: 10.1111/1365-2478.70015.

[7] D. C. Beard and P. K. Weyl. 'Influence of Texture on Porosity and Permeability of Unconsolidated Sand'. In: *AAPG Bulletin* 57 (2 Feb. 1973), pp. 349–369. ISSN: 0149-1423. DOI: 10.1306/819A4272-16C5-11D7-8645000102C1865D.

[8] J. J. Rogers and W. B. Head. 'Relationships between Porosity, Median size, and Sorting Coefficients of Synthetic Sands'. In: *Journal of Sedimentary Petrology* 31 (3 1961), pp. 467–470.

[9] M. Scherer. 'Parameters Influencing Porosity in Sandstones: A Model for Sandstone Porosity Prediction'. In: *AAPG Bulletin* 71 (5 1987), pp. 485–491. ISSN: 0149-1423. DOI: 10.1306/94886ED9-1704-11D7-8645000102C1865D.

[10] R. L. Folk and W. C. Ward. 'Brazos River bar [Texas]; a study in the significance of grain size parameters'. In: *Journal of Sedimentary Research* 27 (1 Mar. 1957), pp. 3–26. ISSN: 1527-1404. DOI: 10.1306/74D70646-2B21-11D7-8648000102C1865D.

[11] G. M. Friedman. 'On sorting, Sorting Coefficients, and the Lognormality of the Grain-Size Distribution of Sandstones'. In: *The Journal of Geology* 70 (6 1962), pp. 737–753. URL: http://www.journals.uchicago.edu/t-and-c.

[12] P. D. Trask. 'Mechanical analysis of sediments by centrifuge'. In: *Economic Geology* 25 (6 Sept. 1930), pp. 581–599.

[13] B. Patro and B. K. Sahu. 'Factor analysis of sphericity and roundness data of clastic quartz grains: Environmental significance'. In: *Sedimentary Geology* 11 (1 May 1974), pp. 59–78. ISSN: 00370738. DOI: 10.1016/0037-0738(74)90005-0.

[14] G.-C. Cho, J. Dodds and J. C. Santamarina. 'Particle Shape Effects on Packing Density, Stiffness, and Strength: Natural and Crushed Sands'. In: *Journal of Geotechnical and Geoenvironmental Engineering* 132 (5 May 2006), pp. 591–602. ISSN: 1090-0241. DOI: 10.1061/(ASCE)1090-0241(2006)132:5(591).

[15] H. S. Suh, K. Y. Kim, J. Lee and T. S. Yun. 'Quantification of bulk form and angularity of particle with correlation of shear strength and packing density in sands'. In: *Engineering Geology* 220 (Mar. 2017), pp. 256–265. ISSN: 00137952. DOI: 10.1016/j.enggeo.2017.02.015.

[16] N. Estrada and W. F. Oquendo. 'Microstructure as a function of the grain size distribution for packings of frictionless disks: Effects of the size span and the shape of the distribution'. In: *Physical Review E* 96 (4 Oct. 2017), p. 042907. ISSN: 2470-0045. DOI: 10.1103/PhysRevE.96.042907.

[17] W. F. Oquendo-Patiño and N. Estrada. 'Finding the grain size distribution that produces the densest arrangement in frictional sphere packings: Revisiting and rediscovering the century-old Fuller and Thompson distribution'. In: *Physical Review E* 105 (6 June 2022), p. 064901. ISSN: 2470-0045. DOI: 10.1103/PhysRevE.105.064901.

[18] W. Rubey and M. Hubbert. 'Role of fluid pressure in mechanics of overthrust faulting: II. Overthrust belt in geosynclinal area of western Wyoming in light of fluid-pressure hypothesis'. In: *GSA Bulletin* 70 (2 1959), pp. 167–206.

[19] D. Eberhart-Phillips, D. H. Han and M. D. Zoback. 'Empirical relationships among seismic velocity, effective pressure, porosity, and clay content in sandstone'. In: *GEOPHYSICS* 54 (1 Feb. 1989), pp. 82–89. ISSN: 00168033. DOI: 10.1190/1.1442580.

[20] J. Wendebourg and J. Harbaugh. 'Chapter 4 Endowing simulated sequences with petrophysical flow properties'. In: *Computer Methods in the Geosciences*. Ed. by W. J. and H. J.W. Vol. 16. Pergamon, Jan. 1997, p. 81. DOI: 10.1016/S1874-561X(97)80005-3.

[21] P. Allen and J. Allen. *Basin Analysis: Principles and Applications*. Blackwell Scientific Publications, 1990.

[22] B. Baldwin and C. Butler. 'Compaction Curves'. In: *AAPG bulletin* 69 (4 1985), pp. 622–626.

[23] M. Giles. *Diagenesis: A Quantitative Perspective. Implications for Basin Modelling and Rock Property Prediction*. 1997, pp. 1–526.

[24] J. G. Sclater and P. A. F. Christie. 'Continental stretching: An explanation of the Post-Mid-Cretaceous subsidence of the central North Sea Basin'. In: *Journal of Geophysical Research: Solid Earth* 85 (B7 July 1980), pp. 3711–3739. ISSN: 0148-0227. DOI: 10.1029/JB085iB07p03711.

[25] P. K. Kaj, H. Abels, A. Barnhoorn, L. V. Meleza and P. Vardon. *Database of Experimental Data on Three Geothermal Plays in the Netherlands from the ProperBase Project*. 2024.

[26] K. Charvin, G. J. Hampson, K. L. Gallagher, J. E. Storms and R. Labourdette. 'Characterization of Controls on High-Resolution Stratigraphic Architecture in Wave-Dominated Shoreface–Shelf Parasequences Using Inverse Numerical Modeling'. In: *Journal of Sedimentary Research* 81 (8 Aug. 2011), pp. 562–578. ISSN: 1527-1404. DOI: 10.2110/JSR.2011.48.

[27] C. Bailly, J. Fortin, M. Adelinet and Y. Hamon. 'Upscaling of Elastic Properties in Carbonates: A Modeling Approach Based on a Multiscale Geophysical Data Set'. In: *Journal of Geophysical Research: Solid Earth* 124 (12 Dec. 2019), pp. 13021–13038. ISSN: 2169-9313. DOI: 10.1029/2019JB018391.

[28] A. Karimzadanzabi, A. Cuesta-Cano and E. Verschuur. 'Analyzing Angle-Gather Spectograms: Going Beyond Seismic Resolution'. In: *85th EAGE Annual Conference & Exhibition*. European Association of Geoscientists & Engineers, 2024, pp. 1–5. DOI: 10.3997/2214-4609.202410931.

Acknowledgements

After four years of adventure — filled with highs and lows, home-office and office days, train rides, carpooling conversations, and solo car-karaoke sessions — it is time to look back and thank all the people without whom this journey would not have been possible. This thesis is not only the result of academic effort but also a journey of personal growth and meaningful connections.

First and foremost, my supervisory team, who juggle a thousand responsibilities and still managed to give me feedback whenever I needed it. To the three of you, I am deeply grateful for the freedom you gave me to find my own voice as a scientist, to develop my ideas, and to take ownership of this project.

Thank you, **Allard**, for knowing how to interpret my mood just from my face—something no one else had ever achieved in a work environment. It has been a pleasure to spend time in the field with you and to learn from your thoughtful feedback. Thank you, **Joep**, for making me feel welcome from day one, even when everything was still online and the office felt deserted. Thank you for steering me away from spirals and guiding me through difficult moments. And **Guillaume**, I hope this was an adventure for you too — not everyone can claim to be someone's "first PhD." Thank you for the time, energy, and care you invested in this project, for your tireless feedback on every document, and for your constant dedication to improving the quality of the work.

This project would not have been possible without my favourite "geophysics-in-crime," **Azin**. You were endlessly patient, generous with your knowledge, and always ready to solve seismic modelling issues or troubleshoot DelftBlue, my dear (and temperamental) supercomputer. From our first online meeting, I knew this collaboration would be a success. I wish you all the best—may you find every success and opportunity you deserve.

To my carpool partners, **Camille** and **Jasper M.** — without you, I might have given up on commuting to the office altogether. Different driving styles, different waking hours, but always great conversations. Those hours in the car allowed me to get to know you both as brilliant scientists and even better human beings.

A special thank-you to the **Delphi consortium** and all its sponsors for funding this research. To **Eric**, for opening the doors to geologists and recognizing that interdisciplinary collaboration is the way forward in science — thank you. And to

Y lo mismo para mi cuadrilla de toda la vida y amigos en casa: **Ibai, Tania, Garri, Vane, Regi, Moni, Mikel, Aitor**. Posiblemente no nos hayamos visto a menudo, o haya cancelado planes de última hora, o haya desaparecido de vez en cuando, pero siempre me he sentido apoyada por vuestra amistad y me siento orgullosa de vuestro progreso. Sois aquello que me recuerda de dónde vengo, personas que nunca me habéis dejado de lado y que sé que os tengo para toda la vida.

Sobre todo a vosotros, **Ama y Aita**. De alguna manera vosotros ya sabíais que este era mi destino mucho antes de que yo me diera cuenta. Gracias, gracias y gracias, por ofrecerme la libertad de elegir mi camino y por animarme a luchar por este sueño. Gracias a esos cascarrabias que tengo por **abuelos** y a las estrellas que nos cuidan desde arriba.

And I must finish with you, *mi rubio*, *schatje* — the person who makes me feel home. **Ruben**, thank you for enduring these four years, for making me smile every day, for making me feel at home, for giving me a Dutch family, for trying to understand every step, for joining every crazy adventure to the other corner of the world or visiting the tulip fields next door, for cooking while I type these lines...

Curriculum Vitæ

Andrea Cuesta Cano

14-04-1995   Born in Valle de Trápaga / Trapagaran, Spain.

Education

2013–2017   BSc in Geology
Universidad del País Vasco EHU/UPV (Spain)

2017–2019   MSc Earth Structure & Dynamics
Utrecht University (The Netherlands)

2021–2025   PhD. Applied Geology
Delft University of Technology
Thesis: Detection of stratigraphic heterogeneities at sub-seismic scale: Lessons from wave-dominated depositional environments
Promotors: Prof. A.W. Martinius & dr. J.E.A. Storms
Supervisor: dr. G. Rongier

Awards

2017   National Award for Excellence in Academic Performance 2017
Issued by Ministry of Education of Spain

2017   Bachelor's Degree Extraordinary Award
Issued by EHU/UPV

Working Experience

Year	Position	Institution
2025–	Customer Success Specialist & Geospatial Data Analyst	Orbital Eye
2020–2021	Research Assistant	Utrecht University
2019	Bright Minds Assistantship	Utrecht University
2018	Geoscience Intern	Total S.A. (Pau, France)
2017	Ikasiker grant (Basque Government)	EHU/UPV (Spain)

Volunteer Work

Year	Position	Institution
2024–	Board member Geocommunication and Public Engagement	EAGE
2023–	Communication volunteer	CENL/SWNL
2022–	LinkedIn manager	SGE
2021–2024	Board member	GAIA Netwerk

List of Publications

- **Cuesta Cano, A.**, Van Stappen, J. F., Wolterbeek, T. K. T., & Hangx, S. J. T. (2021). Uniaxial compaction of sand using 4D X-ray tomography: The effect of mineralogy on grain-scale compaction mechanisms. *Materials Today Communications*, 26, 101881. https://doi.org/10.1016/j.mtcomm.2020.101881

- **Cuesta Cano, A.**, Karimzadanzabi, A., Storms, J. E. A., Rongier, G., & Martinius, A. W. (2023). Use of forward stratigraphic modelling for the detection of sub-seismic scale heterogeneities in shallow marine environments. In *84th EAGE Annual Conference & Exhibition*, 1–5. https://doi.org/10.3997/2214-4609.202310486

- **Cuesta Cano, A.**, Karimzadanzabi, A., Storms, J. E. A., Rongier, G., Martinius, A. W., & Verschuur, D. J. (2025). Discretization of small-scale, stratigraphic heterogeneities and its impact on the seismic response: Lessons from the application of process-based modelling. *Geophysical Prospecting*. https://doi.org/10.1111/1365-2478.70015

- **Cuesta Cano, A.**, Storms, J., Rongier, G., & Martinius, A. (2024). 3D model of a clastic, shallow marine outcrop in the Western Interior Basin (Parkman Sandstone, Judith River Formation, Cretaceous). Database. *4TU.ResearchData*.

- **Cuesta Cano, A.**, Storms, J., Rongier, G., & Martinius, A. (2025). Supplementary material: Characterising reservoir heterogeneity in a wave-dominated system: sedimentological, stratigraphic, and petrophysical analysis of a field analogue (Judith River Formation, Late Cretaceous). Database. *4TU.ResearchData*.

- Karimzadanzabi, A., **Cuesta Cano, A.**, & Verschuur, E. J. (2023). Geologic stratigraphic scenario testing via deep learning: Towards imaging beyond seismic resolution. In *84th EAGE Annual Conference & Exhibition*, 1–5. https://doi.org/10.3997/2214-4609.2023101151

- Karimzadanzabi, A., **Cuesta Cano, A.**, & Verschuur, E. (2024). Analyzing angle-gather spectograms: Going beyond seismic resolution. In *85th EAGE Annual Conference & Exhibition*, 1–5. https://doi.org/10.3997/2214-4609.202410931

- Rongier, G., Storms, J. E. A., & **Cuesta Cano, A.** (2023). pyBarSim. *4TU.ResearchData. Software*.

- **Cuesta Cano, A.**, Martinius, A. W., Storms, J. E. A., & Rongier, G. (2023). Introduction to a new clastic, wave-dominated shoreline system in southern Montana (USA). In *36th IAS Meeting of Sedimentology*, Dubrovnik.

- Trabucho Alexandre, J., de Bresser, H., **Cuesta Cano, A.**, & Veenma, Y. (2020). Watch and Learn: Promoting student autonomy and competence in the field with just-in-time knowledge clips. *EGU General Assembly Conference Abstracts*. https://doi.org/10.5194/egusphere-egu2020-7048